



AFRL-RX-WP-TR-2013-0226

QUANTITATIVE INSPECTION TECHNOLOGIES FOR AGING MILITARY AIRCRAFT

**D. Barnard, L. J. Bond, J. Bowler, N. Bowler, L. Brasche, C.-P. Chiou, A. Frishman,
J. Gray, T. Gray, S. D. Holland, T. Jensen, C. C. H. Lo, F. J. Margetan, W. Q. Meeker,
N. Nakagawa, and R. A. Roberts**

**Iowa State University
Center for Nondestructive Evaluation**

**NOVEMBER 2013
Final Report**

Approved for public release; distribution is unlimited

See additional restrictions described on inside pages

STINFO COPY

**AIR FORCE RESEARCH LABORATORY
MATERIALS AND MANUFACTURING DIRECTORATE
WRIGHT-PATTERSON AIR FORCE BASE, OH 45433-7750
AIR FORCE MATERIAL COMMAND
UNITED STATES AIR FORCE**

NOTICE AND SIGNATURE PAGE

Using Government drawings, specifications, or other data included in this document for any purpose other than Government procurement does not in any way obligate the U.S. Government. The fact that the Government formulated or supplied the drawings, specifications, or other data does not license the holder or any other person or corporation; or convey any rights or permission to manufacture, use, or sell any patented invention that may relate to them.

This report was cleared for public release by the Wright-Patterson Air Force Base (WPAFB) Public Affairs Office and is available to the general public, including foreign nationals. Copies may be obtained from the Defense Technical Information Center (DTIC) (<http://www.dtic.mil>).

AFRL-RX-WP-TR-2013-0226 HAS BEEN REVIEWED AND IS APPROVED FOR PUBLICATION IN ACCORDANCE WITH THE ASSIGNED DISTRIBUTION STATEMENT.

//signature//
CHARLES BUYNAK, Project Engineer
NDE Branch
Metals, Ceramics, and NDE Division

//signature//
STEVE RUSS, Acting Chief
NDE Branch
Metals, Ceramics, and NDE Division

//signature//
ROBERT MARSHALL, Deputy Division Chief
Metals, Ceramics, and NDE Division
Materials and Manufacturing Directorate

This report is published in the interest of scientific and technical information exchange, and its publication does not constitute the Government's approval or disapproval of its ideas or findings.

| REPORT DOCUMENTATION PAGE | | | | | Form Approved OMB No. 0704-0188 | |
|---|-----------------------------|------------------------------|---------------------------------------|---|--|--|
| <p>The public reporting burden for this collection of information is estimated to average 1 hour per response, including the time for reviewing instructions, searching existing data sources, gathering and maintaining the data needed, and completing and reviewing the collection of information. Send comments regarding this burden estimate or any other aspect of this collection of information, including suggestions for reducing this burden, to Department of Defense, Washington Headquarters Services, Directorate for Information Operations and Reports (0704-0188), 1215 Jefferson Davis Highway, Suite 1204, Arlington, VA 22202-4302. Respondents should be aware that notwithstanding any other provision of law, no person shall be subject to any penalty for failing to comply with a collection of information if it does not display a currently valid OMB control number. PLEASE DO NOT RETURN YOUR FORM TO THE ABOVE ADDRESS.</p> | | | | | | |
| 1. REPORT DATE (DD-MM-YY) November 2013 | | 2. REPORT TYPE Final | | 3. DATES COVERED (From - To) 30 April 2004 – 28 February 2013 | | |
| 4. TITLE AND SUBTITLE QUANTITATIVE INSPECTION TECHNOLOGIES FOR AGING MILITARY AIRCRAFT | | | | 5a. CONTRACT NUMBER FA8650-04-C-5228 | | |
| | | | | 5b. GRANT NUMBER | | |
| | | | | 5c. PROGRAM ELEMENT NUMBER 63112F | | |
| 6. AUTHOR(S) D. Barnard, L. J. Bond, J. Bowler, N. Bowler, L. Brasche, C.-P. Chiou, A. Frishman, J. Gray, T. Gray, S. D. Holland, T. Jensen, C. C. H. Lo, F. J. Margetan, W. Q. Meeker, N. Nakagawa, and R. A. Roberts | | | | 5d. PROJECT NUMBER 3153 | | |
| | | | | 5e. TASK NUMBER 27 | | |
| | | | | 5f. WORK UNIT NUMBER X03E (41300100) | | |
| 7. PERFORMING ORGANIZATION NAME(S) AND ADDRESS(ES) Iowa State University Center for Nondestructive Evaluation 1915 Scholl Road, ASCII Building Ames, IA 50011 | | | | 8. PERFORMING ORGANIZATION REPORT NUMBER | | |
| 9. SPONSORING/MONITORING AGENCY NAME(S) AND ADDRESS(ES) Air Force Research Laboratory Materials and Manufacturing Directorate Wright-Patterson Air Force Base, OH 45433-7750 Air Force Material Command United States Air Force | | | | 10. SPONSORING/MONITORING AGENCY ACRONYM(S) AFRL/RXCA | | |
| | | | | 11. SPONSORING/MONITORING AGENCY REPORT NUMBER(S) AFRL-RX-WP-TR-2013-0226 | | |
| 12. DISTRIBUTION/AVAILABILITY STATEMENT Approved for public release; distribution unlimited. | | | | | | |
| 13. SUPPLEMENTARY NOTES PA Case Number: 88ABW-2013-4940; Approved on 21 Nov 2013. Report contains color. | | | | | | |
| 14. ABSTRACT Nondestructive evaluation plays a crucial role in the safety of flight, with an increasing importance as military fleet ages and the mission profile is expanded beyond the original design interest. The program completed by the Center for Nondestructive Evaluation at Iowa State University included development of new capabilities to quantify residual stress profiles in Al, Ti, and Ni alloys; expansion of simulation tools for eddy current, ultrasonics, and radiography; advances in probability of detection methodologies including model-assisted POD; improved understanding of emerging methods such as terahertz imaging and vibrothermography; and development of new education materials. | | | | | | |
| 15. SUBJECT TERMS Nondestructive evaluation, probability of detection, ultrasonics, eddy current, terahertz imaging, vibrothermography, NDE simulator, ultrasonic phased array, guided waves, structural health monitoring | | | | | | |
| 16. SECURITY CLASSIFICATION OF: | | | 17. LIMITATION OF ABSTRACT: SAR | 18. NUMBER OF PAGES 250 | 19a. NAME OF RESPONSIBLE PERSON (Monitor) Charles F. Buynak | |
| a. REPORT Unclassified | b. ABSTRACT Unclassified | c. THIS PAGE Unclassified | | | 19b. TELEPHONE NUMBER (Include Area Code) 937-255-9807 | |

Table of Contents

| Section | Page |
|---|------|
| List of Figures | ii |
| List of Tables | x |
| 1. Summary | 1 |
| 2. Introduction | 3 |
| 2.1 Background | 5 |
| 2.2 Motivation | 12 |
| 2.3 Objectives | 12 |
| 3. Project Summaries | 13 |
| 3.1 Electromagnetic Characterization of Near-Surface Treatment, Roughness, Damage, and Material Deviation..... | 13 |
| 3.2 High Energy X-Ray Diffraction Measurements of Stress Profiles in Bulk Materials..... | 34 |
| 3.3 Simulation of Eddy Current Inspection of Aircraft | 43 |
| 3.4 Model-Assisted Probability of Detection (MAPOD) | 53 |
| 3.5 Eddy Current Model Validation Toward Model-Assisted POD Methodology | 57 |
| 3.6 Probability of Detection Advances | 89 |
| 3.7 Phased Array Measurement Model and POD Calculation | 96 |
| 3.8 Comparison of Defect Standards Versus Real Defects: The Effect of Defect Morphology on NDE Signals..... | 116 |
| 3.9 Fundamental Studies of Guided Wave Propagation for Structural Health Monitoring..... | 126 |
| 3.10 Fundamentals of Detecting Tight Cracks Using Vibrothermography Inspection..... | 142 |
| 3.11 Electromagnetic Characterization of Composite Materials Using Microwave and Capacitive Methods | 151 |
| 3.12 Advanced Terahertz Capabilities for Aerospace Material Inspections | 162 |
| 3.13 Novel NDE Concepts for Inspection of Inaccessible and Complicated Structures..... | 175 |
| 3.14 Contributions to NDE Education | 185 |
| 4. Concluding Remarks..... | 188 |
| 4.1 Future Directions | 197 |
| 5. References | 201 |
| Appendix A | 210 |
| Appendix B | 213 |
| Appendix C | 220 |
| Appendix D | 222 |

List of Figures

| Figure | Page |
|--|------|
| Figure 1. (a) The Previous SHFEC Measurement System Utilizing A Differential Pair Of Spiral Coils On A Single PCB Board. (b) Upgraded SHFEC System With A Pair Of Standalone PCB Coils With On-Board Impedance-Matching Buffers | 15 |
| Figure 2. A) The Simulated Layer Specimen For The Stage 2 Validation Study, Which Consists Of A 103 μm Thick Inconel Foil ($\sigma = 1.342\%$ IACS Measured By DCPD) On An Inconel Block ($\sigma = 1.38\%$ IACS). (B) The Measured And Modeled V-Component Signals For The Layer Specimen. The Inverted Foil Conductivity Of 1.348% IACS Agrees With The DCPD Value Of 1.342% IACS | 17 |
| Figure 3. Inverted Conductivity Profiles For Inconel 718 Shot Peened At 6A, 9A, 13A And 17A | 18 |
| Figure 4. Plots Of The Conductivity Profile Function $g\left(\frac{z}{d}\right)$ For (a) A Constant Shift In Conductivity With One Parameter (The Amount Of Shift) To Describe The Bulk Conductivity Difference Between A Peened Sample And The Reference Sample Used In The V-Component Measurements; (b) The Step Function With Two Parameters (Step Height And Depth) To Account For The Surface Damages By Shot Peening; And (c) A Peak Function With Exponential Decay To Describe Typical Residual Stress Profiles Created By Shot Peening. Also Shown Is The Functional Form Of F In Equation (6) | 20 |
| Figure 5. Swept Frequency V-Component Signals Measured From A Series Of Inconel 718 Samples Shot Peened At 4A, 8A And 12A Using A 12mm, 14-Turn PCB Coil And A Network Analyzer (From 1 MHz To 60 MHz), And A 244-Turn Coil And An Impedance Analyzer (100 KHz To 3 MHz)..... | 20 |
| Figure 6. Scanning And Transmission Electron Micrographs Of Heat Treated Inconel 718 Samples: (a) Sample II; (b) Sample IV Showing γ'' Precipitates; (c) Sample V Showing γ'' Precipitates; (d) Sample VI Showing Coarse γ'' Precipitates And δ At Grain Boundaries; (e) Sample VII Showing Copious δ Platelets And γ'' Inside The Grains (Right) | 23 |
| Figure 7. V-Component EC Signals Versus Frequency (In Log_{10} Scale) Measured From Sample II Before And After Shot Peening At (a) 4A, (b) 8A And (c) 12A. The Error Bars Correspond To One Standard Deviation Of Five Repeated Measurements | 24 |
| Figure 8. V-Component EC Signals Versus Frequency For The Shot Peened Inconel 718 Samples In The Ascending Order Of Hardness: (a) I; (b) VII, (c) VI, (d) III, (e) IV And (f) V..... | 24 |
| Figure 9. A SEM Image Of The Cross-Section Of Sample VI After Shot Peening. Slip Damage Is Observed Up To About 30 μm In Depth Below The Peened Surface | 25 |
| Figure 10. Inverted Conductivity Deviation Profiles Of The Shot-Peened Inconel 718..... | 27 |
| Figure 11. A Schematic Showing The Cross-Section Of Sample VII. Also Shown Are The SEM Images Taken Near The (a) Peened (Top Edge) Surface, (b) Non-Peened (Free) Surface (Bottom Edge), And (c) The Bulk Of The Sample. Larger Amounts Of δ Phase Were Observed Near The Peened And Non-Peened Surface Than In The Sample Bulk. (d) Depth Profiles Of The Volume Fractions Of Secondary Phase Precipitates And The Estimated Conductivity Profiles Based On The Calibration Shown In Figure 12 | 28 |
| Figure 12. Plot Of The Bulk Conductivity Versus Volume Fraction Of Secondary Phase Precipitates For Samples II, VI And VII. The Straight Line Represents A Linear Fit To The Data (Symbol)..... | 28 |
| Figure 13. Θ -2 θ Spectra Measured From The Pristine Surface, And From The Peened Surface Of An Inconel 718 Sample Before And After A 96 Mm-Thick Surface Layer Was Removed. (c) Intensity Ratio Of The (111) Peak To The (022) Peak Versus Depth From The Peened Surface Showing A Change Of Texture With Depth. (d) Schematic Illustration Of The Mass Flow Caused By Shot Peening And The Resulting Texture | 30 |
| Figure 14. (a) Measured And Best-Fitted V-Component EC Signals Measured From The Inconel 718 Sample Shot Peened At 17A. (b) Inverted Residual Stress Profile Compared To That Measured By XRD Layer Removal Method | 31 |

| | |
|--|----|
| Figure 15. Schematic Representation Of The HEXRD System. The X-Ray Source Is Located To The Left, And The Detector To The Right. The Inset Shows Typical Dimensions Of The Probing Volume Used For Studies Of Residual Stress In Metallic Alloys..... | 35 |
| Figure 16. Images Of The HEXRD System Looking, Left, Towards The X-Ray Source, And Right, Towards The X-Ray Detector | 36 |
| Figure 17. Data From A θ - 2θ Scan On An Aluminum Sample Plotted In Terms Of The Energy And Angle Of Diffracted X-Rays As A Two-Dimensional Scatter Plot. Blue And Black Colors Indicate Higher Intensity. These Data Are Then Projected Onto The Horizontal And Vertical Axes For Selected Ranges Indicated By The Dashed Horizontal And Vertical Lines, Respectively | 37 |
| Figure 18. Diffraction Intensity As A Function Of Depth Of Probe Volume In The Sample, For Different Shot-Peen Levels For Aluminum Samples (Left), And Ti-6Al-4V Samples (Right). To Obtain These Plots, We Have Collected Data At Fixed Angles For Each Material And Integrated Over Energies Within 0.5 Kev Of The Tungsten $K_{\alpha 1}$ Line | 38 |
| Figure 19. Comparison Of Pristine And Shot-Peened Inconel 718 Samples. The Plot To The Left Shows θ - 2θ Scans Near The Surface Of The Samples, While The Plot To The Right Shows Diffraction Intensity As A Function Of Depth For The Nominal Diffraction Angle | 39 |
| Figure 20. Strain-Depth Profile Curves Calculated From The Al-6061 Diffraction Data Of Figure 4 Using The Normalized-Intensity Method Described In The Text | 40 |
| Figure 21. Relative Intensity Expected For Diffraction From Different Materials As A Function Of Depth | 40 |
| Figure 22. Diffraction Depth Profiles For Different Lattice Planes In An Aluminum 2024 Alloy Sample | 41 |
| Figure 23. (A) Rotary Coil In A Borehole Interaction With A Semi-Elliptical Crack (B) Test Specimen For Validating Impedance Predictions From The Rotary Probe | 46 |
| Figure 24. (A) Circumferential And (B) Longitudinal Notch Used For Validation Of The Borehole-Crack Calculations. (C) Illustrates A Volume Element Several Of Which Are Used To Construct The Region Of A Circumferential Notch (D) Shows The Volume Element Of The Type Used To Construct The Region Of A Longitudinal Notch | 46 |
| Figure 25. Comparison Of The Variation Of Coil Impedance With Position For (A) Transverse Notch (B) Longitudinal Notch | 48 |
| Figure 26. Scalar Potential Representing The Coil Field Of A Double-D Differential Probe For The Simulation Of Bolt-Hole Inspection..... | 49 |
| Figure 27. Coil Emerging From A Hole In A Conducting Plate Or Half-Space | 51 |
| Figure 28. Variation Of The Coil Impedance With Axial Position As A Coil Emerges From A Hole In A Plate. Experimental Data Is Compared With Theoretical Predictions | 51 |
| Figure 29. Screen Capture From MAPOD Website, Maintained By CNDE..... | 54 |
| Figure 30. Protocol Describing MAPOD Approach To POD Assessment..... | 55 |
| Figure 31. Illustration Showing The Two Step Approach To Relating Open EDM Reference Notches To Actual Cracks. The First Step Is To Develop An Algorithm That Accurately Captures The Notch Width Effect And Use This To Calculate A Signal For An Idealized Crack. The Second Step Involves Relating The Calculated Signal From The Idealized Crack To An Actual Crack With Its Morphology Effects | 59 |
| Figure 32. Close-Up Photograph Of Specimen 1227-51 Notches And Example Photographs Of The Replicas. Six EDM Notches Of Nominally Identical Dimensions (0.030" Long By 0.015" Deep) Are Arranged In Two Rows, Where Row 1 Consists Of Those Of A Rectangular Shape, While Row 2 Consists Of Semi-Circular Notches. Notice The Varying Width Values That Are 0.001" (Column A), 0.003" (Column B), And 0.005" (Column C). 1"=25.4 mm | 60 |
| Figure 33. Examples Of Notch Signal Traces From The 2 MHz Differential Probe Mapped Onto The Output Vector Voltage Plane (Measured And Computed) For The 0.030"-Long Rectangular Notches Of The Varying Widths (0.001", 0.003", 0.005") In The Ti-6246 Specimen, And. In The Labels, "RT" And "SC" Refer Respectively To The Rectangular And Semi-Circular Shapes, And 1-3-5 Stands For The Three Widths..... | 61 |

| | |
|--|----|
| Figure 34. Cumulative Compilation Of Comparison Results Between Theory And Experiment For Peak-To-Peak Signal Voltages, Calculated And Measured For The 2 MHz Commercial Differential Probe. The Short-Hand Notation Is Used To Label The Notches: “30” And “20” Stand For The Length Values Of 0.030” And 0.020”, “RT” And “SC” For Rectangular And Semi-Circular Shapes, And {5,3,1} Denote The Width Values Of 0.005”, 0.003”, 0.001”, Respectively. The Two Sets Of The Twelve Notches Are Placed On The Ti-6-2-4-6 And IN100 Blocks | 62 |
| Figure 35. The Vertical Peak-To-Peak Voltage Signals Vs. The Notch Width Plots. The Experimental Data Are Superposed With The Model Predictions For The 0.030” Notches, Indicated By The Broken Lines. The Model Enables The Extrapolation Of The Notch-Width Dependency Down To The Zero Width, Predicting The 35% Signal Reduction For The Zero-Width Semicircular Notch Compared To The Widest (0.005”) Rectangular Notch..... | 63 |
| Figure 36. (a) Experimental Set Up For <i>In Situ</i> EC Measurements On A Fatigue Crack Sample Grown In An Al Bar Under Cyclic Loads In The Four Point Bending Configuration. (b) Acquired Applied Load And EC Signals From A Fatigue Crack Subjected To Dynamic Load Over A Loading Cycle | 64 |
| Figure 37. Experimental Set For EC Scans On Fatigue Crack Sample Subjected To Tensile Or Compressive Stresses In A Four Point Bending Configuration..... | 65 |
| Figure 38. Plots Of Amplitude Of The Vertical Components Of The Crack Signals Versus The Stress Level For The Al Fatigue Crack Samples (a) S1 (0.055”); (b) S2 (0.162”); (c) S3 (0.195”) And (D) S5 (0.350”)..... | 66 |
| Figure 39. Plots Of The Amplitudes Of The Vertical Component Of The Crack Signals Versus The Stress Magnitude For A 0.114”-Long Fatigue Crack In Ti 6-4..... | 66 |
| Figure 40. Chart Showing Inconel Experimental And Numerical Data As A Function Of Notch/Crack Length. The Solid Line Is A Log-Fit Trend Line Of The Crack Signals Under No-Load Conditions | 68 |
| Figure 41. Chart Showing Titanium Experimental And Numerical Data As A Function Of Notch/Crack Length.. | 69 |
| Figure 42. Drawing Showing The General Configuration Of Scallop Specimens (Left) And Various Radial And Axial Locations Of The Cracks (Right) | 70 |
| Figure 43. Overall Photograph Of The Special Probe Purchased For The Scallop Specimen Experimental Measurements. Sensing Coils Are Shown In The Insert Along Side Of A 0.0038” Diameter Wire | 71 |
| Figure 44. Photographs Of The Edge Crack Scanning Setup: (A) The ECP Probe Element Consisting Of A Pair Of Small Pickup Coils And A Larger Edge-On Drive Coil. (B) Scallop-Shaped Edge Crack Specimens. (C) The Probe Scanning The Interior Of The Scallop Shape Where Cracks Are Located | 72 |
| Figure 45. Example Of The Scan Data Plotted As Both A Wire Mesh Diagram And Contour Plot (Left) And The Resulting Line Plots Of The Slices For The Vertical Portion Of The Signal. Note The Slice Data For Two Scans Is Shown To Demonstrate The Measurement Repeatability..... | 72 |
| Figure 46. A Plot Showing The Correlation Between Signal Strength And Crack Length For The Complete Sample Set Of Scallop Specimens | 73 |
| Figure 47. Probability Of Detection Curves Calculated As A Function Of The Surface Crack Length (In Inches) From The Single Point Max Signal Data. Also Shown Are The A90/95 Etc., i.e., The Detectable Crack Length At The 90% POD With The Lower 95% Confidence..... | 74 |
| Figure 48. CAD Model Of The ECP Probe, Consisting Of Meshed Objects Representing The Drive Coil, Ferrite Core, And Pickup Coil Pair | 75 |
| Figure 49. The CAD Models Used As Input To The EC Simulation Model, Representing The ECP Probe Model That Scans Over The Sample Edge With The Chamfers, Between Which A Rectangular Crack Is Generated..... | 76 |
| Figure 50. The Assumed Crack Mesh Generated By The Model Code During The Model Runs. The Notations TC, CT, And BC Stand For The Top Chamfer, Center, And Bottom Chamfer, Respectively, Indicating Approximate Locations..... | 76 |
| Figure 51. Characteristic Four-Prong (Alternating Peaks And Valleys) Responses Of The “Flag” Probe (Side-Mounted Excitation Coil With A Differential Pair Of Pickup Coils Of A ~0.1 Mm Diameter) As Seen In The Experiment (Left) And Computation (Right) | 77 |

| | |
|---|-----|
| Figure 52. A Typical Experimental Raster Scan Data, Represented By The Sample “45” Data, Exhibiting A Symmetrical 4-Prong Crack Response, Consisting Of Alternating Double Peaks And Valleys. The Peaks And Valleys Are Symmetrical Such That, When Taking The Upper (“R”) And Lower (“L”) Slices Of The Peak-Valley Pairs, One Finds Overlapping Slices After Flipping The Sign Of One Of The Slices | 78 |
| Figure 53. Examples Of Experimental Data Signals In Terms Of Min-Max Voltage Deflections For The Notch (A) And A Crack (B). These Peak-To-Peak Voltage Responses Are Found To Be Repeatable. The EDM Notch Is 1227-26-2A (0.50 X 0.25 X .025 Mm), Yielding $V_p-P = 0$ | 78 |
| Figure 54. Experimental \hat{A} -Vs-A Plots For Edge Cracks And Flat-Surface EDM Notches..... | 79 |
| Figure 55. Computed \hat{A} -Vs-A Relations For Edge Cracks And Flat-Surface EDM Notches. The Crack Sample “53” Is An Outlier And Excluded From The Trend Line Determination | 81 |
| Figure 56. Computed \hat{A} -Vs-A Relations For Edge Cracks And Flat-Surface EDM Notches. The Crack Sample “53” Is An Outlier And Excluded From The Trend Line Determination | 81 |
| Figure 57. Experiment Vs. Theory Plots For The Notches, As Well As For The Cracks. The Notch Data, Or The Gradient Of The Trend, Was Used To Determine The Calibration Constant Of 69 [V/ Ω] For The Instrument Parameters Used. Similarly Plotted Are The Experiment Vs. Theory Correlations For The Edge Cracks That Indicate The Significant Signal Variability..... | 82 |
| Figure 58. The \hat{A} -Vs-A Plots For Both Experimental Data (Symbols) And Computation (Lines) Where The Computed Impedance Values Are Converted To The Voltage By The Calibration Constant 69 [V/ Ω]. Notice The Downward Skewed Crack Data Distributions | 83 |
| Figure 59. A) Illustration Of The 2D Model Geometry; A Square ($A \times a$) Conductive Domain With A Notch-Like Defect ($L \times w$) Where $L/A = 0.5$ While W/A Ranges Between 0.1 And 0.5. (B) The Impedance Plane Plot Of The Impedance Changes With The Crack Width As A Parameter. Note That The Impedance Change Is Normalized Per Unit Length For The 2D Problem | 85 |
| Figure 60. The Real Part Of The Solutions For A Sphere Under The Dirichlet Boundary Condition; (A) The MLS Vs. Exact Solutions, (B) The BEM Vs. Exact Solutions | 86 |
| Figure 61. Overlay Plot Showing The Dark Region Where The Probability Of Detection Is High And The Probability Of An Alarm Is Low | 90 |
| Figure 62. Plot Of Simulated Data That Would Allow The Joint Estimation Of A Crack-Size Distribution And POD | 91 |
| Figure 63. Typical Linear Phased Array Transducer With Rectangular Elements And A Sample Focal Law Showing Time Delays For Focusing..... | 97 |
| Figure 64. Phased Array Probe Field Calculations Showing (Left) Pressure Amplitudes On An Individual Element Face For Several Modeling Assumptions And (Right) Corresponding Pressure Fields In Steel For Full Aperture | 98 |
| Figure 65. Comparisons Of Model Calculations For Phased Array Probe On Lucite Wedge Radiating Into Steel Along X (Left) And Z (Right) Directions, $D/\lambda = 0.68$. Top Plots Are For No Beam Steering (45° Refraction), Middle Plots Are For -15° Steering (30° Refraction), Bottom Plots Are For $+15^\circ$ Steering (60° Refraction)..... | 100 |
| Figure 66. Amplitude Correction Factors For Linear Phased Multigaussian Model Of A Phased Array Probe For A Range Of Steering Angles (θ , Degrees) And Element Widths (D/λ) | 101 |
| Figure 67. Example Of Utsim Display Of Focal Law For Linear Phased Array Probe Applied To An Aerospace Component..... | 102 |
| Figure 68. Schematic Of Phased Array Measurement Contribution For An Element Pair And The Total Response From All Elements..... | 103 |
| Figure 69. Element Errors For A Linear Phased Array Probe. Top Figure Shows Immersion Pulse-Echo Waveforms From A Flat Surface For Two Elements; Bottom Figures Are Zoomed-In Images Of The Dominant Positive Peak (Left) And Primary Zero Crossing (Right) Regions | 105 |

| | |
|---|-----|
| Figure 70. (A)-(B): Magnitudes And Phases Of The Spectra Of The Single-Element Front-Wall Responses, After Modification To Correct For Beam Propagation Effects (I.E, These Are Essentially Single Element Efficiency Functions) . Each Panel Contains 32 Curves, Corresponding To The 32 Elements In The Transducer Array. (C)-(D): The Same Curves After Rescaling And Time Shifting Using The Residual Strength And Time-Delay Parameters..... | 106 |
| Figure 71. Comparisons Of Measured And Predicted Back-Wall Responses For The Stainless Steel Test Block. (A): Descriptions Of The Various Measurements, Including The Nature Of The Reference Signal For Each Test Trial. (B)–(D): Comparisons Of Measured And Predicted Back-Wall Spectra. (E): Comparisons Of Measured And Predicted Time-Domain Signals For Three Of The Cases | 107 |
| Figure 72. Schematic Of Phased Array Grain Noise Modeling Approach | 108 |
| Figure 73. Predicted Rms Grain Noise Profiles For Different Phased Array Modeling Assumptions. Left Plot Shows Rms As A Function Of Depth; Right Plot Is Zoomed-In Display Of The Peak Region | 108 |
| Figure 74. Comparison Of Measured (Top) And Predicted (Bottom) Rms Noise Profiles For Different Model Assumptions And For (Left & Right) Two Different Focal Laws..... | 111 |
| Figure 75. Example Of Anisotropic Ray Tracing Feature In UTsim..... | 112 |
| Figure 76. Comparison Of Beam Offsets For A Single Crystal Sample As Measured (Courtesy Pratt & Whitney) And Computed Using Anisotropic Ray-Tracing In UTsim | 113 |
| Figure 77. Schematic Of A Non-Homogeneous Anisotropic Sample (Top) And Corresponding Anisotropic Ray Trajectories (Bottom)..... | 114 |
| Figure 78. Statistical Descriptors Of Roughness Are Maximum Peak-To-Valley Height And Correlation Length. Profile Autocorrelation Function And Two Representative Profile Realizations For: A) $\gamma=0.13$, B) $\gamma=0.25$. 118 | 118 |
| Figure 79. Mean And Standard Deviation Of Pulse-Echo Signal Amplitude: Comparison Of 100% Bandwidth Broadband Exact (E) BEM And Approximate (A) Kirchhoff Predictions For Perpendicular L-Wave Incidence. Crack Length $L=6.32$, Roughness Correlation Length A) $\gamma=0.25$, B) $\gamma=0.13$ | 119 |
| Figure 80. Mean And Standard Deviation Of Pulse-Echo Signal Amplitude: Comparison Of 100% Bandwidth Broadband Exact (E) BEM And Approximate (A) Kirchhoff Predictions For Perpendicular T-Wave Incidence. Crack Length $L=6.32$, Roughness Correlation Length A) $\gamma=0.25$, B) $\gamma=0.13$ | 119 |
| Figure 81. Mean And Standard Deviation Of Pulse-Echo Signal Amplitude: Comparison Of Single Frequency (ω_0) And 100% Bandwidth (Broadband) Predictions For Perpendicular L-Wave Incidence. Crack Length $L=6.32$, Correlation Length $\gamma=0.25$, For A) BEM Computation And B) Kirchhoff Computation | 120 |
| Figure 82. Comparison Of Single Frequency (Time Harmonic) And Broadband Mean Amplitude Predictions For Crack Length $L=6.32$. A) Smooth Crack BEM, B) Smooth Crack Kirchhoff, C) Rough Crack BEM D) Rough Crack Kirchhoff. Roughness Correlation Length $\gamma=0.25$, Roughness Height $H=0.25$ | 121 |
| Figure 83. Time Domain Signals Contributing To Figure 82. 100% Bandwidth Broadband L-Wave Pulse-Echo Signals At 24 Degree Incidence: A) Flat Crack BEM Prediction B) Flat Crack Kirchhoff Prediction C) Rough Crack BEM Prediction D) Rough Crack Kirchhoff Prediction. $L=6.32$, $\gamma=0.25$, $H=0.25$ | 122 |
| Figure 84. Comparison Of BEM And Kirchhoff Broadband Pulse-Echo L-Wave Mean Amplitude Predictions: $L=6.32$. A) $\gamma=0.25$, $H=0.25$, B) $\gamma=0.25$, $H=0.5$, C) $\gamma=0.13$, $H=0.25$ D) $\gamma=0.13$, $H=0.5$ | 123 |
| Figure 85. Comparison Of Bem And Kirchhoff Broadband Pulse-Echo T-Wave Mean Amplitude Predictions: $L=6.32$. A) $H=0.0$, B) $\gamma=0.13$, $H=0.35$ | 123 |
| Figure 86. Comparison Of Broadband L-Wave BEM (E) And Kirchhoff (A) Mean Amplitude Predictions As A Function Of Angle For Crack Lengths $L=6.32$ And $L=1.57$. A) $H=0.0$, B) $\gamma=0.25$, $H=0.35$ | 124 |
| Figure 87. Dispersion Relation For Guided Modes In 3/16 Inch Thick Cylindrical Shell: A) Flat Plate, B) 10 Inch Inner Wall Radius, C) 2 Inch Inner Wall Radius, D) 0.2 Inner Wall Radius. Vertical Axis Is Circumferential Wave Number At The Inner Radius | 131 |
| Figure 88. Definition Of Motion Vector Components In Cylindrical Shell | 132 |
| Figure 89. Motion Profiles Through Shell Wall For A0 Mode At 100 KHz: A) Flat Plate, B) 10 Inch Inner Radius, C) 2 Inch Inner Radius | 133 |

| | |
|--|-----|
| Figure 90. Motion Profiles Through Shell Wall For S0 Mode At 100 KHz: A) Flat Plate, B) 10 Inch Inner Radius, C) 2 Inch Inner Radius | 133 |
| Figure 91. Guided Mode Transmission At 2 Inch Radius 90 Degree Bend In 3/16 Inch Thick Plate | 134 |
| Figure 92. Energy Transmission And Reflection Coefficients For A0 Mode Incidence On The Geometry Of Figure (1): A) A0 To A0 Transmission, B) A0 To A0 Reflection, C) A0 To S0 Transmission, D) A0 To S0 Reflection | 135 |
| Figure 93. Energy Transmission And Reflection Coefficients For S0 Mode Incidence On The Geometry Of Figure 87: A) S0 To S0 Transmission, B) S0 To S0 Reflection, C) S0 To A0 Transmission, D) S0 To A0 Reflection | 136 |
| Figure 94. Tapered Plate Section: Transitions From 3 Mm To 5 Mm Over A 100 Mm Section..... | 137 |
| Figure 95. Energy Transmission And Reflection Coefficients For 100 KHz To 300 KHz A0 Mode Incidence On The Geometry Of Figure (87): A) A0 To A0 Reflection, B) A0 To A0 Transmission..... | 138 |
| Figure 96. Energy Transmission And Reflection Coefficients For 100 KHz To 300 KHz S0 Mode Incidence On The Geometry Of Figure (87): A) S0 To S0 Reflection, B) S0 To S0 Transmission..... | 138 |
| Figure 97. Generally Curved And Tapered Plate Geometry..... | 139 |
| Figure 98. Energy Transmission And Reflection Coefficients For 100 KHz To 300 KHz A0 Mode Incidence On The Geometry Of Figure 97: A) A0 To A0 Transmission, B) A0 To S0 Transmission | 140 |
| Figure 99. Energy Transmission And Reflection Coefficients For 100 KHz To 300 KHz S0 Mode Incidence On The Geometry Of Figure 97: A) S0 To S0 Transmission, B) S0 To A0 Transmission..... | 140 |
| Figure 100. A Sequence Of Vibrothermography Images Of A Crack Taken Under Different External Loading. As The External Load Increases, The Loci Of Heating Move Toward The Tips And Eventually Vanish Once The Crack Is Entirely Open. The Amount Of Crack Heating Is Dependent On The Closure State..... | 144 |
| Figure 101. (A) Scanning Electron Microscope (SEM) Image Of A Pristine (Unvibrated) Crack In Ti 6-4 Alloy. (B) SEM Image Of A Ti 6-4 Fracture Surface After Vibrothermographic Testing, Showing Numerous Oxide Particles (Small Bright Dots And Patches Concentrated Towards The Upper-Left Region Of The Image). (C) SEM Image Of Fracture Surface Melting On The Ti 6-4 Sample, Evidenced By The Smooth, Featureless Surface. (D, Top) Microscope Image Of The Cross-Section Of A Vibrated Crack Showing A Fretting Band On The Fracture Surface. (D, Bottom) Processed Image Of Surface Infrared Heating Of The Crack, Showing That Vibrothermographic Heating Correlates With The Fretting Band..... | 146 |
| Figure 102. Processed False-Color Representation Of A Vibrothermographic Image Sequence. Hue Is Mapped To A Normalized Source Distance And Brightness To Intensity. The Raw Thermal Image Shows Through As A Grayscale Background. The Characteristic Bulls-Eye Pattern Of Vibrothermographic Indications, With Red In The Center Surrounded By Yellow And Then Green, Can Be Seen At Several Locations, Including The Position Marked With An 'X' And Two Other Indications On The Trailing Edge | 148 |
| Figure 103. Mode Patterns Represented As Heating Of A Vibration Dampening Coating Applied To The Surface Of A Turbine Blade. This Coating Is Thin Enough That It Does Not Substantively Affect The Resonance Characteristics, But Absorptive Enough To Generate Detectable Heat Under Vibration. The Amount Of Heating Of The Coating Can Be Quantitatively Related To The Local Vibration Field In The Specimen | 149 |
| Figure 104. Top View And Cross-Sectional View Of A Rectangular Patch Sensor Covered With A Three-Layer Dielectric Structure. Layer 1 Is The Sensor Substrate, Backed By A Conducting Ground Plane | 152 |
| Figure 105. Schematic (A) Plan View And (B) Cross-Sectional View Of A Square Patch Sensor. (C) Front View And (D) Back View Of The Fabricated Sensor Whose Parameter Values Are Given In (E) | 153 |
| Figure 106. Measured And Theoretical Predicted Resonant Frequencies Of A Patch Sensor Versus Relative Permittivity ϵ_r Of The Test Layer With Different Thickness $h_3 - h_2$, Figure 104. Symbols: Measured; Lines: Theoretical. $h_2 - h_1 = h_4 - h_3 = 0.508 \text{ mm}$, $\epsilon_r2 = \epsilon_r4 = 3.27$, $\epsilon_r5 = 1$ | 154 |

| | |
|--|-----|
| Figure 107. (A) Fiberglass–Honeycomb–Fiberglass Panel G8057 (The Composites Store Inc.) (B) Panel Properties. (C) Test-Piece Top Surface With Water Injected Into One Honeycomb Cell (Within The Circle). The Imaged Region Is Indicated By The Dashed Rectangle, Using The Sensor Geometric Center As The Origin. (D) Sensor Resonant Frequency Measured Over The Scan Region: Length \times Width = 52 \times 42 mm² . The Actual Position Of The Water-Filled Honeycomb Cell Is Indicated By The White Dashed Line | 155 |
| Figure 108. Seven Different Arrangements Of Two Types Of Spheres Within The Tetragonal Unit Cell | 155 |
| Figure 109. Effect On Metamaterial Effective Permittivity Of Varying The Constituent Parameters Shown In The Legend For An Array Of Identical Spheres With Sphere Parameters $\epsilon_r = \mu_r = \mathbf{23.9}$ And Radius $\mathbf{ad = 0.45}$ | 156 |
| Figure 110. Illustrations Of Concentric Capacitive Electrodes On Top Of A Multi-Layer Dielectric: (A) Sensor Configuration And Test-Piece Structure Used In The Numerical Modeling; (B) Assembled Hand-Held Probe Based On The Modeling In (A) | 157 |
| Figure 111. Photograph Of The Assembled Probe: (A) Experiment Setup Used In Probe Lift-Off Measurements; (B) Concentric Capacitive Sensor Fabricated By Photolithography | 158 |
| Figure 112. Schematic Diagram Of Spiral And Concentric Interdigital Coplanar Capacitive Sensors | 159 |
| Figure 113. Capacitance Measured As The Small Spiral And The Disk-And-Ring Sensors Scan Over Glassfiber-Honeycomb-Glassfiber Sandwich Panels Containing Various Volumes Of Injected Water. Percentage Increase In C Is Relative To The Capacitance Measured On A Region Remote From The Injected Water | 160 |
| Figure 114. Inner Working Of A Typical THz Transmitter Using Photoconductive Antenna | 162 |
| Figure 115. Schematics Of Ray Paths In The Diffraction Formulation | 163 |
| Figure 116. Benchmark Beam Field Using G-H Beam Model For A Circular Planar Probe | 165 |
| Figure 117. Same Beam Field As Figure 3 By Using F-K Model Via Equation (2) | 165 |
| Figure 118. Spherically Spreading Beam Field Of Point Source By Using F-K Model Via Equation (1) | 165 |
| Figure 119. Simulated Beam Profile Of The AFRL THz TDS System..... | 166 |
| Figure 120. Signal Ratio By Wiener Filter Deconvolution | 167 |
| Figure 121. Absorption Coefficient Estimates In Good Agreement With [130] | 167 |
| Figure 122. Good Agreement In Polyimide Signals Between Experiment And Model | 168 |
| Figure 123. The FTIR Sample And Measurement Settings | 169 |
| Figure 124. The High-Average-Low Deviations (From The True Value) Of The Best-Fit Refractive Index Vs. Different Noise Levels | 170 |
| Figure 125. The High-Average-Low Deviations (From The True Value) Of The Best-Fit Extinction Coefficient Vs. Different Noise Levels | 170 |
| Figure 126. The Multilayer Dielectric Structure Considered In The Layer Fresnel Model..... | 171 |
| Figure 127. (Right) Reflecting Irradiance As A Function Of Frequency And Layer Thickness For Incident Angle 25 Deg. And Complex Refractive Index (4.5, 0.2); (Left) A Cross-Sectional Profile At 0.5 THz | 172 |
| Figure 128. “Matched Thickness” Under Unpolarized Illumination As A Function Of The Complex Refractive Index (N, K). The Incident Angle Is 25 Degrees And Frequency Is At 0.5 THz..... | 173 |
| Figure 129. Irradiance Under Unpolarized Illumination As A Function Of The Complex Refractive Index (N, K) For Layer Thickness At 0.1mm (Left) And 0.05mm (Right). The Incident Angle Is 25 Degrees And Frequency At 8 THz | 173 |
| Figure 130. Irradiance Under Unpolarized Illumination As A Function Of The Complex Refractive Index (N, K). For Frequency At 8 THz (Left) And 15 THz (Right). The Layer Thickness Is At 0.01mm And Incident Angle At 25 Degrees | 173 |
| Figure 131. Sample Photograph Of Complex Aircraft Structure [5]..... | 176 |
| Figure 132. Assembled Pantograph Scanner With Encoding Components And EC Probe , Top, And Tracing/Scaling Capability And Linkage Reference Points Noted | 177 |
| Figure 133. Aircraft Mockup With EDM Notches Marked As Red Dots And Numbered In Magnified Photos ... | 178 |

| | |
|---|-----|
| Figure 134. First Test Of The Pantograph Scanner On The Mockup Aircraft Structure Panel, Showing EDM Notch Locations As Well As Liftoff And Edge Signatures | 179 |
| Figure 135. Test Of Pantograph Scanner To Determine Coverage (Operator Did Not View PC Screen To Gauge Areas Not Covered, Shown As Red Pixels). EDM Notches Are Shown Circled In Each Image | 179 |
| Figure 136. Inverted Tests Of Pantograph Scanner To Evaluate Rigidity Of Linkages And Ability To Support Probes And Cabling So To Eliminate Liftoff Of The Probes And Minimize Operator Fatigue | 180 |
| Figure 137. CAD Model Of Arc Scanner And Simulated Aircraft Fitting Mockup Panel | 181 |
| Figure 138. Electronic Hardware For The Arc Scanner Are Shown, Left, A Close-Up Of The Scanner, Right.... | 182 |
| Figure 139. Testing Of The Arc Scanner, With Zoom Of LCD Screen Showing EDM Notch Indications And Edge/Liftoff Effects At Top And Bottom Of Image Corresponding To The Edges Of The Arc Section On The Mockup Panel | 182 |
| Figure 140. Scan Results From Arc Section Of Mockup Panel Of Aircraft Structure, Showing Indications From EDM Notches And Edge Effect Signals From Bottom Of Mockup Panel Tapered Edge | 183 |

List of Tables

| Table | | Page |
|-------|--|------|
| 1 | Heat Treatment Conditions, Rockwell C-Scale Hardness (HRC) And Bulk Conductivity Of The Inconel 718 Samples..... | 22 |
| 2 | Experimental Max-Min Data..... | 79 |
| 3 | Predicted Max-Min Signals..... | 80 |
| 4 | Three Investigated Combinations Of Sphere Types..... | 156 |

1. Summary

Nondestructive evaluation plays a crucial role in the safety of flight, with an increasing importance as military fleet ages and the mission profile is expanded beyond the original design interest. The program completed by the Center for Nondestructive Evaluation at Iowa State University included development of new capabilities to quantify residual stress profiles in Al, Ti, and Ni alloys; expansion of simulation tools for eddy current, ultrasonics, and radiography; advances in probability of detection methodologies including model-assisted POD; improved understanding of emerging methods such as terahertz imaging and vibrothermography; and development of new education materials. Key accomplishments follow:

- A laboratory-based procedure of swept high-frequency eddy current measurements and model-based conductivity profile inversion has been established, and demonstrated to work on shot-peened Inconel 718 specimens.
- Depth of penetration up to 1 mm in aluminum, 0.05 mm in titanium and 0.2 mm in nickel has been demonstrated using high energy x-ray diffraction measurements.
- Models are available to improve transient eddy current system performance including image/signal processing approaches and provide quantitative estimates of material loss due to corrosion.
- The analytical methods for calculating coil fields have been extended jointly to deal with coil interaction with edges, e.g., right angled corners, borehole edges, and the edge of a plate.
- Modeling accomplishments include completion of a multi-Gaussian model for rectangular aperture probes, measurement procedures to characterize the ultrasonic radiation from phased array probes, and UT models for anisotropic media.
- Established web site to share results of model-assisted POD with the broader NDE community and promoted expansion of MAPOD methodologies.
- Crack vs. notch studies were completed under static and dynamic loading, confirming that response from low cycle fatigue cracks is lower than similar sized notches. Differences were found between Al and typical engine materials, Ti and Ni, due to surface oxide effects in Al.
- New methods for excitation and the acquisition and analysis of thermal acoustic data have been developed and tested. New excitation approach for vibrothermography for use in crack detection has been developed which has provided useful data indicating that induced heating at a crack is a strong function of the frequency and mode of vibration.
- Understanding of the effect of vibrational stress levels and crack closure on crack heating, and preliminary indications that vibrational loading mode (i.e., normal stress vs. shear stress) does not have a substantial effect on crack heating has been developed.
- A novel microstrip sensor has been designed that is relatively small, potentially portable, low-cost and robust. The sensitivity of the sensor to the presence of water behind a 1 mm thick dielectric plate simulating a radome skin has been demonstrated.
- Various physics-based procedures for processing multi-dimensional T-ray data, the advance in computer models for simulating T-ray three-dimensional flaw responses, the estimation of electromagnetic properties of materials from FTIR reflection data obtained

in multi-configurations, and the use of statistical pattern recognition for T-ray flaw detection/classification.

2. Introduction

Declines in full-mission capable rates and increases in the logistics support burden were of concern to the United States Air Force (AF) at the turn of the century and continue to be a focus in current budget scenarios. With the increased deployment and utilization of our weapons systems, it has become critical to complete inspection tasks quickly and effectively at the depots, and to provide unique techniques for use in forward locations. Recent assessments of inspection capability have also pointed to the need for improvements in inspection performance through more diligent use of existing technology and/or development and implementation of new technology solutions. For logistics and cost reasons, transition of inspection processes from depot situations to field or base operations has increasing priority with the AF. In the program performed under contract number # FA8650-04-C-5228, entitled, "Quantitative Inspection Techniques for Assessing Aging Military Aircraft", four primary topics were identified for which the AF defined the need for Nondestructive Evaluation (NDE) technology solutions:

1. Structural systems: Development of inspection techniques are needed which cover larger areas, have a greater sensitivity to detect smaller defects, and/or require less teardown. Structural inspections are of interest that both detect and quantify damage in simple (lap joint) and thick, complex metallic structures. Detection of cracking, corrosion, battle- or service-induced damage, and aging mechanisms is needed for both metallic and composite structures. A comprehensive study of these problems in the context of the activities of the Air Force is contained in the document "Aging of U.S. Air Force Aircraft". Among the recommendations are the need for the development of an integrated quantitative NDE capability based on life-cycle management principles, development of hybrid inspection technologies that use multiple techniques simultaneously, development of NDE techniques for composite repairs, development of signal and image processing techniques that could be used by maintenance facilities to detect damage development and maintenance trends, increased R&D in automation, and the development of techniques for the early stages of corrosion and composite damage progression, including delaminations.
2. Low observables (LO): Of increasing concern is inspection of "low observable" or stealth materials which play a key role in most modern weapons systems. The ability to characterize the electromagnetic signature of LO materials to detect precursors to damage and assure continued effectiveness after damage and/or repair is needed.
3. Propulsion systems: Propulsion capability remains a valuable asset in our nation's overall defense. Many life extension efforts are in place to enable utilization of existing propulsion components well beyond their original design life. Economic pressures are also driving tighter design specifications for modern and emerging weapon's systems. Life extension of older designs and performance expectations for new engines are driving the need to detect flaws of smaller size and requiring quantification improvements for characterization methods.
4. System health monitoring: More proactive approaches to prognostics and maintenance planning are necessary to address the increasing budgetary pressures by reducing the

costs of traditional inspection. Sensors which give sufficient forewarning to enable more cost-effective repair/replace decisions for both structural and propulsion components would have great benefit to DOD. The development of new sensors and the interpretation of sensor data are necessary in order to move to routine use. NDE methods that sense the microstructural state of materials during processing, potential damage encountered during operation, such as engine operation, and anisotropy effects are needed.

Given these four primary topics, a program that included technology development, validation, and transition efforts was proposed by Iowa State University in 2002 and contract # FA8650-04-C-5228 was awarded with a period of performance of April 30, 2004 through May 31, 2013.

This document reports on results from the following technical areas:

- Residual Stress Assessment and Instrumentation Development
- Simulation-Based Inspection Design, Evaluation and Optimization
- Probability of Detection Studies and Demonstration
- Materials Characterization and Damage (Crack, Corrosion) Detection
- Vehicle Health Monitoring and Prognosis
- Education, Technology Transition, and Infrastructure Support

2.1 Background

The Air Force is challenged with the procurement, operation, and maintenance of a wide variety of aircraft and their accompanying propulsion systems. The challenges range from maintaining aircraft that are well past their original design life to the operation of advanced weapon systems like the F-22 and F-35. Safe and reliable operation of the military fleet is critical to the defense of the country and protection of military personnel. Inspection requirements for the Air Force's aging fleet have increased dramatically in recent years. Retention of aircraft in the fleet for periods beyond 50 years in some cases, and higher utilization rates for most platforms have created inspection requirements which are not satisfied with existing instrumentation and methodologies. Recent military conflicts are placing even more pressing demands on this aging aviation infrastructure, driving the need for more sensitive and reliable inspection methods than are currently available.

Nondestructive evaluation plays a critical role in the manufacture and operation of military systems. NDE technologies are used to monitor process changes as part of manufacture of a product, to sense changes in mechanical or physical properties which affect the performance of a system (materials characterization), to detect defects and service-induced damage, and to sense the health of a component during use. A comprehensive program that addressed a range of inspection needs was completed as a partnership between the Center for Nondestructive Evaluation (CNDE) at Iowa State University (ISU) and the NDE Branch of the AF Research Laboratory at Wright Patterson AFB under contract number # FA8650-04-C-5228. CNDE researchers have developed new technology solutions, validated the most promising methods, and focused on technology transition plans for resulting processes, procedures, and equipment. CNDE utilized their extensive network within the NDE community to address the technology development and implementation challenges.

A comprehensive program that includes activities ranging from basic, fundamental research through applied technology solutions, to full prototype demonstration was completed to address the needs of the Air Force. An overarching tenet of the program is to deliver better understanding of inspection physics which can lead to improved procedures, new sensors, and better educational materials that support military aviation needs. CNDE staff work closely with AF personnel to understand physical (material, component geometry, etc.) and environmental (design, production, inservice depot, onwing, forward base) constraints under which technology solutions are expected to perform.

As one example, the USAF has identified the need to measure residual stress in propulsion components as a necessary step in life extension of engine disks. Having a nondestructive tool that can provide a depth profile to verify the existence of compressive residual stresses and the depth and magnitude of those stresses could purportedly save the AF \$500M. Relying on CNDE's extensive contacts with the industrial NDE community, ISU organized and hosted a workshop in April 2005 that gathered input from aerospace and non-aerospace companies regarding the state-of-the-art in residual stress assessment and identified the requirements for engine applications from relevant defense OEMs. Projects to address residual stress characterization in advanced electromagnetic NDE and high energy x-ray diffraction methods were then initiated under this contract.

The effort in advanced electromagnetic NDE has included measurement of deviations of apparent electrical resistivity of aerospace propulsion materials using swept frequency at high frequencies and model-based layer inversion procedures to quantify the variation in material properties in the depth direction that are responsible for those deviations. A key contributor to data interpretation has been the use of state-of-the-art materials characterization tools to access the near-surface microstructure independently. The wide-band swept high frequency eddy current (SHFEC) measurements were validated against simulated layer samples, using the proprietary SHFEC instrumentation to cover the 0.3-65 MHz band, while using conventional coil probes driven by an impedance analyzer to cover the 10 KHz-5 MHz band. A study of the impact of precipitation on conductivity variation of shot-peened, nickel-base superalloys was initiated by performing scanning electron microscopy (SEM) over the cross section of a shot-peened Inconel 718 block. Visual and preliminary numerical examinations show that, in agreement with expectations, the concentration of precipitation is higher near the peened surface than in the middle of the sample. Full results are reported in Section 3.1.

While advances in residual stress assessment in nickel-based alloys have been demonstrated, titanium-based alloys are more allusive for electromagnetic approaches due to the effects of crystallographic orientation on the measurements. Investigators at ISU have demonstrated the feasibility of high energy x-ray diffraction (HEXRD) to measure surface stress profiles at depths up to 1 mm in aluminum, 0.5mm in titanium, and 0.2 mm in nickel. The basis for using relative intensity measurements of tungsten characteristic x-ray diffraction to determine residual strain in metals has been established. Following initial technique demonstrations, two prototype HEXRD systems were built at ISU and AFRL. In addition to studies of specific samples for the Air Force, the ISU system has been utilized to investigate the effects of aggressive machining damage in Ti and Ni samples for an FAA-funded program, and for preliminary studies of ceramic materials in an Army Research Laboratory (ARL) program. Residual stress measurements have been made on a handful of Ti and Ni samples provided by aerospace and nuclear industries. A method was developed to convert the intensity data typically collected by the instrument to strains in the material. A forward model has been developed for the diffraction system to aid in optimization of the experimental setup and configuration. Finally, the system was used for PhD research, including preliminary work on measuring annealing of shot peened strain profiles in aluminum. A fully functional system and data analysis strategy was developed as described in section 3.2.

This is one of many examples of successful project maturation during the performance of efforts on contract # FA8650-04-C-5228. A brief summary of the full spectrum of projects is provided in Table 1 with details from individual investigation teams in Section 3.

| Task Title | Accomplishments: |
|---|--|
| Electromagnetic Characterization of Near-surface Treatment, Roughness, Damage, and Material Deviation | A laboratory-based procedure of swept high-frequency eddy current measurements and model-based conductivity profile inversion has been established, and demonstrated to work on shot-peened Inconel 718 specimens with data acquisition times reduced to ~ 2 minutes per step. A series of microstructural studies of the surface material reactions to the shot peening have been completed, which have generated a materials model to convert conductivity deviation profiles into residual stress profiles. Inversion calculation times have been reduced from hours to minutes with the latest perturbation theory approach. A study of the impact of precipitation on conductivity variation of shot-peened nickel-base superalloys included scanning electron microscopy (SEM) to understand the extent to which the stress-induced conductivity profiles depend on microstructure and hardness. An improved understanding of the relationship of surface damage, secondary phase precipitation, and texture on piezoresistivity has been developed. Additional effort to understand the effect of cold work and potential of Hall effect measurements is underway with FAA support. |
| High Energy Diffraction Measurements of Stress Profiles in Bulk Materials | Depth of penetration up to 1 mm in aluminum, 0.05 mm in titanium and 0.2 mm in nickel has been demonstrated using high energy x-ray diffraction measurements. Fully integrated hardware and software laboratory prototype has been developed for use with shot-peened samples and determination of residual stress profiles. A duplicate system was installed at AFRL in January 08. Characterization measurements have been extended to assessment of machining-induced stresses and armor ceramics with funding from the FAA and Army, respectively. Recommendations for improved inspection speed are provided which include beam collimation improvements, algorithm development which would estimate strain profiles from few measurements, and use of higher energy sources. |
| Transient Eddy Current Signal Calculation and Evaluation | Provided support to complete TTCP transient eddy current activities. ISU developed transient eddy current models which were validated using data from other TTCP partners. Models are available to improve transient eddy current system performance including image/signal processing approaches and provide quantitative estimates of material loss due to corrosion. Input was provided to the final report of the TTCP initiative. |
| Simulation of Eddy Current Inspection of Aircraft | Tools developed to solve a class of demanding problems involving flaws near edges and cracks under installed fasteners with a goal of one or two orders of magnitude reduction in computation speed and improved accuracy. A new analytical method was developed in which the coil interaction with an edge is computed. To date new analytical solutions have been found for ferrite cored probes, tilted coils on plates, offset bobbin coils in boreholes and rotary coils in boreholes (coil axis perpendicular to the axis of the hole). The analytical methods for calculating coil fields have been extended jointly to deal with coil interaction with edges, e.g., right angled corners, borehole edges, and the edge of a plate. |

| Task Title | Accomplishments: |
|--|--|
| Phased Array Measurement Model and POD Calculation | Modeling accomplishments include completion of a multi-Gaussian model for rectangular aperture (i.e., single element of array) for use in ultrasonic calculations, a superposition model for linear or 2-D phased arrays comprising rectangular elements, and grain scattering noise model for phased array probe. Development of measurement procedures to characterize the ultrasonic radiation from phased array probes was completed including experimental verification of linear phased array model predictions, including far-field directivities, beam patterns for ball targets in water, and responses from reflectors, such as FBH and planar surfaces. Development of UT models for anisotropic media was also a focus of the effort. The first phase of work developed and integrated the ability to perform ray tracing in homogeneous, anisotropic media. The analytical method involves solving the appropriate Christoffel eigenvalue problem, applying Snell's law to the slowness at reflection or transmission interfaces, and tracing rays along group velocity vectors. This was initially implemented as stand-alone code and tested for single crystal materials. The method has now been successfully integrated into UTSim, which allows full use of its CAD and geometry engines. Currently, final testing of this new UTSim tool is in progress with the cooperation of Pratt & Whitney. |
| Coordination of Model Assisted POD (MAPOD) Activities | ISU has served as the coordinator of the MAPOD Working Group which included drafting the prospectus on behalf of the group, hosting over a dozen meetings, and establishing/maintaining the MAPOD website. The website is fast becoming a resource to the larger POD community with empirical and model-assisted POD information residing there. |
| EC POD Methodology for Rapid Assessment of Engine Inspection | Established AF partnership with PW on engine application with strong coupling to FAA-funded activity on structures which included Cessna. Activities included development of the validation protocol utilized to guide sample design/fabrication, data acquisition, and model validation. Improvements were incorporated in the 07 versions of the PLATE and BEM codes and transferred to OEMs for use in internal validation activities. Validation efforts included commercial absolute and differential probes. Crack vs. notch studies were completed under static and dynamic loading, confirming that response from low cycle fatigue cracks is lower than similar sized notches. Differences were found between Al and typical engine materials, Ti and Ni, due to surface oxide effects in Al. |

| Task Title | Accomplishments: |
|-----------------------------------|--|
| Probability of Detection Advances | <p>Collaboration between Li, Meeker, and Pete Hovey (UDRI) developed a model and estimation methods to allow joint statistical estimation of signal strength and crack size distributions. This work, extending previous efforts of Hovey and Meeker, included various extensions to make the model more general and useful. These extensions included allowing for estimation of crack-growth rates (which in previous work were assumed to be known), use of a hierarchical Bayesian model that allows crack-growth rates to vary from one aircraft to another, but borrowing strength in estimation across different aircraft to estimate initial crack-size distributions, and incorporation of the noise-interference model into the joint estimation structure allowing statistical differentiation between readings that are from a real flaw versus signals that are the result of a noise-causing artifact near the target. It was possible to do the estimation with all of these model features with Bayesian estimation using the freely-available Winbugs program. This work was presented in the WFNDEC POD short course and the Joint Statistical Meetings in summer 2010. Subsequently, the work was published in Volume 23 of <i>Research in Nondestructive Evaluation</i>. The second collaboration among Li, Holland, and Meeker developed of an algorithm to make crack/no-crack decisions from the sequence-of-images data that come from the vibrothermography inspection method. The algorithm uses a matched filter to improve the signal-to-noise ratio. A simple signal-to-noise ratio criterion is then used to decide if a crack is present or not. The new algorithm is shown to have an importantly better POD function when compared to the traditional method of using the hottest group of pixels in the hottest frame to make a decision. This work was also presented in the WFNDEC POD short course and the Joint Statistical Meetings in summer 2010 and was published with written discussion in volume 26 of <i>Applied Stochastic Models in Business and Industry</i>. Work previously completed by Gao and Meeker developed another a statistical method for crack detection using vibrothermography inspection data. This paper was recently published in Volume 9 of <i>Quality Technology and Quantitative Management</i>.</p> |

| Task Title | Accomplishments: |
|---|--|
| Fundamentals of Detecting Tight Cracks Using Thermal Acoustic Inspection | This project provided a major increment in scientific understanding of the thermal acoustic (vibrothermographic) process. In addition, new and better methods for excitation and the acquisition and analysis of thermal acoustic data have been developed and tested. New excitation approach for vibrothermography for use in crack detection has been developed which has provided useful data indicating that induced heating at a crack is a strong function of the frequency and mode of vibration. A method to measure and quantify internal vibrations that lead to crack heating was developed with initial data indicating a strong relationship to the amount of crack closure. Most significantly, an understanding of the effect of vibrational stress levels and crack closure on crack heating, and preliminary indications that vibrational loading mode (i.e., normal stress vs. shear stress) does not have a substantial effect on crack heating has been developed. The effect of thermal acoustic excitation on crack surfaces has been demonstrated and several image processing algorithms for maximizing the resolution and sensitivity of the inspection have been developed. |
| Development of One-sided Capacitive Measurements for NDE of Low Conductivity Materials and Structures | Researched present applications of one-sided microwave NDE that may be suitable for defect detection in radomes. A novel microstrip sensor has been designed that is relatively small (~ 1cm diameter), potentially portable, low-cost and robust. The sensitivity of the sensor to the presence of water behind a 1 mm thick dielectric plate simulating a radome skin has been demonstrated. One-sided rectangular waveguide NDE measurement system has been constructed. Future applications include other layered structures of interest to the AF. |
| Advanced Infrared and Terahertz Capabilities for Aerospace Material Characterizations and Inspections | Significant progress was made in terahertz radiation and Fourier transform infrared spectroscopy (FTIR). Novel techniques have been developed and successfully tested in the areas of material characterization, modeling and data processing. Good examples include the development of various physics-based procedures for processing multi-dimensional T-ray data, the advance in computer models for simulating T-ray three-dimensional flaw responses, the estimation of electromagnetic properties of materials from FTIR reflection data obtained in multi-configurations, and the use of statistical pattern recognition for T-ray flaw detection/classification. These developments have generated many new, useful tools to be added into the "NDE tool box". |

| Task Title | Accomplishments: |
|---|--|
| Study of Real-Time Damage Detection Methodologies | <p>The focus of the project was to improve understanding of the response from naturally occurring flaws, with particular emphasis on eddy current and ultrasonics. Effort in electromagnetics has sought to establish the relationship between EC signals arising from notches and cracks, specifically filling the signal gaps occurring between idealized zero-width notches and tightly closed fatigue cracks. A study of crack closure effects was conducted on EC signals by way of comparing signals from zero-width notches obtained by extrapolation with signals from fatigue cracks with and without external loading present. Investigation of frequency dependence of the notch width effects on the resulting estimation of the idealized zero-width notch signals, by way of measuring the slopes of the signal vs. notch width relations was complete and probe-to-probe variability of the notch-width effect was evaluated among EC signals from nine selected probes which were all of the pencil probe type so that a usable signal was obtained from the small notches. The results show universality in the notch width effect for a given probe type (e.g., absolute pencil probe), namely the effect did not vary greatly from probe-to-probe. In ultrasonics, a measurement concurrently applicable to the eddy current fatigue crack specimens under loading was configured. The measurement used a 10 MHz linear phased array mounted outside the volume under stress, allowing the crack growth volume to be scanned electronically as loads are varied. Crack reflectivity was observed to display the anticipated decrease under closure. Ultrasound was used to obtain a detailed map the crack morphology in a specimen selected for sectioning, using 80 MHz acoustic microscopy. Computational models for ultrasound response were then applied to predict the signal loss contributed by the measured non-ideal (non-planar) crack morphology. In applying the computational models, questions arose regarding the validity of underlying mathematical assumptions (Kirchoff scattering theory), which lead to definition of a consequent program of study. In this study, the expectation and variance of crack scattering amplitude were computed for randomly rough crack surface profiles, where profiles are characterized by peak-to-valley height and correlation length. The computation implemented a Monte Carlo compilation of probability density, using ensembles of up to 1000 realizations for each configuration of parameters, consisting of roughness correlation length, roughness height, crack size/wavelength, angle of pulse-echo incidence, spectral bandwidth, and wave mode type. The approximate Kirchhoff scattering theory in question was compared to numerically exact boundary element method (BEM) calculations, to assess the range of validity of the approximate theory. For this purpose, the study was limited to 2D scattering problems, to accommodate BEM predictions on large cracks several wavelengths in extent. This approach is based on the assumption that the phenomena underlying failure of the approximate theory are common to 2D and 3D problems. The study revealed that the approximate scattering theory performed quite well over a significant parameter range, possibly representing the entirety of that relevant to NDE applications.</p> |

2.2 Motivation

Nondestructive inspection plays a critical role in the manufacture and operation of military systems. Nondestructive evaluation technologies are used for materials characterization to sense changes in mechanical or physical properties which affect the performance of a system, to detect defects and service-induced damage, and to monitor process changes as part of manufacture of a product or to sense the health of a component during use. As important as the development of new technologies is the quantification of a techniques performance, with probability of detection (POD) being the most common metric.

POD is a statistics based assessment of the capability of a given inspection system/operator/method. Traditionally, empirical based approaches have been used to generate POD results as input into life calculations for aircraft and engine components. MIL-HDBK 1823, entitled, "Nondestructive Evaluation System Reliability Assessment" provides the guideline for generating POD results. More recent efforts have included model-assisted probability of detection (MAPOD) approaches, a collaborative focus of this program. MAPOD allows the user to supplement experimental data with model-assisted predictions from validated physics-based simulation tools.

Given the ubiquitous role of NDE in the lifecycle of aviation systems, aircraft and engines, a comprehensive program that addressed a range of inspection requirements and POD methodology development and applications was delivered over the course of this ten year effort. CNDE researchers worked with AF personnel in development of new technology solutions, validation of the most promising methods, and establishment of technology transition plans for resulting processes, procedures, and equipment. The objective to provide inspection technology which supports enhanced readiness of the U.S. military fleet through more cost-effective and reliable solutions to defect detection, materials characterization, and health monitoring for aircraft and propulsion systems was met thru the performance of multiple tasks with major efforts described in Section 3 below.

2.3 Objectives

- To provide inspection technology which supports enhanced readiness of the U.S. military fleet through more cost-effective and reliable solutions for use in defect detection, materials characterization, and health monitoring for aircraft and propulsion systems.
- To support the implementation of new inspection tools and solutions to the benefit of the US Air Force.

3. Project Summaries

3.1 Electromagnetic Characterization of Near Surface Treatment, Roughness, Damage, and Material Deviation (Nakagawa, Lo)

Investigation Team: Norio Nakagawa, Chester Lo, Anatoli Frishman

Students: Yuping Shen and Ramya Chandrasekar

Motivation:

Jet engines are among the most critical and expensive parts of an aircraft. Some jet engine components, for example rotors, are surface-treated to improve fracture toughness by methods such as shot peening, which introduces compressive residual stresses that impede potential crack growth. It has been shown that significant benefits of component service life extension and high levels of system reliability can be gained by maintaining the compressive residual stress state [1]. However, during operations of jet engines at elevated temperatures and under tensile loads, the surface compressive residual stress is diminished or completely relieved. As a result the likelihood of component failure increases. Knowing the state of residual stress is essential to determining the remaining component life. Therefore, an in-service nondestructive method is needed to monitor the residual stress state of components periodically, so that appropriate maintenance actions can be taken when residual stress protection is lost, by either replacing or retreating the part, in order to fully exploit the benefits of shot peening in extending the component service life.

Background - Nondestructive Methods For Residual Stress Characterization

There is a long history of developing nondestructive methods for residual stress characterization, including X-ray diffraction (XRD) [2], neutron diffraction, ultrasonic [3] electromagnetic-acoustic and eddy current (EC) methods [4-7]. Among them, EC was identified as a leading candidate due to its potential as an economical, nondestructive technique for assessing residual stresses, in particular in nickel-base superalloys [8]. Correlations between EC signals and residual stresses in shot-peened alloys have been reported, and were attributed to the piezoresistivity effect, which refers to stress-induced changes in electrical conductivity [9-10]. For shot-peened surface under an isotropic stress τ , the relative conductivity change $\frac{\Delta\sigma}{\sigma_0}$ from the stress-free value σ_0 can be described empirically as

$$\frac{\Delta\sigma}{\sigma_0} = -(\pi_{11} + \pi_{12}) \cdot \tau = (\kappa_{11} + \kappa_{12}) \cdot \frac{\tau}{E} \quad (1)$$

where E is the elastic modulus, π_{ij} are the piezoresistivity constants, and $\kappa_{ij} \equiv -\pi_{ij}E$ are the electroelastic coefficients. Early studies on nickel-base alloys, such as Inconel 718 that are widely used in jet engines, showed that the apparent eddy current conductivity (AECC) increased after shot peening [8, 11-13]. The results are attributed to the peening-induced compressive residual stress which, in the case of Inconel 718 with negative electroelastic coefficients κ_{ij} [10], would raise the near-surface conductivity as indicated by Equation (1). The results of these early

studies highlighted a window of opportunity to develop the EC method for assessing residual stresses in shot peened engine components.

Task Objectives:

The objectives of this task were to

1. Develop high-frequency eddy current probe and instrumentation suitable for characterizing near-surface conditions of jet propulsion components, including surface treatment such as shot peening, coating, roughness, damage, and other material deviations;
2. Advance the EC measurement technique for better signal-to-noise and higher stress sensitivity;
3. Improve profile inversion method, and better understand the effect of peening-induced changes in material conditions on EC signals.

Challenges and Progress Towards EC Residual Stress Characterization

Despite the significant potential of EC residual stress characterization, several challenges were identified against development of the measurement technique, and its application to shot-peened engine components. For engine materials such as nickel-base or titanium alloys with low electrical conductivities ranging typically from 1 to 2% IACS (100% IACS=58 MS/m), high frequency EC measurements of up tens of MHz are needed to achieve small enough skin depths to interrogate peening-induced stress profiles, which typically extend to about 200 μm in depth. Such high frequency operations were considered difficult due to increased measurement noises from any liftoff variations and parasitic elements. We have overcome these difficulties through the development of advanced instrumentation and coil design, measurement procedures that significantly suppresses the liftoff and parasitic noises, and analytical physics models for profile inversion. The result is a validated methodology for measuring swept high frequency EC (SHFEC) signals up to 60 MHz and converting into conductivity deviation profile, from which surface material conditions, such as residual stress or surface damages, can be inferred, provided that the correlations between conductivity and the material conditions of interest are known.

Another issue with EC residual stress measurements is that in general the electrical conductivity of metallic alloys has a low sensitivity to stress. For example, using the literature values of the electroelastic coefficients $\kappa_{11} + \kappa_{12} = -1.57$ [10], and Young's modulus $E = 200$ GPa, the conductivity of Inconel 718 is estimated to increase only by about 1 % (relative) under a compressive stress of 1.2 GPa. The situation is compounded by the fact that other peening-induced changes in material conditions, such as roughness, surface damage and cold work, could also affect the EC signals. In view of this, the later stage of our research was primarily devoted to obtaining better understanding of the influences of the competing factors on EC stress measurements. Specifically, fundamental studies were carried out to investigate how the EC signals of Inconel 718 with different microstructures may respond to shot peening, the effects of peening-induced surface damages and near-surface microstructure on SHFEC signals, and how such effects can be compensated for so as to isolate the stress-induced conductivity deviation for use in residual stress assessment.

Results – Theory and Experiments

The major project outputs are summarized in the following sub-sections. Further details and results are included in the appendix.

3.1.1 Swept High Frequency EC Measurement Systems

We have developed a SHFEC measurement system operational up to 60 MHz (Figure 1 (a)), and have continually improved it for better signal-to-noise and ease of use [14-16]. The original system utilizes a differential pair of spiral coils fabricated on a printed circuit board (PCB) with two balancing resistors to form an ac bridge [14]. The bridge is connected to a network analyzer (Agilent E5061A) which drives the coils and detects the bridge output. Fabricating the bridge differential probe on a single PCB allows short connections between components to reduce parasitic noise, but limits its use to primarily inspecting samples with flat surfaces due to its relatively large footprint and rigidity.

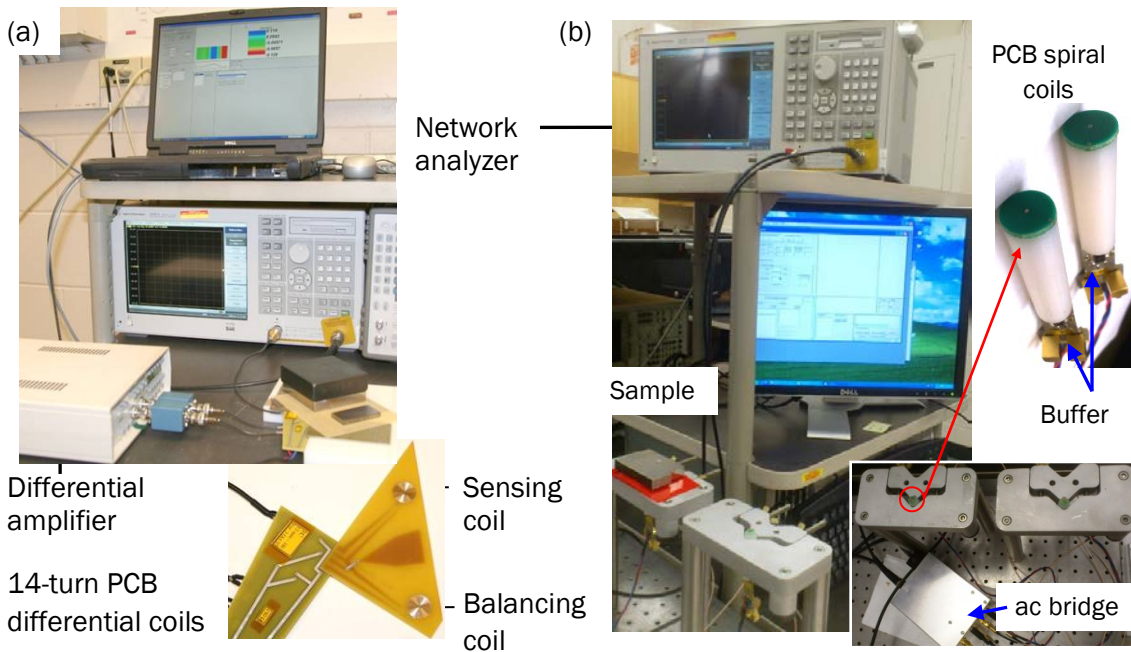


Figure 1. (a) The Previous SHFEC Measurement System Utilizing A Differential Pair Of Spiral Coils On A Single PCB Board. (b) Upgraded SHFEC System With A Pair Of Standalone PCB Coils With On-Board Impedance-Matching Buffers

The system has recently been upgraded (Figure 1(b)) through the development of a differential pair of standalone EC probes, and the use of an external amplifier to increase drive levels when needed. Each of the standalone probes consist of a PCB spiral coil connected to an on-board buffer circuit. The probes are connected via 50- Ω coaxial cables to two resistors to form an ac bridge. The bridge is buffered at its input and output for impedance matching to 50- Ω lines. A

network analyzer is used to generate the excitation signals, which can be amplified using a high frequency (10 KHz — 250MHz) amplifier (model: 25A250A, Amplifier Research) if needed, and to detect the bridge output. The upgraded system was found to offer a better signal-to-noise ratio than original system. The use of standalone probes with a smaller coil footprint improves their applicability for inspecting samples of various sizes and shape, or with curved surfaces.

The proprietary SHFEC is supplemented by a more conventional Swept Frequency Eddy Current (SFEC) system based on an air-core detection coil driven by an impedance analyzer (Agilent 4294A). This system is used for measurements in a lower frequency band, i.e., from 100 KHz to 5MHz. Despite the dissimilar probes and instrumentation used in different frequency bands, we can obtain continuous signals in the combined frequency band, i.e., 100 KHz to 60 MHz, thanks to our use of the vertical component signals as explained in the subsequent sections 3.1.2 and 3.1.3.

3.1.2 Measurement Technique: Vertical Component EC Signals

A key aspect of the SHFEC technique is the use of the vertical component (V-component) signals, where the liftoff and parasitic noises are suppressed significantly. It also removes the signal dependence on instrumentation, thus allowing direct comparison between experimental and modeling results for model-based inversion of conductivity profiles [17-19].

Specifically, the experimental V-component signal V_{EX} is defined as

$$V_{EX} \equiv \text{Im} \left(\frac{V_T^O - V_R^O}{V_L^O - V_R^O} \right) \quad (2)$$

where V_R^O , V_L^O , and V_T^O , denotes, as complex variables, the reference signal measured from a pristine surface, the liftoff signal measured from the pristine reference with a known additional coil liftoff, and the test signal from a surface-treated material, respectively. By taking the imaginary part of the complex ratio, only the signal component perpendicular to the liftoff direction is used, thus suppressing the liftoff noise [14]. For direct comparison with experiment, a theoretical vertical-component signal V_{TH} is introduced as

$$V_{TH} \equiv \text{Im} \left(\frac{Z_T - Z_R}{Z_L - Z_R} \right) \quad (3)$$

where Z_R , Z_L , and Z_T are the coil impedances calculated for the reference, liftoff, and test configurations, respectively. Given an impedance deviation due to different conductivity profiles of the reference and test samples, the output voltage shows a corresponding deviation. The proportionality constant (i.e., the multiplicative transfer function) is instrument-dependent but material-independent. If the instrumentation conditions are kept fixed for the three measurements, the transfer function cancels out in the ratios, and therefore $V_{EX} = V_{TH}$. Possible parasitic element effects, including the wire-to-wire capacitive couplings within the coils, are suppressed in V_{EX} , because they are part of the transfer function.

3.1.3 Model-Based Inversion of Conductivity Profiles

Another important aspect of our technique is the use of model-based inversion to convert SHFEC signals into conductivity profiles for material characterization. This approach offers the advantage over other calibration-based methods (e.g., AECC [8-13] in that model-based inversion determines the near-surface conductivity profile directly. In contrast, the calibration-based methods show frequency dependence arising from the nontrivial depth profile of the true conductivity deviation near the surface.

Two inversion schemes and software codes were developed and implemented, under the assumption that the conductivity deviation of shot-peened surfaces is uniform in the surface directions and varies only as a function of depth. The first inversion scheme is based on the analytical EC model developed by Cheng-Dodd-Deeds (CDD) for multilayered structures [19]. The SHFEC measurement and inversion procedures were validated in a four-stage study on simulated layer specimens [20]. The specimens consist of one or two alloy foils placed on a metal substrate. The details of sample configurations and a complete set of inversion results are given in the Appendix 3.1.A. As an example, the configuration and results of the stage 2 study, which was aimed at validating the inverse model, are shown in Figure 2. In this case, an Inconel 718 foil with a slightly different conductivity from the substrate was used to simulate modified surface layers of shot-peened components. The foil conductivity was determined by inversion using the CDD model to be 1.348 %IACS, which is in good agreement with the directly measured value of 1.342 %IACS using the direct current potential drop (DCPD) method with a four-point probe.

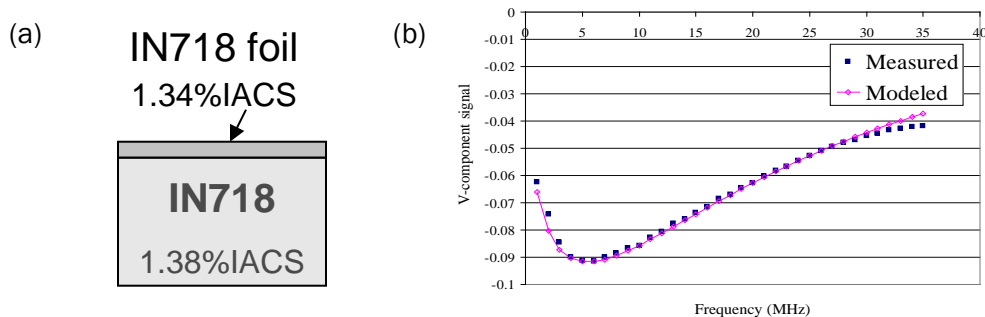


Figure 2. A) The Simulated Layer Specimen For The Stage 2 Validation Study, Which Consists Of A 103 μ M Thick Inconel Foil ($\sigma = 1.342\%$ IACS Measured By DCPD) On An Inconel Block ($\sigma = 1.38\%$ IACS). (B) The Measured And Modeled V-Component Signals For The Layer Specimen. The Inverted Foil Conductivity Of 1.348%IACS Agrees With The DCPD Value Of 1.342%IACS

For practical calculations, conductivity profile can be described by parameterized empirical or phenomenological functions, which are chosen according to the underlying mechanisms (e.g., piezoresistivity effect of residual stresses) that produce the conductivity profiles. For example, the following empirical function was used to describe the conductivity profiles of a series of Inconel 718 samples shot peened at various Almen intensities [17]

$$\frac{\sigma - \sigma_0}{\sigma_0} = e^{-x/\lambda} \sum_{i=0}^N a_i x^i \quad (4)$$

The exponentially decaying function depicts the overall conductivity behavior that may deviate significantly near the peened surface but returns smoothly to the bulk value with increasing depth. The polynomial function captures the fine structure of the profile near the peened surface. Figure 3 shows the inverted conductivity profiles based on Equation (4) for a series of Inconel 718 samples shot peened at various Almen intensities [17]. All profiles show a peak between 50 μ m to 80 μ m in depth, consistent with the fact that shot peening often produces compressive residual stress profiles with the peak position < 100 μ m in depth depending on the Almen intensity. It should be remarked that this early result happened to show near-surface ($\sim 20 \mu$ m or below) negative conductivity deviations, attributable to near-surface damage to be described below in Sect. 3.1.4.B.

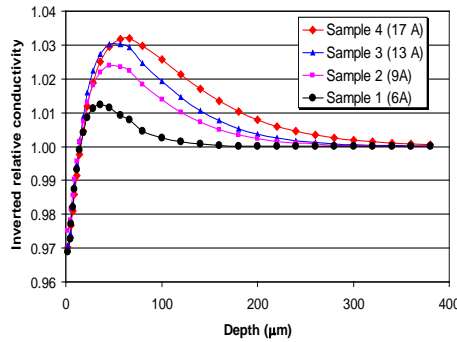


Figure 3. Inverted Conductivity Profiles For Inconel 718 Shot Peened At 6A, 9A, 13A And 17A

Subsequently, another inversion scheme based on perturbation theory was developed in this project. It was found that, when the outer diameter of the EC coil is much larger than any other length parameters (e.g., coil height, skin depth, etc.), the theoretical V-component V_{TH} can be expressed in terms of the small relative conductivity deviation profile $\Delta\sigma(z)/\sigma_0$ as

$$V_{TH} = -\frac{1}{l} \text{Im} \int_0^{\infty} \exp((-2 - 2j)z/\delta) \frac{\Delta\sigma(z)}{\sigma_0} dz, \quad (5)$$

where l is the additional coil liftoff ($\cong 25 \mu$ m in our measurements), and $\delta = \sqrt{1/\pi\mu_r\mu_0\sigma_0 f}$ is the skin depth which depends on the frequency f , conductivity σ_0 , and relative permeability μ_r .

The perturbative formula [5], when applicable, offers several advantages over the CDD model. It substantially reduces the computation time. It allows the use of simple, analytical profile functions to describe the conductivity profiles, from which closed-form expressions of V_{TH} can be obtained for use in profile inversion [21]. Specifically, given a conductivity profile $\Delta\sigma(z)/\sigma_0 = g(\frac{z}{d}, \alpha, \beta, \dots, \frac{d'}{d}, \dots)$, Equation (5) can be written as

$$(4l/\delta)V_{TH} = F\left(\frac{2d}{\delta}, \alpha, \beta, \dots, \frac{d'}{d}, \dots\right) = F\left(\sqrt{f}, \dots\right). \quad (6)$$

The left hand side of Equation (6) is proportional to the product of \sqrt{f} and V_{TH} , and the right hand side is simply a function of \sqrt{f} . If the function form of $F(\sqrt{f})$ is known by calculating the integral of Equation (5), it can be used to fit the data in the form of $\sqrt{f} \cdot V_{TH}$ vs. \sqrt{f} , from which the profile parameter (α , β , etc.) and hence the profile function $g(\frac{z}{d}, \alpha, \beta, \dots, \frac{d'}{d}, \dots)$ can be determined. Several profile functions used in this study are shown in Figure 4. These functions were chosen because they are simple, and yet they can capture some of the key features of conductivity profiles of peened surfaces, some of which were revealed by detailed characterization of the near-surface microstructure as described in section 3.1.4. Other conceivable profile functions examined in this study are tabulated in Appendix 3.1.B.

A striking feature of Equation (5) is that V_{TH} is entirely independent of the coil parameters. This allows us to use multiple coils optimized for EC measurements in different frequency bands, while yielding continuous broad-band SFEC spectra. An example is shown in Figure 5. In this case, two sets of V-component signals measured by two different coils and instrumentation form a continuous curve over frequencies ranging from 100 KHz to 60 MHz. The broadband EC measurements allow both the near-surface conductivity profile and the bulk conductivity to be determined by model-based inversion [22]. Such profiling capability offers the opportunity to detect any pre-existing spatial variations of bulk conductivity commonly found in forged components, so that their effects on the detected EC signals can be separated from those induced by surface treatments such as shot peening.

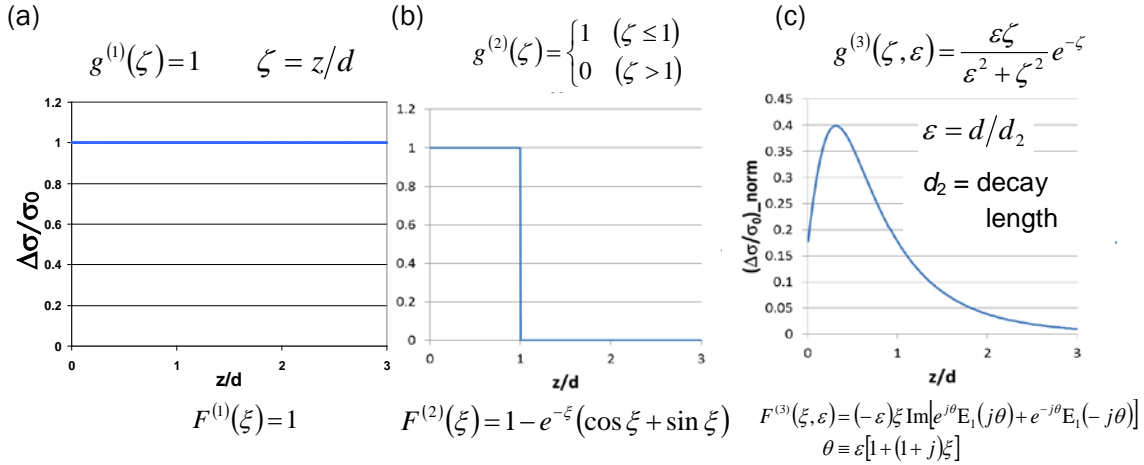


Figure 4. Plots Of The Conductivity Profile Function $g(\frac{z}{d})$ For (a) A Constant Shift In Conductivity With One Parameter (The Amount Of Shift) To Describe The Bulk Conductivity Difference Between A Peened Sample And The Reference Sample Used In The V-Component Measurements; (b) The Step Function With Two Parameters (Step Height And Depth) To Account For The Surface Damages By Shot Peening; And (c) A Peak Function With Exponential Decay To Describe Typical Residual Stress Profiles Created By Shot Peening. Also Shown Is The Functional Form Of F In Equation (6)

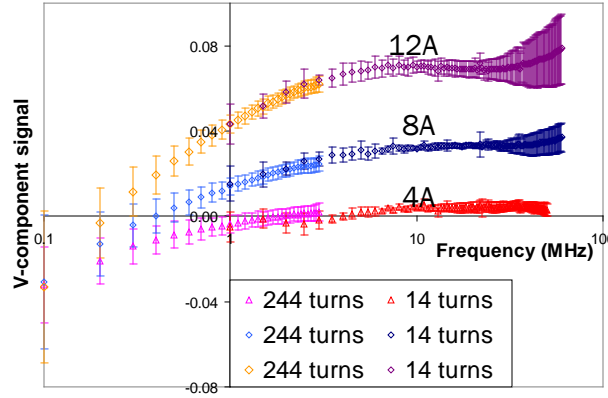


Figure 5. Swept Frequency V-Component Signals Measured From A Series Of Inconel 718 Samples Shot Peened At 4A, 8A And 12A Using A 12mm, 14-Turn PCB Coil And A Network Analyzer (From 1 MHz To 60 MHz), And A 244-Turn Coil And An Impedance Analyzer (100 KHz To 3 MHz)

3.1.4 Effects of Microstructure on EC Responses to Shot Peening

We have carried out a comprehensive study of the origins of conductivity variations in shot peened Inconel 718. This was motivated by the observation that the shot-induced EC responses in Inconel 718 depend on the underlying microstructures [23-25]. These findings indicate the important role of microstructure in EC residual stress measurements, and raised doubts about the

applicability of the empirical piezoresistivity relationship (Equation (1)) to shot-peened surfaces without modification.

To this end, a study plan was formulated based on the hypothesis that near-surface conductivity deviations induced by shot peening could be contributed by several competing factors, including (i) residual stress via piezoresistivity; (ii) microstructure such as peening-induced surface damages or variations in secondary phase content, and (iii) cold work (e.g., lattice defects, dislocations). Systematic studies were carried out accordingly to investigate the influences of microstructure on EC stress measurements. Specifically, we studied the shot-peening induced changes in EC responses of a series of Inconel 718 that was heat treated to produce various secondary phase contents (section 3.1.4.A). This portion of the study aimed to investigate the extent to which the stress-induced conductivity deviations profiles depend on the microstructure and hardness of the samples. The microstructure of the peening-affected zone of selected samples, including surface damage (section 3.1.4.B), secondary phase content (sections 3.1.4.C) and texture (section 3.1.4.D), was characterized in detail and compared with those observed in the non-peened regions. This aspect of the study aimed to identify the microstructural changes caused by shot peening, and assess their effects on SFEC signals. A complementary study of the cold work effects is being carried out in parallel under a companion project funded by the Federal Aviation Administration.

3.1.4.A Microstructure Effects on EC Responses to Shot Peening

The microstructural effects on EC responses to shot peening were studied in terms of a series of Inconel 718 samples heat treated under different conditions (Table 1) to produce various secondary phase precipitates (γ' , γ'' and δ as shown in Figure 6) and hence different hardness levels [21]. The dependence of the bulk conductivity and sample hardness on microstructure is discussed in Appendix 3.1.C. SFEC signals were measured between 100 KHz and 50 MHz from the heat treated samples before and after they were shot peened at Almen intensities 4A, 8A and 12A.

Table 1. Heat Treatment Conditions, Rockwell C-Scale Hardness (HRC) And Bulk Conductivity Of The Inconel 718 Samples

| Sample | Heat treatment | Hardness HRC (HRB) | Bulk electrical conductivity (%IACS) |
|--------|---|--------------------------|--|
| I | As-received | 11.4* (91.4) | 1.383 ± 0.001 |
| II | Solutionized at 1024°C/0.5 hr | 9.0* (89.4) | 1.381 ± 0.001 |
| III | Solutionized, aged at 620°C/10 hrs | 27.5 | 1.353 ± 0.003 |
| IV | Solutionized, aged at 680°C/50 hrs | 41.1 | 1.474 ± 0.003 |
| V | Solutionized, aged at 718°C/8 hrs, furnace-cooled to 621°C, aged at 621°C/8 hrs | 42.9 | 1.483 ± 0.001 |
| VI | Solutionized, aged at 850°C/10 hrs | 26.1 | 1.464 ± 0.001 |
| VII | Solutionized, aged at 900°C/20 hrs | 20.4* (98.4) | 1.428 ± 0.003 |

* Hardness values measured in Rockwell B-scale (HRB) and converted into C-scale (HRC).

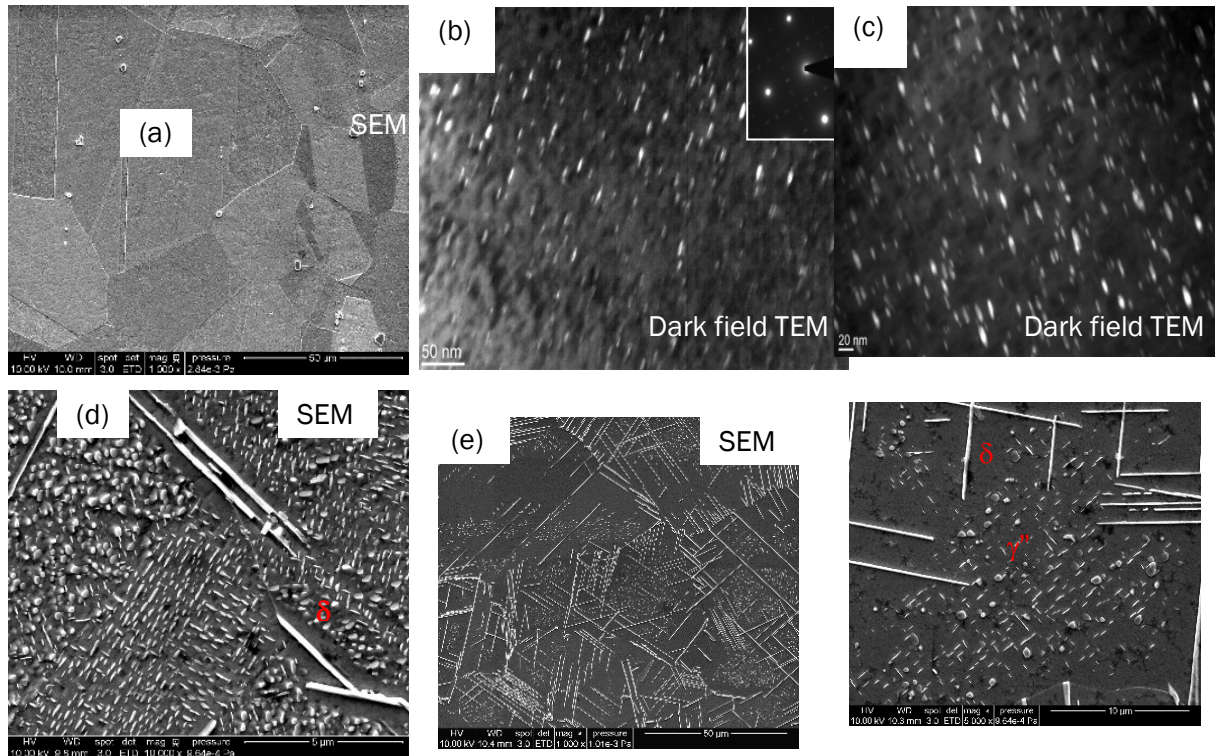


Figure 6. Scanning And Transmission Electron Micrographs Of Heat Treated Inconel 718 Samples: (a) Sample II; (b) Sample IV Showing γ'' Precipitates; (c) Sample V Showing γ'' Precipitates; (d) Sample VI Showing Coarse γ'' Precipitates And δ At Grain Boundaries; (e) Sample VII Showing Copious δ Platelets And γ'' Inside The Grains (Right)

Figure 7 shows the V-component EC signals measured from the solutionized Sample II before and after shot peening. The signals measured in the two frequency bands using different sets of coils and instruments show a continuous curve over the entire frequency range in accordance with Equation (5). The baseline V-component signals measured before shot peening are close to zero, indicating the absence of any pre-existing conductivity profiles. After shot peening, the test V-component signals become more positive than the baseline signals, and the signal increase is larger for a higher Almen intensity.

As shown in Figure 8, the shot-peening induced changes in V-component EC signals vary from sample to sample, depending on the sample hardness which is dictated by the secondary phase content. This aspect of the present results is consistent with those reported in the previous study [23-25]. However, this was considered to be inconsistent with what was expected from the piezoresistivity effect. The electro-elastic coefficients of Inconel 718 have been found to be affected by precipitation hardening. In particular, the sum ($\kappa_{11} + \kappa_{12}$) was measured to be -1.14 for a fully hardened Inconel 718 (HRC = 46) and -1.57 for an annealed sample [24]. Despite the difference in magnitude, both solutionized and fully hardened Inconel 718 show negative values of ($\kappa_{11} + \kappa_{12}$) and therefore, according to Equation (1), the near-surface conductivity is expected to increase due to the shot-peening induced compressive residual stress, irrespective of the

sample hardness. Such stress-induced conductivity increase is expected to cause positive changes in V-component EC signals, in apparent contradiction to the measurement results (Figure 8 (f)).

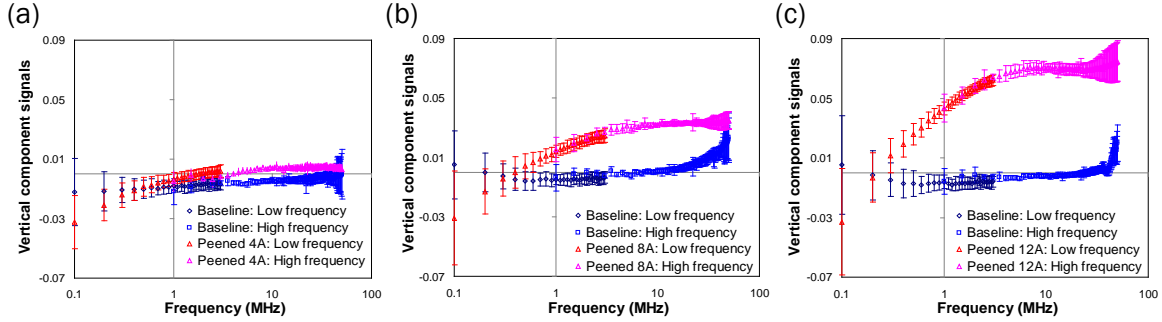


Figure 7. V-Component EC Signals Versus Frequency (In Log₁₀ Scale) Measured From Sample II Before And After Shot Peening At (a) 4A, (b) 8A And (c) 12A. The Error Bars Correspond To One Standard Deviation Of Five Repeated Measurements

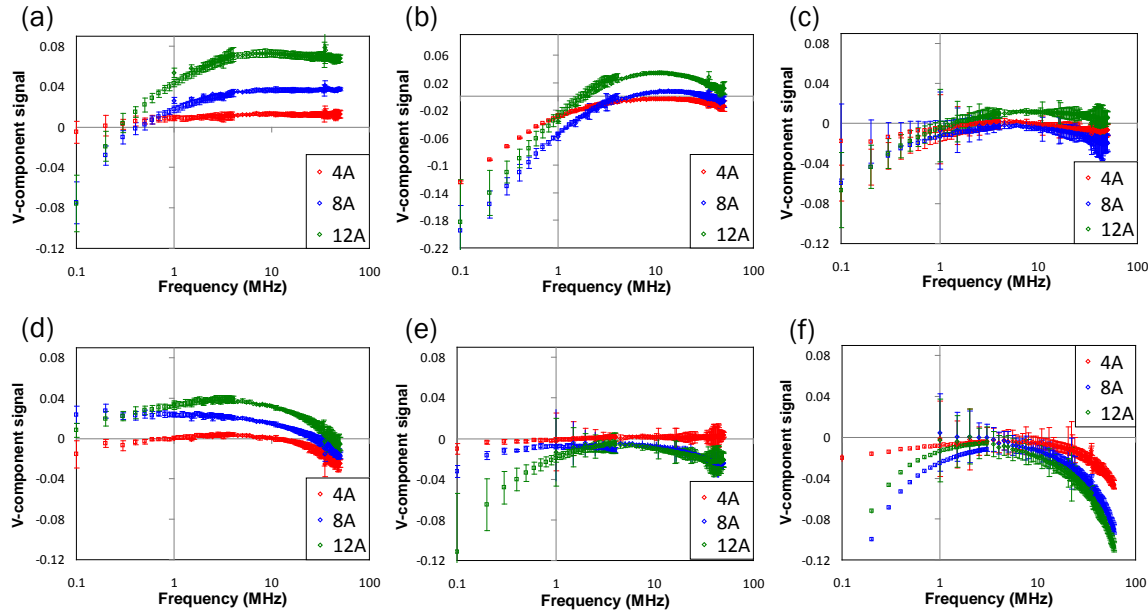


Figure 8. V-Component EC Signals Versus Frequency For The Shot Peened Inconel 718 Samples In The Ascending Order Of Hardness: (a) I, (b) VII, (c) VI, (d) III, (e) IV And (f) V

3.1.4.B Shot Peening-Induced Surface Damage and Inversion of Conductivity Profiles

The inconsistency between the observed EC signal changes and piezoresistivity effect indicates the existence of other factors that compete against the shot-induced residual stress in affecting

the EC signals. Detailed characterization of the cross-sections of the shot peened samples revealed the presence of a surface damaged layer that is 20-30 μm thick (Figure 9).

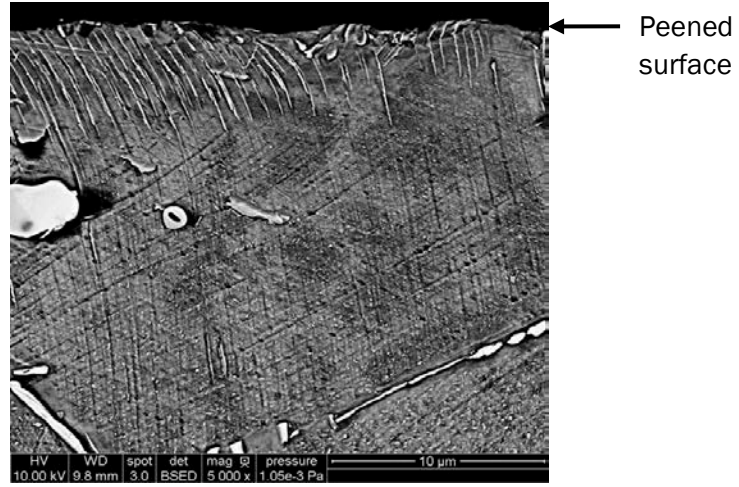


Figure 9. A SEM Image Of The Cross-Section Of Sample VI After Shot Peening. Slip Damage Is Observed Up To About 30 μm In Depth Below The Peened Surface

The effects of this damaged layer on EC signals should be accounted for when inverting SFEC signals into conductivity profiles. Technically, we employ a matched filter approach (See Table B-1 of Appendix 3.1.B, or Ref. [21], with the introduction of a shallow step-like conductivity deviation profile,

$$\left(\frac{\Delta\sigma(z)}{\sigma_0} \right)^{(I)} = \alpha_0 + \beta_0 g(d_0 - z) = \alpha_0 + \beta_0 \begin{cases} 1 \\ 0 \end{cases} \quad \text{when } \begin{cases} z \leq d_0 \\ z > d_0 \end{cases}, \quad (7)$$

that exists only within the damaged layer (i.e., $d_0 < 30 \mu\text{m}$). The V-component EC data is computed as a linear combination of $F(\xi)$ for Type 1 and 2 profiles (Table B-1), namely,

$$V_{TH}^{(I)} = \frac{\delta}{4l} \left\{ \alpha_0 + \beta_0 \left[1 - \sqrt{2} e^{-\xi} \sin\left(\xi + \frac{\pi}{4}\right) \right] \right\}, \quad \xi \equiv \frac{2d_0}{\delta} \quad (8)$$

which is fitted to the SFEC data. After subtracting the effects of the damaged-layer, the residual SFEC signals are processed further with the second matched filter, described by the following profile function (Type 1 + 7, Table B-1):

$$\left(\frac{\Delta\sigma(z)}{\sigma_0} \right)^{(II)} = \alpha + \beta \frac{\varepsilon(z/d)}{\varepsilon^2 + (z/d)^2} \exp\left(-\frac{z}{d}\right) \quad (9)$$

and thus correspondingly

$$V_{TH}^{(II)} = \frac{\delta}{4l} \left\{ \alpha - \beta \varepsilon \xi \operatorname{Im} \left[e^{j\theta} E_1(j\theta) + e^{-j\theta} E_1(-j\theta) \right] \right\}, \quad \theta \equiv \varepsilon [1 + (1+j)\xi], \quad \xi \equiv \frac{2d}{\delta}. \quad (10)$$

The second assumed profile (9) captures the typical shape of peening-induced residual stress profiles to a depth of 500 μm (i.e., $\varepsilon d < 500 \mu\text{m}$). In the process of nonlinear least square minimization, the strength of the damaged-layer effect was constrained to be less than 20% (i.e., $|\beta_0| \leq 0.2$) in addition to the constraints $d_0 \leq 30\mu\text{m}$, $30\mu\text{m} \leq \varepsilon d \leq 500\mu\text{m}$, and $0 \leq \varepsilon \leq 0.5$.

The stress-induced conductivity deviation profiles thus defined and calculated from the data are presented in Figure 10. The conductivity deviations are (i) nominally of the same order of magnitude among all samples, (ii) all showing non-negative changes in the correct sequence according to the Almen intensities of 4A, 8A and 12A, and (iii) exhibiting only weak dependence on sample unlike the V-component EC signals. On the other hand, the estimated conductivity changes are still above 1%, being larger than those expected from the piezoresistivity effect, which is estimated using Equation (1) to be about 1%.

3.1.4.C Effects of Near-Surface Variations of Secondary Phase Content

In addition to slip damages, near-surface variations in the secondary phase content were also observed in some of the samples [26]. Although a question remains regarding the origins of the observed depth profiles of secondary phase content, their presence is expected to affect the conductivity profile, as the formation of secondary phase precipitates withdraws alloy elements from the matrix and in turn affects electron scattering by impurity atoms. In view of this, we have characterized the volume fraction of secondary phase precipitates at different depths from the non-peened and shot peened surfaces of a heat-treated Inconel 718 sample, and estimated, based on an empirical calibration, the conductivity deviation profiles in order to quantify the effects of phase content variations on SFEC signals.

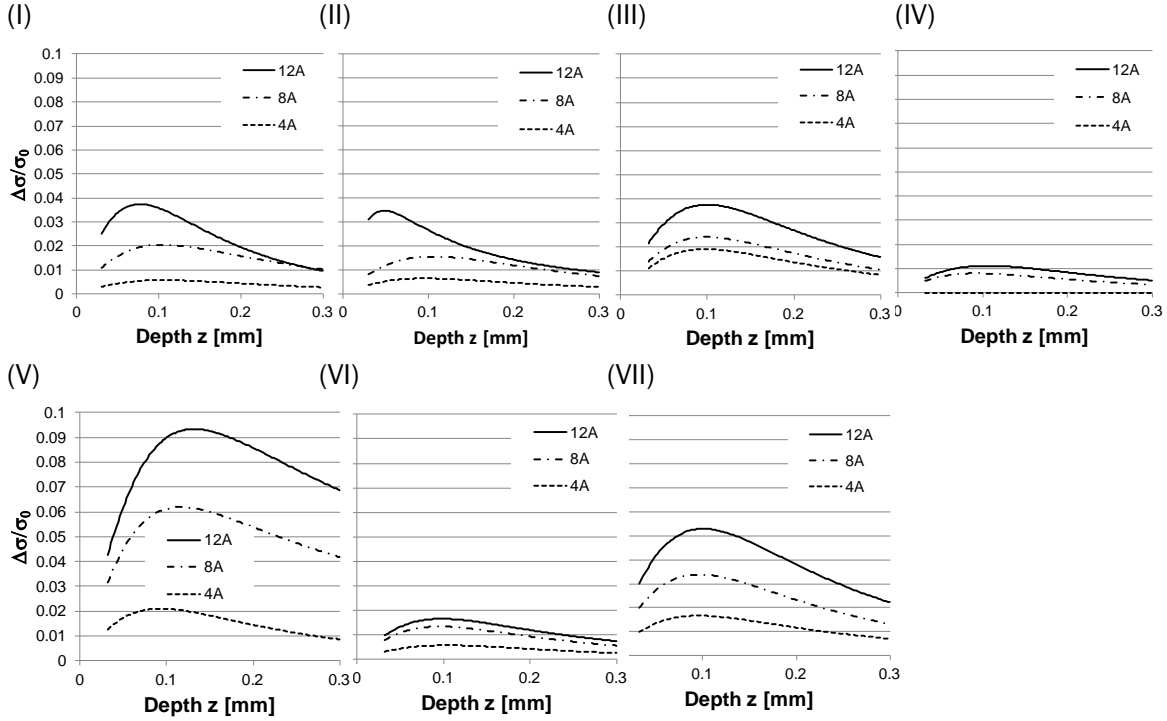


Figure 10. Inverted Conductivity Deviation Profiles Of The Shot-Peened Inconel 718 Samples

Specifically, scanning electron microscopy (SEM) images were taken at different depths from the non-peened and shot peened surfaces, and in the bulk region (~ 1.5 mm below the peened surface) of Sample VII (Figure 11) that consists of predominantly δ platelets and γ'' in the grain interior. The volume fraction of δ and γ'' phases combined was measured from the micrographs, and is plotted as a function of depth in Figure 11 (d). It is evident that the volume fraction, V_f , of δ and γ'' is largest near the peened and non-peened surfaces compared to the sample bulk, and it gradually decreases with depth to the bulk level.

The dependence of conductivity on secondary phase content was determined by measuring the bulk conductivities σ_b and the volume fractions V_f of secondary phase precipitates in the heat-treated Samples II, VI and VII using SEM. As shown in Figure 12, the bulk conductivity varies linearly with the secondary phase content as

$$\sigma_b \text{ (in \% IACS)} = 0.0077 V_f \text{ (in \%)} + 1.3816 \text{ (in \% IACS)}. \quad (11)$$

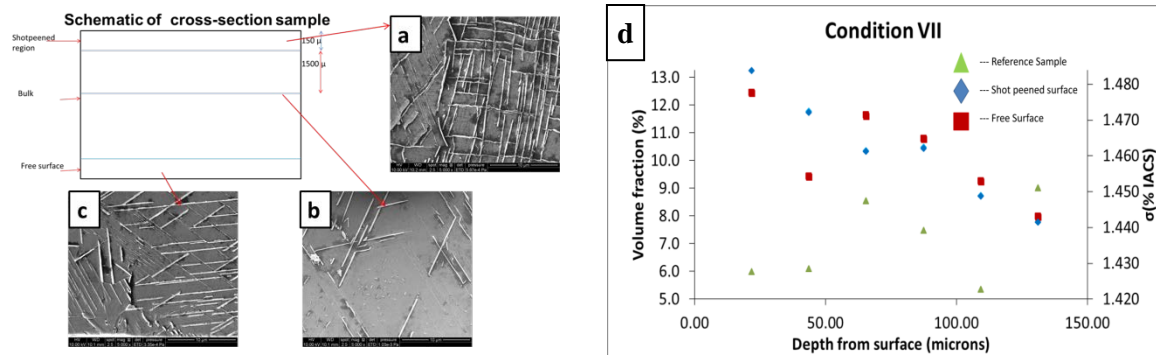


Figure 11. A Schematic Showing The Cross-Section Of Sample VII. Also Shown Are The SEM Images Taken Near The (a) Peened (Top Edge) Surface, (b) Non-Peened (Free) Surface (Bottom Edge), And (c) The Bulk Of The Sample. Larger Amounts Of δ Phase Were Observed Near The Peened And Non-Peened Surface Than In The Sample Bulk. (d) Depth Profiles Of The Volume Fractions Of Secondary Phase Precipitates And The Estimated Conductivity Profiles Based On The Calibration Shown In Figure 12

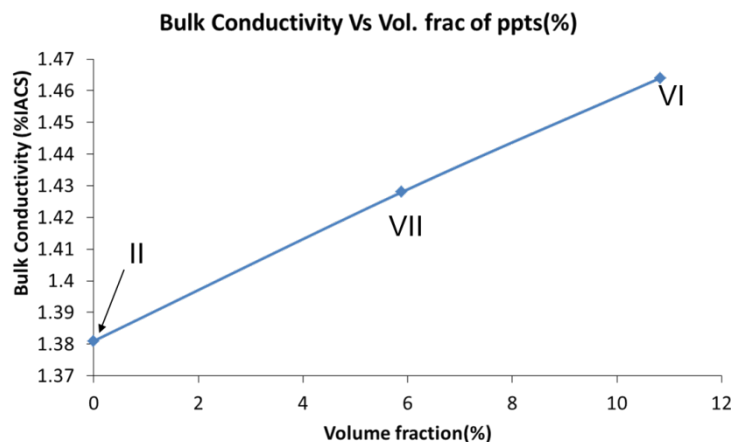


Figure 12. Plot Of The Bulk Conductivity Versus Volume Fraction Of Secondary Phase Precipitates For Samples II, VI And VII. The Straight Line Represents A Linear Fit To The Data (Symbol)

Based on this calibration, the conductivity profiles due to the observed variations in secondary phase content were calculated and are shown in Figure 11 (d). Both the non-peened and peened surfaces show a higher conductivity, which gradually rolls back to the bulk value. Of special note is that the near-surface conductivity (1.48% IACS) is about 2.8% higher than the bulk value (1.44% IACS). Such conductivity change is significantly larger than the typical conductivity increase of ~1% caused by compressive residual stress induced by shot peening. The present results indicate the important role of the material microstructure in EC residual stress measurements, especially the amount and distribution of secondary phase precipitates, as this

factor can compete with the piezoresistivity effect of residual stress in affecting the near-surface conductivity profiles.

3.1.4.D Shot-Induced Texture and Its Influences on Piezoresistivity

Shot-induced changes in crystallographic texture with depth were also observed in our early studies of an Inconel 718 sample that was shot peened at high Almen intensity of 17A [27]. Figure 13 shows the XRD θ - 2θ spectra measured from the pristine (non-peened) surface, and from the peened surface of the sample before and after a 96 μm -thick surface layer was removed. At the peened surface, the (111) peak is enhanced while the (022) peak was suppressed compared to the non-peened surface, indicating a preferred orientation of {111} over {022} lattice planes parallel to the plane of the peened surface. At the depth of 96 μm , the (111) peak is suppressed while the (022) peak becomes stronger compared to the peened surface. This shows a change in texture between these two depth points. The intensity ratio of the (111) peak to the (022) peak, which was determined as a measure of the texture by Rietveld refinement of the peak profiles, is plotted as a function of depth in Figure 13 (c). Within about the first 60 μm of the peened surface, the XRD data show a preferred {111} grain orientation (i.e., grains with their {111} planes parallel to the sample plane) over {011} orientation. Below that depth, {011} orientation gradually dominates over {111} orientation and the peak intensity ratio reaches the minimum value at a depth of about 74 μm . The texture gradually diminishes beyond that point, as suggested by the intensity ratio which approaches an asymptotical value of 1.58 corresponding to the value obtained before shot-peening.

The observed texture profile can be explained by considering geometrically necessary dislocations resulting from shot peening (Figure 13(d)). Consider a shot hitting the sample surface into the maximum depth. In order for the sample to geometrically adapt the shape of the impact surface, material beneath the bottom of the shot needs to be pushed down. This process is most likely realized by movement of edge dislocations from the surface into the bulk. For Inconel 718 with an fcc (gamma phase) matrix, the easiest slip planes are {111} and sometimes {211} planes while the easiest slip directions are $\langle 011 \rangle$. For those grains without perfect orientation with sliding plane and sliding direction parallel to the shear stress, plastic deformation is probably accommodated by grain rotation (i.e., reorientation of the crystal lattices of the grains) to such an orientation that one of the slip systems becomes operative so that further deformation could proceed by slip. It is this kind of rotation below the bottom of the single shot that leads to preferred [111] and [211] zone axis perpendicular to the peened surface and {011} planes parallel to the peened surface.

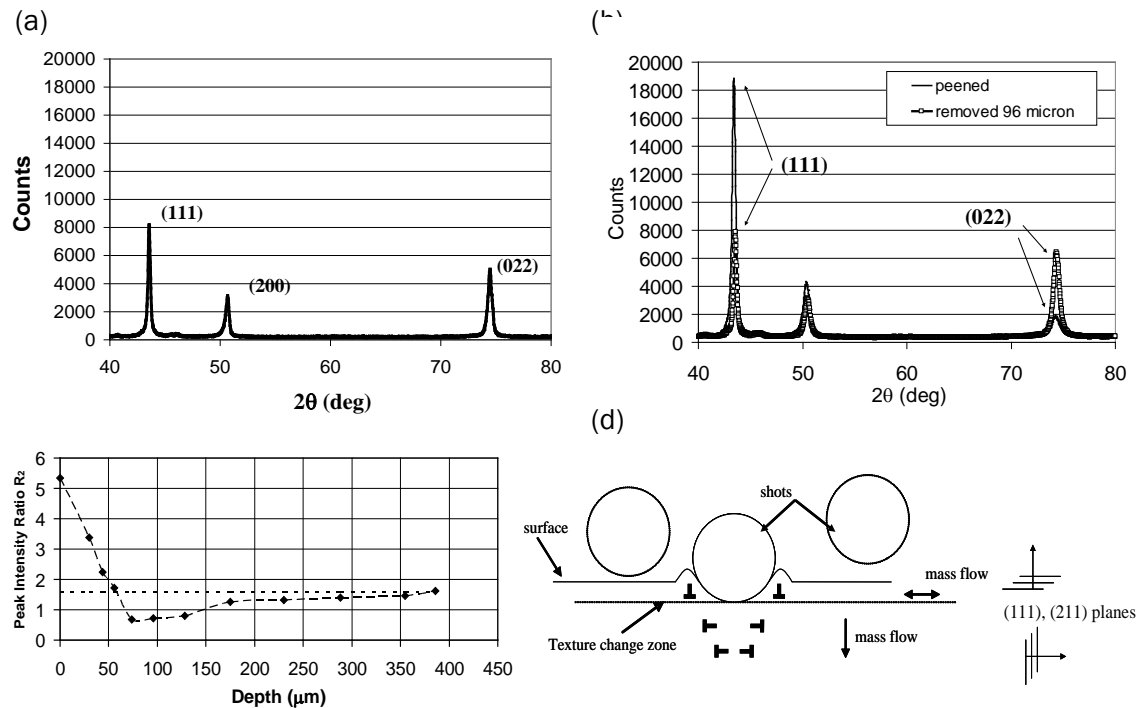


Figure 13. Θ -2 θ Spectra Measured From The Pristine Surface, And From The Peened Surface Of An Inconel 718 Sample Before And After A 96 Mm-Thick Surface Layer Was Removed. (c) Intensity Ratio Of The (111) Peak To The (022) Peak Versus Depth From The Peened Surface Showing A Change Of Texture With Depth. (d) Schematic Illustration Of The Mass Flow Caused By Shot Peening And The Resulting Texture

Based on this observation, a texture-influenced piezoresistivity relationship was derived as [27]

$$\frac{\Delta\sigma(z)}{\sigma_0} = -(\pi_{11}' + \pi_{12}')_{no\ texture} \cdot \left[1 + \frac{48\sqrt{2}\pi^2}{77} \cdot p \cdot W_{400}(z) \right] \cdot \tau'(z), \quad (8)$$

where π_{11}' and π_{12}' are the polycrystalline piezoresistivity constants, W_{400} is the orientation distribution coefficient (ODC) describing the texture, and p is given in terms of the single-crystal piezoresistivity constants π_{11} , π_{12} and π_{44} as $p \equiv \frac{11}{3} \frac{\pi_{11} - \pi_{12} - \pi_{44}}{4\pi_{11} + 6\pi_{12} + \pi_{44}}$. Equation (8) describes the effect of cylindrically symmetric texture (perpendicular to the sample surface) as a correction to the linear, isotropic piezoresistivity relationship (Equation (1)).

The texture-influenced piezoresistivity relationship was used in model-based inversion of the residual stress profile, in order to examine whether shot-induced texture could account for the observed inconsistency between the conductivity deviation inverted from SHFEC data ($\sim 3\%$ increase in σ as shown in Figure 3) and the expected stress-induced conductivity change of $\sim 1\%$ based on the isotropic piezoresistivity relation (Equation (1)). The ODC depth profile $W_{400}(z)$

was calculated from the peak intensity ratio (Figure 13(c)) [27]. The factor p was treated as a fitting parameter since the values of π_{11} , π_{12} and π_{44} were not available. The residual stress profile is described using a parameterized function $\tau' = e^{-x/\lambda} \sum_{i=0}^2 a_i x^i$ (c.f. Equation (4)), where λ

and a_i ($i = 0$ to 2) are fitting parameters. The measured and best fitted V-component signals are plotted in Figure 14 (a). Figure 14 (b) shows the inverted residual stress profile, which roughly agrees with the directly measured profile by the $\sin^2\psi$ XRD method with destructive layer removal.

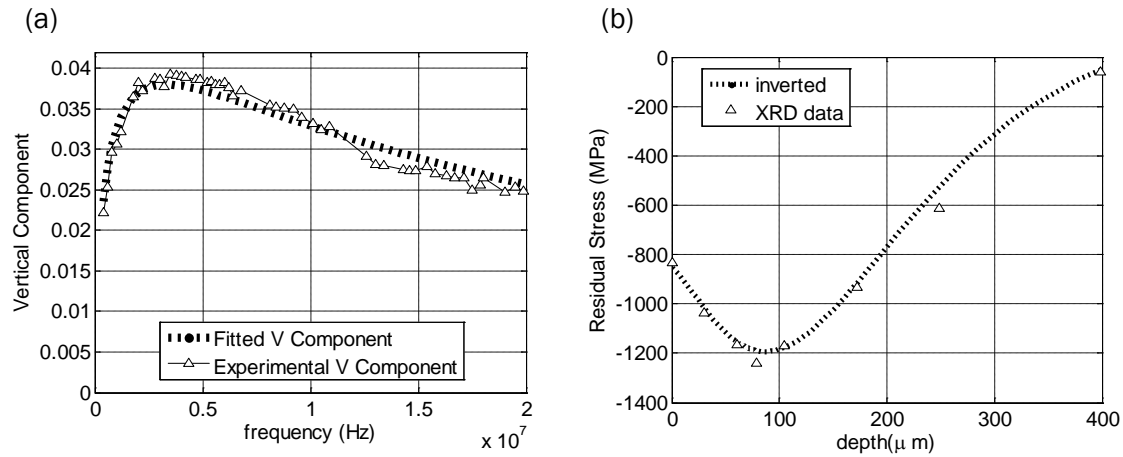


Figure 14. (a) Measured And Best-Fitted V-Component EC Signals Measured From The Inconel 718 Sample Shot Peened At 17A. (b) Inverted Residual Stress Profile Compared To That Measured By XRD Layer Removal Method

Conclusions

The multi-year efforts have achieved several accomplishments including:

1. Developments of high-frequency eddy current probe and instrumentation suitable for characterizing near-surface material conditions
2. Developed SHFEC measurement systems operational up to 60 MHz, and have continually improved it for better signal-to-noise and ease of use (Sec. 3.1.1).
 - a. The original system (Figure 1 (a)) utilizes a differential pair of spiral coils fabricated on a printed circuit board (PCB) with two balancing resistors to form an ac bridge. The single PCB probe system minimizes parasitic noises, but limits its applicability due to its relatively large footprint and rigidity.
 - b. The upgraded system (Figure 1 (b)) operates with a differential pair of standalone buffered EC probes, and allows the use of an external amplifier as needed. This system offers a better signal-to-noise ratio than the original system, while the

- standalone probes with a smaller coil footprint improves their applicability for inspecting samples of various sizes and shape, or with curved surfaces.
3. Advancement of the swept frequency EC measurement technique, and establishment of a near-surface conductivity deviation profile inversion methodology
 4. Established a measurement technique by the use of the vertical component (V-component) signals, which permits direct comparison between experimental and modeling signals, thus enabling model-based inversion of conductivity profiles (Sec. 3.1.2).
 - a. The liftoff and parasitic noises, as well as instrumentation dependency, are suppressed significantly.
 5. Established a model-based inversion technique to convert SHFEC signals into conductivity profiles for material characterization (Sec. 3.1.3).
 - a. This approach is advantageous in terms of determining the near-surface conductivity profile directly, as opposed to calibration-based methods that yield frequency-dependent “apparent conductivity changes.”
 - b. Two inversion schemes and software codes were developed and implemented; the first inversion scheme is based on the analytical EC Cheng-Dodd-Deeds model. The second inversion scheme is based on perturbation theory applicable under our measurement conditions. The perturbation-based method offers a distinct advantage of permitting analytical calculation of V-component signals from assumed conductivity deviation profiles, thus streamlining the data-fitting process significantly.
 - c. The methodology for measuring SHFEC signals up to 60 MHz and converting them into conductivity deviation profile is validated through its application to simulated layer samples.
 - d. The perturbation-based formula (Equation (5)) also predicts that the V-component signals are virtually independent of the coil parameters, thus proving their universality across dissimilar measurement systems (Figure (5)).
 6. Progress toward understanding the effects of near-surface material condition deviations on EC signals, particularly those induced by shot peening. The understanding gained in this project is beneficial to other related NDE problems including characterization of coating, roughness and anomalous machining damages.
 7. Carried out a fundamental study of the origins of conductivity variations in shot peened Inconel 718, with the focus of this project on the relative importance of the stress and microstructure effects (Sec. 3.1.4), in conjunction with the examination of the cold work effects conducted in a companion project. Specifically, we:
 - a. Studied the shot-peening induced changes in EC responses of a series of Inconel 718 that was heat treated to produce various secondary phase contents, showing the extent to which the stress-induced conductivity deviations profiles depend on the microstructure and hardness of the samples (Sec. 3.1.4.A).
 - b. Found in the cross-sections of the shot peened samples that there exists a surface damaged layer which is 20-30 μm thick (Figure 9, Sec. 3.1.4.B). We then established a specific conductivity profile inversion procedure, in which the effect of the damaged layer is accounted for and eliminated from the inverted profiles (Figure 10).

- c. Measured near-surface variations in the secondary phase content, or their depth profiles, for a selection of the samples (Sec. 3.1.4.C). Leaving aside the question about the origins of the observed secondary phase content profiles, we showed their presence and estimated their effect on the conductivity profile, by characterizing the volume fraction of secondary phase precipitates at different depths from the non-peened and shot peened surfaces of a heat-treated Inconel 718 sample, and estimated the effects of phase content variations on SFEC signals (Figure 11), based on an empirical calibration (Figure 12)).
- d. Examined the possible influence of crystallographic texture on the piezoresistivity (Sec. 3.1.4.D). In our early studies of an Inconel 718 sample that was shot peened at high Almen intensity of 17A, we observed shot-induced changes in crystallographic texture with depth (Figure 13). We thus generalized the piezoresistivity relationship to account for the texture effect, and showed a possibility of fitting the AFEC data to the texture-influenced piezoresistivity theory (Figure 14).

Recommendations

It is recommended to continue the fundamental studies being conducted. The project goal is to complete the efforts to uncover complex relationships between EC signals and near-surface alloy material states generated by shot peening and other surface treatments. To date, experience has directed our attention to three underlying material conditions contributing conductivity changes, i.e., residual stress, microstructure (damages and precipitates), and cold work. The follow-on project should:

Determine quantitatively the relative importance of the competing EC signal sources.

Determine whether shot-peening may or may not modify the near-surface concentration profiles of precipitates.

Develop sample fabrication techniques that allow us to measure near-surface precipitate concentration profiles via TEM.

Establish an EC model that can predict EC signals arising from the damaged layer, when the layer is regarded as a simulated collection of slip damages.

Examine other possible underlying material conditions, such as magnetism, which may potentially contribute to EC signals.

To achieve these fundamental goals, the follow-on project should make additional efforts to improve the sensitivity and applicability of the EC inspection method, the targets including:

Development of high-frequency coil elements of small foot prints, such as a ~1mm diameter, presumably by the use of deposition methods.

Development of probe elements fabricated on flexible substrate.

Improvement of the on-board electronics toward higher S/N ratio, desirably implementing constant current drive.

Enhancement of coil sensitivity in lower frequency measurements, by developing stable constant current drive electronics.

3.2 High Energy X-Ray Diffraction Measurements Of Stress Profiles In Bulk Materials (Jensen, J. Gray)

Investigation Team: Joe Gray and Terry Jensen
Student: Mohammad Al Shorman

Motivation

An understanding of internal strain fields in samples is important for fundamental studies of material properties and damage evolution, as well as for engineering design and component lifetime analysis. Typically shot peening is used to induce compressive residual stress near the surface of critical components to inhibit crack growth. Through operation cycles this residual stress may relax, making the component more susceptible to cracking. A means for measuring the remaining depth of the compressive zone would enable a retirement for cause program to be implemented, where only those components that have an insufficient remaining compressive zone are retired. Currently there is no good way to nondestructively measure the depth profile of remaining residual stress, especially in nickel and titanium, so components are conservatively retired after a fixed length of service. Knowledge of remaining beneficial residual stress could be used in lifing calculations, resulting in significant financial savings.

X-ray diffraction (XRD) is the standard that is used for comparing residual stress measurements by different techniques [28]. To obtain a stress profile using traditional XRD, it is necessary to successively remove layers of material and make a series of XRD measurements [29]. Hole drilling [30] is another technique that has been used for profiling. Both of these methods are destructive. Neutron diffraction [31] can be used for nondestructive profiling, but the spatial resolution is ~1 mm, and access to high-intensity neutron beams is limited. High resolution profiling has been demonstrated using x-ray synchrotron beams [32], but access to these beams is also limited.

Results – Theory and Experiments

3.2.1 Basic Concept

X-ray diffraction (XRD) produces a direct measurement of strain through the detection of the diffraction peak angle shift, which measures inter-atomic distance deviations. This follows from Bragg's law, which can be written as

$$E(\text{keV})d_{\text{hkl}}(\text{\AA})\sin\theta = 6.199n, \quad (1)$$

where x-rays of energy, E , are diffracted at an angle, 2θ , from crystal planes having spacing d_{hkl} , and n is an integer. Traditional XRD instruments use the copper (8.04778 keV) K_{α} line to measure diffraction angles. At this low energy, the x-rays can penetrate the sample surface only a few microns. To obtain a residual stress profile it is therefore necessary to etch away successive layers of the sample and repeat the measurement. Our High-Energy XRD (HEXRD) approach uses the very narrow (43eV) tungsten $K_{\alpha 1}$ line (59.318 keV) from a conventional

tungsten-target x-ray tube, which can penetrate much deeper into a sample, and thereby produce a truly nondestructive profile of residual stress.

The system that we have developed for HEXRD measurements is depicted schematically in Figure 15 and in the images of Figure 16. The output of a high-power industrial-inspection x-ray tube (320 kVp, 640W) is collimated to form a narrow incident beam that strikes a sample mounted on rotation and translation stages. The diffraction angle is defined by a pair of collimators that are mounted on an arm that rotates along with the x-ray detector. The intersection of the incident and diffracted beams forms a diamond-shaped probing volume in the sample. The sample can be scanned through this volume to map out a strain profile.

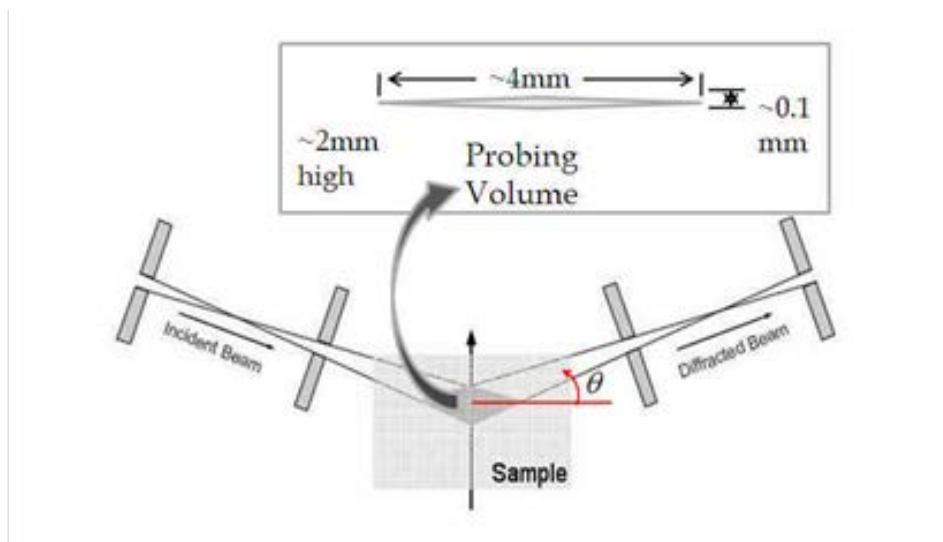


Figure 15. Schematic Representation Of The HEXRD System. The X-Ray Source Is Located To The Left, And The Detector To The Right. The Inset Shows Typical Dimensions Of The Probing Volume Used For Studies Of Residual Stress In Metallic Alloys

The x-ray tube (Comet MXR-320/23) is operated at a focal spot size of 1.9 mm, at 270 kVp and 2.2 mA. In addition to the continuum Bremsstrahlung output of this tube, there are four strong tungsten characteristic lines. The $K_{\alpha 1}$ line at 59.318 keV has the highest intensity, and thus is used extensively in our diffraction measurements. The x-ray detector (at the end of the diffraction arm in Figures 15-16) is a liquid-nitrogen cooled High-Purity Germanium (HPGe) detector manufactured by ORTEC. The energy resolution of the detector was measured to be 0.4 keV FWHM at 60 keV. For our work, the opening of the collimators has been set within the range 100-140 μm . For these collimation dimensions the resulting incident and diffracted beam divergence is approximately 0.006-0.008°.

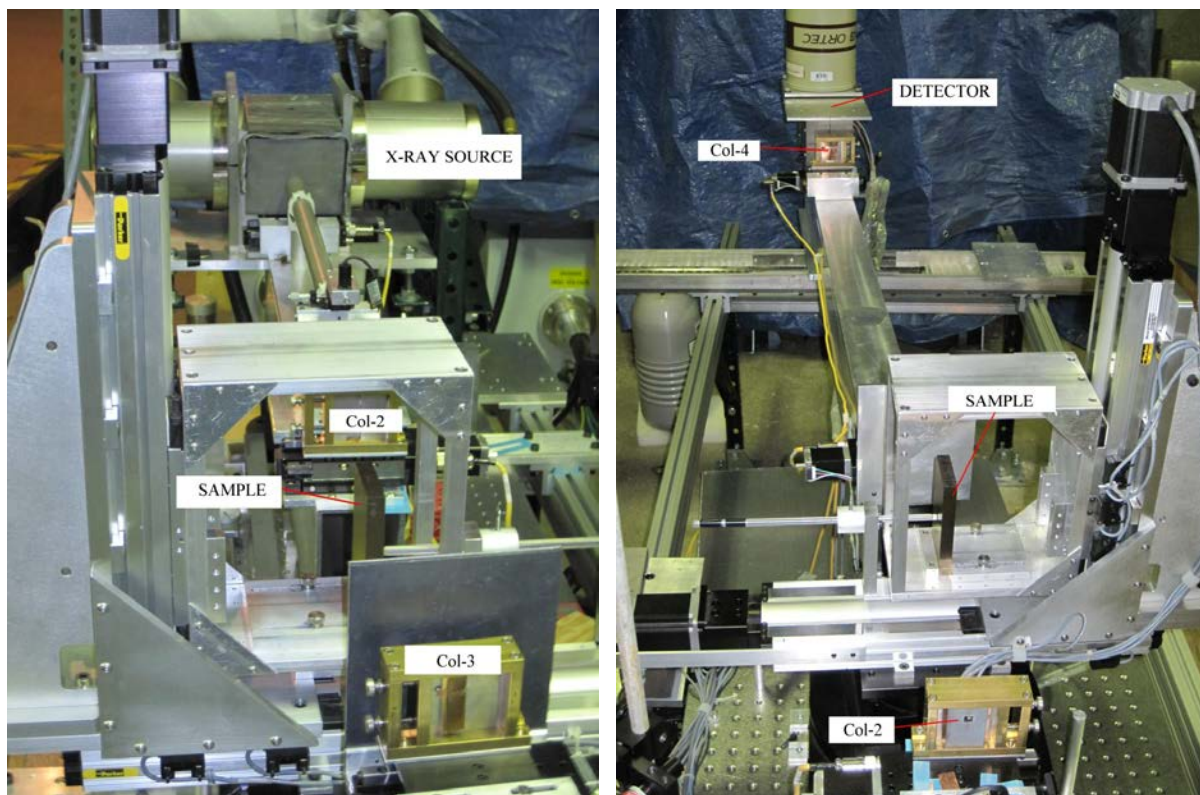


Figure 16. Images Of The HEXRD System Looking, Left, Towards The X-Ray Source, And Right, Towards The X-Ray Detector

Figure 17 shows an example of data from a θ - 2θ scan on an aluminum 6061 alloy sample. The two-dimensional plot shows x-ray energy vs. diffraction angle, with the color indicating the intensity. Diffraction is produced both from the Bremsstrahlung continuum and the tungsten characteristic lines. Although it does not show up very clearly in the two-dimensional plot, the intensity along each of the diffraction curves shows a strong enhancement when the energy matches one of the characteristic lines. If we select data from a narrow range of energies, corresponding to the tungsten $K_{\alpha 1}$ energy, indicated by the horizontal dashed line, we get the projection at the bottom of the plot, which is in the form of a traditional θ - 2θ scan. Alternatively, selecting data at a fixed angle (vertical line) produces the projection to the left that is in the style of Energy-Dispersive XRD (EDXRD). Within the range covered by this scan, diffraction from four different sets of aluminum planes is observed. The width of the diffraction bands is dominated by the energy resolution of the detector. However, there is also a contribution due to the angular divergence mentioned above.

The key, new idea in our approach is utilizing the intrinsic sharpness of 43 eV for the K_{α} characteristic line. We select a detector position in 2θ such that for a normal d_{hkl} (unstrained) we get diffraction at the K_{α} tungsten energy. Examination of Equation 1 illustrates that for the fixed detector position, a small change in d_{hkl} will shift the energy required to meet the Bragg diffraction condition. Even a very small energy shift will be outside the intrinsic K_{α} line width, resulting in a dramatic drop in observed diffraction intensity. This implies that the observed diffraction intensity is a very sensitive measure of changes in lattice parameter. To produce a

comparable narrow-width beam at a synchrotron requires using a crystal monochromator, which greatly reduces the beam intensity. Thus, the method we have developed is competitive in terms of sensitivity with measurements done at a synchrotron, but at a greatly reduced cost.

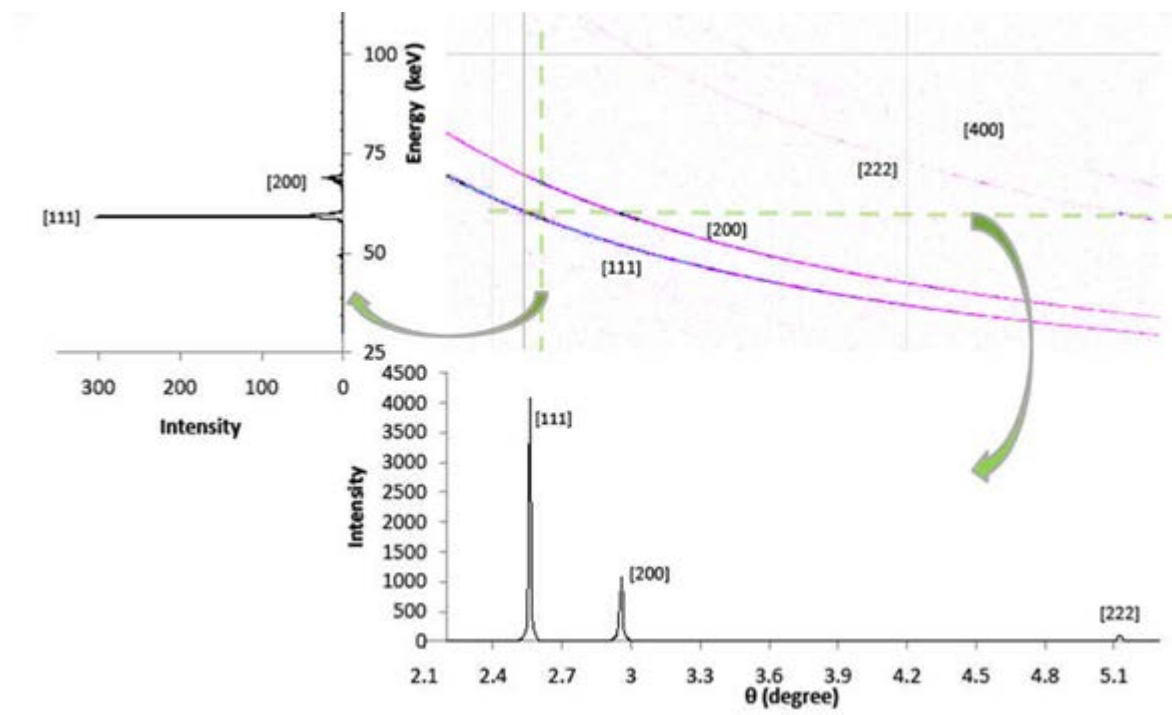


Figure 17. Data From A θ -2 θ Scan On An Aluminum Sample Plotted In Terms Of The Energy And Angle Of Diffracted X-Rays As A Two-Dimensional Scatter Plot. Blue And Black Colors Indicate Higher Intensity. These Data Are Then Projected Onto The Horizontal And Vertical Axes For Selected Ranges Indicated By The Dashed Horizontal And Vertical Lines, Respectively

3.2.2 Initial Applications to Al, Ti, and Ni

By setting the instrument at a fixed angle and scanning the sample through the probing volume we can obtain a profile of the diffraction intensity vs. depth as indicated in Figure 18. The examples on the left are for an Al-6061 alloy that has been shot peened to different levels. The top curve is for a sample that has been annealed so that uniform lattice spacing is expected throughout the sample. The diffraction angle (2.562°) was chosen to correspond to the tungsten $K_{\alpha 1}$ peak for the nominal Al [111] lattice constant. Only x-rays within 0.5 keV of the $K_{\alpha 1}$ energy are included in this plot. As the annealed sample enters the probing volume, the intensity rises, until a maximum is reached when the probing volume is entirely within the sample. Beyond the maximum, the intensity falls exponentially due to greater attenuation as the path length increases. Any deviation from this shape, such as seen for the shot-peened samples, is an indication of a change in lattice constant. There is good sensitivity for distinguishing the different shot peen levels. In each case, the intensity eventually reaches that of the pristine material, indicating that this is the depth to which the lattice constant has been modified. The plot to the right shows a similar example for Ti-6Al-4V samples. In this case, the greater attenuation limits the probing depth and reduces the statistics. Figure 19 shows results from Inconel 718 samples [33]. The

shot-peened sample produced a very broad θ - 2θ plot, and a resulting very low-intensity depth scan. The highly attenuative nature of nickel limits the penetration depth to about 150 μm , which is comparable to the width of the probing volume.

With the beam angular divergence, the characteristic line width, and the typical changes in the lattice parameters of strained metallic samples all being of the same order of magnitude, a direct application of Bragg's law is not sufficient to understand experimental results from the HEXRD system. To convert the raw x-ray diffraction data seen in Figure 4 to quantitative changes in lattice parameters, we developed a computer program that models the experimental setup [34]. This model includes the geometry of all collimators, beam divergence, the x-ray source spatial and energy distributions, attenuation in the sample, and finite width of the tungsten $K_{\alpha 1}$ line (43 eV).

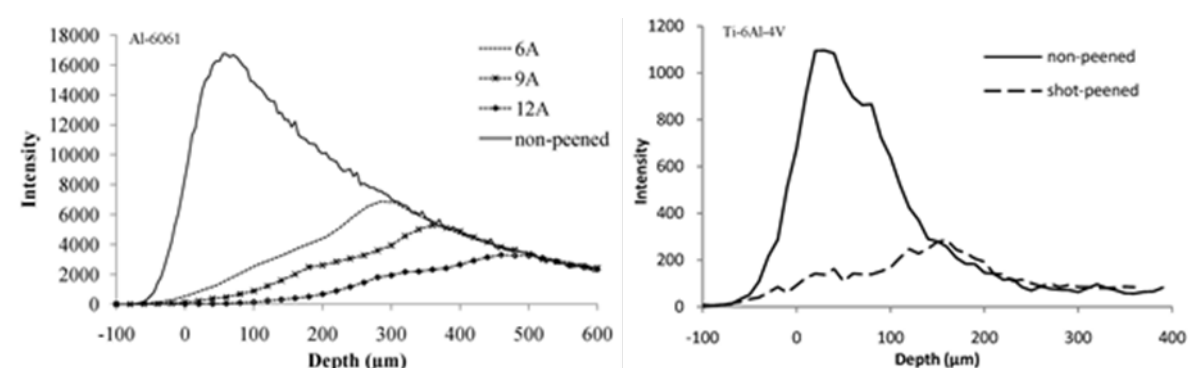


Figure 18. Diffraction Intensity As A Function Of Depth Of Probe Volume In The Sample, For Different Shot-Peen Levels For Aluminum Samples (Left), And Ti-6Al-4V Samples (Right). To Obtain These Plots, We Have Collected Data At Fixed Angles For Each Material And Integrated Over Energies Within 0.5 Kev Of The Tungsten $K_{\alpha 1}$ Line

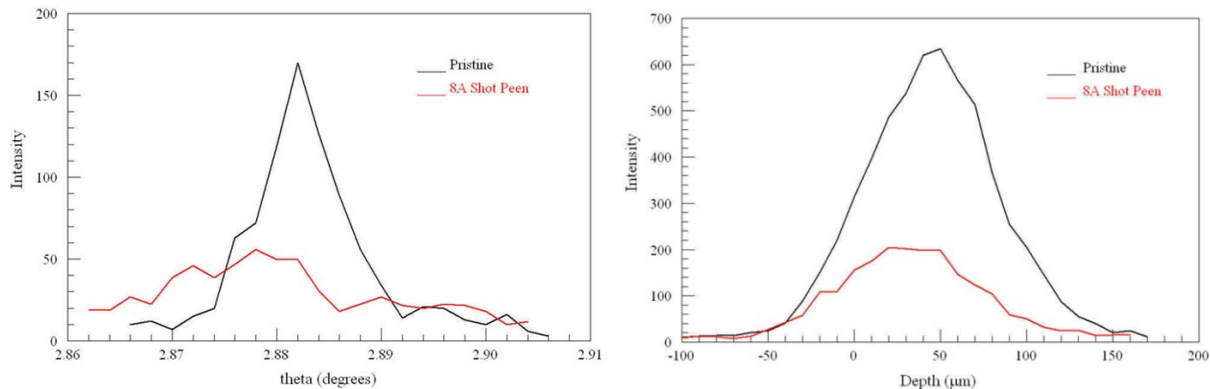


Figure 19. Comparison Of Pristine And Shot-Peened Inconel 718 Samples. The Plot To The Left Shows θ - 2θ Scans Near The Surface Of The Samples, While The Plot To The Right Shows Diffraction Intensity As A Function Of Depth For The Nominal Diffraction Angle

A relation between the normalized intensity and the change in lattice constant, Δd , can be constructed by running the simulation program for every probing-volume location inside the sample, and considering a range of strain values at each location. Normalization is done with respect to the intensity expected for unstrained materials. In the case of shot peening, it is generally valid to assume that material deep in the sample is unstrained, such that data from this region can be used for normalization. This is justified by the observation in Figure 18 that all of the intensity profiles converge at depths beyond 500 μm . The result of this series of simulations is a lookup table relating experimentally measured intensity to strain. The depth profiles of the lattice constant deviation for the shot peened Al-6061 samples of Figure 18, as calculated using this lookup table are shown in Figure 20. The reader who is familiar with traditional XRD will observe that the strain is opposite of what is traditionally plotted. This is because, unlike traditional XRD, the small-angle HEXRD method measures the lattice parameter perpendicular to the sample surface. When a lattice is compressed in the directions parallel to the sample surface, the lattice must expand in the perpendicular direction. It should also be noted that the intensity normalized method by itself cannot be used to determine whether the strain is compressive or tensile. However, an observation of the direction of the shift in diffraction x-ray energy can be used to determine the sign of the strain. At present, we have carried out this detailed modeling only for aluminum materials.

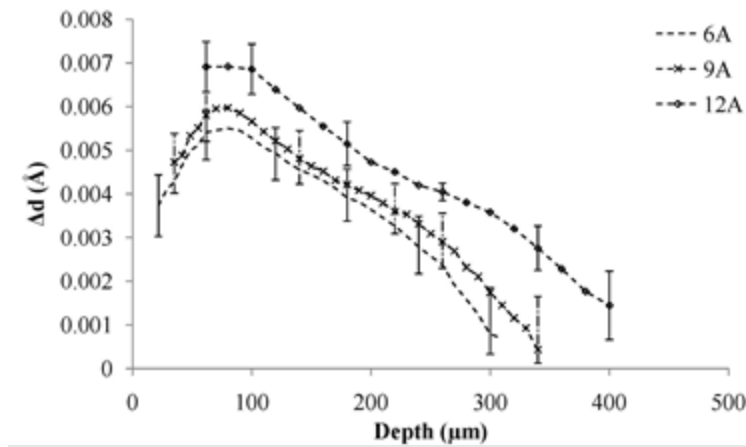


Figure 20. Strain-Depth Profile Curves Calculated From The Al-6061 Diffraction Data Of Figure 4 Using The Normalized-Intensity Method Described In The Text

For the existing system, we have extensive data for Al, Ti, and Ni samples. In addition to the differences in attenuation, these different materials have different atomic form factors, crystal-symmetry multiplicity factors, and Lorentz polarization factors [35]. Under the assumptions used for powder diffraction, the plot in Figure 21 shows the relative intensity as a function of depth for Al [111], Ti [101], Fe [110], and Ni [111] diffraction. Considering that we have observed Ni diffraction at 150 μm depth, Ti at 400 μm , and Al at $>1\text{mm}$, these estimates are in good agreement. Note that for highly-attenuative materials, such as Ni and Fe, an order of magnitude increase in intensity will increase the penetration depth by only 40-50 microns.

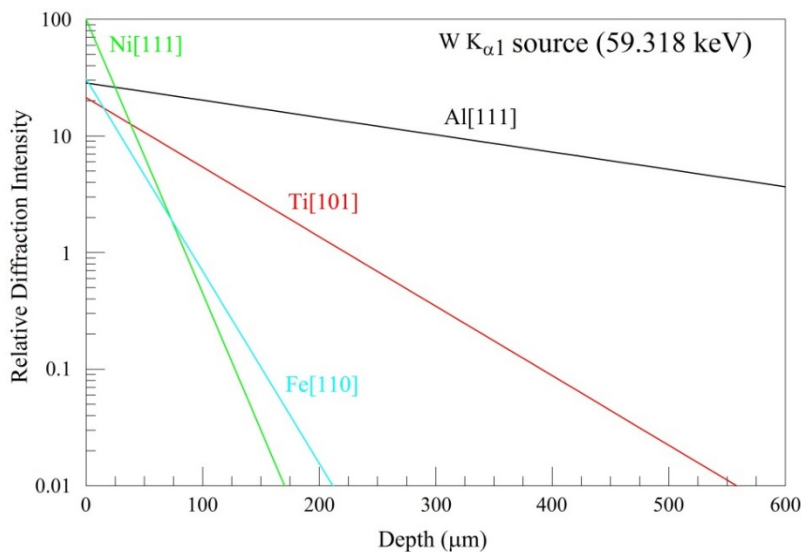


Figure 21. Relative Intensity Expected For Diffraction From Different Materials As A Function Of Depth

The assumptions required for powder diffraction are not always satisfied for manufactured materials though. In particular, the manufacturing process can produce relatively large grains having preferred orientations with respect to the sample surface. We have noticed this to be quite prominent in aluminum materials. The examples shown above in Figures 17 and 18 are from an extruded bar with grains that emphasize diffraction from the [111] planes. If we cut the bar along a different direction, we observe very weak [111] diffraction.

An interesting example of grain orientation effects is displayed below in Figure 22. This shows diffraction depth profiles for an aluminum alloy 2024 sheet of the type used in aircraft skins. This is a rolled material 1mm thick with a 25 μm cladding of pure aluminum to inhibit corrosion. It is clear that the cladding layer has grains oriented to favor [200] diffraction, whereas the bulk of the material has more randomly oriented grains.

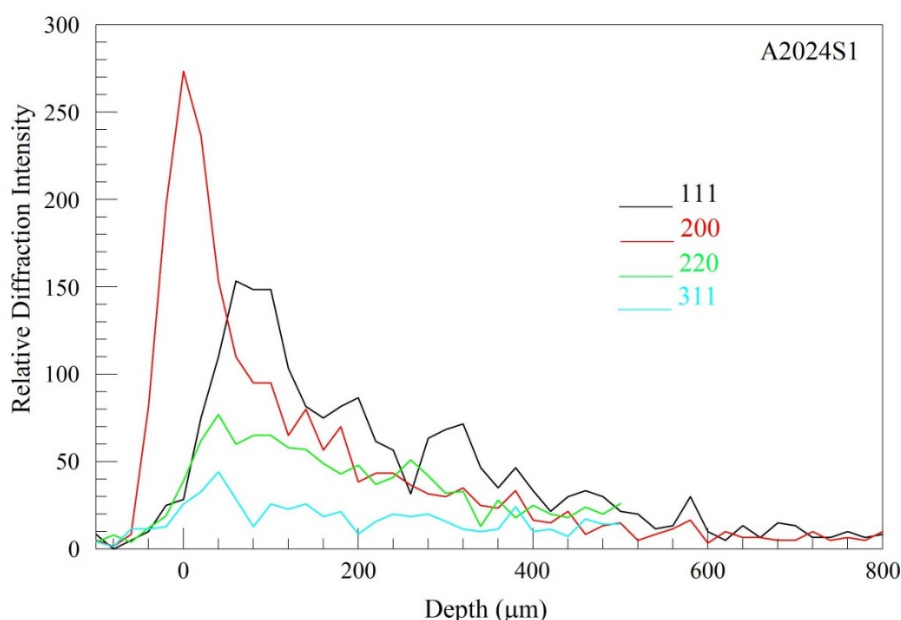


Figure 22. Diffraction Depth Profiles For Different Lattice Planes In An Aluminum 2024 Alloy Sample

Conclusions

X-ray diffraction is a well-established method for measuring surface residual stress. We have demonstrated that the technique can be extended to nondestructively measure strain profiles in samples by using a high-energy x-ray source. We fabricated a system from standard off-the-shelf equipment, albeit, configured in a unique way. Using this first generation prototype we have measured strain profiles in aluminum, titanium and nickel alloys ranging to depths of several millimeters in aluminum, to 300-400 microns in titanium and up 200 microns in nickel. The probing volume thickness for the depth scan ranges from 75 microns to 150 microns. At present this method is the only demonstrated nondestructive measurement that works for titanium and nickel alloys. These measurements were compared to standard θ - 2θ angular scans, with excellent agreement.

While these laboratory measurements remain slow, typically taking several hours, we have identified a number of straightforward modifications to the instrument that can reduce the measurement time by 10-50x and increase the penetration depth by a factor of two. These include a more compact method of beam collimation, and a laser distance gauge to give a better definition of the sample surface. It should also be possible to develop an algorithm for determining the strain profile that is based on theoretical models. This approach will require fewer data points to determine the strain profile, thus speeding up measurement. Finally, the measurement speed can also be improved by using a more intense source. A custom design will optimize the flux for HEXRD measurements.

Recommendations

1. Implement design for more compact, robust HEXRD system.
2. Improve analysis algorithms to incorporate knowledge of expected stress profile.
3. Work with manufacturers to develop custom x-ray tube optimized for HEXRD.

3.3 Simulation Of Eddy Current Inspection Of Aircraft (J. Bowler)

Investigation Team: John R. Bowler, (Iowa State University, CNDE) and Theodoros Theodoulidis (University of Western Macedonia, Greece)
Student: Hui Xie (Graduate Student)

Motivation

The models developed for the simulation of eddy current inspection of aircraft are designed to assist in estimating probabilities of detection (POD), in damage characterization and in structural health monitoring. In the case of POD estimation, models do not provide a complete answer for any given inspection task but they can greatly reduce the need for large numbers of test samples to be manually inspected thereby providing a cost savings in establishing detection metrics. In the case of damage characterization, one can take advantage of the fact that a well-crafted and efficient model used to predict inspection signals from flaw parameters via a forward model can be put into reverse to determine flaw parameters from measured data through various procedures notably, non-linear iterative inversion. Finally, the scope, performance and coverage of a structural health monitoring system can be evaluated and optimized with the aid of simulation tools. In summary, the models provide knowledge and insight to guide improvements in inspections and cost savings in estimating detection probabilities.

Although computer simulation and modeling has been widespread for more than forty years, the general availability of highly effective and efficient computer models remains limited and largely in the hands of specialists. The “essential tension” in model development is the desire to have available computational tools that can simulate complex configurations rapidly and reliably without the need for users to have a detailed knowledge of the underlying code or a detailed understanding of the methods for fine tuning its precision. At present, the general purpose codes require a great deal of investment by users in order to learn techniques to control the accuracy of the outcomes, as anyone who has used commercial finite element code can testify. This knowledge of software control and performance from the user’s point of view is largely ephemeral, narrowly focused and unfulfilling; since scientist and engineers benefit most, in the long run, from investment in learning that is generic and transferable. General purpose codes typically require a discretization of the field throughout the solution space and consequently are computationally intensive and hence the time taken to produce results is rarely as short as one would like.

For specific model-assisted tasks such as the optimization of an eddy current inspection, codes have been developed based on integral methods. These are undemanding for the user, fast and the accuracy is easily controlled, but they are restricted to specific configurations. Vic3D by Victor Technologies and the eddy current codes in CIVA follow this approach, both of which are based largely on volume integral schemes [36]. The calculations can be orders of magnitude faster than those that use the finite element method (FEM) since the population of unknowns in computations based on integral formulations is often small. The essential advantage of these methods stems from the fact that an integral kernel is used to represent the electromagnetic field due to an arbitrary dipole source distribution. The kernel can take account of the boundary conditions at the surface of the part automatically, without adding to the number of unknowns in

the problem, provided the part geometry is simple; for example a flat plate or an infinite cylinder. In this way a mesh filling the problem domain is not needed because the kernel is used in a calculation to estimate the field in a flaw that takes into account the part geometry without adding discrete elements. A set of volume or boundary elements is used to represent the field in the flaw which requires only a few unknowns and the accuracy is easily controlled by giving users a simple choice; e.g., high, low or medium accuracy, which simply controls the number of volume element cells per skin depth in a particular direction. Typically the speed of the calculation is two or three orders of magnitude faster than a finite element code for three-dimensional problems.

The kernel can be determined analytically for simple geometries such as an infinite borehole or tube or an infinite plate or a sphere. In each case uniform layers conforming to the basic geometry can be included without adding unduly to the computational cost. But in these cases, we are restricted to canonical structures in which a basic solution, such as the dedicated integral kernel for the structure representing the dipole field at an arbitrary point, can be found by the fundamental analytical method of separating variables and whose mathematical expression represents an exact result.

If one could find such a kernel for components of any shape, then the speed, accuracy and ease of use of the integral methods would be allied with the capability of dealing with complex structures. Recently, a possible way of achieving this ultimate goal is emerging and some preliminary steps have been taken to compute integral kernels for flaws in structures bounded by arbitrary surfaces. To approach the general problem, we have computed kernels dedicated to special structures such as ones containing edges using an approach we refer to as the truncated region eigen-function expansion (TREE) method. In the summary of the technical achievement of the current program, we shall refer to some of these solutions indicating how they form part of a general strategy to determine kernels for non-canonical geometries that we believe will lead to a new generation of computational tools based on the development of integral methods for structures bounded by complex surfaces. First however we shall review advances made during the current program.

Results – Theory & Experiment

3.3.1 Integral Methods for Cylindrical Systems - Applications

The applications of integral methods to cylindrical systems is a class of problems in which eddy current signals due to flaws such as cracks and corrosion are determined in the region of fasteners or boreholes or tubes. The inspection of fastener holes can take place with the fastener in place, using, for example, a slider probe excited at relatively low frequency on the surface of an aircraft. A related task involves the inspection of holes following the removal of a fastener or bolt in which the inspection is carried out by using a rotating differential probe operated at relatively high frequency. In either case, a calculation of the interaction of an eddy current probe with a crack adjacent to the hole can be carried out by using integral techniques.

In order to compute the effect of cracks under installed fasteners, a straightforward simulation can be carried out using a volume element calculation in which the effect of the crack and the

fastener is represented by volume elements. This involves a relatively large number of elements to represent the entire region of the fastener and hence a substantial computation burden is involved, although, perhaps not as large as that needed to compute the results via a finite element method. Currently we are developing an approach for reducing the computational cost of the cracks-under-fasteners problem but this has not been the main thrust of the current program.

3.3.2 Borehole Inspection

In the present program we have focused mainly on the second problem which is the calculation of signals due to cracks in boreholes using rotary probes. The logical starting point is the canonical problem of computing the eddy current probe interactions with a crack adjacent to a hole, neglecting, initially, edge effects such as those encountered at a countersunk region or at the interfaces between plates. Recall that a canonical (flawless) structure is defined as one in which a basic solution such as the dipole field at any point can be expressed in a form that represents an exact result. A uniform conductor with infinite circular hole through it is one such fundamental structure.

Instead of simulating the inspection with a differential ferrite cored probe as is commonly used in practice, we have considered a probe in the form of an absolute rotary coil as shown in Figure 23 (A). The reason for this is that we wish to test the flaw model separate from that of the probe field evaluation. The validation of differential probe model is being pursued in collaboration with Jeremy Knopp and colleagues at AFRL and will be incorporated into our available models after validation.

We have determined eddy current probe impedance changes due to an absolute probe interacting with a crack in a borehole. The problem is formulated using a scalar decomposition of the field into transverse magnetic and transverse electric scalar components [37]. The theory includes several innovations. Firstly, we have calculated the field due to an absolute rotary coil in a borehole using a new analysis which is an advance on one introduced by Burke and Theodoulidis [38]. The flaw calculations use a Green's kernel for an infinite borehole, derived from first principles using the scalar decomposition formulation to get the exact expression appropriate for a canonical structure. The approach used in CIVA [39] by contrast, is a restatement of the work of W.C. Chew [40]. Other simulation codes available such as Vic3D and ECSim are reportedly using a flat plate treatment to approximate the effect of the flaw in cylindrical systems. Clearly this is not an accurate approximation in general, although it may give reasonable results for some limiting cases. However there is a strong temptation to use the flat plate approximation in this context since the derivation of the borehole kernel in cylindrical coordinates is complicated, as is the implementation of the required code.

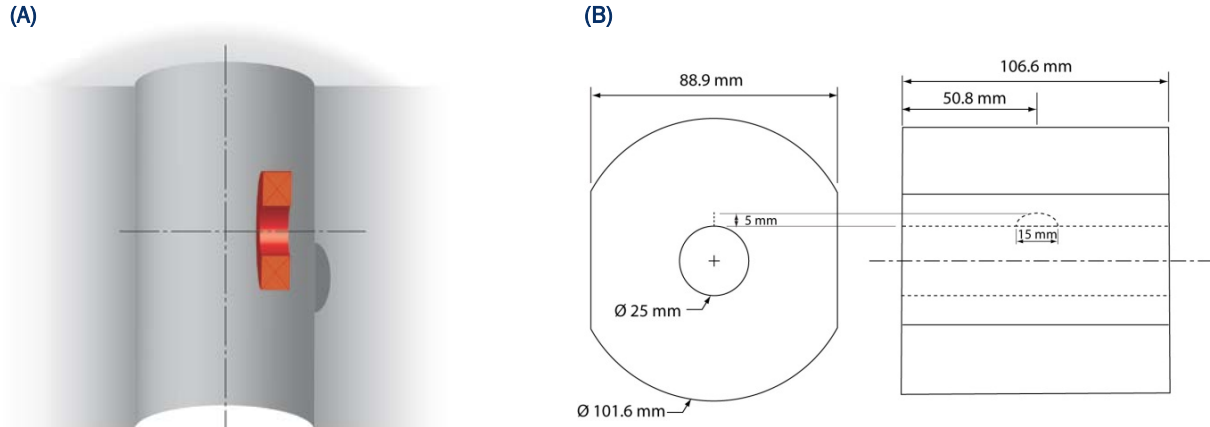


Figure 23. (A) Rotary Coil In A Borehole Interaction With A Semi-Elliptical Crack (B) Test Specimen For Validating Impedance Predictions From The Rotary Probe

3.3.3 Initial Calculations

We have determined eddy current probe impedance changes due to an absolute probe interacting with a crack in a borehole. The problem is formulated using a scalar decomposition of the field into transverse magnetic and traverse electric scalar components [37]. The theory includes several innovations. Firstly, we have calculated the field due to an absolute rotary coil in a borehole using a new analysis which is an advance on one introduced by Burke and Theodoulidis [38]. The flaw calculations uses a Green's kernel for an infinite borehole, derived from first principles using the scalar decomposition formulation to get the exact expression appropriate for a canonical structure.

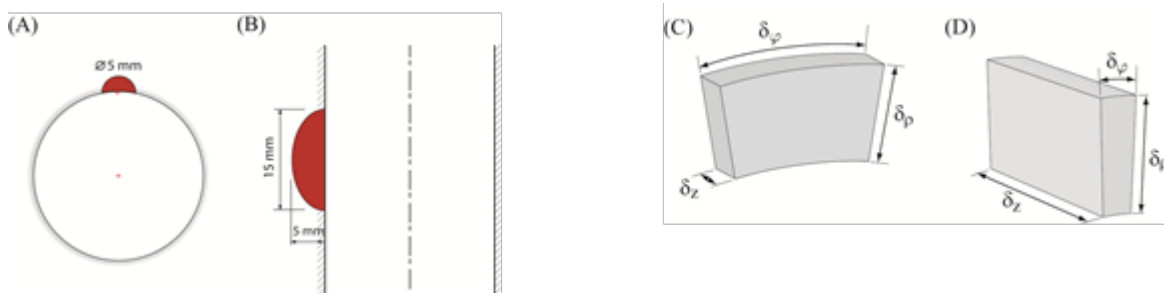


Figure 24. (A) Circumferential And (B) Longitudinal Notch Used For Validation Of The Borehole-Crack Calculations. (C) Illustrates A Volume Element Several Of Which Are Used To Construct The Region Of A Circumferential Notch (D) Shows The Volume Element Of The Type Used To Construct The Region Of A Longitudinal Notch

The approach used in CIVA [39] by contrast, is a restatement of the work of W. C. Chew [40]. Other simulation codes available such as Vic3D and ECSim are reportedly using a flat plate treatment to approximate the effect of the flaw in cylindrical systems. Clearly this is not an accurate approximation in general, although it may give reasonable results for some limiting cases. However there is a strong temptation use the flat plate approximation in this context since

the derivation of the borehole kernel in cylindrical coordinates is complicated, as is the implementation of the required code.

The derivation of the kernel involves the evaluation of coupled reflection and transmission coefficients for the TE and TM modes to match solutions on either side of the borehole surface. Because the modes are coupled at the air-conductor interface, the transmission and reflection coefficients are in the form of 2x2 matrices in which the off-diagonal terms represent mode coupling [37]. We use volume elements to represent the field in the crack, Figure 24 (C) and (D), but carry out point matching at the surface of the element in a moment method scheme to determine the effect of the flaw. We represent the source of the flaw field as an electric dipole layer occupying the region between the crack faces, the dipole orientation being perpendicular to the faces of the crack.

Model predictions have been compared with experimental measurements of probe impedance variations with position due to electrical discharge machined (EDM) notches. Two test specimens were used, one of which, shown in Figure 23 (B), is a longitudinal semi-elliptical notch and the other is a transverse notch with a circular arc profile. Figure 24 (A) and (B) show the shape and dimensions of the notches and Figure 25 shows that the predictions of the model are in good agreement with experiment.

Recently we modified the integral kernel for bolt-holes to deal with cracks in tubes and created a new benchmark problem in the World Federation of NDE Centers series of such problems. The modified kernel and the updated code, has been tested by comparing probe impedance prediction with experimental data on a longitudinal notch in an inconel tube. At the same time we studied the convergence of the kernel, which is in the form of a series, and refined the calculation in order to include higher order terms and ensure greater accuracy. In addition, our experimental technique has improved to the extent that the new predictions are for the most part within 1% of the measurements for the recent tube validation. This work was carried out under the NSF Industry University Program at Iowa State University.

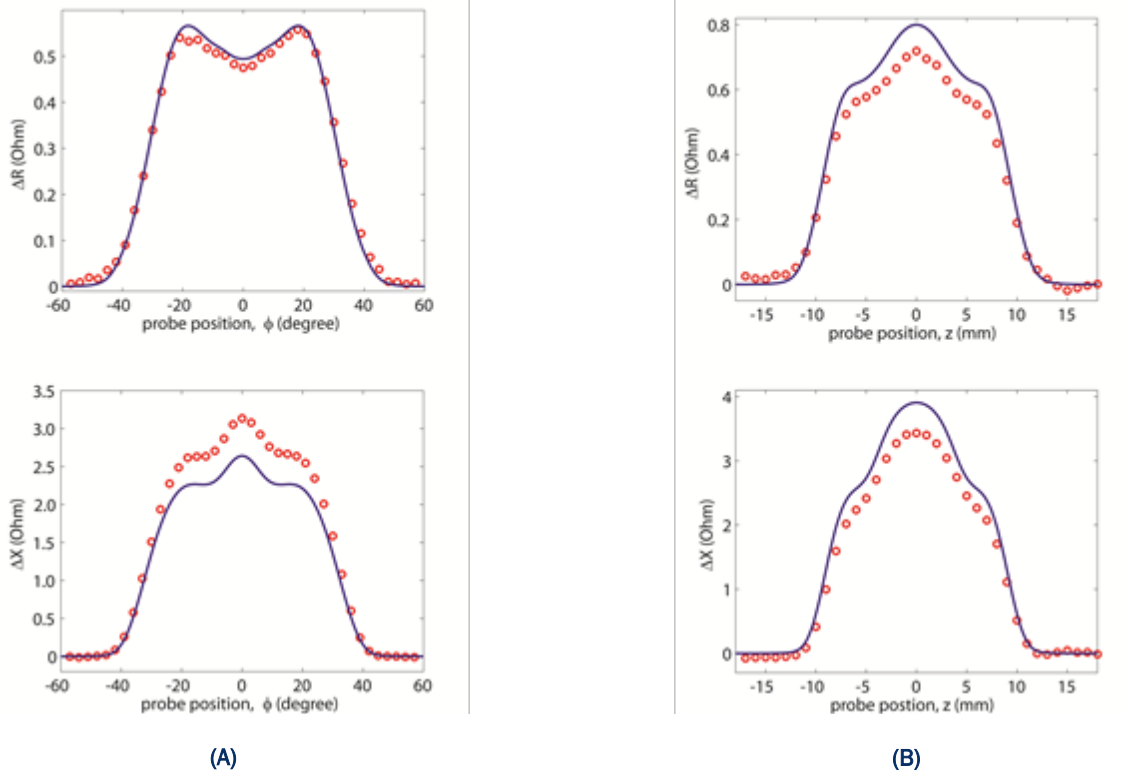


Figure 25. Comparison Of The Variation Of Coil Impedance With Position For (A) Transverse Notch (B) Longitudinal Notch

3.3.4 Extension on the Basic Borehole Problem

We have carried out investigations to extend the capability of simulating the effect of flaws in bolt-holes and developed a strategy called **new generation approaches** to extend the range of problems that can be dealt with using integral equation techniques without greatly increasing the computation cost of the method beyond that which is entailed for the basic canonical geometries; i.e., infinite plates, tubes and holes. In this section we shall summarize extensions to the basic bolt-hole problem outlined above and in the next, describe how the next generation strategy can be extended to deal with eddy current simulation of the components with arbitrary surfaces as discussed earlier.

The inspection of bolt-holes in aircraft is often carried out at relatively high frequencies at which the skin depth is small compared with the depth of a substantial proportion of the detectable cracks. For example, at 500 KHz, the skin depth in aluminum is roughly 100 microns (4 mil). For surface breaking cracks whose depth is greater than four skin depths, a thin-skin approximation can be used to produce accurate results without recourse to traditional numerical methods such as the moment method for the integral equation approach or the finite element method for approaches formulated from differential equations. The approximation implies that eddy currents in the plane of a crack, at $z = 0$ for example, can be represented by a potential with the form

$$\psi(x, y, z) = \varphi(x, y)e^{ik|z|} \quad (1)$$

Here, the coordinate z is in the direction normal to the crack face. In the thin skin regime, $\varphi(x, y)$ satisfies the Laplace equation in the domain of the crack face and $k^2 = i\omega\mu\sigma$. The problem then reduces to a simple one of finding a solution to the Laplace equation in two dimensions using boundary conditions at the edge of the crack and at the mouth [41]. The mouth boundary condition depends on the geometry of the surface and for the borehole problem this condition has been derived from first principles using the coupled boundary conditions for the TE and TM modes at the surface of the borehole. A solution of the inverse problem for the thin skin theory has been developed [42] and an improved inverse problem solution is to be submitted for publication for the bolt-hole configuration.

Two other developments related to bolt-hole inspection have been completed. We have developed a method for computing the fields due to a double-D differential probe as illustrated in Figure 26. In addition we have developed a means of representing surface roughness for the bolt-hole problem. This was motivated by a desire to create, in the long term, a means of doing flaw characterization for bolt-hole inspection that would include the ability to take account of the fact that the holes, after a period of service, are not necessarily circular. In the near future, damage characterization can be carried out automatically by providing a means of analyzing the inspection data through inverse methods but to do this effectively, it will be necessary to take account of non-ideal surface effects and may require new inspection methods that are aimed at obtaining flaw parameters and not simply aimed at improving detectability.

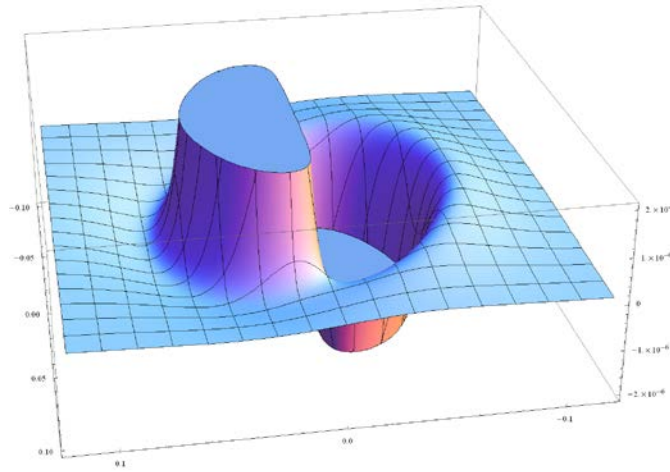


Figure 26. Scalar Potential Representing The Coil Field Of A Double-D Differential Probe For The Simulation Of Bolt-Hole Inspection

3.3.5 New Generation Approach

The theoretical treatment of rough surfaces is linked to the way in which it is possible to model arbitrary surfaces without populating the interfaces between regions having different material

properties with boundary elements. The latter approach has been pursued to produce commercial codes that rival finite element methods in flexibility but both these approaches, while capable of addressing a wide range of problems, suffer from similar deficiencies, namely the need for extensive user intervention, knowledge, and experience plus the inability of the code to deliver accurate results rapidly.

This raises the question, “Can codes be developed that will deliver accurate results quickly and autonomously for a general class of problems without a high computational cost?” It may be possible to answer positively by adapting the way rough surfaces are currently represented by curvilinear coordinates and thus deal with arbitrary surfaces in a field theory that uses integral methods to solve for the effects of an embedded inhomogeneity.

3.3.6 Domain Truncation

Having established an accurate and efficient basic model for borehole inspection, we have developed, in parallel, the truncated region eigen-function expansion (TREE) method for treating the effects of edges. This method is somewhat related to the generalized integral equation approach using curvilinear coordinates and comes under the heading of a new generation approach. We define such approaches as those that use integral formulations with dedicated kernels for non- canonical structures. The canonical structures being those for which symbolically exact analytical solutions are available for a homogeneous structure, by separation of variables. As noted earlier, for many practical purposes these structures are infinite plates, tubes and holes.

In the TREE method, which offers addition flexibility for dealing with non-canonical structures, an analytical expression for the solution is used in the form of a series but the coefficients are determined by numerical methods, typically by matching fields across interfaces “in the weak sense;” which means that this step is done by taking moments of the equation expressing the field continuity condition at an interface and forming a matrix equation for the series coefficients.

A prime example is that of a hole in a finite plate or a half-space. In the corresponding canonical structure we have an infinite hole and can take account of the field continuity conditions at the circular cylindrical hole analytically to construct exact expressions for the field of a probe or the Green’s kernel for the structure. But if the hole intersects the surface of a plate, we have two surfaces, one planar and one cylindrical, intersecting at the edge of the hole. To get a dedicated kernel for this structure, we need to satisfy continuity conditions at the two surfaces simultaneously. Although we cannot write down in symbolically an exact solution for this case, we can get an accurate solution using the TREE method and satisfy both sets of interface conditions. This is done by truncating the domain of the problem in the axial direction, thus creating a solution in the form of a series (43). By taking moments of the interface conditions across the boundary of the hole and its extension into air, one gets a matrix equation to be solved numerically for the series coefficient. Thus the solution is semi-analytical.



Figure 27. Coil Emerging From A Hole In A Conducting Plate Or Half-Space

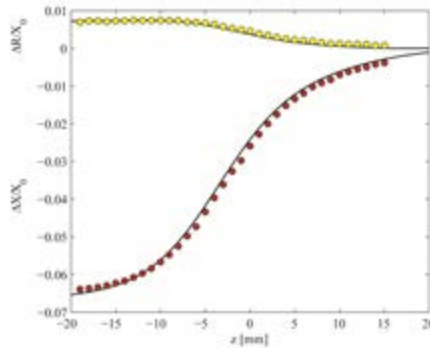


Figure 28. Variation Of The Coil Impedance With Axial Position As A Coil Emerges From A Hole In A Plate. Experimental Data Is Compared With Theoretical Predictions

The TREE procedure has been used to calculate the response of a coil emerging from a hole, Figure 27 and 28, and the integral kernel associated with the structure and a code developed to deal with a crack in the corner region of the hole [43]. Under another program a similar task has been addressed again using the TREE method; that of computing signals due to corner cracks in plates and validating the results [44].

The significance for the Air Force Program, however, is that these improvements, reported at the 2012 QNDE conference [45], are included in the code for predicting borehole inspection signals.

We have not attempted to create a new code for dealing with cracks-under-fasteners in the current program but the work described here on borehole inspection has implication for creating an efficient method for modeling fastener inspection. Using the TREE approach for the borehole opening with straight-forward modifications, one can get the kernel for a prototype fastener in the form of conductive plug filling the hole. Using this kernel, the cracks-under-fasteners problem requires fewer unknowns since one need only account for the countersunk region and the crack by adding a few volume elements compared with the number required to account for the whole fastener and the crack. In this way a problem that takes several hours to run on a computer can be reduced to one that takes only a few minutes with assured accuracy.

Conclusions

We have developed a comprehensive modeling scheme for borehole inspection, including a capability for crack characterization using inverse methods which estimate crack profiles using non-linear iterative inversion. The forward model and the inversion in the codes produced deal with both moderate frequencies, where the skin depth is of the order of the crack size, and with the thin-skin regime, where the skin depth is small compared with the crack depth. We have also evaluated a representation of surface distortion and surface roughness in bolt, bore, and fastener holes with a view to accounting for such effects in procedures for damage characterization.

The main accomplishment of this project is the development of a means of calculating crack signals in cylindrical systems based on a scalar decomposition formulation. The code to implement the theoretical model is fast, accurate and at least internationally competitive with others reported in the current literature.

Recommendations

1. Computer based tools should be developed for automatic damage characterization of flaws in boreholes using eddy current data. This would include simulation of commercial probes to characterize damage in holes in near real time.
2. The high speed modeling and inversion capability should be extended to deal with the cracks-under-installed-fasteners problem using the methods outlined in this report.

3.4 Model-Assisted Probability Of Detection (MAPOD) (Brasche, Meeker)

Investigation Team: R. Bruce Thompson, Bill Meeker, and Lisa Brasche

Motivation:

Damage tolerant design approaches are at the heart of military aviation operations, beginning with the introduction of the ASIP program in 1958 [46]. The approach recognizes that the potential exists for anomalous conditions that could result from inherent design parameters, manufacturing conditions or use of a component with associated exposure to fatigue loading, corrosion, and other environmental exposures. The anomalies are accounted for in the life management calculations using expected defect distributions coupled with fracture mechanics calculations. A critical element in the life calculations is the capability of the inspection methods applied during production to remove components with manufacturing defects and during service to cull out fatigue, creep or other aging/use based damage. Inspection effectiveness is measured using a statistical assessment known as probability of detection (POD) with values measured during the POD process serving as inputs to the life management calculations. To support the management of the structural integrity of aircraft and engines, the AF also developed guidance regarding the design and analysis of POD studies in Mil-Hdbk 1823 [47], “Nondestructive Evaluation System Reliability Assessment”. While guidance in the 1823 document has been utilized by the aviation and other industries since the late 80’s, that guidance and the practices of the community were based on empirical studies which require the fabrication of a statistically significant sample set and associated measurements to properly capture variabilities. This can be a time-consuming and costly process which often leads to abuses of existing data, i.e., assumptions that an available result is applicable to a new situation without adequate validation/verification. The availability of validated, physics-based inspection simulation tools can help remedy this situation. Model-based POD, or MAPOD, approaches allow the NDE engineer to consider a broader range of inspection space with a fewer number of samples and provide a more realistic assessment of inspectability.

Results – Theory and Experiments

It is widely recognized among the aviation community the important role that POD plays in the life management of critical structures and systems [46, 48-51]. In 2003, the Air Force Research Laboratory (AFRL), Federal Aviation Administration (FAA), and National Aeronautics and Space Administration (NASA) brought the community together the NDE community with organizational support from the Nondestructive Testing Information Analysis Center (NTIAC) to discuss the status of POD methodologies and the needs associated with moving forward with model-assisted POD approaches. A summary report [47] to document the meeting discussions and actions was prepared. The meeting included a review of computational NDE and POD modeling activities, development of consensus on priorities associated with moving MAPOD approaches forward as well as roadblocks and potential solutions. The formation of a consortium to promote MAPOD activities was discussed with the final conclusion being that a public-domain, MAPOD working group would have the benefits of collaborative interactions without the complexities of establishing funding relationships, legal documents, etc. ISU was selected by the AF, FAA and NASA to serve as coordinator for the Model-assisted Probability of

Detection (MAPOD) Working Group with funding for formal MAPOD working group activities provided by contract no. FA8650-04-C-5228.

MAPOD's established objective is to promote the increased understanding, development and implementation of model-assisted POD methodologies. From September 2004 through October 2011, a dozen meetings were coordinated by CNDE in collaboration with AFRL. An outcome of the initial workshop hosted by TRI-Austin/NTIAC was the development of a prospectus that guided the efforts of MAPOD. The draft prospectus was prepared by a CNDE team led by Thompson. After review with AFRL, it was distributed with the broader working group membership for fine-tuning. A copy is of the final version is posted on the MAPOD website at <http://www.cnde.iastate.edu/mapod/POD%20WORKING%20GROUP-Prospectus.pdf> and provided in Appendix C.

The results of the MAPOD working group interactions have been shared with the broader community through activities held in conjunction with various technical conferences including the Air Transport Association NDT Forum, Airworthiness Assurance and Sustainment Conference, American Society of Nondestructive Testing (ASNT) Fall and Spring conferences. To document those interactions, CNDE established a website to house the minutes and those presentations and other documents that could be placed in the public domain. Figure 29 shows a screen capture of the "Meeting Minutes" section of the site. Clicking on the link for each meeting will take the user to minutes of the meeting as well as presentations shared by participants. Considerable progress was made in the establishment of the MAPOD Working Group and initial demonstrations of this approach to generation of POD data were shared.

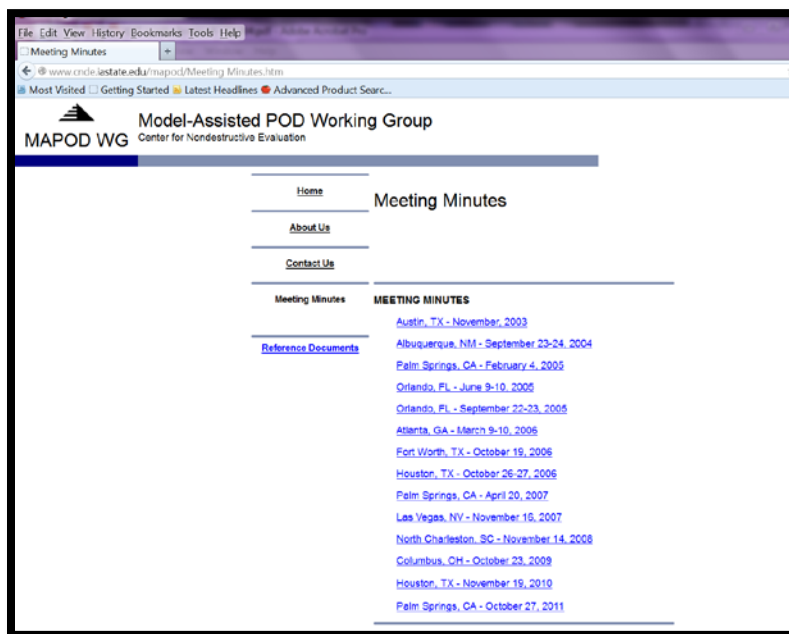


Figure 29. Screen Capture From MAPOD Website, Maintained By CNDE

The MAPOD website is viewed as a key repository for POD related information, both empirically-based and model-based, including a number of key references and historical documents. Among the resources is a 1993 Workshop organized by Iowa State on behalf of the FAA and held in conjunction with the ASNT Spring Conference. In 2007, a POD tutorial was organized at the request of AFRL and included presentations by Floyd Spencer, retired Sandia National Laboratory statistician, and Bill Meeker, Distinguished Professor of Statistics, ISU. In addition to the two ASNT events, materials were added that summarize prior empirical POD studies, crack vs. notch studies, and results of key MAPOD studies. All materials can be accessed at <http://www.cnde.iastate.edu/mapod>. In addition to the website input, numerous presentations, articles and conference proceedings documents [53-62] were generated. Among the products of the MAPOD working group were protocols for the generation of MAPOD studies. Based on the leading efforts of ISU and Pratt & Whitney [63], the steps to generate POD were placed in the public domain. The approach to full-model assisted POD and transfer function methods were shared at the 2004 through 2005 meetings and resulted in the approach shown in Figure 30. Thompson also supported the development of the revised military handbook, MIL-HDBK-1823B, prepared by Chuck Annis by providing a chapter for inclusion regarding MAPOD approaches. This enabled a much broader application of the approaches as evidenced by the numerous conference presentations and publications that occurred since the origination of the MAPOD Working Group [64-72].

| | |
|--|--|
| <p>Microsoft Word - STEPS TO GENERATE MAPOD_Thompson.doc - ST... http://www.cnde.iastate.edu/mapod/2005 February/STEPS TO GENERA...</p> <p>STEPS TO GENERATE MODEL-ASSISTED POD</p> <ol style="list-style-type: none"> 1. Identify controlling factors whose influence on a flaw response signal can be deterministically predicted using a physics-based model with appropriate input parameters. 2. Develop appropriate model. 3. Validate the accuracy of the physics-based model in the laboratory through well controlled experiments <ol style="list-style-type: none"> a. This step should include a careful analysis of uncertainties <ol style="list-style-type: none"> i. Uncertainties in the experimental measurements ii. Uncertainties in the values of input parameters to the model iii. Sensitivity of model predictions to the latter b. It will be necessary to establish what level of agreement between experimental measurements and the predicted results is satisfactory 4. Determine values of input parameters (or parameter ranges) that describe field application 5. Use simulation tool to predict mean response and those components of variability controlled by well understood physical phenomena <ol style="list-style-type: none"> a. In this context, "simulation tool" refers to a computer code, based on a physics model and provided with a set of input parameters, that makes a deterministic prediction of a flaw response. b. A simulation tool can also be used to predict the distribution of signals that would be produced by a distribution of input parameters 6. Identify additional sources of variability associated with components of variability not controlled by either <p>1 of 2 3/25/2013 4:52 PM</p> | <p>Microsoft Word - STEPS TO GENERATE MAPOD_Thompson.doc - ST... http://www.cnde.iastate.edu/mapod/2005 February/STEPS TO GENERA...</p> <ol style="list-style-type: none"> a. well understood physical phenomena or b. variations of input parameters that cannot be fully controlled in the production environment <ol style="list-style-type: none"> 7. Determine if these are statistically independent so that variances add 8. Design experiments to determine these additional sources of variability <ol style="list-style-type: none"> a. This will generally require less time/cost than the experiments required for a fully empirical POD determination because one will be seeking less information from the data. b. This may be a necessary step to assess the variability attributed to system/operator which are not calculable but rather require an empirical assessment. 9. Conduct those experiments 10. Compute POD <ol style="list-style-type: none"> a. Assume variance is the sum of the variances predicted in terms of models and the additional variances that must be determined empirically <p>2 of 2 3/25/2013 4:52 PM</p> |
|--|--|

Figure 30. Protocol Describing MAPOD Approach To POD Assessment

Conclusions

Given the importance of probability of detection to the aviation community, federal agencies most interested in safe commercial and military flight operations, i.e., the US Air Force, FAA and NASA, have worked collaboratively to develop and promote the use of Model-assisted POD methodologies. To ensure broader impact and perspectives, colleagues from energy, nuclear power generation, infrastructure and transportation were also invited to participate in MAPOD activities. The MAPOD Working Group was established in 2004 and support from this contract enabled a series of meetings which are fully documented in a companion website, www.cnde.iastate.edu/MAPOD. Through a series of a dozen formal meetings and numerous other interactions and collaborations, several demonstrations were reported by members of the working group, providing a foundation upon which future MAPOD studies can build. As of November 2012, activities of the MAPOD working group transitioned to the Reliability Committee of ASNT. CNDE continues to host and provide updates to the MAPOD website.

Recommendations

- While several MAPOD examples have been demonstrated for eddy current and ultrasonic inspections, extension of the approach to image-based methods, such as radiography, is needed. This would likely require collaboration with the suppliers which would have the added benefit of engaging a broader community in POD applications.
- Studies to assess the contributors to variability and development of approaches to account for those sources in MAPOD estimates would be beneficial. Among the needed efforts are assessment of flaw morphology for typical materials and flaw types of interest to aviation.

3.5 Eddy Current Model Validation Toward Model-Assisted POD Methodology (Nakagawa)

Investigation Team: Norio Nakagawa, Bruce Thompson, Bill Meeker, Lisa Brasche, Chester Lo, Brian Larson, Terry Jensen, Zhigang Chen, David Raulerson, Kevin Smith
Students: David Raithel, Alex Chase, Erin Madison, Ryan Mooers

Motivation

The maximum life extension of engine components can be achieved when NDE inspections are characterized in terms of some quantitative figure of merit. There is a general consensus that the probability of detection (POD) provides an acceptable figure of merit. It is desirable to have every component inspection supported by a POD estimate. To date, however, only subsets of inspections are characterized in terms of empirically determined POD. The obstacle against broader use of POD is the cost of empirical determination. A breakthrough is needed for expanding the POD usage without incurring prohibitive costs.

One of the promising candidates for a cost-effective POD methodology is the model-assisted POD approach (MAPOD). Recent collaborative efforts at ISU and PW have demonstrated a MAPOD approach for ultrasonic inspection of disks. These efforts demonstrated the feasibility of incorporating physics-based NDE models into the POD estimation procedure in order to enable broader use of POD than currently practiced. In principle, physics models bring universality to POD calculations, by providing quantitative relationships among NDE signals arising from a variety of inspection conditions. The model-assisted POD consequently provides the ability to convert POD results of known (e.g., empirically characterized) inspections into POD estimations for uncharacterized inspections. Once this capability is available, POD calculations can be provided for many currently uncharacterized inspections through translation from known POD results, without requiring expensive empirical determinations. Reduced needs for empirical POD determination lead to substantial reduction of maintenance costs. As indicated, the CNDE-PW collaboration has prior experience in developing model-assisted POD procedure for UT inspections. This project attempts to apply the methodology to eddy current (EC) inspections.

Several key elements of research are needed to establish model-assisted EC POD including the following:

- To develop/validate EC NDE model with a sufficient scope of applicability.
- To establish the relationship between crack and notch responses.
- To establish methods to characterize model input parameters.
- To generate system/operator data.
- To integrate these components to form a model-assisted EC POD methodology.
- To validate and demonstrate the resulting methodology.

These are significant challenges, some aspects of which will be addressed in this project. From the long-term perspective, this project represents a stage-1 strategy to achieve these goals, where focus is on tasks associated with the modeling capability enhancements and validation, with additional basic research toward input parameter determination methods. In later stages,

subsequent work will be toward integrating the stage-1 results into the prospective POD methodology. The specific stage-1 tasks consist of:

- Critical examination of the current status of modeling capabilities with validation studies.
- Identification of necessary model capability developments and/or improvements.
- Development of the next-generation EC model code, implementing the needed capabilities (crack response, notch response, and geometry response in a single software tool).
- Explore methods for characterizing model input parameters such as probe parameters and noise distributions.

Objectives

- To validate the EC models, namely to establish the relationship between model predictions and experimental observations, while assessing accuracy and capability limits leading to necessary developments and/or improvements.
- To develop the next-generation EC model code, implementing the needed capabilities (crack response, notch response, and geometry response in a single software tool) for use in model-assisted POD methodologies.
- To search for practical methods for characterizing given unknown probes, other than the x-ray method.

The long-term objectives are:

- To develop a model-assisted EC POD methodology.
- To develop a fully validated EC model code, being applicable to the model-assisted POD methodology.

Results – Theory and Experiments

3.5.1 Notch vs. Crack Signal Relationship in EC NDE

This portion of the study addresses the question of the EC signal relationship between those due to cracks and notches. Two particular applications are of interest in the context of this project. One application has to do with notch-based instrument calibration. When conducting an eddy current inspection for cracks, it is necessary to setup the eddy current flaw detector using a reference specimen with a known discontinuity. Since it is often expensive and sometimes impractical to grow representative cracks, electrical discharge machining (EDM) is often used to place notches in the reference specimen. It has been a long-standing problem for the NDE community to understand the quantitative correlation between the signals from a crack (of a typically semi-elliptical shape) and a similar-size notch (of a usually rectangular shape). It is desirable to establish the quantitative relationship so that the deviation between notch and crack signals can be compensated for. The second application is intended toward cost-effective POD determinations. Again, since it is expensive and often impractical to fabricate a large number of crack specimens for POD study, it has been contemplated to develop POD transfer

methodologies that allow conversion of POD of notches to POD of cracks. Notch vs. crack signal relationships will play the central role here.

This study considers the notch vs. crack signal relationship in the two step approach as illustrated in Figure 31. Namely, in addition to a notch [(a)] and a crack [(c)], we consider a mathematically idealized crack, i.e., zero-width discontinuity [(b)]. We then compare signals from (a) and (b) first, and next those from (b) and (c).

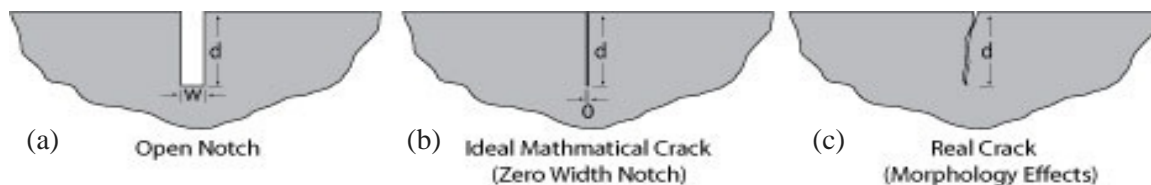


Figure 31. Illustration Showing The Two Step Approach To Relating Open EDM Reference Notches To Actual Cracks. The First Step Is To Develop An Algorithm That Accurately Captures The Notch Width Effect And Use This To Calculate A Signal For An Idealized Crack. The Second Step Involves Relating The Calculated Signal From The Idealized Crack To An Actual Crack With Its Morphology Effects

The first step comparison, i.e., between open notch vs. closed notch, amounts to the study of notch volume effects on EC signals. We carried out such study both experimentally and theoretically, with the results summarized briefly in the subsequent sections. Experimentally, we prepared samples of varying width notches, and measured EC signals as a function of widths, from which we calculated zero-width notch signals by extrapolation. Theoretically, we used a version of our EC NDE model codes (Plate version where the part geometry is restricted to layered half space) to compute width-dependent impedance signals, including the idealized crack signals. Both experimental and theoretical trends agreed with each other, thus validating the modeling capability in calculating notch volume effects. Naturally, modeling can eliminate the need for costly sample preparation.

The second step comparison, i.e., between idealized and real cracks, amounts to the study of the crack morphology effect, which is expected to reduce EC signals due to possible leakage currents through contacting asperities. We conducted experimental research and estimated the reduction factor by mechanically loading and unloading fatigue crack samples to modify crack morphology. No model estimation is attempted to calculate the reduction factor due to the crack morphology effect, because it is fundamentally a stochastic variable and unamenable to model calculations. The resulting crack signal variability is better taken into account in the POD analysis. We will come back to this point below in the section describing edge crack detections.

3.5.1.1 Notch Width Effects and Plate Code Validation

Electrodischarge-machined (EDM) notches are often used to set instrument parameters, with their size chosen to match target crack-like discontinuities. It is important to understand the quantitative correlation between the signals from a crack and a similar-size notch. In Ref. (73), we reported on a study to explore the effect that the width of a discontinuity has on signal

strength when inspecting low conductivity materials for small cracks with eddy current surface probes. EDM notches of different sizes and shapes were placed in Ti-6246 and IN-100 specimens. Each of the two materials received six 0.020 inch long by 0.010 inch deep notches and six 0.030 inch and 0.015 inch deep notches. Three of the notches of each size were rectangular shaped and three were semicircular shaped. One of the notches in each material size group was 0.005 inch wide, one was 0.003 inch wide and one was 0.001 inch wide. Each of the notches was scanned using absolute and differential pencil probes driven at several different frequencies. The experimental results were compared with numerically generated results, which allowed for a zero width notch to be considered. The results indicated that the signal reduction factor from a 0.005 inch wide, rectangular notch to a theoretical zero-width notch of the same size ranged from 25 to 42%. Through the theory vs. experiment comparisons, the plate version of the EC NDE modeling code has been validated.

Specifically, we prepared four pieces of 5" x 1.7" x 1/4" metal blocks made of Ti-6246 (Ti-6Al-2Sn-4Zr-6Mo) and IN-100 alloys, two from each material. (They are identified by the serial numbers of 1227-26, 1227-51, 2010, and 2013.) EDM notches of different sizes and shapes were planted in the specimens. Each of the two materials received six 0.020 inch long by 0.010 inch deep notches (on 1227-26 and 2010) and six 0.030 inch and 0.015 inch deep notches (on 1227-51 and 2013). Each sample plate holds six notches arranged in two rows, one row consisting of rectangular notches, and the other containing three semicircular notches. Further, each row consists of three notches of nominally the same size, except that their width values are set to be 0.001", 0.003", and 0.005". Each of the notches was scanned using absolute and differential pencil probes driven at several different frequencies. The experimental results were compared with numerically generated results to be described below. Selected examples of microscope images of the notches are shown in Figure 32.

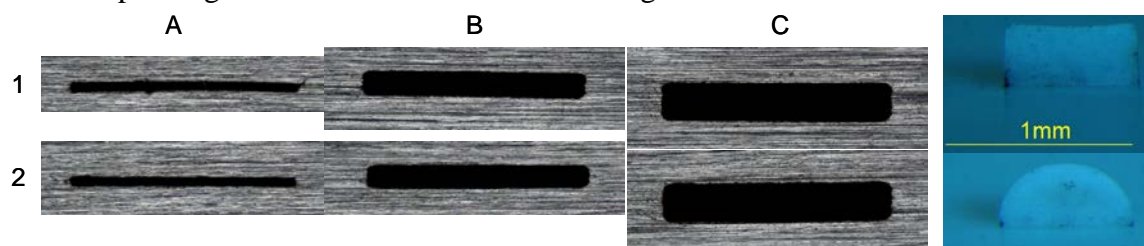


Figure 32. Close-Up Photograph Of Specimen 1227-51 Notches And Example Photographs Of The Replicas. Six EDM Notches Of Nominally Identical Dimensions (0.030" Long By 0.015" Deep) Are Arranged In Two Rows, Where Row 1 Consists Of Those Of A Rectangular Shape, While Row 2 Consists Of Semi-Circular Notches. Notice The Varying Width Values That Are 0.001" (Column A), 0.003" (Column B), And 0.005" (Column C). 1"=25.4 mm

This study involved four commercial probes, two differential (2 MHz and 6 MHz) and two absolute (500 KHz and 5 MHz) probes. To run the EC NDE model, the probes were characterized by digital radiography, and from the x-ray images, we constructed CAD models of the probes to feed the EC NDE simulation model, along with the other input parameters describing the measurement configurations and conditions, including the explicitly measured sample conductivities. (See [73] for details.)

Model Validation Two validation results are reproduced here, one in terms of the vector voltage traces (Figure 33) and the other of the peak-to-peak amplitudes (Figure 34).

Notch Width Effects on EC Signals A typical result to quantify the notch width effects is similarly presented in Figure 35, for the Ti-6246 specimens. The superposed modeling results allow one to extrapolate down to the zero-width notches, for which we predict further signal reductions down to 35 % instead of 28 % for the 0.030" notches.

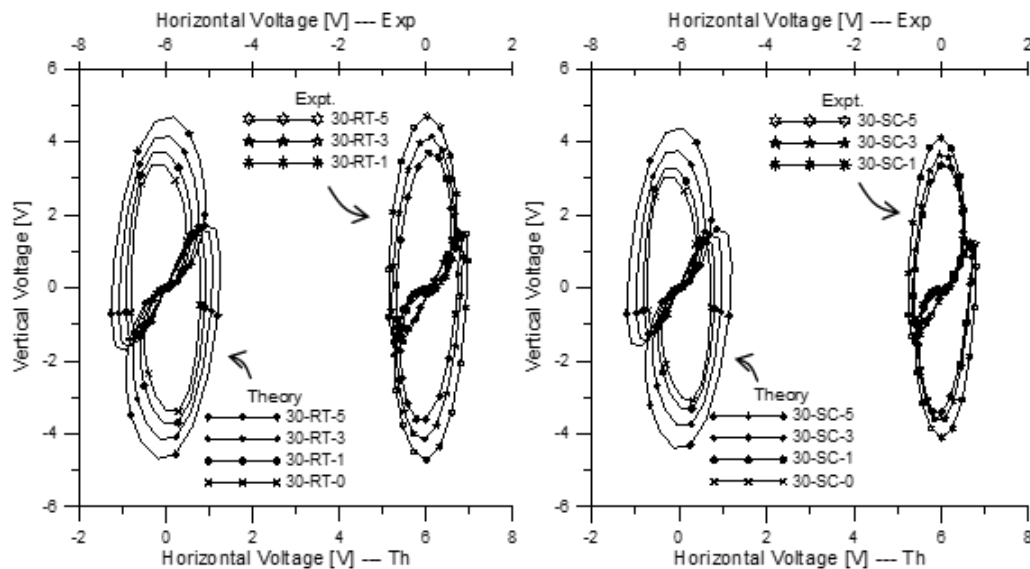


Figure 33. Examples Of Notch Signal Traces From The 2 MHz Differential Probe Mapped Onto The Output Vector Voltage Plane (Measured And Computed) For The 0.030"-Long Rectangular Notches Of The Varying Widths (0.001", 0.003", 0.005") In The Ti-6246 Specimen, And. In The Labels, "RT" And "SC" Refer Respectively To The Rectangular And Semi-Circular Shapes, And 1-3-5 Stands For The Three Widths

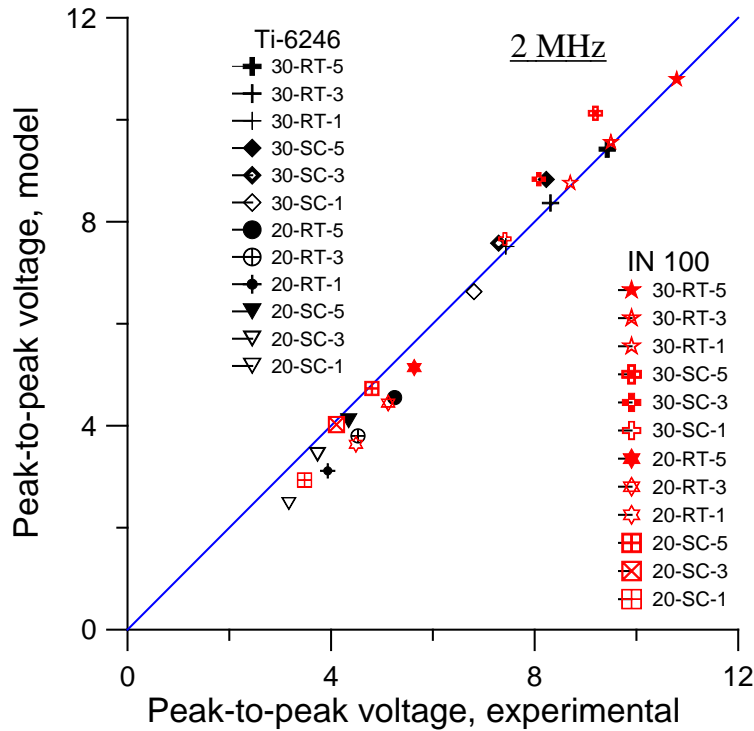


Figure 34. Cumulative Compilation Of Comparison Results Between Theory And Experiment For Peak-To-Peak Signal Voltages, Calculated And Measured For The 2 MHz Commercial Differential Probe. The Short-Hand Notation Is Used To Label The Notches: “30” And “20” Stand For The Length Values Of 0.030” And 0.020”, “RT” And “SC” For Rectangular And Semi-Circular Shapes, And {5,3,1} Denote The Width Values Of 0.005”, 0.003”, 0.001”, Respectively. The Two Sets Of The Twelve Notches Are Placed On The Ti-6-2-4-6 And IN100 Blocks

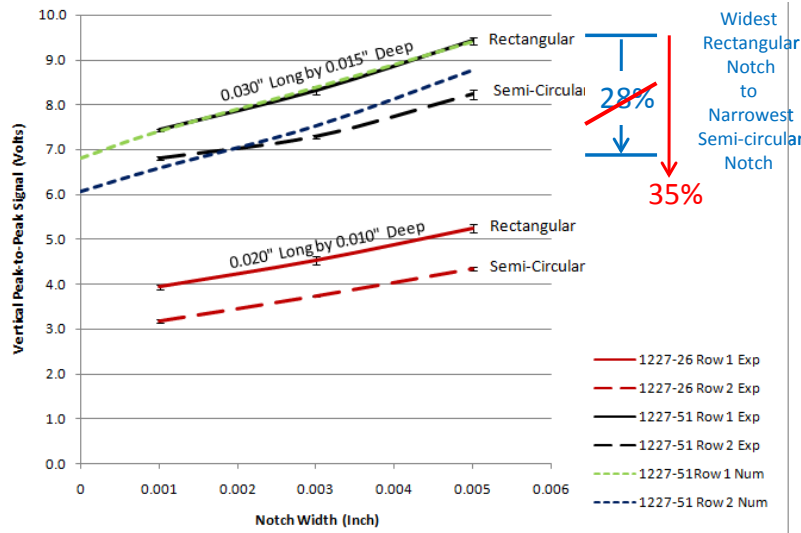


Figure 35. The Vertical Peak-To-Peak Voltage Signals Vs. The Notch Width Plots. The Experimental Data Are Superposed With The Model Predictions For The 0.030" Notches, Indicated By The Broken Lines. The Model Enables The Extrapolation Of The Notch-Width Dependency Down To The Zero Width, Predicting The 35% Signal Reduction For The Zero-Width Semicircular Notch Compared To The Widest (0.005") Rectangular Notch

In conclusion, the paper presented validation results of an eddy current NDE model based on the boundary element method, implemented for test specimens of generalized half space geometry with a probe of any constructions and dimensions. The comparison of the probe signals between theoretical predictions and experimental data is made through a calibration approach, where the largest and widest notch within each sample material is used for calibration. Model-predicted notch signal traces mapped to the vector voltage plane have been shown to agree with experimental signals in the same voltage plane. The validation results are obtained for commercial absolute and differential probes. The overall magnitude comparisons, as well as the matching trends of the notch width effects, are shown within approximately 10% errors or less. It has been shown that the EC signal will be reduced by ~35% for a tightly closed but mathematically ideal crack of no leakage current, compared to the 0.005" wide notch of otherwise identical dimensions.

3.5.1.2 Effects Of Dynamic And Static Loading On Eddy Current NDE Of Fatigue Cracks

In Ref. [74], we reported on the effects of dynamic and static loading on eddy current (EC) crack signals in aerospace materials including Al and Ti alloys. The work was motivated to estimate the effect of crack morphology on EC signals that could influence accuracy of quantitative measurements such as crack sizing. Systematic studies on the effects of crack opening and closure on EC signals are needed.

To meet the specific objective, i.e., to investigate the effects of crack opening and closure on EC signals, we carried out EC measurements *in situ* on a series of fatigue crack samples grown in Al 6061 when the cracked surfaces were subjected to dynamic tension and compression. It was found that the EC signals detected at a fixed location on the fatigue cracks vary periodically with

cyclic loading. Under dynamic tension, the amplitude of the vertical signal component, which is perpendicular to the liftoff direction, increases in correlation with the load amplitude and the effect is stronger for longer cracks. Such changes in EC signals are attributable to crack morphology changes (i.e., crack opening) under tension, indicating increase of the resistance across the crack face. In contrast, the signal amplitude remains relatively unchanged under compression, presumably due to the insulation effect of the oxidation layer on the crack face. The loading effects on crack signals were confirmed by obtaining eddy current c-scan images of the fatigue cracks under static loads. In contrast, c-scans conducted on a series of Ti 6-4 fatigue crack samples under static loads revealed significantly stronger stress effects on crack signal than in the Al samples, in particular under compression. The results are interpreted in terms of possible formation of an insulating oxide layer in Al which impedes current flow when the cracks were forced to close under compression.

A series of fatigue crack samples with lengths ranging from 0.055" to 0.350" were grown in Al 6061 bars of dimensions 6"(l)×1"(w)×0.5"(t) for *in situ* EC measurements under dynamic and static loads.

Initially, we applied cyclical dynamic loading to the Al fatigue crack samples, and conducted *in situ* EC measurements, with the cracked surface subjected to tension or compression in a four-point bending configuration (Figure 36). The EC signal variations were measured as a function of dynamic loads, maximum applied loads, crack lengths, etc. It was observed that, for Al fatigue crack samples, compressive loading has very weak effects on EC signals, compared to the tensile loading. We considered the results to be inconclusive because there is a possibility of the crack position deviating from the no load position during the loading, thus apparently reducing probe responses. We therefore proceeded to static loading.

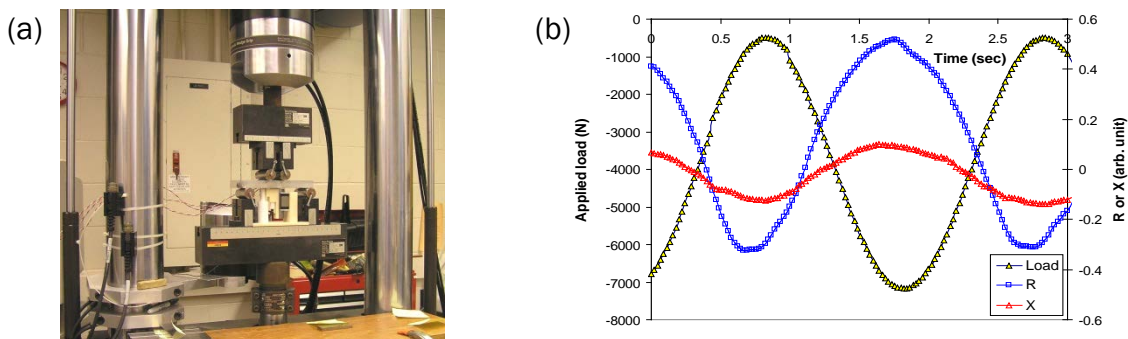


Figure 36. (a) Experimental Set Up For *In Situ* EC Measurements On A Fatigue Crack Sample Grown In An Al Bar Under Cyclic Loads In The Four Point Bending Configuration. (b) Acquired Applied Load And EC Signals From A Fatigue Crack Subjected To Dynamic Load Over A Loading Cycle

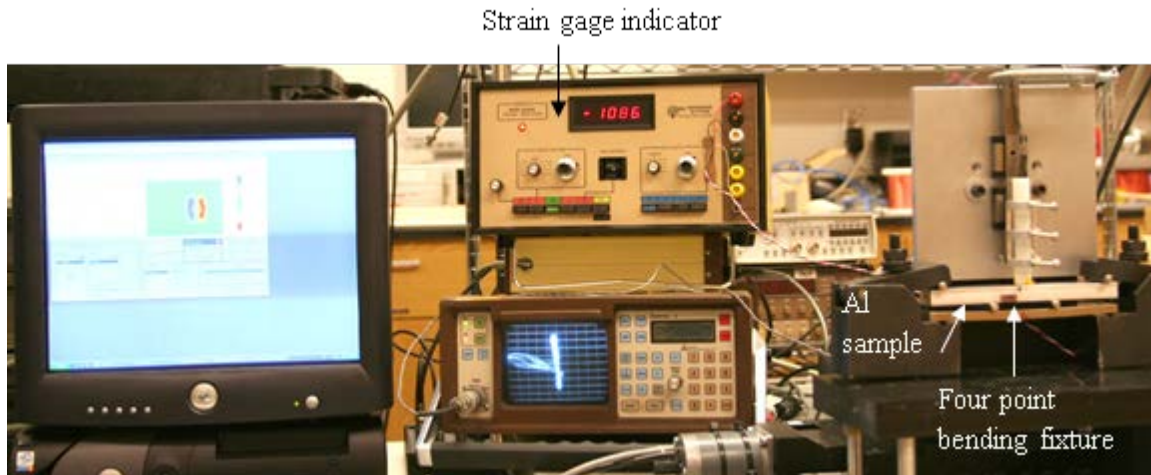


Figure 37. Experimental Set For EC Scans On Fatigue Crack Sample Subjected To Tensile Or Compressive Stresses In A Four Point Bending Configuration

We built a static loading fixture, and mounted it on an EC scanner station, so that EC c-scans can be conducted in-situ (Figure 37). Raster scan data ensures that maximum signal positions are not missed. In order to verify the observed effects of dynamic loads on crack signals, EC scans were carried out on the same set of Al fatigue crack samples subjected to static tension or compression in a four point bending configuration. For comparison, c-scans were also performed on a series of fatigue cracks grown in Ti 6-4 bars.

The stress dependence of the crack signals measured from various Al crack samples of different lengths is shown in Figure 38, where the peak-to-peak vertical deflection in the scan data is plotted as a function of applied stress. The crack signal became stronger under tension compared to that measured with no stress, while the signal became weaker under compression. The decreasing trend under compression is weaker than the increasing trend under tension.

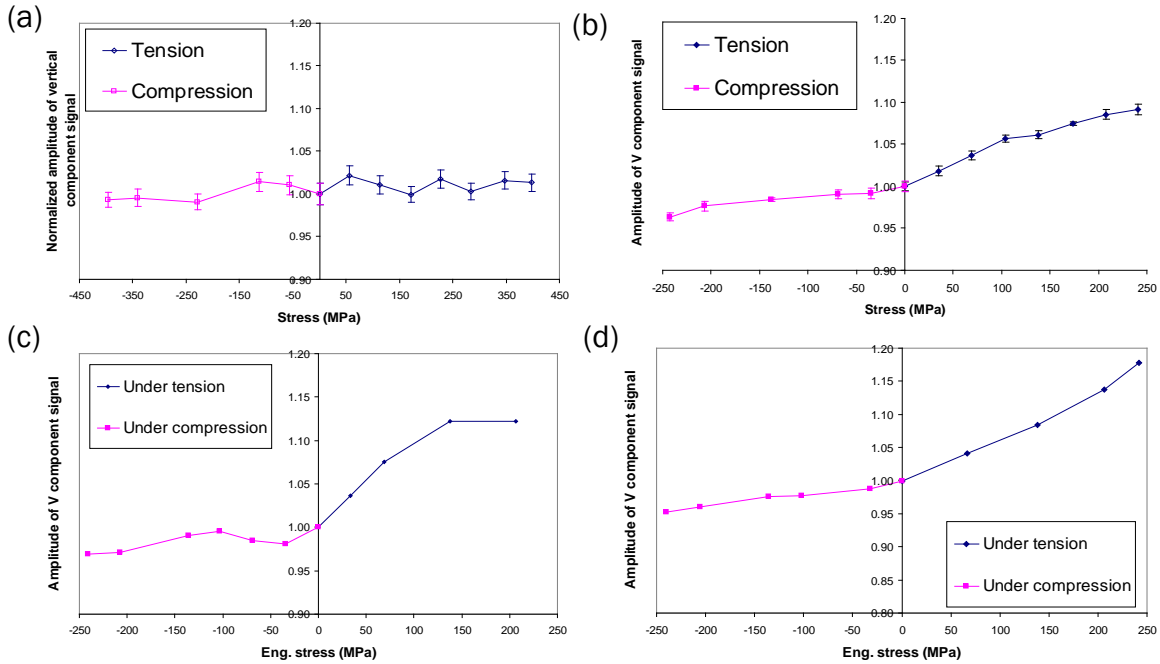


Figure 38. Plots Of Amplitude Of The Vertical Components Of The Crack Signals Versus The Stress Level For The Al Fatigue Crack Samples (a) S1 (0.055"); (b) S2 (0.162"); (c) S3 (0.195") And (D) S5 (0.350")

Results of the EC c-scans from a series of Ti 6-4 fatigue crack samples (with crack length ranging from 0.056" to 0.246") show substantially larger stress-induced changes in crack signals under both tension and compression, compared to the Al 6061 results. The crack signals increase (by as large as a factor of 2) under tension and decrease under compression (Figure 39).

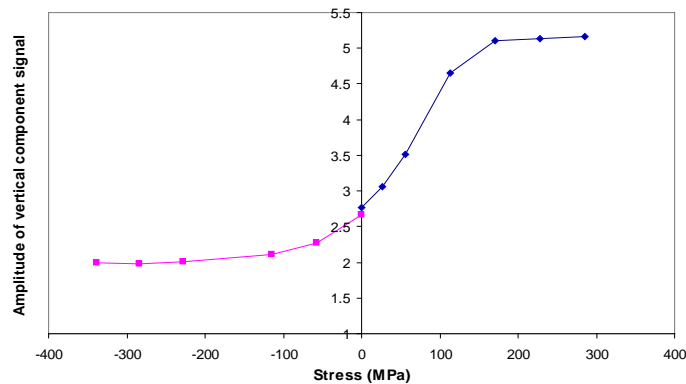


Figure 39. Plots Of The Amplitudes Of The Vertical Component Of The Crack Signals Versus The Stress Magnitude For A 0.114"-Long Fatigue Crack In Ti 6-4

In conclusion, results of in situ tests on Al crack samples show that, under dynamic tension, the amplitude of the vertical component of the EC signal increases with the load amplitude and the effect is stronger for longer cracks. Such effects are attributable to crack morphology changes

(i.e., crack opening) under tension. In contrast, the signal amplitude remains relatively unchanged under compression, and we have given a presumptive explanation that it is attributable to the insulation effect of the oxidation layer on the crack face. Results of the EC scans on Al fatigue cracks under static loads confirmed the loading effects on crack signals observed in the dynamic loading tests. The c-scans conducted on Ti 6-4 fatigue cracks under static loads revealed significantly stronger stress effects on crack signal than in the Al samples, particularly under compression. The results are interpreted in terms of difference in leakage current across the crack faces when the cracks were forced to close under compression.

3.5.1.3 Notches Versus Cracks: Effects on Eddy Current NDE Signals from Defect Volume and from Crack Morphology Altered by Mechanical Loading

The comprehensive two-step comparisons were made and reported in Refs. [75] and [76]. Specifically, the study was made for eddy current (EC) signal comparisons between those arising from artificial defects (notches) and from laboratory-grown fatigue cracks. This part of the study builds upon the aforementioned results which studied the effects of the notch volume (Sec. 3.5.1.1) and of the externally altered crack morphology (3.5.1.2) separately. To put a closure on the signal relationship between the artificial defects and lab-grown cracks, the two studies have been combined into one research project that has produced the results presented here, as well as in the quoted papers. The scope of the work was also expanded to apply the previous analyses to both aerospace engine materials (titanium-base and nickel-base alloys) and airframe materials (aluminum alloys). To this end, additional samples with notches of various widths have been produced, and a larger number of Ti and Ni base alloy samples with fatigue cracks have been procured.

The combined effort integrated all the work elements into one comprehensive study, namely: (A) Data was collected from EDM notches of different widths to establish the relationship between notch width and EC signal. (B) The notch experimental data was used to validate calculations made using a numerical modeling algorithm based on the boundary element method. (C) The model was used to calculate EC signals for idealized zero-width discontinuities of various lengths. (D) Experimental data was also collected from low-cycle fatigue crack specimens for comparison to the EC signals calculated for the zero-width discontinuity. (E) Signals from the crack specimens were collected with a loading fixture, under no load, tension and compression loading conditions.

The alloys chosen for this study were Inconel 718, Ti-6Al-4V, and aluminum alloy 6061-T6. These materials had electrical conductivities of 0.870 (1.50), 0.597 (1.03), and 27.740 MS/m (47.8% IACS), respectively. We also used the IN-100 and Ti-6Al-2Sn-4Zr-6Mo notch width specimens from the previous studies, with the electrical conductivities of 0.597 (1.03) and 0.748MS/m (1.29% IASC), respectively. A small number of EDM notches were placed in Inconel 718 and Ti 6-4 so that direct comparisons to the fatigue crack results could be made. Notch width specimens for Al 6061 were produced for this study since this alloy was not included in the previous notch width investigation. Since aluminum is often used in applications where longer cracks can be tolerated, notches up to 0.120" were included. No 0.001" wide notches could be manufactured for these deeper notches.

The low-cycle fatigue cracks specimens were produced in three-point bending with a max load of 80% of yield strength and an R ratio of 0.1. An EDM starter notch was used to initiate the crack. The surface was then milled and ground to remove the starter notch and loading was resumed to grow the crack to final size. A number of cracks were fractured open to determine that the crack grew with a length-to-depth aspect ratio of 2.8:1. All the specimens were 6.0" (15 cm) long, 0.5" (1.27 cm) thick and 1.0" (2.54cm) wide for the Al and Ti, and 1.5" (3.8cm) wide for Inconel.

Experiment and modeling procedures were described in the quoted papers.

The papers also presented a number of the experimental and numerical results, from which we reproduce here Figures 40 and 41 as representatives. In Figure 40, the Inconel 718 notch and crack data has been plotted as a function of discontinuity length. From this plot, it can be seen that for the shorter crack lengths, the experimental data falls close to the numerical results for a zero-wide discontinuity. At the longer crack lengths, there is a great deal of scatter in the experimental data. Also shown on this plot is the effect of applying a small bending load to the specimen. Due to a limitation in the loading fixture, it was only possible to apply a maximum bending stress of 5 percent of the materials yield strength. It can be seen that this stress in both tension and compression produced little change in the relatively short crack (#056). However, the signal from an intermediate sized crack (#034) was significantly below the numerical prediction for a crack of this size but when it was loaded in tension, the crack saw a 78% increase in the signal strength and this brought the experimental results into nearly perfect agreement with the numerical results for a zero-width discontinuity. When loaded in compression the signal decreased by 22% indicating that in the unloaded condition, this crack was more closed than open. In contrast, specimen #093 (the largest of the three cracks) saw only a 3% increase in signal strength when loaded in tension but a 45% decrease in signal when loaded in compression. This would seem to indicate that this crack is open when no load is applied.

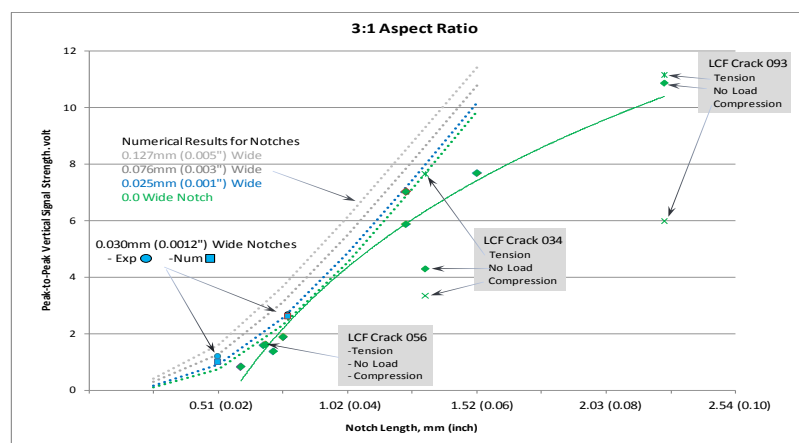


Figure 40. Chart Showing Inconel Experimental And Numerical Data As A Function Of Notch/Crack Length. The Solid Line Is A Log-Fit Trend Line Of The Crack Signals Under No-Load Conditions

The results for the titanium specimens (Figure 41) were similar to those of the Inconel specimens. When the Ti 6-4 specimens were loaded in tension, the signal increases ranged from

1% to 35%. The smallest crack saw the smallest change and the larger cracks generally saw the larger increases. As can be seen in the plots, tensile loading shifted the trend line for the experimental data nearer to the numerical prediction. The experimental and numerical datasets never quite overlapped but the tensile loading stresses were kept fairly low at around 40% of the material's yield strength. Compression produced reductions in signal strengths ranging from 4% to 34%. The specimens that produced the smallest percent signal change in tension, tended to produce the highest percent signal change in compression. This would tend to indicate that some cracks are in an open state and some are in a tightly closed state.

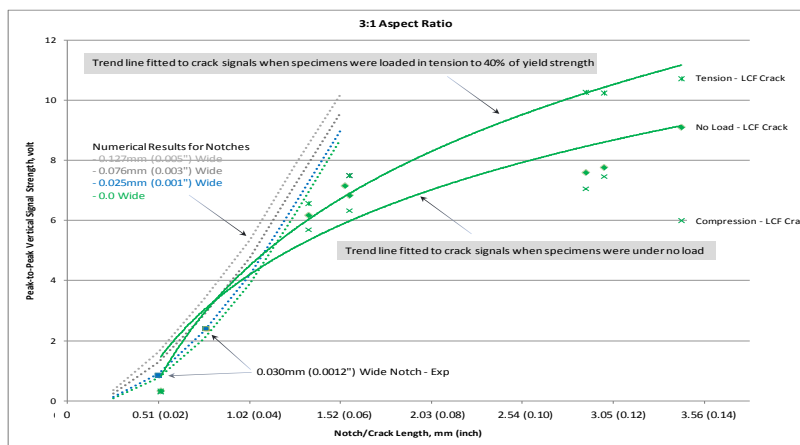


Figure 41. Chart Showing Titanium Experimental And Numerical Data As A Function Of Notch/Crack Length

In summary, the study was conducted to investigate the relationship between EDM calibration notches and fatigue cracks in aluminum, titanium and nickel-base superalloys. It was found that the signals from low-cycle fatigue cracks were smaller in magnitude than the signals from similar sized EDM notches, as expected. The investigation determined that for Al, the signals from the fatigue crack specimens correlate very well to the predicted zero-width notch signals that were established by extrapolating the experimental data from notches that were nominally identical except for their width. Mechanical loading of the Al crack specimens produced only minor changes in the EC signal. This indicates that there is measurable discontinuity volume effects but the insulating surface oxide layer that forms on Al prevents most, if not all, current leakage across the fracture. However, for the titanium and nickel-base super alloys, it was found that mechanical loading could produce a significant change in the eddy current signal from the cracks. The amount of change is dependent on the length of the crack and its stress state; tension produced large signal changes in closed cracks, while compression produced large changes in relatively open cracks. The signal change is too large to be attributed solely to the volume effect so it is believed that the change is due to the amount of current leakage across the fracture faces, which is a function of the contact area.

3.5.2 Edge Crack Detection Problem and Three Dimensional Model Validation

This project selected an edge crack inspection problem by EC, to test quantitative EC NDE inspection and its modeling capabilities against an industrially relevant inspection problem.

Validating a complex geometry EC NDE modeling code is a part of this study. Demonstrating the edge crack inspection capability itself is a similarly important project output.

3.5.2.1 Eddy Current Edge Crack Detection Experiment

An existing POD sample set owned by Pratt & Whitney (P&W), consisting of fatigue crack specimens in nontrivial (i.e., not flat) geometry was used in this study. The P&W Combination Fluorescent Penetrant/Eddy Current Inspection Elongated Scallop Reliability Specimen Set consists of 90 scallop specimens with the configuration showing in Figure 42. The specimens were machined from PWA 1216 (Ti-6-2-4-2) material. The scallop edges have been doubly chamfered flat. Eighty of the specimens have a low-cycle fatigue crack propagated at a preselected location within a target inspection zone and ten specimens do not contain cracks. The target inspection zones consisted of 14 radial positions along the scallop and three axial positions (top edge, center, and bottom edge). The fatigue cracks range in size from 0.0025" long by 0.0018" deep to 0.071" long by 0.0283" deep, where the depths are only estimated and not provided on a per-sample basis. The study also included the flat surface EDM notch specimens 1227-26 and 1227-51 as described above in the notch width study section, also made of the same alloy Ti-6-2-4-2.

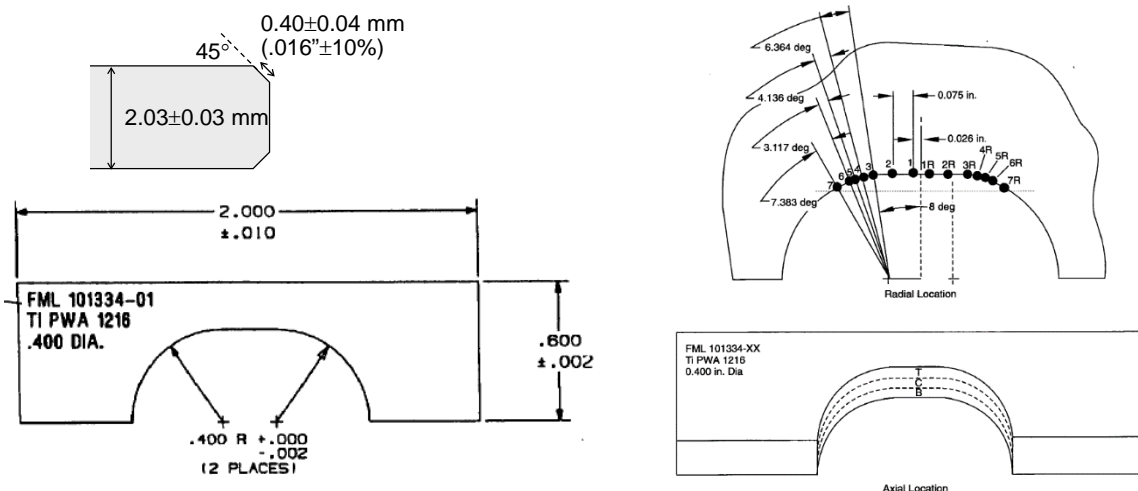


Figure 42. Drawing Showing The General Configuration Of Scallop Specimens (Left) And Various Radial And Axial Locations Of The Cracks (Right)

The project team purchased a special Pratt inspired probe that largely suppresses the edge effect. This probe operates in the reflection mode and makes use of a solenoid as the drive coil and a pair of tiny (0.013" diameter) pickup coils. A photo of the probe and the pair of sensing coils is shown in Figure 43. The ECP-1010 probe was developed with the design goal of minimizing edge signals.

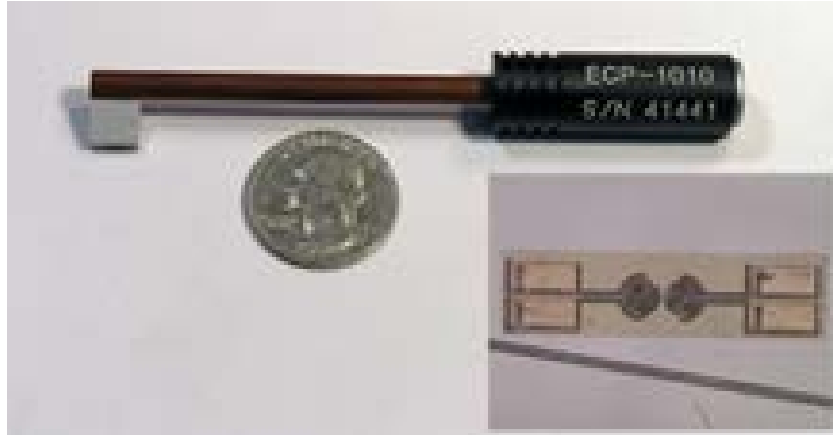


Figure 43. Overall Photograph Of The Special Probe Purchased For The Scallop Specimen Experimental Measurements. Sensing Coils Are Shown In The Insert Along Side Of A 0.0038" Diameter Wire

Experimental data collection was accomplished with a UniWest 454 Eddy Current instrument and a CNDE custom configured scanning and data acquisition system. Photographs of the probe elements, specimen set, and scanner setup are shown in Figure 44. The setup permits a small, high-resolution raster scan over the target flaw location for each specimen. The scan data is then processed to produce a slice through each of the peaks in the data and the minimum and maximum values for each of the four signal peaks are recorded. An example of the scan data plotted as both a wire mesh diagram and contour plot and the resulting line plots of the slices for the vertical portion of the signal are shown in Figure 45. Throughout, the instrument (US-454) parameters were set to the frequency 6 MHz, the instrument gain of 60 dB, and the phase angle of 163° so that the crack signal locus ("Figure 8") points vertically.

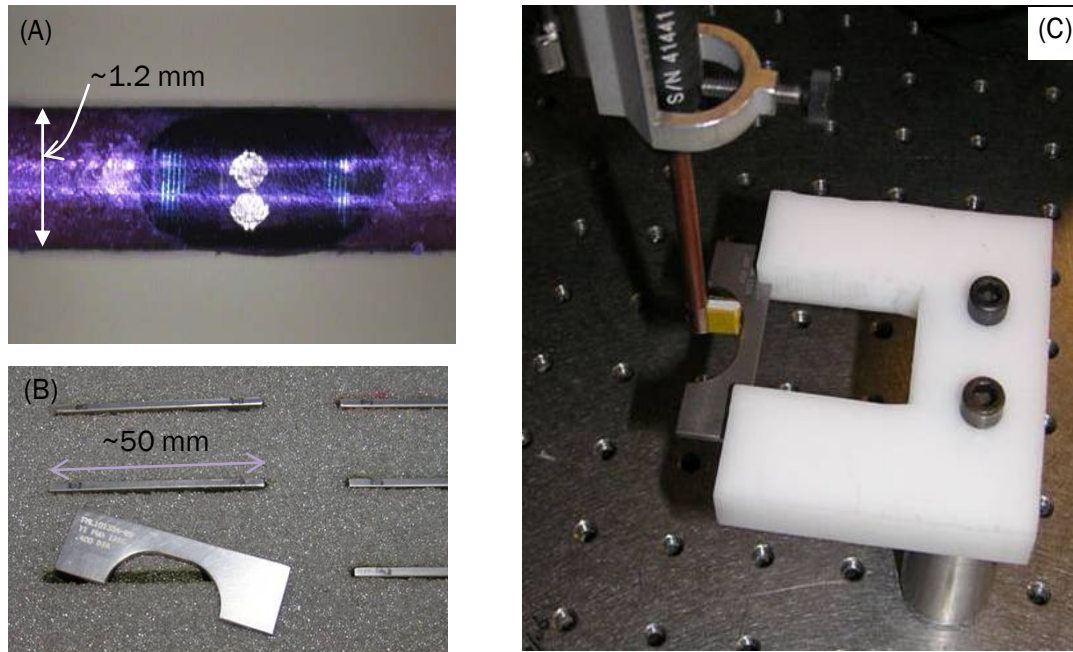


Figure 44. Photographs Of The Edge Crack Scanning Setup: (A) The ECP Probe Element Consisting Of A Pair Of Small Pickup Coils And A Larger Edge-On Drive Coil. (B) Scallop-Shaped Edge Crack Specimens. (C) The Probe Scanning The Interior Of The Scallop Shape Where Cracks Are Located

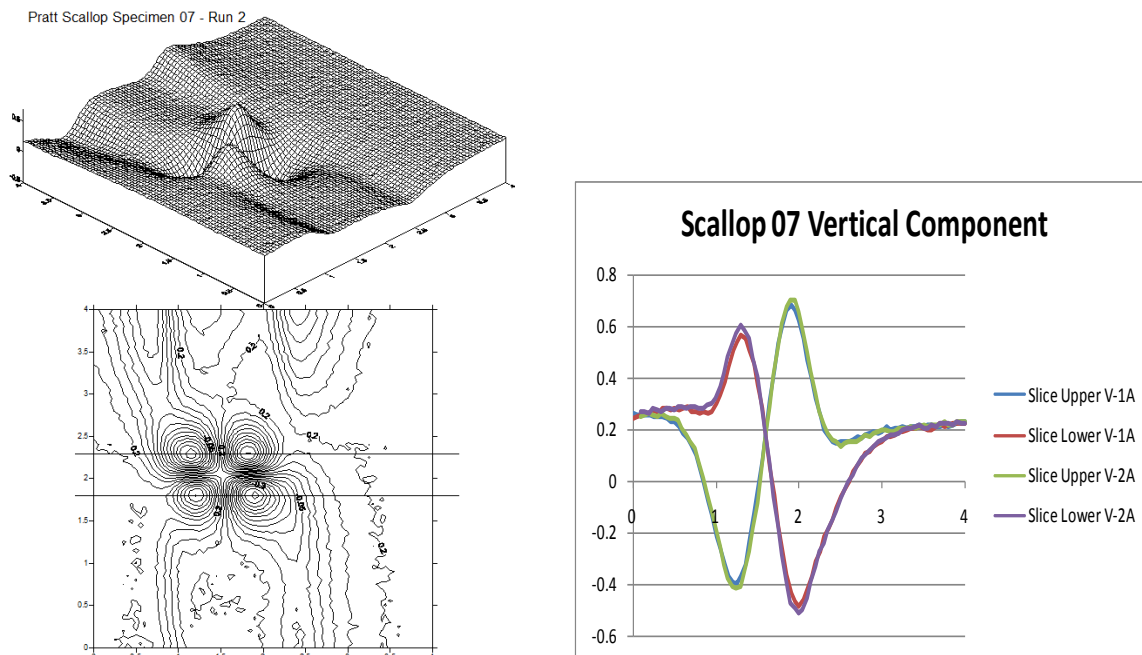


Figure 45. Example Of The Scan Data Plotted As Both A Wire Mesh Diagram And Contour Plot (Left) And The Resulting Line Plots Of The Slices For The Vertical Portion Of The Signal. Note The Slice Data For Two Scans Is Shown To Demonstrate The Measurement Repeatability

3.5.2.2 Edge Crack Signal Data and Preliminary POD Estimation

Raster scan data thus collected were processed to capture the peaks and valleys in each scan. Nominal scan images show two peaks and two valleys for a single crack, except that, when a crack runs into the chamfer of the edge, the scan may produce only one peak and one valley. There are several possibilities for extracting quantitative crack signatures such as peak-to-valley deflections and individual maximum peak/valley magnitudes. It turned out that the single point maximum absolute value showed the best correlation with the surface length with the optimum R^2 value (see Figure 46). There are a few notable outliers, particularly Sample #3 and #52, which produced much lower response voltages than those anticipated from the surface lengths. From the scattered correlation plot, we can calculate POD as in Figure 47 in terms of the statistical log-normal regression model with a maximum likelihood estimator (MLE).

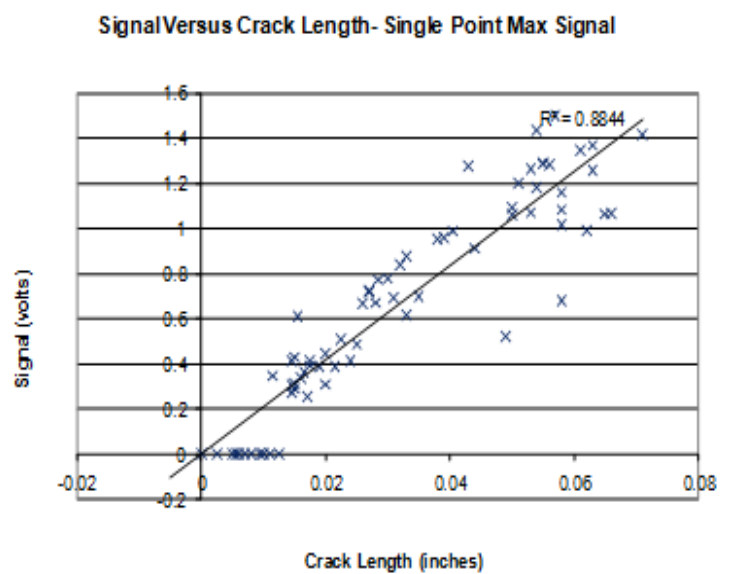


Figure 46. A Plot Showing The Correlation Between Signal Strength And Crack Length For The Complete Sample Set Of Scallop Specimens

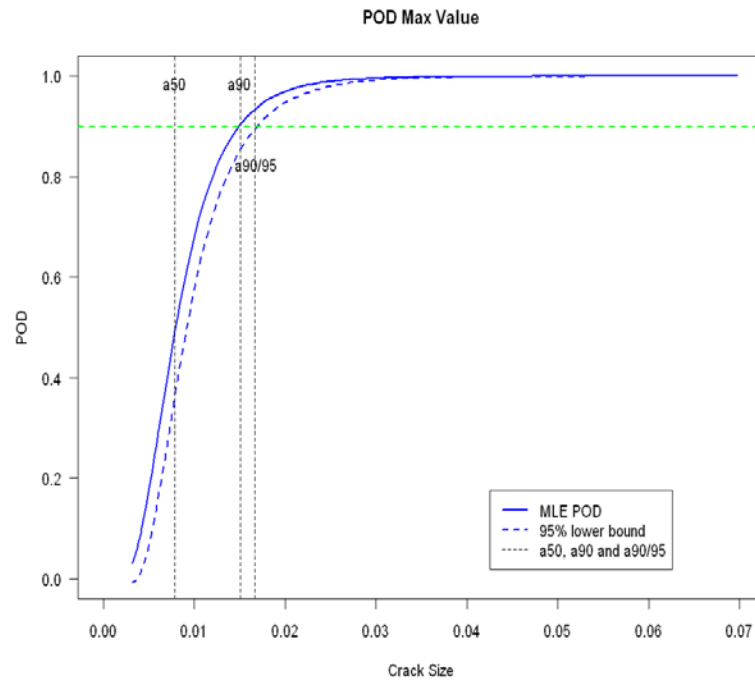


Figure 47. Probability Of Detection Curves Calculated As A Function Of The Surface Crack Length (In Inches) From The Single Point Max Signal Data. Also Shown Are The A90/95 Etc., i.e., The Detectable Crack Length At The 90% POD With The Lower 95% Confidence

3.5.2.3 Modeling Edge Crack detection by Boundary Element Model

We used the EC NDE simulation model. Briefly, it is a numerical model based on the boundary element method (BEM), and simulates conceptual EC inspections of arbitrary probe size/configuration and general 3D part geometry. The modeling code has been implemented and demonstrated to run on MS Windows and Linux platforms, with a supporting GUI code running on Windows to assist users to assemble input parameters and files.

Model calculations were made to simulate the edge crack detection for a selected subset of the elongated scallop edge crack set. The subset consisted of {#7, #45, #52, #53, #59, #61, #63, #68, #74}, being selected based on the criteria of (a) a crack in the linear section, (b) a single ligament crack, and (c) generating the characteristic 4-prong response signal. We also computed notch signals for the samples 1227-26 and 1227-51.

Our general geometry EC NDE model code based on BEM requires input of meshed versions of the geometrical objects, which we generated for the ECP probe (Figure 48), the plate with chamfered edges (Figure 49), and the crack profile (Figure 50). It should be remarked that we simply assumed the crack locations, depths, and depth profiles because they are unknown.

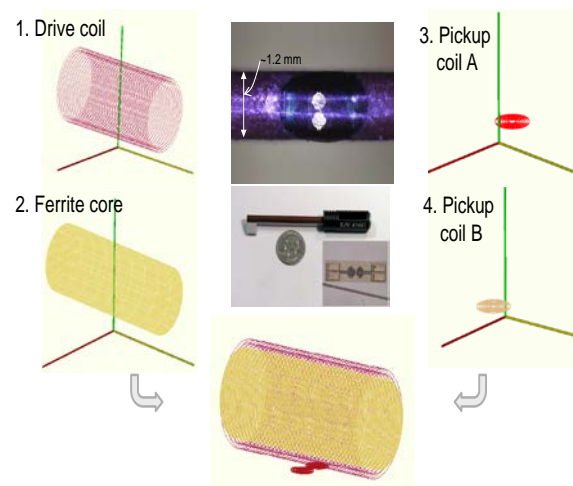


Figure 48. CAD Model Of The ECP Probe, Consisting Of Meshed Objects Representing The Drive Coil, Ferrite Core, And Pickup Coil Pair

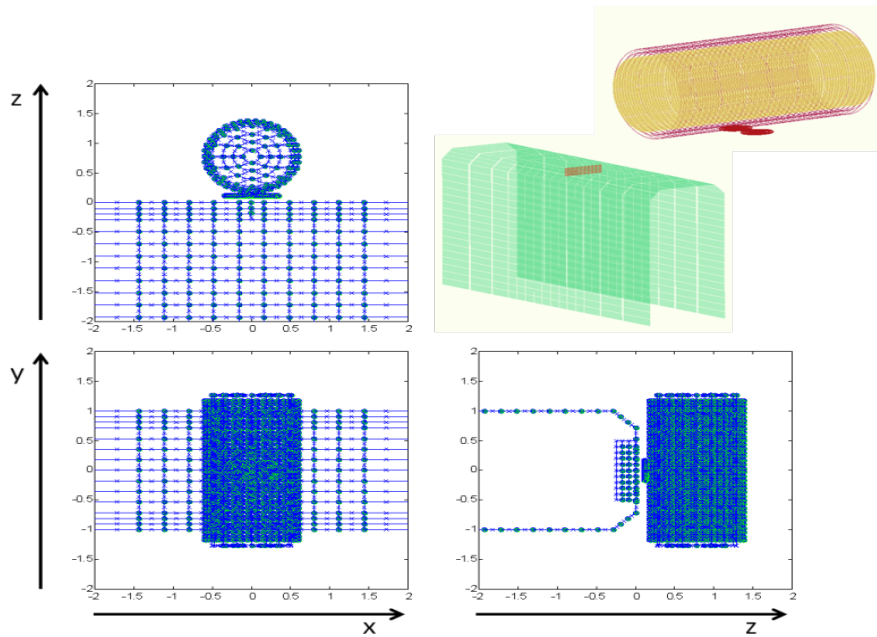


Figure 49. The CAD Models Used As Input To The EC Simulation Model, Representing The ECP Probe Model That Scans Over The Sample Edge With The Chamfers, Between Which A Rectangular Crack Is Generated

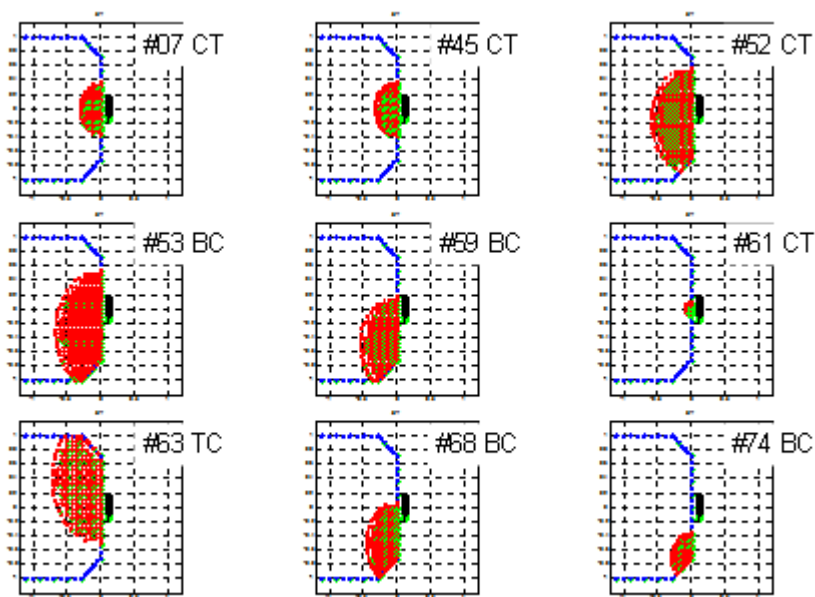


Figure 50. The Assumed Crack Mesh Generated By The Model Code During The Model Runs. The Notations TC, CT, And BC Stand For The Top Chamfer, Center, And Bottom Chamfer, Respectively, Indicating Approximate Locations

Computations indeed reproduce the four-prong crack responses in the computed impedance plane images, as shown in Figure 51 in comparison with an experimental c-scan images.

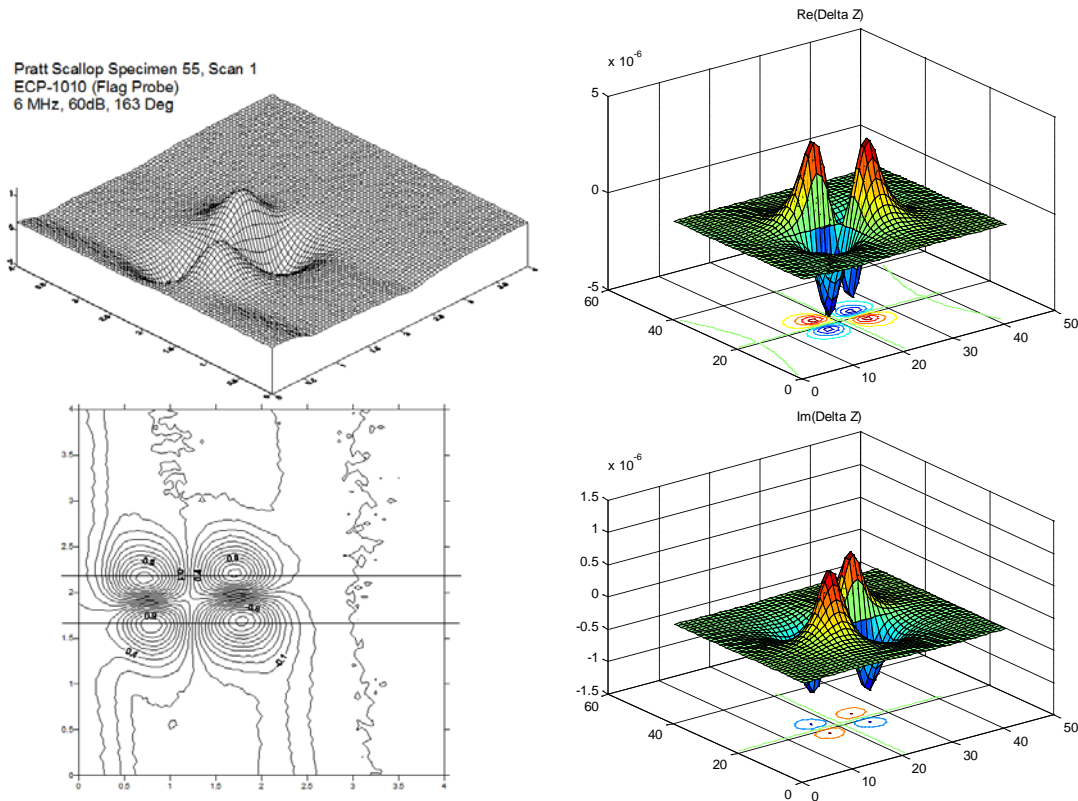


Figure 51. Characteristic Four-Prong (Alternating Peaks And Valleys) Responses Of The “Flag” Probe (Side-Mounted Excitation Coil With A Differential Pair Of Pickup Coils Of A ~0.1 Mm Diameter) As Seen In The Experiment (Left) And Computation (Right)

3.5.2.4 Theory vs. Experiment

After obtaining raster scan images both experimentally and theoretically as shown in Figure 51, we proceeded to extract quantitative crack signatures, by way of the peak-to-valley deflections, on an equal footing from the model and measured data.

On the experimental side, the data extraction procedure was conducted as shown in Figure 52, for Sample #45 as an example. The same procedure was applied to the raster scan data over the flat-surface notches, for the purpose of calibration. The notch and crack signal examples are shown in Figure 53.

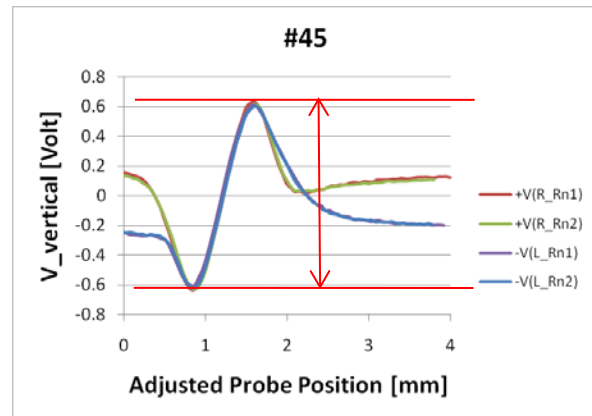
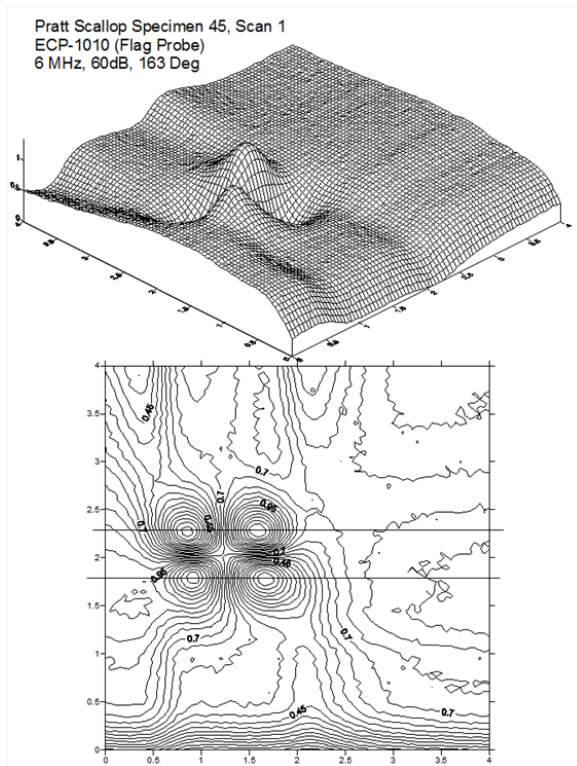


Figure 52. A Typical Experimental Raster Scan Data, Represented By The Sample “45” Data, Exhibiting A Symmetrical 4-Prong Crack Response, Consisting Of Alternating Double Peaks And Valleys. The Peaks And Valleys Are Symmetrical Such That, When Taking The Upper (“R”) And Lower (“L”) Slices Of The Peak-Valley Pairs, One Finds Overlapping Slices After Flipping The Sign Of One Of The Slices

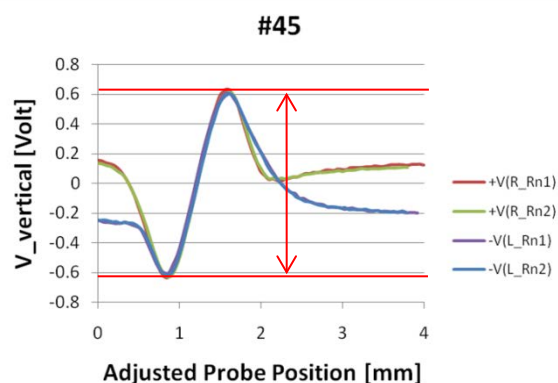
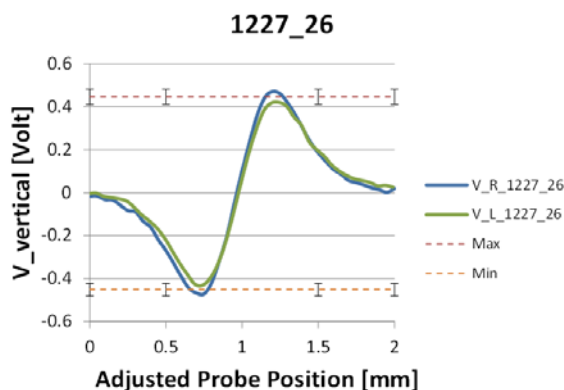


Figure 53. Examples Of Experimental Data Signals In Terms Of Min-Max Voltage Deflections For The Notch (A) And A Crack (B). These Peak-To-Peak Voltage Responses Are Found To Be Repeatable. The EDM Notch Is 1227-26-2A (0.50 X 0.25 X .025 Mm), Yielding $V_p-P = 0$

The resulting experimental data for the selected edge cracks and notches are compiled in Table 1, and plotted in Figure 54 by way of the \hat{a} -vs- a plots. (Remark: This is a linear plot, and not log-

log plot.) Notice that, unlike intuitive expectations, the trend lines for the notches and cracks are not parallel to each other, i.e., the notch line is steeper due to the increase of the notch volume effect. This non-parallel relation has been nominally reproduced by the model results below, but with a small discrepancy. Notice, again, that Sample #52 is a significant outlier.

Table 2. Experimental Max-Min Data

| Sample ID | Loc ^{*)} | Surface length [mm] | V _{p-p} [V] |
|-----------|-------------------|---------------------|----------------------|
| 07 | C | 0.724 | 1.091±.032 |
| 45 | C | 0.762 | 1.236±.027 |
| 52 | C | 1.473 | 0.761±.047 |
| 53 | BC | 1.676 | 1.391±.047 |
| 59 | BC | 1.346 | 1.850±.016 |
| 61 | C | 0.178 | 0.080±.022 |
| 63 | TC | 1.803 | 2.110±.039 |
| 68 | BC | 1.118 | 1.193±.078 |
| 74 | BC | 0.686 | 1.028±.022 |
| 1227-26 | - | 0.483 | 0.897±.064 |
| 1227-51 | - | 0.759 | 1.781±.133 |

*) TC = Top chamfer; C = Center; BC = Bottom chamfer

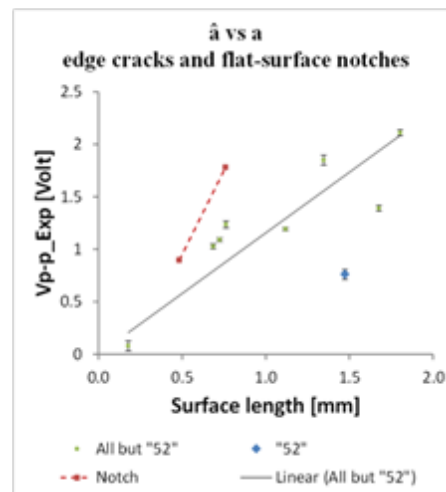


Figure 54. Experimental \hat{A} -Vs-A Plots For Edge Cracks And Flat-Surface EDM Notches

Table 3. Predicted Max-Min Signals

| Sample ID | Loc ^{*)} | Surface Length [mm] | Z _{p-p} [Ω] |
|-----------|-------------------|---------------------|----------------------|
| 07 | C | 0.724 | 0.0161 |
| 45 | C | 0.762 | 0.0176 |
| 52 | C | 1.473 | 0.0367 |
| 53 | BC | 1.676 | 0.0282 |
| 59 | BC | 1.346 | 0.0319 |
| 61 | C | 0.178 | 0.00066 |
| 63 | TC | 1.803 | 0.0464 |
| 68 | BC | 1.118 | 0.0259 |
| 74 | BC | 0.686 | 0.0131 |
| 1227-26 | - | 0.483 | 0.0115 |
| 1227-51 | - | 0.759 | 0.0277 |

*)TC = Top chamfer; C = Center; BC = Bottom chamfer

On the theory side, we processed the series of model run results obtained for the selected crack samples listed Table 2. The computations were performed similarly for the flat-surface notches by the use of the same probe CAD model for the custom edge-detection probe, in the same way as we conducted previously for the edge crack signal calculations, except that, in the notches, the part geometry is a simple, truncated flat surface. An example of extracting peak-to-valley crack impedance deflections from the computed raster data is shown in Figure 55.

The resulting predicted crack response signals for the assumed edge cracks and for the flat-surface notches are compiled in Table 3, and plotted in Figure 56 by way of the \hat{a} -vs- a plots. As promised, the crack trend line has come out less steep than the notch trend line, i.e., the model captures the notch volume effect. However, the relative gradient decrease of the predicted crack trend line turned out to be smaller than the experiment. The analysis that follows explains the likely origin of this discrepancy and potential implication to the POD transfer by MAPOD. Incidentally, the crack sample ID “53” is a computational outlier. This is presumably because it is shallower than assumed in the computation.

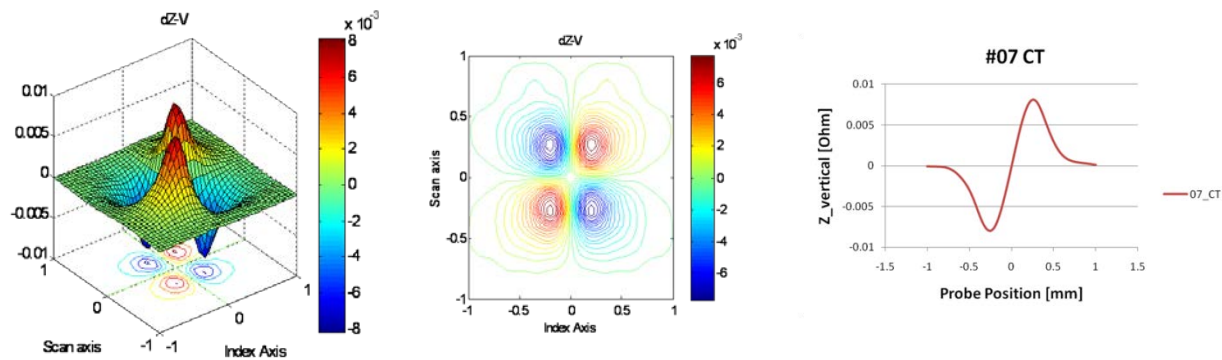


Figure 55. Computed \hat{A} -Vs-A Relations For Edge Cracks And Flat-Surface EDM Notches. The Crack Sample “53” Is An Outlier And Excluded From The Trend Line Determination

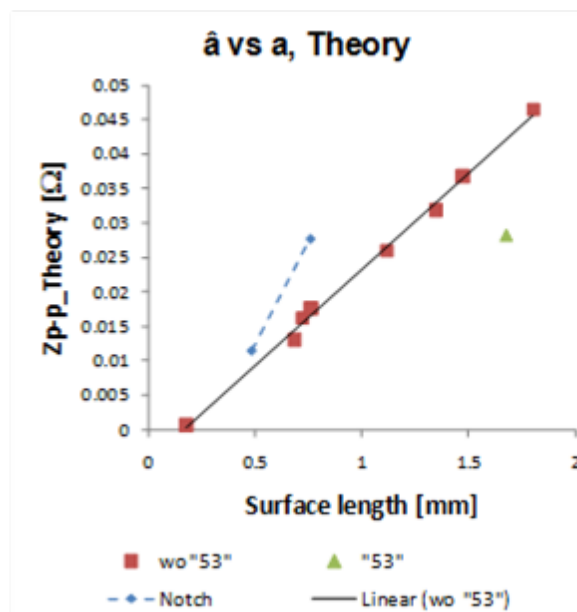


Figure 56. Computed \hat{A} -Vs-A Relations For Edge Cracks And Flat-Surface EDM Notches. The Crack Sample “53” Is An Outlier And Excluded From The Trend Line Determination

We included the results for the notches on flat surface samples, to serve the two purposes: One is to establish the calibration constant between experimental voltages and theoretical impedances. The second purpose is to work toward MAPOD, examining the possibility of POD transfer, i.e., estimating POD of cracks on edges from POD of notches on flat surface. Indeed, in what follows, we present experimental and theoretical data comparisons, showing the movement of the \hat{a} -vs-a trend lines from notches to cracks.

The theoretical and experimental signatures thus obtained correlate with each other, as shown explicitly in Figure 57. From the notch data correlation, the calibration constant, or the instrument transfer function, is determined to be 69 [V/Ω]. Recall that all the notch parameters including depths and widths are known, and explicitly used in the computation. The notches sustain no morphological signal reductions either. The crack signals correlate less well, and this is presumably due to the crack morphology effects, observed explicitly in our defect morphology

study. The unknown depths and depth profiles are expected to contribute to the variability as well.

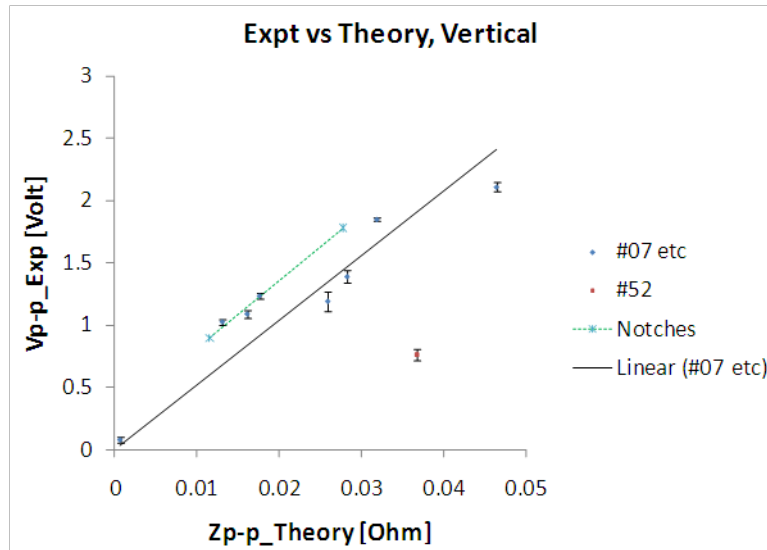


Figure 57. Experiment Vs. Theory Plots For The Notches, As Well As For The Cracks. The Notch Data, Or The Gradient Of The Trend, Was Used To Determine The Calibration Constant Of 69 [V/ Ω] For The Instrument Parameters Used. Similarly Plotted Are The Experiment Vs. Theory Correlations For The Edge Cracks That Indicate The Significant Signal Variability

Given the calibration constant of 69 [V/ Ω], we can now plot the measured and computed \hat{a} -vs- a relations together in Figure 58. This amounts to the principal result of this task, indicating the plausibility (or a potential obstacle) for the trend line prediction for edge crack detections from those of the flat-surface notches. Notice the two crack signal trend lines, i.e., the red line (the predicted crack signal trend) and the blue line (the measured crack signal trend). They are close to each other, but not coincidental.

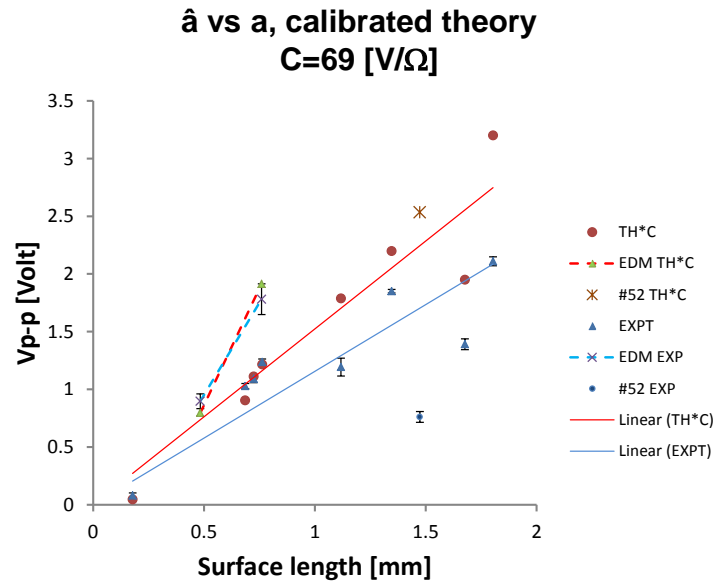


Figure 58. The \hat{A} -Vs-A Plots For Both Experimental Data (Symbols) And Computation (Lines) Where The Computed Impedance Values Are Converted To The Voltage By The Calibration Constant 69 [V/ Ω]. Notice The Downward Skewed Crack Data Distributions

Figure 58 indicates that the measurement data have a tendency to appear below model predictions, particularly for longer cracks. Such behaviors are expected from both crack morphology effects and a potentially large variability of edge crack depths. Because of this tendency, the data fluctuation tends to show a skewed distribution downward. Thus, if one takes the predicted trend line (the red line) as the median, then it is necessary to consider a skewed signal distribution around the median, being a clear departure from the standard 1823 POD. Suppose that, instead, one forces to use the symmetric normal distribution as usual. If so, then it is necessary to modify the predicted trend line even further down, in order to capture the downward fluctuation of the data, thus bringing down the trend line closer to the experimental one (the blue line). The issue to the second approach is that the determination of the final trend line must rely on some knowledge of the data variability, thus losing the predictability of the trend line.

Thus, at this stage of the development, we conclude tentatively that we:

- Demonstrated advanced experimental and theoretical capabilities on EC edge crack detection and simulation. The experimental method has achieved large suppression of edge effects. The computation has demonstrated the ability to simulate industrial inspection problem.
- Demonstrated correlation between computed and measured signals by the use of the notch-signal-based calibration.
- Gave prospect toward MAPOD approach, i.e., it may be possible to convert POD from notches on flat surface to cracks on edge, except that one must pay attention to skewed (downward) crack signal distributions.

3.5.3 Development of Element-Free Boundary Integral Equation Method for Numerical EC Modeling

This aspect of the efforts is to conduct fundamental research, motivated toward significant enhancement of efficiency in solving quasi-static electromagnetism (eddy current problems) numerically.

Joined by an expert (Chen) in solving EM scattering problems by numerical methods, we started the task by a broad survey of recent advancements in numerical solution technologies. We then focused our attention to a class of discretization methods based on the moving least square (MLS) algorithm. The algorithm lays foundation for various, so-called “meshfree” approaches. The technique is applicable to solve boundary integral equations (BIEs), and it is claimed that the method has an advantage in the accuracy of the calculation because it can adaptively determine the optimum location of nodes within each local expansion domain according to the local shape (curvature) of the local domain. It was previously shown that the MLS method is applicable to discretize and solve BIEs in potential theory and linear elasticity.

In the MLS BIE method, the unknown functions u is expressed in a local compact support domain as

$$u(\mathbf{x}) = \sum_{i=1}^m p_i(\mathbf{x}) a_i(\mathbf{x}) = \mathbf{p}^T(\mathbf{x}) \mathbf{a}(\mathbf{x}), \quad (1)$$

where $p_i(\mathbf{x})$ ($i = 1, 2, \dots, m$) are monomial basis functions, m is the number of terms in the basis, and $a_i(\mathbf{x})$ are the coefficients of the basis functions. A part of the MLS, prescription states that the coefficients $\mathbf{a}(\mathbf{x})$ are determined from the minimization of a weighted least squares norm, R_u , of the form

$$R_u = \sum_{I=1}^n w(\mathbf{x}, \mathbf{x}_I) [u(\mathbf{x}, \mathbf{x}_I) - \hat{u}(\mathbf{x}_I)]^2 = \sum_{I=1}^n w(\mathbf{x}, \mathbf{x}_I) \left[\sum_{i=1}^m p_i(\mathbf{x}_I) a_i(\mathbf{x}) - \hat{u}_I \right]^2, \quad (2)$$

where $w(\mathbf{x}, \mathbf{x}_I)$ is an appropriately selected weight function with a compact support, \hat{u}_I is the approximation to the real nodal value, u_I , and \mathbf{x}_I ($I = 1, 2, \dots, n$) are the nodes in the compact support domain of point \mathbf{x} . The minimization of R_u (i.e., $\partial R_u / \partial a = 0$) yields an expansion of the form

$$u(\mathbf{x}) = \sum_{I=1}^n \Phi_I(\mathbf{x}) \hat{u}_I, \quad (3)$$

in terms of \hat{u}_I instead of u_I , where the functions $\{\Phi_I(\mathbf{x})\}$, $I = 1, \dots, n$, act as the MLS version of the shape functions (i.e., expansion functions) [77]. Notice that the MLS shape functions are determined for each compact support domain adaptively to the local geometry according to the minimization principle, Equation (2), without the topological connectivity constraints.

It is straightforward to apply the expansion Equation (3) to solve BIE problems. We first tested the MLS BIE method for a Helmholtz problem with a complex wave number in a 2D domain

against the exact solution with both the Dirichlet and Neumann boundary conditions. It was shown that, for an equal number of nodes, the MLS BIE has given more accurate solutions than the constant-element BEM, with better than 1% relative accuracies. It particularly gives better field estimates in the vicinity of corners.

Second, we tested the MLS BIE method against a two-dimensional (2D) EC problem with a notch-like defect in a square conductive domain (Figure 59A). We considered EC generated in the domain by a large encircling solenoid coil, and calculated the impact of the width of an open crack in a conductor on the impedance change detected by the coil (Figure 59B). The resulting impedance signal behavior confirms the intuitive expectation, i.e., the resistance decreases (due to the less material) and reactance increases (due to the reduced reflection) as the defect width increases.

Third, we tested the MLS BIE method against 3D diffusion problems with several object shapes. Specifically, we considered the Helmholtz problem with a complex wave number in the object shapes being a sphere, a cylinder and a square cube, and obtained the solutions for both Dirichlet and Neumann problems. We present the results for the sphere Dirichlet problem only (Figure 60) with the MLS results compared with the traditional BEM results.

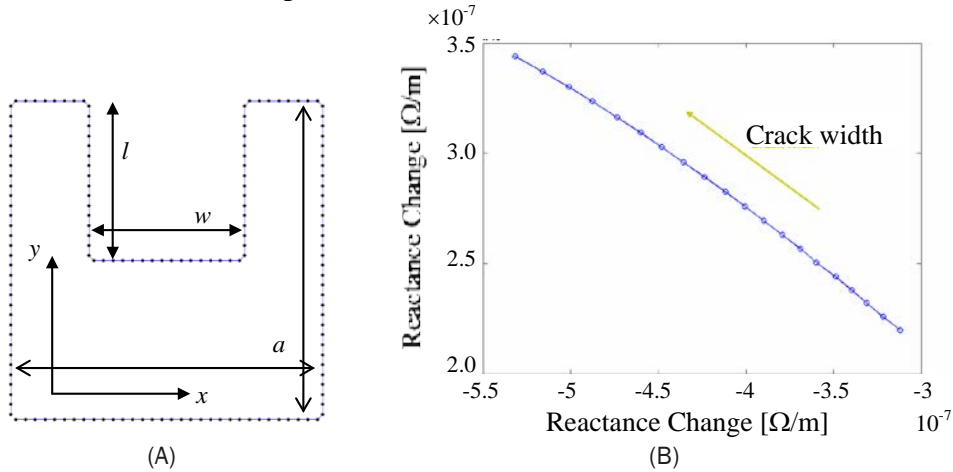


Figure 59. A) Illustration Of The 2D Model Geometry; A Square ($A \times a$) Conductive Domain With A Notch-Like Defect ($L \times w$) Where $L/A = 0.5$ While W/A Ranges Between 0.1 And 0.5. (B) The Impedance Plane Plot Of The Impedance Changes With The Crack Width As A Parameter. Note That The Impedance Change Is Normalized Per Unit Length For The 2D Problem

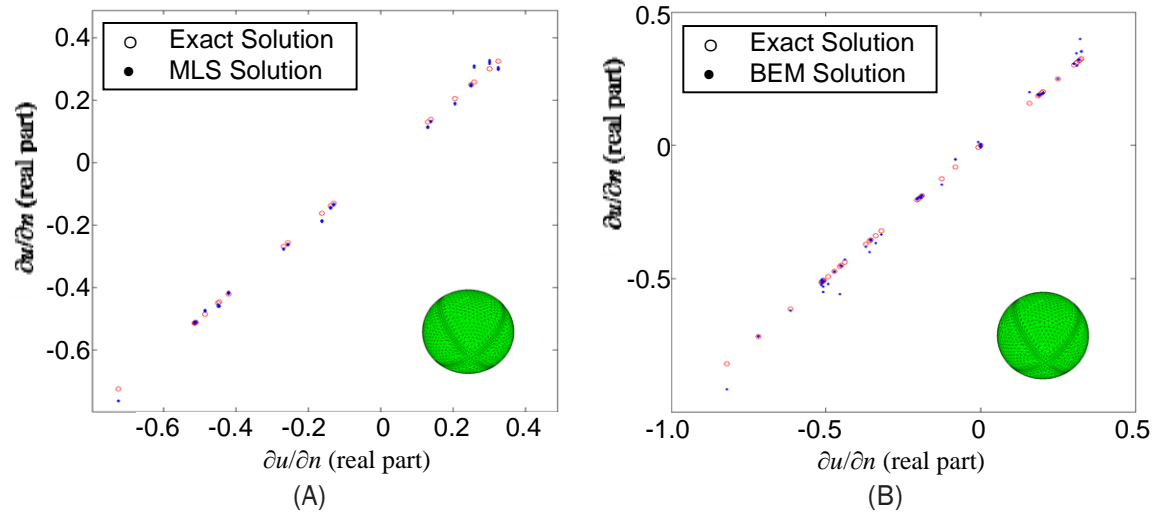


Figure 60. The Real Part Of The Solutions For A Sphere Under The Dirichlet Boundary Condition; (A) The MLS Vs. Exact Solutions, (B) The BEM Vs. Exact Solutions

The results show that the element-free BIE method works well for diffusive problems such as EC. As the combination, the MLS BIE method retains both the element-free attribute of the MLS approximation and the dimensionality advantage of the BIE method. The method has shown an added advantage of producing better solutions, i.e., those of higher accuracies for a less number of unknowns than the traditional BEM, for several test problems. This means that, for a given accuracy, the MLS BIE is a faster method.

In parallel, we also examined another possible method to enhance efficiency by the use of the fast multipole method (FMM) in a companion project [78].

Conclusions

The study of the notch width effects on EC signals presented validation of an eddy current NDE model based on the boundary element method, implemented for test specimens of generalized half space geometry with a probe of any construction and dimensions. Specifically, the study:

- Established a calibration approach that enables the comparison between theoretical predictions and experimental data.
- Showed that, after being mapped to the vector voltage plane, model-predicted notch signal traces agree with experimental signals in the same voltage plane.
- Obtained the validation results for commercial absolute and differential probes.
- The overall magnitude comparisons, as well as the matching trends of the notch width effects, are shown within approximately 10% errors or less.
- Showed ~35% reduction of the EC signal for a tightly closed (mathematically idealized) crack of no leakage current, compared to the 0.005" wide notch of the otherwise identical dimensions.

The study of EC crack signals under dynamic and static loading presented the crack morphology effects on EC responses:

- Under dynamic tension, Al crack samples showed that the EC signal amplitude increases with the load amplitude, while the effect is stronger for longer cracks.
- Under compression, Al crack signal amplitude remains relatively unchanged, presumably due to the insulation effect of the oxidation layer on the crack face.
- EC scans on Al fatigue cracks under static loads confirmed the load-signal relations observed under dynamic loading.
- EC scans on Ti 6-4 fatigue cracks under static loads revealed significantly stronger stress effects on crack signal than what the Al samples exhibited, notably under compression. It was argued that the difference comes from the propensity difference toward oxide layer formation.

The overall study of the notch vs. fatigue crack signal relationship comparison study confirmed that the signals from low-cycle fatigue cracks were smaller in magnitude than the signals from similar sized EDM notches. However, there is a difference in reduction factors between cracks in Al and the other materials examined.

- For Al, the signals from the fatigue crack specimens correlate very well to the predicted zero-width notch signals, indicating that there is measurable (but calculable) discontinuity volume effects but minimal current leakage effects due to insulating surface oxide layer formation.
- For the titanium and nickel-base super alloys, it was found that mechanical loading could produce a significant change in the eddy current signal from the cracks. Crack signals tend to be further reduced from zero-width notch signals, where the reduction factor is strongly dependent on the crack's stress state, indicating current leakage effects being present. Because of the randomness of contacting asperities, the reduction factor is hence random in nature, with significant variability.

The study of edge crack detection and its modeling is an industrially relevant and thus complex problem. Nevertheless, progress has been made in the study, and at this stage of the development, the conclusions are that we:

- Demonstrated advanced experimental and theoretical capabilities on EC edge crack detection and simulation. The experimental method has achieved large suppression of edge effects. The computation has demonstrated the ability to simulate industrial inspection problem.
- Demonstrated correlation between computed and measured signals by the use of the notch-signal-based calibration.
- Gave prospect toward MAPOD approach, i.e., it may be possible to convert POD from notches on flat surface to cracks on edge, except that one must pay attention to skewed (downward) crack signal distributions.

As a part of this project, draft documents were generated to describe recommended protocols for steps of EC NDE model validation.

Recommendations

The results presented here are sufficiently encouraging to call for a follow-on project to be conducted, with the following well-defined tasks and objectives.

- Procure a sample set for POD studies of EC inspections in flat surface geometry, and conduct an integrated theoretical and experimental research that is similar to the present study, paying particular attention to the likely skewness in the crack signal variability.
- Fabricate notch samples of the same material and similar inspection opportunities, and conduct a similar integrated theoretical and experimental research in parallel.
- Make three-way comparisons among the integrated study results on edge crack detections, flat surface crack detections, and notch detections, and discover pathways to transfer POD results from one set of measurements to another.
- Update the EC NDE simulation models so that they can calculate crack signals for multiligament cracks.

3.6 Probability Of Detection Advances (Meeker)

Investigation Team: William Meeker

Students: Chunwang Gao, Ming Li, and Yew-Meng Koh

Motivation

POD is the most commonly used metric for inspection capability in NDE. For example, in aerospace applications, POD is an input to the processes for making accept/reject criteria decisions, scheduling inspections, doing lifing calculations, and performing risk analyses. It is important to obtain good estimates of POD and also to quantify uncertainty in POD.

Results – Theory and Experiments

3.6.1 Vibrothermography Crack Detection Algorithm and POD

Vibrothermography, also known as Sonic Infrared (IR), thermoacoustics and thermosonics, is a promising new NDE technique used for detecting cracks in metal structures such as engine disks and air foils, particularly in aerospace applications. Because the method is new, little work has been done in the area of finding good detection algorithms, determining optimum inspection methods, signal processing, and estimation of POD.

As reported in Gao and Meeker [79] an image-based method for the analysis of sequence-of-images (movie) sonic IR inspection data was developed. Sonic IR data were obtained by inspecting 70 experimental plates, 60 of which contained fatigue cracks. We developed a detection algorithm, based on fitting a spatial-temporal regression model to an expected flaw signature. Principal components regression modeling was used to provide a simple low dimensional detection criterion. The method was illustrated on inspection data from a controlled experiment using specimens containing fatigue cracks. The results of applying the algorithm agreed well with the conclusions of an inspector who had viewed the movies except in four cases where the algorithm did not give a detect signal. These same results, with additional technical details and figures illustrating the method, were presented in Gao and Meeker [81].

Vibrothermography Inspection Optimization and POD

Gao, Mayton, and Meeker [80] describe the analysis of data from vibrothermography (sonic IR) inspections on turbine blades. The paper describes separate but similar analyses done for two different purposes. In both analyses, they fit statistical models with random effects to describe important amounts of crack-to-crack variability and the effect that the experimental variables have on the responses. For the particular vibrothermography equipment used in the study, the operator can control the variables vibration amplitude, pulse length, trigger force. For example, increasing the levels of these variables will tend to increase the strength of the signal from a crack (amount of heat generated). Certain combinations of the settings of these variables (especially those that generate the largest amounts of heat) would, however, tend to cause the system to “alarm” resulting in no signal at all.

In the first analysis, the purpose of the study was to find vibrothermography equipment settings that will provide good crack detection capability over the population of similar cracks in the particular kind of jet engine turbine blades that were inspected, and have a small probability of an alarm. Contour plots were prepared to map out the favorable regions for these variables. Figure 61. 61 is an overlay plot showing, for a pulse length of 217 ms, the region of trigger force and vibration amplitude values that result in high probability of detection and low probability of an alarm.

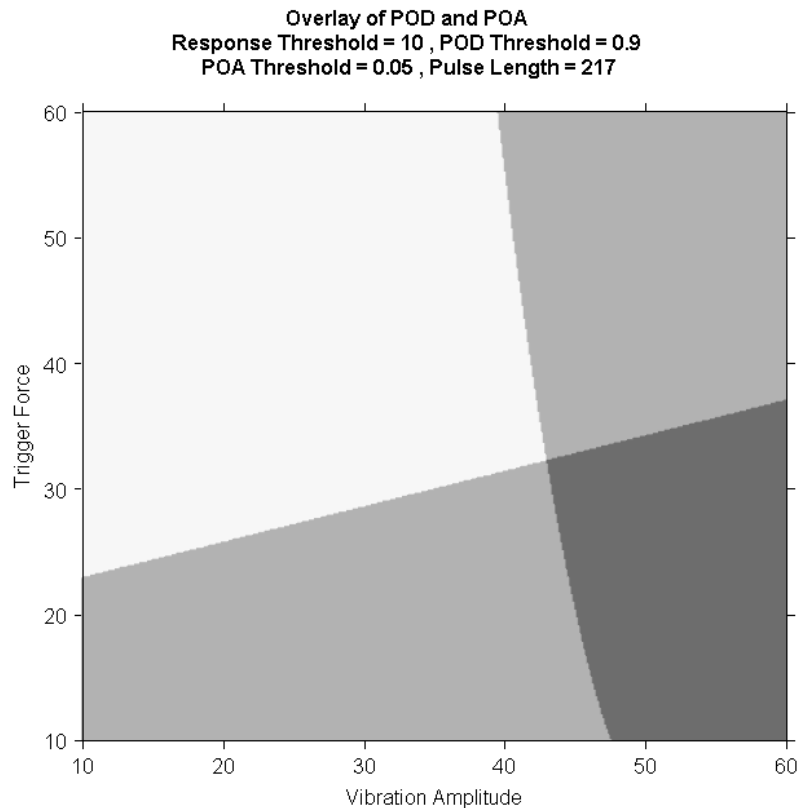


Figure 61. Overlay Plot Showing The Dark Region Where The Probability Of Detection Is High And The Probability Of An Alarm Is Low

In the second analysis, crack size information was added and a similar model was fit to the data. This model provides an estimate of POD as a function of crack size for specified test conditions. Gao, Meeker, and Mayton [82] present the same results with an additional study of the Wald-based confidence interval procedure that they used and more technical detail and additional figures to illustrate the method.

3.6.2 Joint Estimation of Crack-Size Distributions and POD

Life prediction and inspection interval decisions in aerospace applications require knowledge of the size distribution of unknown existing cracks and the probability of detecting a crack (POD), as a function of crack characteristics (e.g., crack size). The POD for a particular inspection method is usually estimated on the basis of experiments using a given specimen set. These experiments, however, cannot duplicate the actual conditions of in-service inspections. The task of quantifying the size distribution of unknown existing cracks is more difficult. Figure 62. 62 illustrates the kind of data that is required.

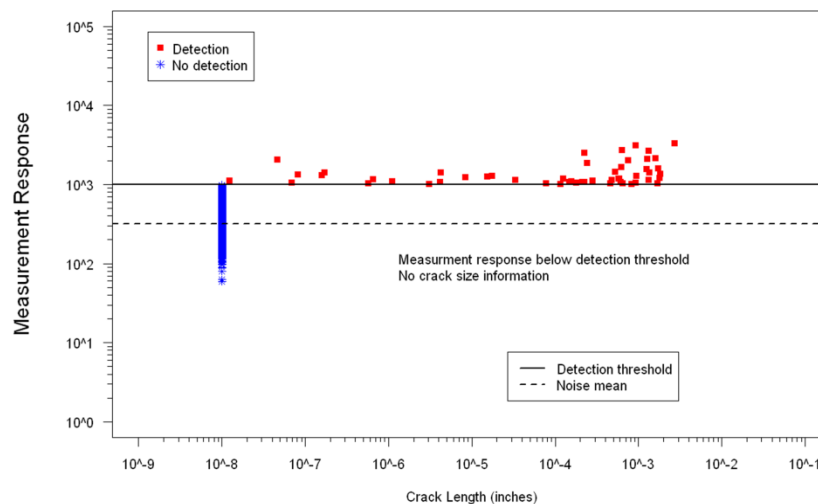


Figure 62. Plot Of Simulated Data That Would Allow The Joint Estimation Of A Crack-Size Distribution And POD

If signal-response is recorded for all inspection locations and if reasonably precise crack size information is available for locations with “crack find” decisions through inspection procedures, it is possible to estimate the joint distribution of crack size and signal response. This joint distribution can then be used to estimate both the in-service POD and the crack size distribution. Hovey, Meeker, and Li [83] present a statistical model and methodology to do this estimation based on a model that describes the joint distribution of initial crack size and signal strength with a bivariate lognormal distribution and a constant crack growth model having a given rate. Because the type of data needed to utilize this model is not currently being collected, the paper illustrates the method with simulated data.

Li, Meeker, and Hovey [87] extended the work reported in Reference [83] to deal with a more complicated situation where there are different crack growth rates for different aircraft. They use a hierarchical model and Bayesian estimation methods with diffuse prior distributions that allows joint estimation of the same bivariate lognormal distribution model used in Reference [83] along with the parameters of the crack-growth rate model. This work was described more completely in Li, Meeker, and Hovey [88].

3.6.3 Estimation of Quantile POD for Hit-Miss Data

There are a number of sources of variability in NDE inspections. These include, for example, operator-to-operator differences and flaw morphology differences (e.g., different cracks having the same length will have different inspection signal strengths). From this point of view, the POD curve for a given type of inspection can be viewed as random, varying with the particular operator and crack combination. Traditional methods for estimating POD (e.g., those in MIL-HDBK 1823) provide an estimate of the mean of this POD distribution. Some NDE professionals without good understanding of variability mistakenly say that the 90/95 point (95% upper confidence bound on the flaw size that can be detected with probability 0.90) will quantify POD variability. A confidence bound, however, does *not* quantify POD variability in NDE inspections. A confidence bound only quantifies the statistical uncertainty due to limited data. In a study with a large amount of data, the upper confidence bound will be close to the true POD value.

In some applications involving NDE, the traditional inference on the “mean POD” may not be appropriate. This would be especially true in NDE applications where there is a substantial amount of inspection-to-inspection variability (e.g., variability caused by operator, setup, flaw morphology, and/or calibration variability) and when there is concern about the smallest POD that could arise in an inspection. Such concern should arise in applications involving safety. In such an application one cannot simply average good inspections with poor inspections and still be safe.

In order to quantify variability in the distribution of POD curves, one can estimate a quantile of the POD distribution. We call such an estimate a quantile POD. For example, the true POD realized in a given inspection would fail to exceed a 0.10 quantile with probability 0.10.

The concept of a Quantile POD was recently developed in recent FAA-funded forging inspection work for a hat-versus-a type data. This work has been extended to hit/miss data by Koh and Meeker [84] and uses an illustrative example data taken from the famous “Have cracks, will travel” POD study in which specimen sets were inspected multiple times by different inspectors. The paper illustrates the ideas of a POD conditional on a particular operator/flaw combination. It then shows how to estimate the operator and target sources of variability in the estimation of POD from binary data, allowing estimation of a quantile of the POD distribution. Methods for obtaining a lower credible bound on the quantile POD are also described.

3.6.4 Planning Studies to Estimate POD

Planning a study to estimate POD generally requires that one obtain a set of specimens that contain flaws of interest (e.g., fatigue cracks in flat plates). A frequently asked question related to the preparation of a sample set of specimens for a POD study is how many such specimens are needed and what should be the distribution of the flaw sizes. The answer to the number-of-specimens and the distribution-of-flaw-size questions depends on the amount of variability in the NDE inspection signals, the desired degree of precision that is needed to estimate quantities of interest (e.g., mean POD or quantiles of the POD distribution), and the range of flaw sizes that

could be used in the study. Thus, in order to properly plan a POD study, one must have “planning information.” Sufficient planning information would consist of a statement of the assumed model and the parameters of the model.

Koh and Meeker [85] show how to compute a relevant measure of precision for estimating the a_p value (e.g., a_{90}) for a given test plan, assuming signal-response (ahat versus a) data. They then compare various classes of plans to gain insight into how the distribution of cracks should be chosen. First, they use such computations to determine how the number of distinct crack sizes affects precision. Concentrating all the cracks at two sizes at the extremes of the given range will provide the best precision for estimating a_p . The optimum allocation to those two points depends on the value of p with more units allocated at the larger crack size if $p > 0.5$. A two-point plan, while optimum, would not be practical. Testing at a larger number of points (with fewer cracks at each point) would allow better checking of model assumptions and provide more robustness to departures from the assumed planning information. Our evaluations show that as the number of distinct crack sizes grows, with uniform allocation, the efficiency decreases by about 15% in the limit, and the limit is reached quickly. Thus there is little loss of efficiency if one plans a test with crack sizes spread over the region of interest.

It has been conjectured that if primary focus is on estimating a_p for a particular value of p (e.g., to estimate a_{90}), then there could be improvements over the simpler non-equal allocation. We developed a ramp-allocation scheme in which the ratio of the allocations at the extreme crack sizes is the same at the optimum two-point plan, but the number of crack sizes is allowed to increase with allocation linearly increasing over the range of stresses. The results shown that ramp stress plan results in approximately 15% more efficiency when estimating a_{90} and about 18% more efficiency when estimating a_{99} . Of course if one were to use a ramp allocation to improve the estimation of say a_{90} , the precision for estimating a_{10} would go down.

Koh and Meeker [86] have done a similar study for test planning when the study will produce hit-miss data. Test planning with binary data is more challenging. First, with binary data, there is a positive probability that the resulting data will not be sufficient to estimate the POD curve. In particular, if all of the misses are at crack sizes that are less than the crack sizes corresponding to the hits, then the ML estimates do not exist and computer programs that do not trap this condition will encounter convergence problems. The theoretically optimum plan would again concentrate all test units at two points, but the optimum points, in the binary case, cannot be too far apart, to protect against the not-estimable condition. Koh and Meeker [86] developed and present formulas that can be used to compute measures of precision for estimating a POD curve with binary data. Calculations based on these formulas show that the optimum value of p_{\max} is close to 0.90 with equal allocation, independent of the value of which a_p is to be estimated. As with the signal-response test planning, the optimum two-point plan would not be practically useful. It turns out, however, that using a larger number of distinct crack sizes results in only a modest loss of estimation precision. Thus spreading out crack sizes more or less uniformly is a good compromise strategy. The challenging part of planning a POD study with hit-miss data is

choosing the endpoints of the range in the face of uncertainty about the true POD curve. Little useful information is obtained by inspecting cracks that are certain to produce a hit or a miss.

Conclusions

Modern quantitative nondestructive evaluation, given the data that is generated, is inherently a statistical operation. While existing methods for estimating POD (e.g., those described in MIL-HDBK 1823) can answer many of the needed questions, as new technologies are developed, it may be necessary to develop new approaches. Use of inappropriate statistical methods can increase the probability of making bad decisions related to inspection outcomes. There is no magic in statistics, but the application of appropriate statistical methods will ensure that available information is used as efficiently as possible. Methods of statistical design of experiments and careful use of Bayesian methods can be usefully employed to obtain efficiency needed for economical experimentation, even in complicated situations.

Recommendations

1. In vibrothermography inspection, it is critically important to continue to run the IR camera until there through the cooling-down phase, as that temporal pattern is an important part of the signature of the signal that will allow one to separate signal from noise.
2. In vibrothermography inspection, until more is known about the underlying fundamental mechanisms relating inserted energy, resultant vibration the corresponding relationship to heat generation, in any new vibrothermography application (system type and part-type/flaw type), it will be necessary to conduct experiments to help determine appropriate inspection setting system settings.
3. For a given specimen and inspection setting, there can still be a large amount of variability in the amount of heat generated from a vibrothermography inspection. It would be useful to conduct experiments that would focus on identifying and understanding the relative magnitudes of the main sources of this variability. Quantitative information about the sources and amounts of variability in the inspection process will suggest methods that can be used to reduce variability and thus improve inspection capability.
4. It is feasible to simultaneously estimate POD and crack-size distributions from actual inspection data is possible if the right data are collected as part of the inspection process. To be able to do such estimation it would be necessary to collect and retain signal-response readings from each inspection and also to obtain reasonably precise measurements on the size of detected flaws. We recommend that steps be taken to collect such data at least in some important applications.
5. Traditional statistical methods, developed in the 1980's and codified in MIL-HDBK 1823 (both versions), give methods for estimating what should be called "mean POD," the mean over all possible POD curves that could arise due to different operators, crack morphology, and other sources of variability. The lower confidence bound on POD (or $a_{90/95}$ confidence bound) quantify only the statistical uncertainty (arising from limited) data and does not quantify the inherent variability in a POD curve. POD curves are used to make in-service inspection-interval decisions. One can see why mean POD would be

relevant in backing out the initial cracks size distribution. It is hard, however, to understand why the mean POD used to quantify the largest crack that could be missed in an inspection, where one should be focusing on the worst-possible inspection that could occur. It should be determined whether the lifing community recognizes this difference or not.

6. Although the recent work of Koh and Meeker has more light on the question of how to plan a POD study, the use of the guidelines is a little less than straightforward because of the need to provide “planning information.” It would be possible to extend the results of Koh and Meeker to a Bayesian approach in which prior distributions would be specified for the planning information. Actually, there could (and should) be two separate prior specifications: one for the planning information and one that would allow incorporating information directly into the estimation procedure. In some applications, a diffuse prior would be used for the latter prior distribution, so that the data, primarily, determine the POD function.

3.7 Phased Array Measurement Model And POD Calculation (T. Gray and F. Margetan)

Investigation Team: Tim Gray, Frank Margetan, Les Schmerr, Mike Garton, Ron Roberts

Motivation:

Ultrasonic (UT) phased array (PA) techniques are becoming more common in aerospace applications for several reasons. For example, one PA probe can be used to generate a variety of apertures and focal lengths and, hence, can replace many specialized single crystal transducers. In addition, a PA probe can improve inspection speed by electronically scanning instead of mechanically moving the probe. Examples include linear scanning, sectorial scanning, and dynamic depth focusing. Another advantage of PA systems is that they often incorporate novel data display features, such as s-scan (sectorial display), which can improve inspector interpretation of the ultrasonic data.

In order for PA methods to see more widespread use, especially on geometrically challenging aerospace components, analytical model-based computer simulations are needed, both for defining the delay laws used to operate the PA probe and for establishing the efficacy of the resulting inspection. In recent years, considerable effort at CNDE has been devoted to the application of computer models to assessment of probability of detection (POD) for inspections performed using conventional UT transducers. The primary goal of this project is to extend that capability via implementing analytical models for the ultrasonic beams generated by phased arrays comprising rectangular elements and to integrate them into the Thompson-Gray (T-G) measurement model. The analytical framework for the beam models is the multiGaussian (MG) model, which is a computationally efficient paraxial model that easily treats ultrasonic beam transmission through curved surfaces and has been successfully employed in such applications as predicting UT signals from reflectors and estimating backscattered grain noise. These applications are included in the new PA developments. Due to the paraxial approximation, inaccuracies are expected in modeling PA probe radiation since contributions from widely spaced array elements are summed to form the propagating fields, and, hence, the summed fields can be relatively far from the central axis of those elements. To counter this, a novel correction approach is presented that assumes the fields from individual elements are steered relative to their central axes and an amplitude correction is introduced based upon comparison to exact radiation from the elements. This approach greatly improves the model accuracy while maintaining computational speed.

Other applications of PA methods involve their use on anisotropic materials. Aerospace examples include both metallic components, such as single crystal turbine blades, and composite materials, such as are common in airframe or body structures. Similar advantages to these applications derive from PAUT as are described above for isotropic media, including improved coverage, inspection speed, and inspection sensitivity. However, new difficulties present themselves, such as determining PA focal laws in the presence of beam steering that arises from anisotropy. This difficulty is compounded further when such components also have complex geometries. Extensions to the CNDE simulator package, UTSim [92], to allow focal law

generation in these cases will provide an important tool to simplify the application of PAUT to anisotropic components.

Results – Theory and Experiments

3.7.1 Phased Array Modeling

The main emphasis of this work concerns implementation of a model for predicting the ultrasonic fields of a linear 1-D array comprising rectangular piezoelectric elements. (Extension is straightforward for 2-D array of rectangular elements but is not considered here.) Such a probe is illustrated in Figure 63, which depicts a 5 MHz, 32-element linear array that was used in much of the work described here. The bottom of the figure illustrates time delays that are applied to both the firing and reception process to generate an aperture equivalent to a single element transducer with a 250mm focal length in water. The combination of such delay times applied to the elements of a PA probe are typically referred to as a focal law. Different focal laws can be used to generate different beam formations – a linear focal law causes beam steering, parabolic laws cause focusing, and a combination of the two generates both steering and focusing. This flexibility is the advantage of phased arrays. Please note that additional details concerning the developments presented here can be found in Appendix D.

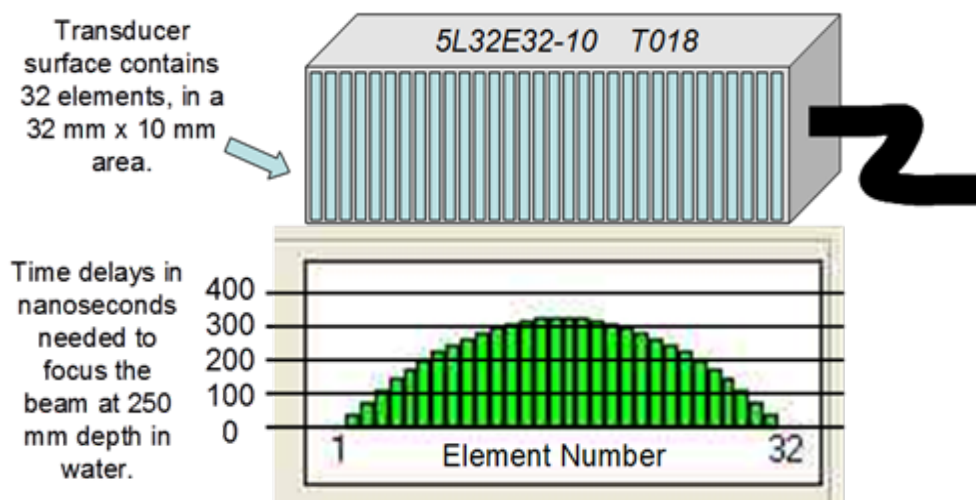


Figure 63. Typical Linear Phased Array Transducer With Rectangular Elements And A Sample Focal Law Showing Time Delays For Focusing

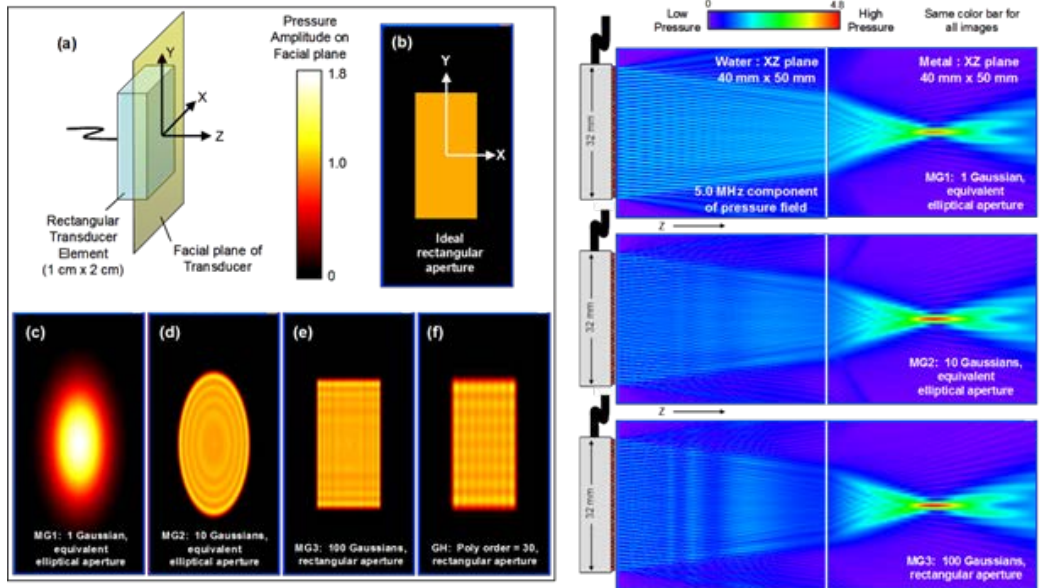


Figure 64. Phased Array Probe Field Calculations Showing (Left) Pressure Amplitudes On An Individual Element Face For Several Modeling Assumptions And (Right) Corresponding Pressure Fields In Steel For Full Aperture

The approach to modeling a PA probe is to extend current modeling approaches for single element transducers, which was developed as the Thompson-Gray measurement model [89]. To extend this model to the case of PA probes, the approach is to treat each combination of pairs of elements as an instance of the T-G model, either in pulse-echo mode or pitch-catch mode. The model for predicting the ultrasonic fields generated by an individual rectangular element of a PA probe is an extension of the multiGaussian model devised by Wen and Breazeale [90, 91]. The Wen and Breazeale model treats elliptical elements; the extension to the rectangular case is shown in Appendix D. By the MG model, the paraxial approximation to the radiation of an elliptical element is computed as the sum of 10 or 15 Gaussian functions with appropriate width and amplitude scale factors that are tabulated in Refs. [90, 91]. For the rectangular element, the same tabulated factors are used in a double summation of the products of all combinations of the elliptical factors; thus either $100=10^2$ or $225=15^2$ Gaussian terms are used. Examples of MG calculations are shown in Figure 64, which on the left shows the predicted fields on the face of a single elliptical or rectangular element and on the right shows predicted radiation patterns for the PA probe shown in Figure 63 for different model assumptions. The differences among the images are as follows. In subimage (c) on the left and in the top image on the right, the calculations use a single Gaussian term for an elliptical aperture. Subimage (d) on the left and the middle image on the right use the 10 term MG model. Subimage (e) on the left and the bottom image on the right use the rectangular aperture MG model with 100 terms. Subimage (f) on the left shows a rectangular aperture based upon the Gaussian-Hermite model, which was the workhorse for beam model calculations in earlier T-G model developments and is included only for comparison. The reason for showing the results for elliptical apertures is that reasonably accurate model predicted PA fields can be estimated using the elliptical models which are 1 or 2 orders of magnitude faster computationally than the rectangular model. This can be a benefit in

noise model calculations described in Section 3.7.2 below due to the need to perform integrations of the fields. In general, though, the rectangular aperture MG model is used throughout the report.

The MG model largely owes its flexibility and speed by taking advantage of the paraxial approximation, which implies that it is most accurate in terms of both amplitude and directivity near the central axis of the UT beam. For single element transducers, this is not a big problem, but this approximation can lead to significant errors for PA probe modeling since the total ultrasonic fields are synthesized by summing the fields of the individual elements. If two elements are widely separated on the PA probe face, then the summed fields midway between those two elements may not be in the paraxial regime. This effect is compounded for a steered beam, since then none of the summed fields may be paraxial. Figure 65 illustrates this effect. The scenario is shown at the top of the figure, comprising the PA probe from Figure 63 on a Lucite wedge radiating into a steel block. The wedge angle is set to produce a 45° refracted longitudinal wave in the steel. Consider three focal law cases – -15° steering, 0° steering, and $+15^\circ$ steering, which correspond to refracted angles of 30° , 45° , and 60° in the steel, respectively. The amplitude profiles are for 5 MHz. For the 45° case, the top two plots show the beam amplitude along the x-direction at a depth of $z=50\text{mm}$ (top left) and along the z-direction at a position of $x=40\text{mm}$ (top right). The MG solution is plotted as a dashed line. Also shown is the exact solution based upon the Rayleigh-Sommerfield integral (RSI), which is a solid blue line. Agreement is quite good between the two calculation methods in terms of the magnitude and shape of the profiles, particularly in the main lobe of the beam. The middle and bottom rows of plots show similar comparisons for the refracted 30° and 60° cases, respectively. In both of those cases, there is significant error between the MG and the RSI calculations, both in magnitude and in the shape of the main lobes.

Those errors are due to the paraxial approximation, particularly for large steering angles or large overall apertures. Although the RSI approach is rigorously correct, it is computationally intensive and is not flexible for handling complex geometries. A novel approach to correcting these errors is to employ two corrections to the MG model that improve its accuracy while maintaining its speed and flexibility. The first correction is to include a directivity correction based upon the steering angle of the PA probe. The steering correction is shown in Appendix D. In effect, each element is assumed to radiate as if it were tilted in the steering direction. The second correction is to scale the amplitude of the steered MG fields to agree with the corresponding RSI amplitude. This model is referred to as the Linear Phased MG (LPMG). Comparisons of the LPMG calculations for the three steering examples above are also shown in the plots of Figure 65 as solid red lines. As can be seen, the LPMG and RSI calculations agree

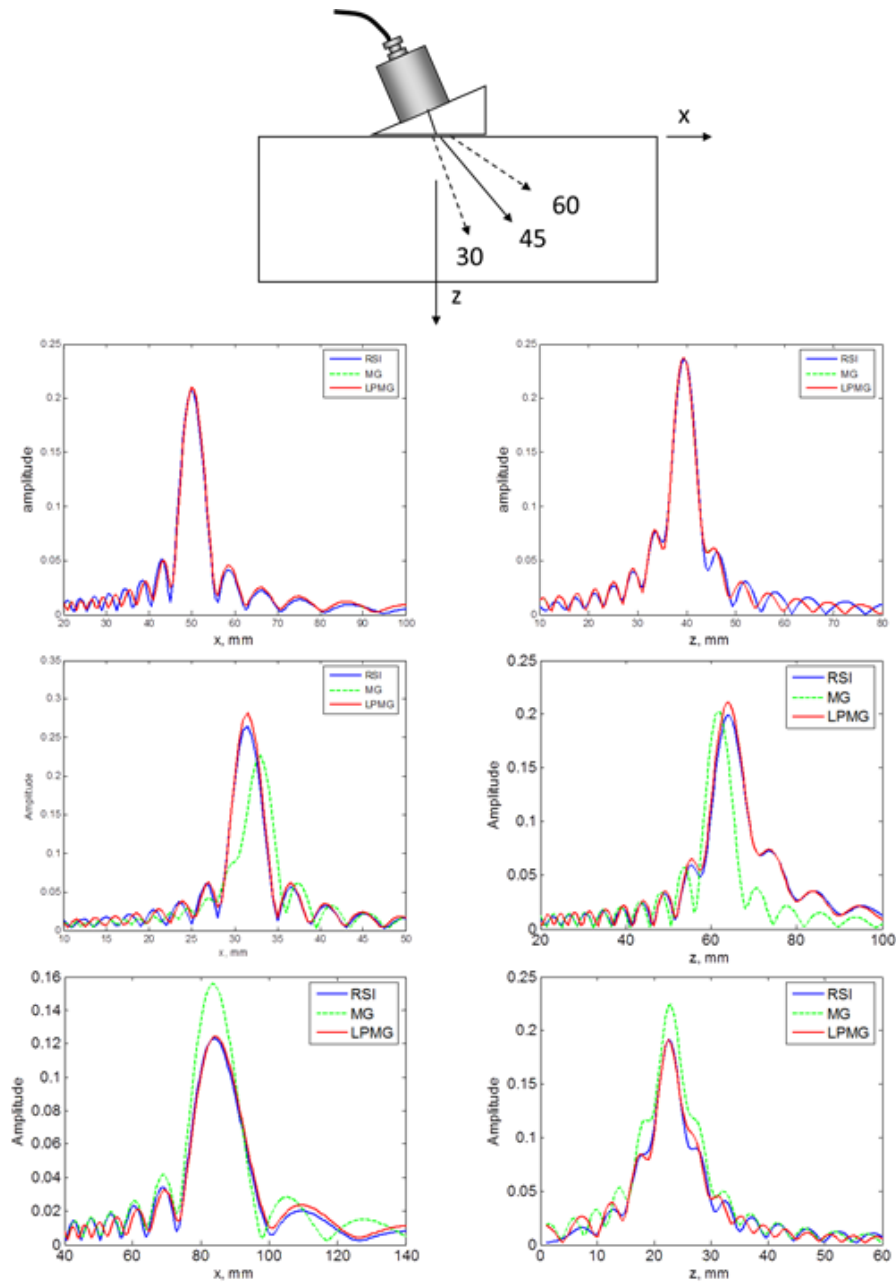


Figure 65. Comparisons Of Model Calculations For Phased Array Probe On Lucite Wedge Radiating Into Steel Along X (Left) And Z (Right) Directions, $D/\lambda = 0.68$. Top Plots Are For No Beam Steering (45° Refraction), Middle Plots Are For -15° Steering (30° Refraction), Bottom Plots Are For $+15^\circ$ Steering (60° Refraction)

| $\frac{d}{\lambda} \backslash \theta$ | 0.25 | 0.33 | 0.42 | 0.5 | 0.58 | 0.67 | 0.75 | 0.83 | 1.0 | 1.08 | 1.25 | 1.5 | 1.67 | 1.83 | 2.0 |
|---------------------------------------|--------|--------|--------|--------|--------|--------|--------|--------|--------|--------|--------|--------|--------|--------|--------|
| 5 | 0.9933 | 0.9924 | 0.9912 | 0.9901 | 0.9889 | 0.9912 | 0.9891 | 0.9869 | 0.9824 | 0.9800 | 0.9724 | 0.9662 | 0.9596 | 0.9525 | 0.9477 |
| 10 | 1.0028 | 0.9998 | 0.9963 | 0.9923 | 0.9877 | 0.9861 | 0.9796 | 0.9724 | 0.9568 | 0.9482 | 0.9292 | 0.8967 | 0.8723 | 0.8459 | 0.8180 |
| 15 | 1.0187 | 1.0124 | 1.0050 | 0.9963 | 0.9863 | 0.9782 | 0.9645 | 0.9494 | 0.9160 | 0.8975 | 0.8585 | 0.7889 | 0.7388 | 0.6856 | 0.6321 |
| 20 | 1.0418 | 1.0312 | 1.0183 | 1.0030 | 0.9852 | 0.9688 | 0.9451 | 0.9193 | 0.8623 | 0.8310 | 0.7664 | 0.6531 | 0.5746 | 0.4938 | 0.4121 |
| 25 | 1.0734 | 1.0572 | 1.0372 | 1.0132 | 0.9856 | 0.9543 | 0.9233 | 0.8843 | 0.7990 | 0.7529 | 0.6661 | 0.5016 | 0.3971 | 0.2943 | 0.1960 |
| 30 | 1.1155 | 1.0920 | 1.0630 | 1.0285 | 0.9889 | 0.9444 | 0.8955 | 0.8476 | 0.7301 | 0.6679 | 0.5435 | 0.3446 | 0.2233 | 0.1097 | |
| 35 | 1.1700 | 1.1378 | 1.0980 | 1.0507 | 0.9969 | 0.9370 | 0.8717 | 0.8146 | 0.6606 | 0.5926 | 0.4392 | 0.1991 | 0.0682 | 0.0589 | |
| 40 | 1.2409 | 1.1981 | 1.1452 | 1.0828 | 1.0123 | 0.9345 | 0.8505 | 0.7617 | 0.5961 | 0.5008 | 0.3242 | 0.0680 | 0.0854 | 0.1852 | |
| 45 | 1.3328 | 1.2773 | 1.2090 | 1.1286 | 1.0384 | 0.9399 | 0.8347 | 0.7250 | 0.4999 | 0.4279 | 0.1793 | 0.0807 | 0.2010 | 0.2752 | |
| 50 | 1.4538 | 1.3835 | 1.2961 | 1.1941 | 1.0804 | 0.9574 | 0.8278 | 0.6943 | 0.4273 | 0.2995 | 0.0680 | 0.1931 | 0.2930 | 0.3327 | |

correction factors are < 1 dB
 correction factors > 6 dB

Figure 66. Amplitude Correction Factors For Linear Phased Multigaussian Model Of A Phased Array Probe For A Range Of Steering Angles (θ , Degrees) And Element Widths (D/λ)

very well in terms of both amplitude and profile shape, particularly near the main lobe of the beam. To aid in the application of the LPMG, an interpolatable lookup table of correction factors has been precomputed for a range of values of steering angle θ versus element width scaled by wavelength, d/λ . This table is shown in Figure 66. For the PA probe illustrated in Figure 63 which was used for the calculations in Figure 65, the element width is 0.8mm, so $d/\lambda = 0.68$ at 5 MHz in steel. For radiation into steel with a steering angle of $\pm 15^\circ$, we find from Figure 66 an amplitude correction factor of approximately 0.98.

An important adjunct to the analytical model development and implementation is its deployment as a useful tool to PA users and inspection designers. Integration into UTSim is one means for exposing the use of the PA models to the NDE community. That effort was partially completed and is a subject of continued development in the future. Initial integration steps included building the capability to represent linear array PA probes into the GUI and linking to the ray-tracing engines in UTSim. Currently, UTSim has the ability to define a linear PA probe, specify individual element steering angles and to generate the associated delay times which comprise a focal law. Figure 67 shows a sample display of these features in UTSim applied to an aerospace component. The particular example shown is a 16-element linear array with a 0° wedge on a flat surface of the component, two view of which are shown in the inset images to the right. A combination steering and focusing focal law has been applied to focus on a small reflector, which is highlighted in yellow, within the component. The plot at the top of the screen shows the delay time versus element number.

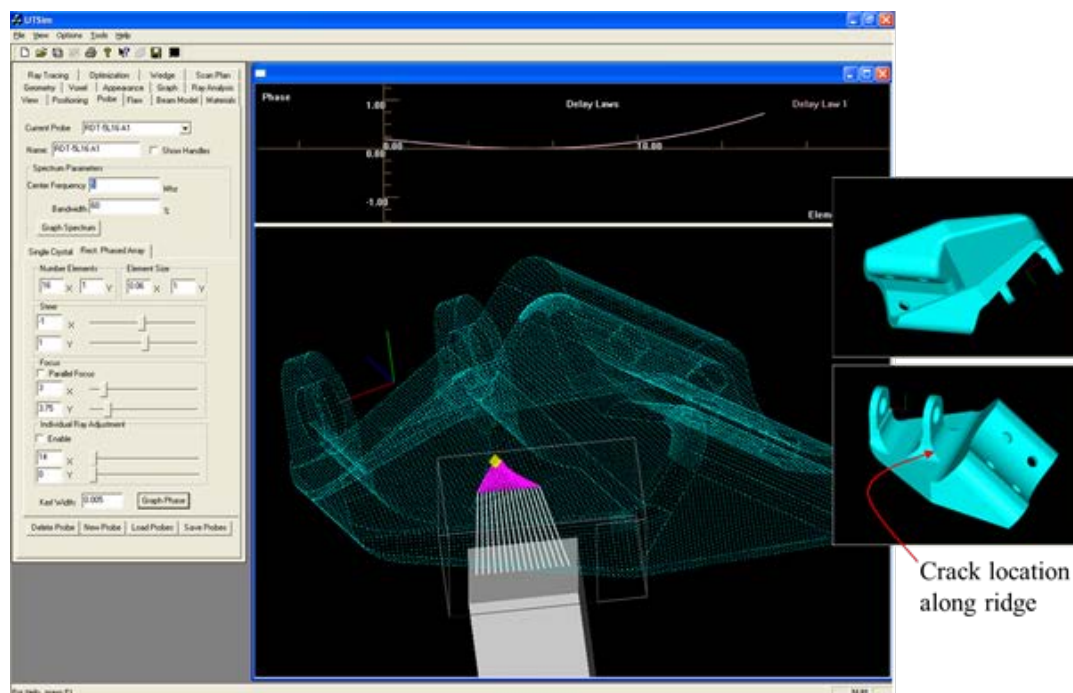


Figure 67. Example Of Utsim Display Of Focal Law For Linear Phased Array Probe Applied To An Aerospace Component

3.7.2 Model-Assisted POD Considerations

Use of the PA measurement model for MAPOD applications relies strongly on the ability to predict performance of actual, real-life UT measurements [93]. This requires the ability to directly compare computed UT signals to physically measured results using actual measurement units, such as volts, dB, etc. One of the strengths of the T-G measurement model is that its history has included development of methods to characterize ultrasonic probes and inspection instruments that permit its output to be directly and absolutely compared to real measurements. Additionally, extensions to the T-G model have resulted in related measurement models that predict grain noise signals that are also directly comparable to measurement. Therefore, signal-to-noise (S/N) ratios can be computed, which form a modeling basis for assessing detectability. The modeling techniques for probe characterization and for grain noise prediction have been extended to the PA case.

3.7.2.1 PA Probe Characterization

Ultrasonic probe characterization is a key factor in the ability of the T-G measurement model to predict ultrasonic signals in physically meaningful units, such as volts or dB. For single element transducers, this typically requires measuring dimensional parameters of the probe, such as effective diameter and geometric focal length, as well as a system efficiency factor, which quantifies the frequency response and “strength” of the probe. These quantities are essential input parameters to the measurement model, but are also valuable as indicators of the state of operational fitness of a probe. Experience with linear PA probes has indicated that, in contrast with most common single element transducers, the dimensions of the elements and their spacing are well specified by their nominal values. However, other properties can vary substantially

from element to element. For example, a single PA probe may exhibit significant inter-element variability in their respective amplitudes and time delays. Therefore, proper usage of the probe as well as accuracy of model input parameters requires some method of probe characterization.

The measured response for a PA measurement, as illustrated in Figure 68, can be expressed as the sum $\sum \sum \beta_{ij} \tau_{ij}$ where each summand is a T-G measurement model expression for transmitting with element i and receiving with element j . The summations are taken over all combinations of transmit and receive elements. The β_{ij} are the system efficiency factors, and the τ_{ij} are the remainder of the T-G expression, which includes factors such as beam amplitude, transmission coefficient, attenuation factor, etc. Both β_{ij} and τ_{ij} are functions of frequency. For a PA probe with N elements, there are $N*(N-1)$ distinct summands since, by reciprocity, interchanging “ i ” and “ j ” subscripts yields identical results. The purpose of characterization in this context is determination of the system efficiency factors, β_{ij} . Two limiting cases are (1) all elements have different responses, so full $N*(N-1)$ characterizations are needed, or (2) all elements are identical, only one element needs to be characterized.

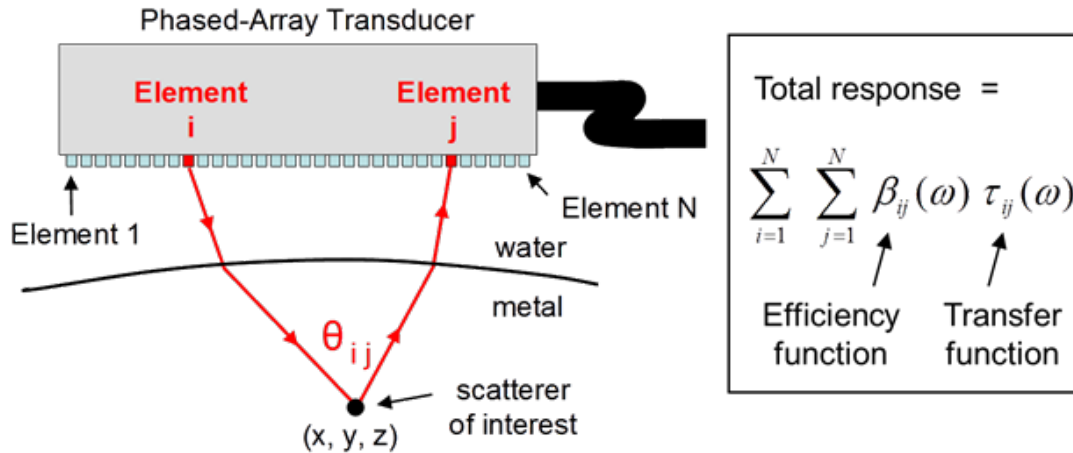


Figure 68. Schematic Of Phased Array Measurement Contribution For An Element Pair And The Total Response From All Elements

For this work, a middle ground is considered – using just the pulse-echo response from each element individually, so N measurements. The pulse-echo system efficiency factors β_{ii} for the individual elements are obtained via a deconvolution procedure from a reference measurement, such as the reflected signal from a flat plate at normal incidence [89]. We assume that the pulse-echo responses from the different elements differ only by a constant amplitude factor (different “hotness”) and by a relative time delay between elements. In this case, the $N*(N-1)$ efficiency factors in the PA model can be approximated by

$$\beta_{ij} = \beta_{ave} * \text{SQRT}(A_i * A_j) * \exp[-i\omega(\Delta t_i + \Delta t_j)/2], \quad (1)$$

where β_{ave} is the average of the single element efficiency factors, A_i is the ratio of the peak of the waveform from element i to the average peak amplitude, and Δt_i is the difference in time delay of element i to the average time delay. Additional details are in Appendix D.

By way of example, Figure 69 shows pulse-echo waveforms from each of the 32 elements of the PA probe illustrated in Figure 63. The data were acquired as front-surface reflected signals from a flat plate in immersion. The top graph shows the pulse-echo waveforms from two neighboring elements, numbers 7 and 8, indicating an appreciable difference in peak signal amplitude. The bottom left graph displays just the main peak of all 32 element waveforms and shows the variability in amplitude among the elements which are used to determine the amplitude ratios A_i . The lower right graph shows the delay time differentials among the 32 element responses that are used to determine the Δt_i . Next, Figure 70 shows the raw and corrected single element system efficiencies derived from the pulse-echo waveforms. The top graphs show the magnitude (left) and phase (right) of the as-measured system efficiencies. The corresponding plots in the bottom of Figure 70 show the magnitude and phase of the corrected system efficiency factors according to Equation 1.

The efficacy of this characterization approach can be seen by considering the results shown in Figure 71 which shows comparisons of simulated and experimentally measured frequency spectra and waveforms obtained using the corrected system efficiency factors described above. The various plots show results for a variety of different focal laws applied to the PA probe, including cases where the focal depth was varied and, in some cases, a portion of the elements of the PA probe were turned off. Agreement is very good. Note that these results were all generated for reflection from the back surface of the metal plate, while the reference measurements used to generate the system efficiency factors were obtained from a front surface reflection.

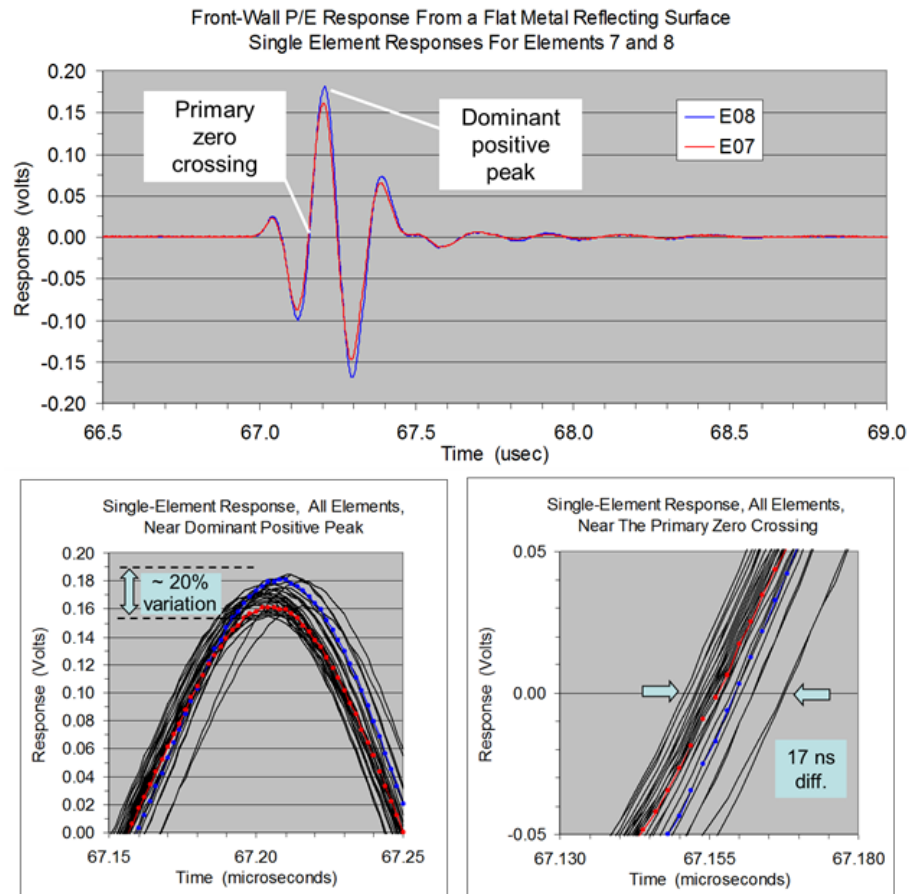


Figure 69. Element Errors For A Linear Phased Array Probe. Top Figure Shows Immersion Pulse-Echo Waveforms From A Flat Surface For Two Elements; Bottom Figures Are Zoomed-In Images Of The Dominant Positive Peak (Left) And Primary Zero Crossing (Right) Regions

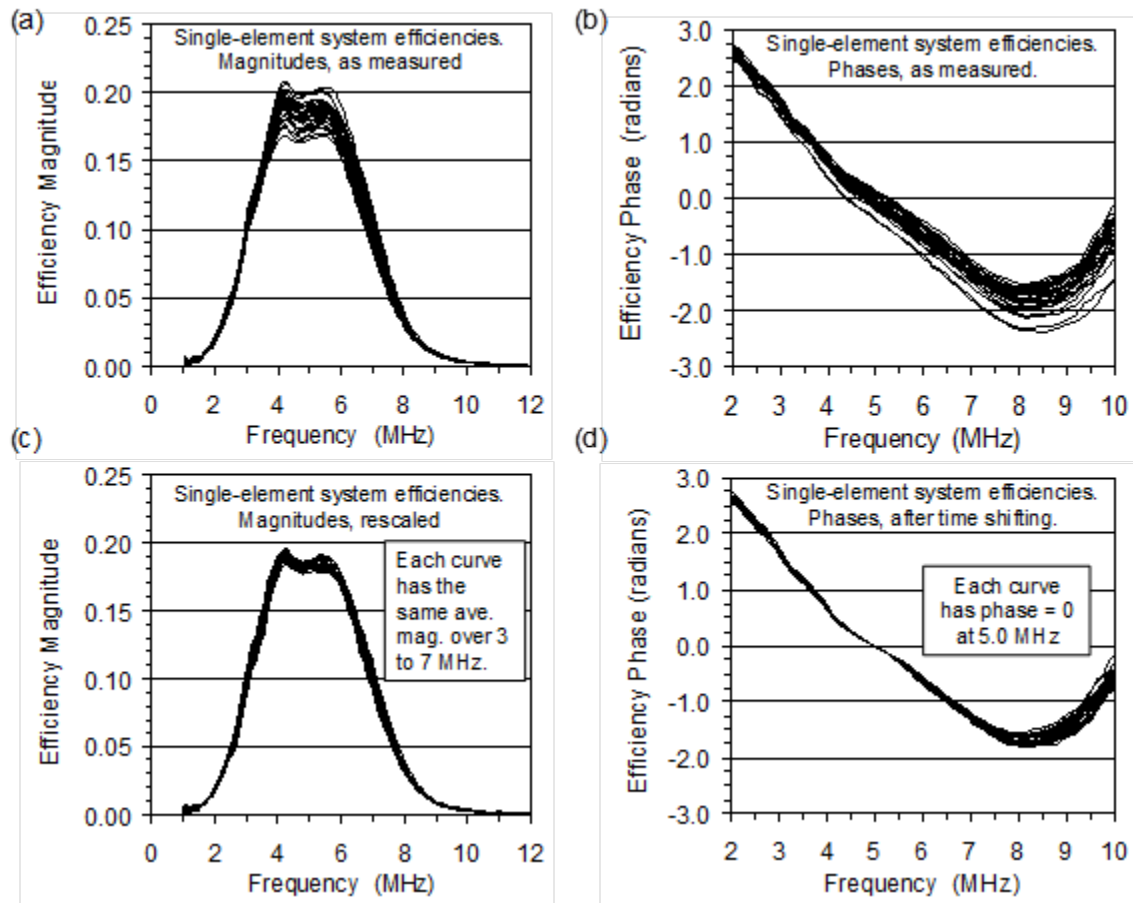


Figure 70. (A)-(B): Magnitudes And Phases Of The Spectra Of The Single-Element Front-Wall Responses, After Modification To Correct For Beam Propagation Effects (I.E, These Are Essentially Single Element Efficiency Functions) . Each Panel Contains 32 Curves, Corresponding To The 32 Elements In The Transducer Array. (C)-(D): The Same Curves After Rescaling And Time Shifting Using The Residual Strength And Time-Delay Parameters

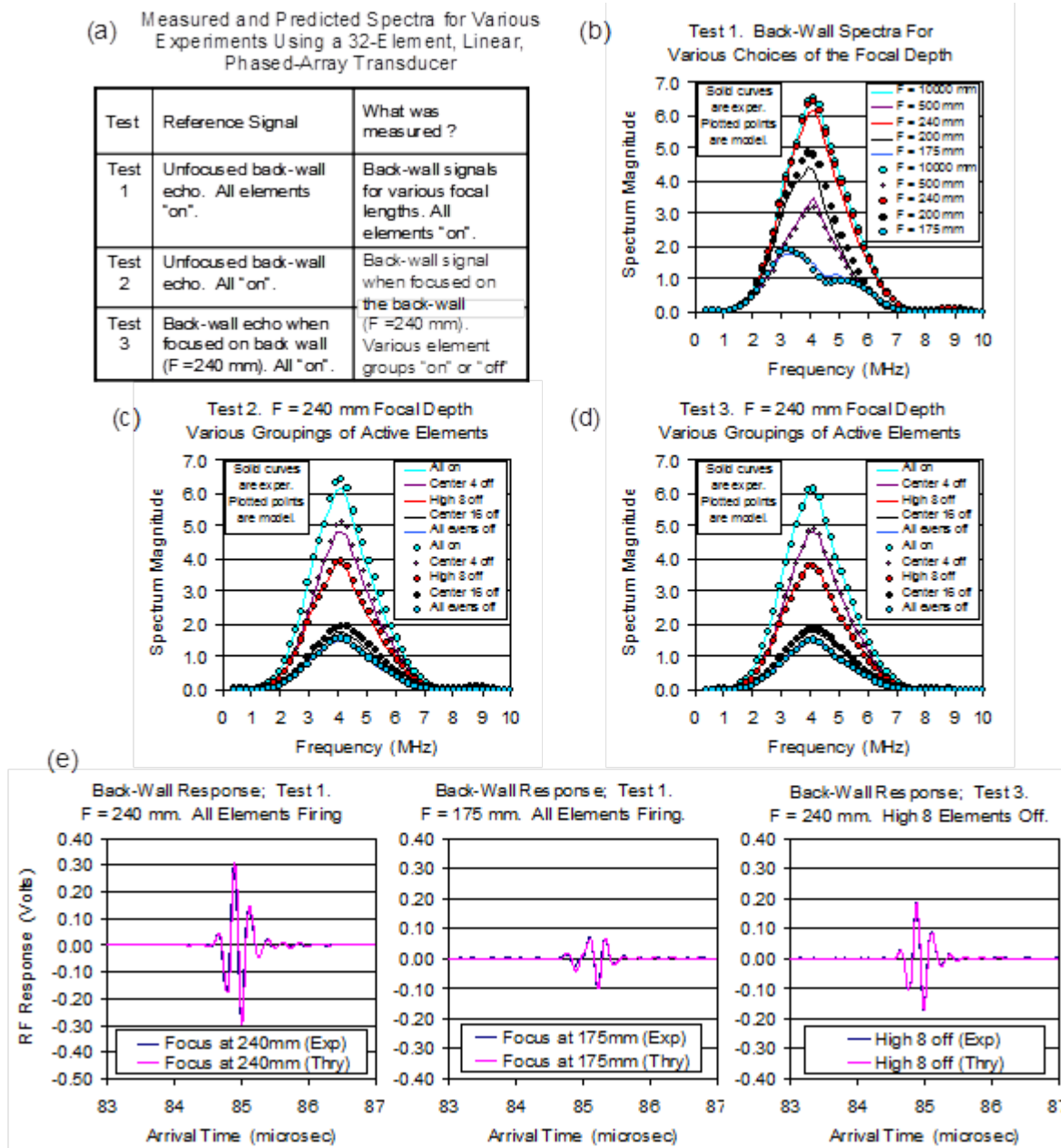


Figure 71. Comparisons Of Measured And Predicted Back-Wall Responses For The Stainless Steel Test Block. (A): Descriptions Of The Various Measurements, Including The Nature Of The Reference Signal For Each Test Trial. (B)–(D): Comparisons Of Measured And Predicted Back-Wall Spectra. (E): Comparisons Of Measured And Predicted Time-Domain Signals For Three Of The Cases

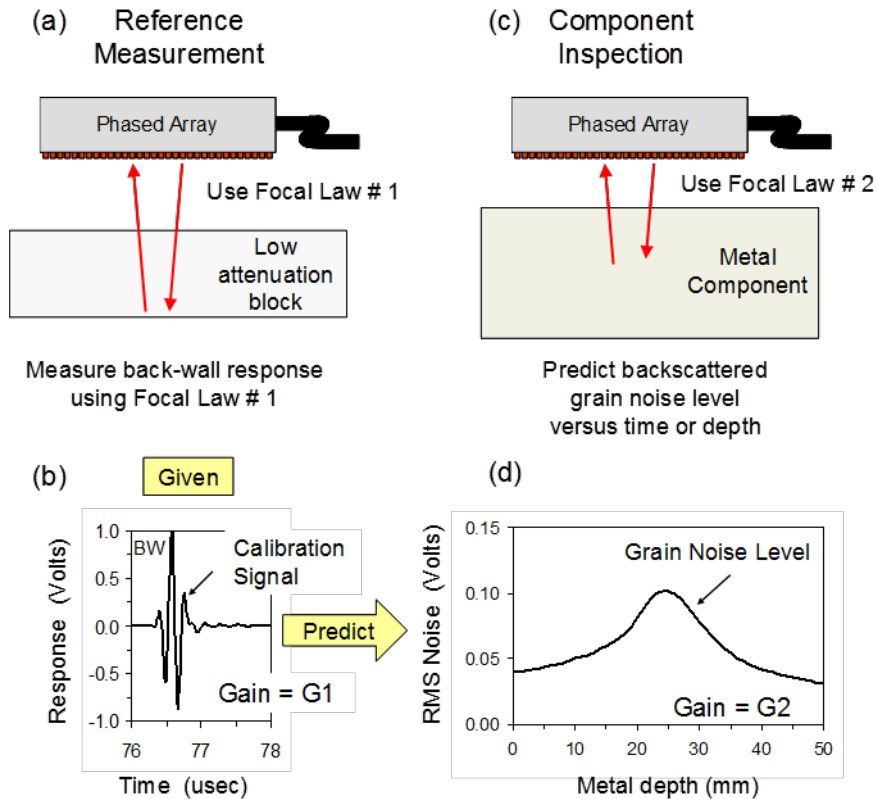


Figure 72. Schematic Of Phased Array Grain Noise Modeling Approach

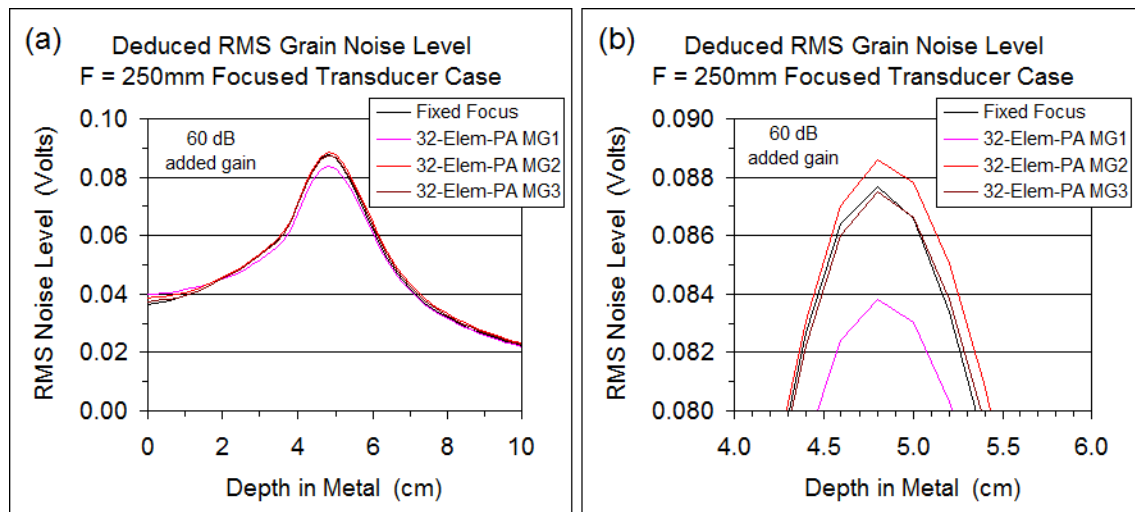


Figure 73. Predicted Rms Grain Noise Profiles For Different Phased Array Modeling Assumptions. Left Plot Shows Rms As A Function Of Depth; Right Plot Is Zoomed-In Display Of The Peak Region

3.7.2.2 PA Modeling of Grain Noise

Previous research has led to the development and testing of model-based approaches to relate ultrasonic grain noise to the properties of the microstructure of a component, including both the average size and the scattering amplitude of the grains. Previous work was limited to the use of single element ultrasonic transducers operating in either pulse-echo or pitch-catch modes [94]. Application to PA measurements is a fairly straightforward extension of that work, since a PA measurement is a combination of pulse-echo and pitch-catch measurements among the individual elements. The basic framework for modeling the root-mean-square (RMS) grain noise is illustrated in Figure 72. In the current project, the interest is on using PA models to predict RMS grain noise for a given microstructure, so it is assumed that appropriate microstructural parameters have been determined by independent means, such as is described in Ref. [94]. A reference measurement is used to obtain the PA system response, according to the probe characterization procedure discussed in Section 3.7.2.1. The form of the grain noise model is shown in more detail in Appendix D. For the work presented here, the MG model was used rather than the LPMG.

The PA version of the grain noise model was applied to a sample problem of predicting RMS grain noise in a stainless steel plate using the PA probe illustrated in Figure 63. The microstructure of the plate had previously been characterized and its grain scattering parameter, called the figure-of-merit for grain scattering, or FOM, had been determined [94]. An example of PA model predictions of the RMS noise as a function of depth in the plate for a pulse-echo measurement using focal laws to generate a 250mm focal length is shown in Figure 73. The full depth profile of the RMS noise is shown on the left, and a zoomed image of the peak noise region is shown on the right. To ascertain the accuracy of the PA model, different probe model calculations were performed, corresponding to the cases illustrated previously in Figure 64. Namely, the UT fields were computed using (1) a single element, fixed focus probe model for the same overall aperture as the PA probe, (2) a PA model using a single Gaussian beam representing an elliptical beam for each element, (3) a PA model for elliptical beam using 10 Gaussian functions for each element, and (4) the rectangular element MG PA model using 100 Gaussian functions. We see from the plot on the right of Figure 73 that the fixed focus and the rectangular PA results are nearly identical, with slight differences seen in the elliptical beam approximations. This is consistent with previous single element probe results [94].

Finally, experimental measurements were performed to measure the RMS grain noise in the stainless steel sample for two different PA focal laws and the results compared to the PA model calculations using the three PA model cases just mentioned, i.e., single Gaussian elliptical, multiGaussian elliptical, and multiGaussian rectangular. Comparisons between model and experiment are shown in Figure 74. As can be seen, the PA models do a good job of predicting the measured RMS noise profiles, in terms of both the shape of the profiles and their absolute amplitudes.

3.7.3 Modeling for Anisotropic Media

An important next step in UT measurement modeling, both for single element and for PA probes, is the ability to consider anisotropic media. A formal model based upon MG has been developed at ISU which can form the basis of this approach. As in the case of MG and other paraxial models, a key first step in model implementation is determining the ray paths along which the UT beams are assumed to propagate. Work in this area was initiated late in the project, so efforts were limited to addressing the ray-tracing in anisotropic media. The primary emphasis was upon developing the ray-tracing process and implementing it in UTSim.

The analytical basis for ray-tracing in an anisotropic solid is based upon the solution of the elastic Christoffel equation for a bulk medium and involves computation of slownesses, group velocities, and wave polarizations. A handy reference to the mathematics and method is available online at the URL in Reference [95]. The key precept is to identify ray paths as the directions of energy flow, or group velocity vectors. In the present task, a computer code was developed and verified to perform the Christoffel equation solutions and to apply the anisotropic version of Snell's law at ray-surface intersections. In this case, Snell's law means that the tangential phase component of incident and transmitted/reflected waves, or equivalently, the horizontal components slowness, must match. The resulting bulk-wave ray-tracing procedure uses the group velocity direction to define the trajectory of the ray and the magnitude of the group velocity to determine time of flight along the ray. Currently, only the rays for the three bulk modes – quasi-longitudinal (QL), fast and slow quasi-shear (QS1, QS2) – are derived. Other parameters, such as interface transmission and reflection coefficients are not computed.

This method has been integrated into UTSim to provide a visualization tool for rays in homogeneous, anisotropic components of arbitrary geometric complexity. The geometry is imported into UTSim via a CAD file (IGES or STL format). A simple example of the UTSim implementation is shown in Figure 75. In this figure, an incident ray from an immersion probe transmits into an anisotropic block. The transmitted quasi-longitudinal ray reflects and mode converts at the bottom surface into three rays – QL, QS1, and QS2. Additional transmitted and reflected rays can be selected from the GUI. As visualization aids, the displayed rays have “barbs” and “tails” to indicate the polarization and phase velocity directions associated with each mode.

This UTSim module has been used rather extensively by an OEM partner (Pratt & Whitney) in several inspection scenarios involving anisotropic components of complex geometry. The main use has been to visualize coverage for UT inspections using single element transducers. Their work has also included some experimental testing of the ray predictions. Figure 76 shows an example of their test results. The experiments involved measuring the through-transmitted beam deflection caused by tilting a coupon of single crystal alloy, as shown in the top left of the figure. The bottom left image is a screen capture from UTSim showing how this measurement was rendered in the model. The top right plot shows a comparison of the measured and predicted beam offsets as a function of the tilt angle. The agreement is good; differences are believed to be due to experimental precision in measuring the deflection. Further testing is needed.

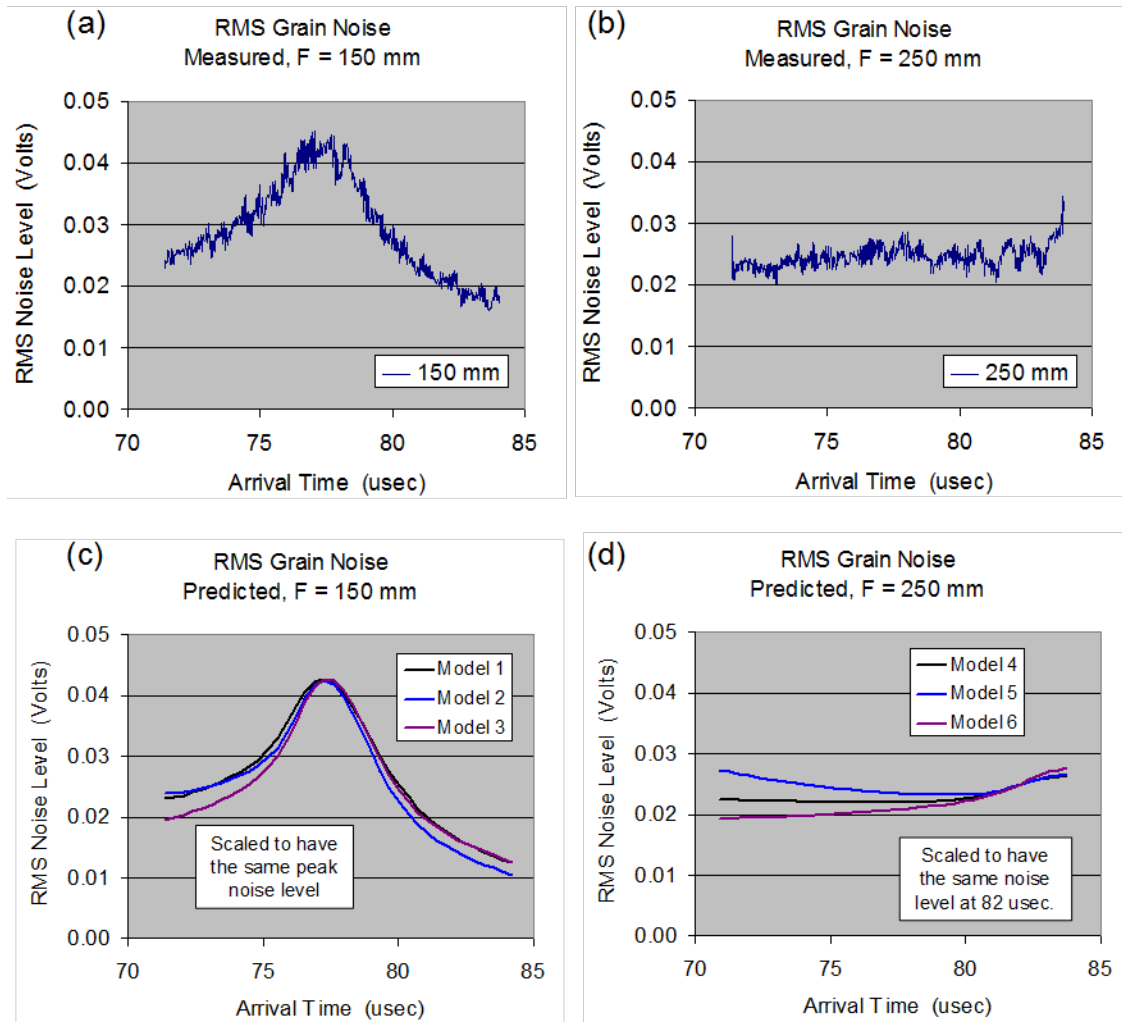


Figure 74. Comparison Of Measured (Top) And Predicted (Bottom) Rms Noise Profiles For Different Model Assumptions And For (Left & Right) Two Different Focal Laws

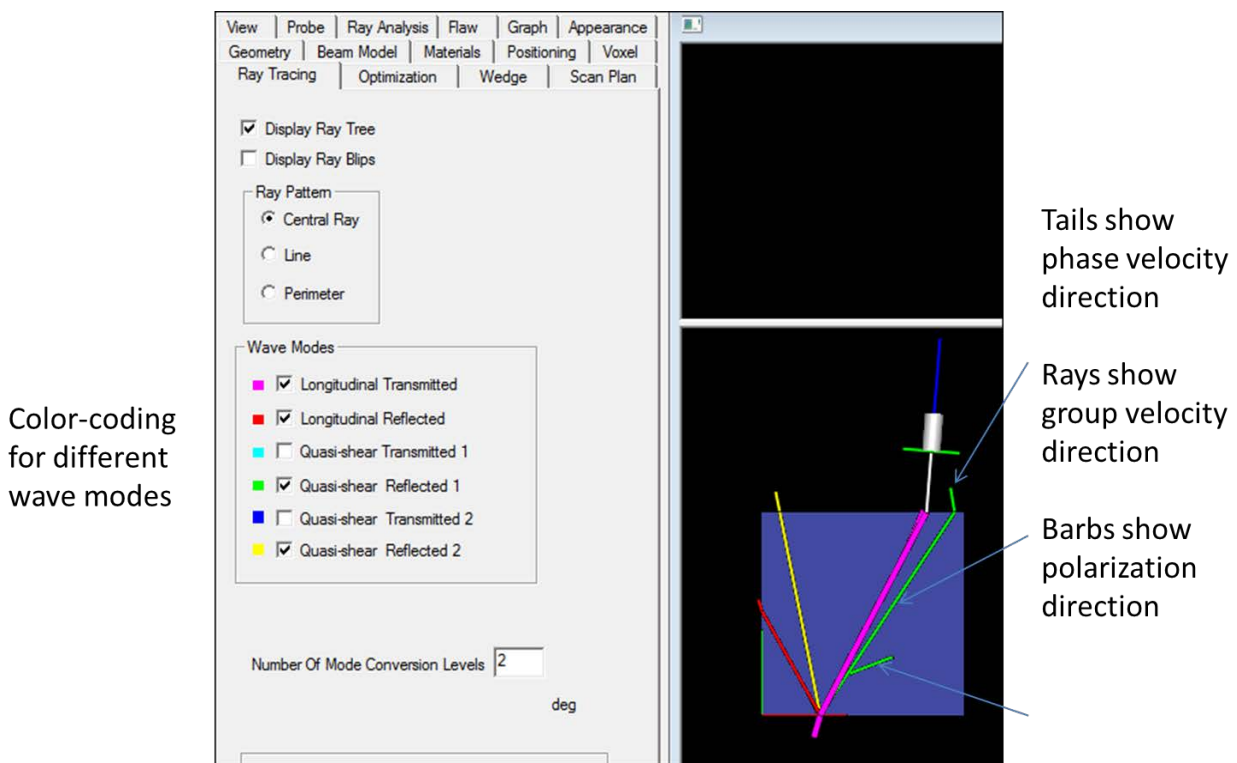


Figure 75. Example Of Anisotropic Ray Tracing Feature In Utsim

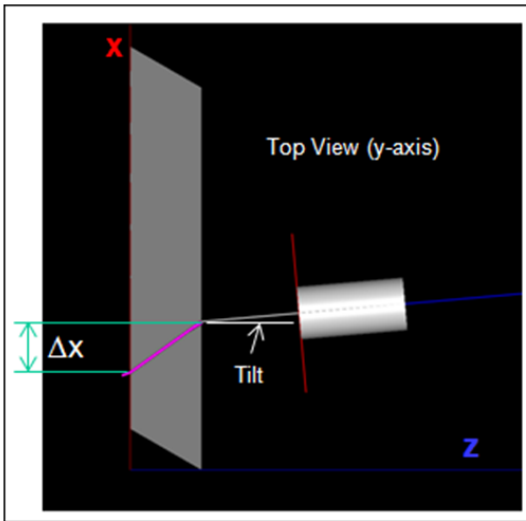
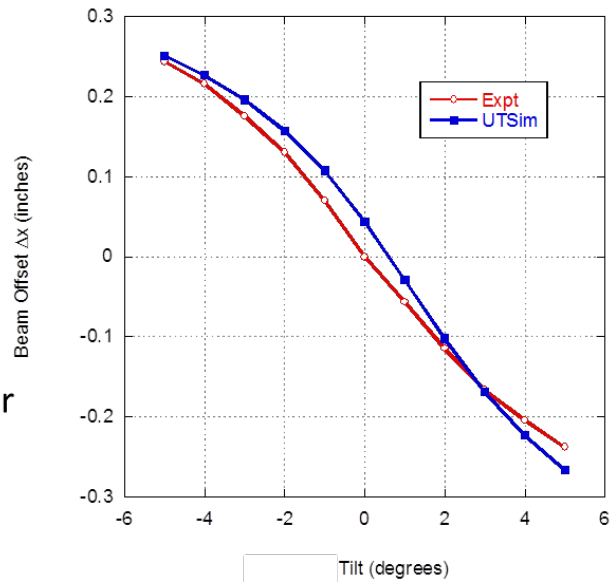
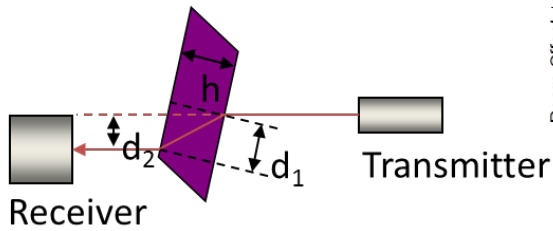
In addition to the work just described for homogeneous anisotropic media, an iterative method has been formalized for the case of an anisotropic medium for which the principal directions of the elastic stiffness matrix vary with position. Examples of this type of structure might include curved composite layups or centrifugally cast components. The method consists of breaking up the medium into thin layers within which we assume spatial homogeneity of the elastic constants. Thus, each anisotropic ray travels in a straight line within each layer, and the methods already in hand for homogeneous media can be used. As a ray crosses the boundary into the next sequential layer, it will refract slightly and travel in a straight line to the next layer, etc. An example is illustrated in Figure 77.

The top of the figure shows a conceptual description of a block of anisotropic material, which has cubic symmetry at any point in space. However, it is assumed that the elastic coefficient matrix rotates smoothly and proportional to depth below the top surface, as suggested by the slowness curves shown in the figure. I.e., at the entry surface, the elastic matrix is symmetric with the surface. As depth increases, the matrix is rotated by the angle θ shown in the figure and such that $\theta = 90^\circ$ at the bottom surface. Ray trajectories are then computed for each of the wave modes assuming the incident ray is vertical at the entry surface. The plot at the bottom of Figure 77 shows the resulting ray trajectories for the quasi-longitudinal and the two quasi-shear modes.

For the horizontally polarized quasi-shear (QSH) mode shown in green, we note that the ray trajectory in Figure 77 is a straight line. This occurs because its slowness curve in the plane is, in fact, isotropic. That is, its slowness, and hence group velocity, is independent of θ in the

vertical plane, as is evident by its circular slowness curve shown in the top of Figure 77. On the other hand, the quasi-longitudinal (QL) and vertically polarized quasi-shear (QSV) modes, shown in red and blue, respectively, have anisotropic slowness curves. Therefore, the ray trajectories for those modes are not straight. We note that all of the trajectories in Figure 77 lie within same vertical plane. This is due to the assumed simple rotation of the stiffness matrix about a single axis. In general, the ray paths need not be coplanar.

Experiment measured offset (d_2) between transmit and receive probe for a range of sample tilt angles



UTSim calculated offset (Δx) between entry and exit of QL ray for a range of probe tilt angles

$$\Delta x = d_1 = d_2 / \cos\theta + h \tan\theta$$

Figure 76. Comparison Of Beam Offsets For A Single Crystal Sample As Measured (Courtesy Pratt & Whitney) And Computed Using Anisotropic Ray-Tracing In UTsim

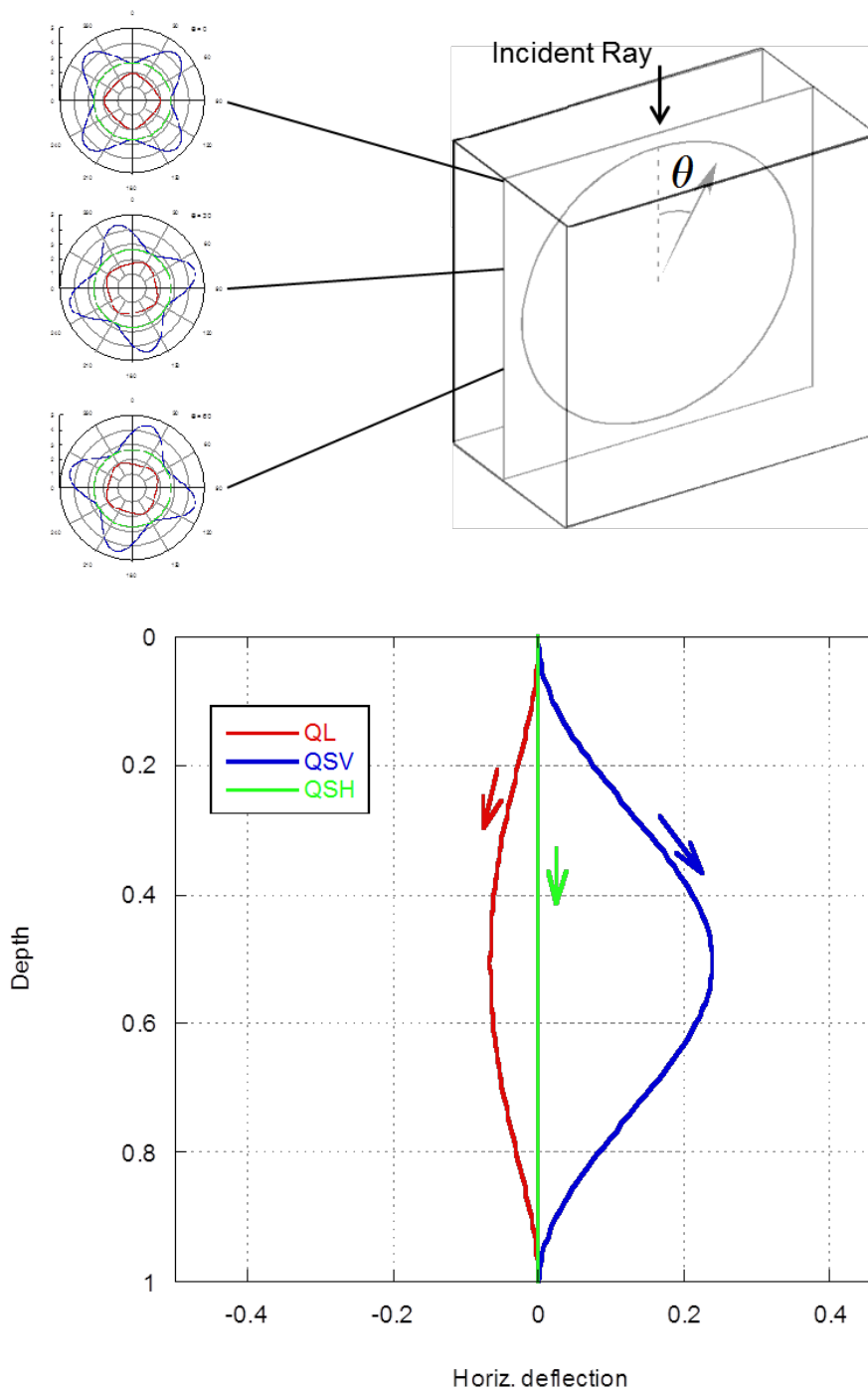


Figure 77. Schematic Of A Non-Homogeneous Anisotropic Sample (Top) And Corresponding Anisotropic Ray Trajectories (Bottom)

Conclusions

1. Analytical models for phased array transducers were implemented for linear probes made up of rectangular elements. The probe and beam model employs the multiGaussian approximation, which is a paraxial model. The Thompson-Gray measurement model is employed to integrate the MG model into a tool for predicting a measured ultrasonic response using PA probes. This approach is computationally efficient and has the flexibility to handle complex geometrical components.
2. Due to the paraxial approximation used in the MG model, there are errors in its predictions of the UT fields generated by linear PA transducers comprising rectangular elements. A semi-analytical improvement to the MG model was developed by modifying the directivity of PA probe elements to point in the steering angle and by applying an amplitude correction factor. That correction factor has been tabulated for a range of steering angles as a function of the dimensionless element width, d/l , where l is the ultrasonic wavelength in the propagating medium. This model, dubbed the Linear Phased MultiGaussian model, significantly reduces the paraxial errors while maintaining computational efficiency and flexibility of the model.
3. A new, streamlined approach to PA probe characterization was developed for obtaining the system efficiency factors for element pairs in a PA probe. The method uses the pulse-echo response measured from each element, applies corrections based upon differences in amplitude and time delay among the elements, and computes all of the inter-element system efficiency factors from the pulse-echo responses.
4. A model was developed and demonstrated for predicting grain noise for a pulse-echo PA measurement using linear arrays. The model is an extension of models for grain noise in pulse-echo and pitch-catch UT measurements from single element transducers.
5. Ray-tracing approaches for anisotropic media were developed and demonstrated for homogeneous and, in a limited fashion, for nonhomogeneous media. The homogeneous case has been integrated into UTSim and initial experimental tests performed in partnership with an OEM.

Recommendations

1. The full measurement model for PA probes needs to be fully integrated into UTSim, as well as the related PA noise model. This will permit the model-based prediction of ultrasonic signals and noise for PA measurements, which has direct application to MAPOD.
2. Extension of the PA beam models to more general probe configurations needs to be done. This includes 2-dimensional arrays of rectangular elements as well as more complex PA probe configurations, such as non-planar and non-rectangular elements. These extensions may require more advanced modeling approaches than the MG and LPMG models presented here.
3. The PA models need to be extended to anisotropic media. A multiGaussian model for single element probes for anisotropic media has been formally developed. Extension to PA probes will be straightforward.
4. Full MAPOD applications for realistic aerospace examples using PA measurements should be performed.

3.8 Effect Of Defect Morphology On Ultrasonic NDE Signals (Roberts and Lo)

Investigation Team: Ron Roberts and Chester Lo

Motivation

Ultrasonic inspection sensitivity is most often quantified as the response to a reflector having a canonical geometry such as a flat bottomed hole or EDM notch. It is well understood that the reflectivity of an actual flaw can vary substantially from that of a canonical reflector of comparable size, due in large part to variation in flaw morphology. Furthermore, it is understood that it is important to account for flaw morphology when assessing probability of detection (POD). The present work was motivated by recognition of the need for a systematic study of the influence of flaw morphology on inspection sensitivity. To this end, a computational study was performed which examines the influence of flaw morphology on the ultrasonic response from cracks, where morphological variation is in the form of crack face roughness. A planar crack face is distorted by imposing a random crack profile, parameterized by profile height and correlation length. By generating ensembles of crack realizations for fixed profile height and correlation length, mean and variance of signal amplitude are compiled as a function of these crack roughness parameters.

Results – Theory and Experiments

3.8.1 Problem Formulation

The crack scattering problem is formulated under an assumption of a linearly elastic, homogeneous, isotropic host medium, for which wave propagation and scattering is governed by corresponding elastodynamic field equations [96]. The computational study simultaneously examined two mathematical model formulations of the scattering problem. An “exact” problem formulation was employed which computes the solution to the governing field equations to within a specified error tolerance. Specifically, exact solutions to the field equations are formulated using boundary integral Green functions methods, and solutions numerically computed using the Boundary Element Method (BEM). Along with the exact computation, the solution to a widely-employed approximate problem formulation was computed, to examine the limits of applicability of the approximate formulation. Specifically, the approximate model formulation prescribes wave motions on the crack surface locally using non-diffracting ray theory, an approach referred to as the Kirchhoff approximation. Kirchhoff scattering theory is often employed when computing scattering from large, complex geometry flaws, due to its simplicity and computational efficiency. Use of the Kirchhoff approximation inherently carries with it the question of its validity. A goal of the present work was to rigorously compare the accuracy of Kirchhoff predictions to exact BEM predictions over a range of flaw sizes and morphologies. To facilitate this comparison, it was noted that the phenomena which determine Kirchhoff limits of validity function equivalently in 3D and 2D scattering problems (a 2D scattering problem can be viewed as a 3D problem with no dependence on one dimension). Restricting consideration to 2D scattering enables practical application of the BEM to much larger crack dimensions, correspondingly expanding the establishment of Kirchhoff limits of validity. Results were obtained which compare 2D Kirchhoff and BEM predictions of pulse-

echo crack response amplitude mean and variance as functions of random crack profile height and correlation length, crack length, angle of incidence, wave mode type, and signal frequency bandwidth.

3.8.2 Computational Model Formulation

Model predictions of pulse-echo signals in this work are based on evaluation of Auld's reciprocity theorem for scattering by a crack, expressed

$$v(\omega) = E(\omega) \int_{\text{crack}} u_i^{\text{tot}}(x, \omega) \tau_{ij}^{\text{inc}}(x, \omega) n_j(x) dx \quad (1)$$

where $v(\omega)$ is response voltage as a function of frequency ω , $E(\omega)$ is the pulse-echo system frequency response of the measurement (including transducer and electronics), $u_i^{\text{tot}}(x, \omega)$ is the total motion on the crack face as a function of position x , and $\tau_{ij}^{\text{inc}}(x, \omega) n_j(x)$ is the traction (contraction of stress and surface normal) on the crack face associated with the incident wave field (field in the absence of the crack) [97]. The numerical study assumes plane wave incidence of either longitudinal (L) or vertically polarized transverse (T) motion, and a system response function $E(\omega)$ in the form of a Hanning window having bandwidth characterized by the ratio of 6 dB bandwidth to center frequency. Time domain signals are obtained by Fourier transformation of Equation (1) in frequency ω . The heart of the scattering calculation is the determination of the surface displacements u_i^{tot} for a given incident field. An approximation of the surface displacement is obtained through application of non-diffracting ray theory, leading to the Kirchhoff evaluation of Equation (1) [98]. An integral equation exactly determining the motion of the crack surface is obtained through application of elastodynamic reciprocity with the associated Green function [99]. The solution to the integral equation is projected onto a basis set defined over the crack surface (boundary elements), thereby transforming the problem to a matrix equation, which is inverted numerically to obtain an exact (to within numerical convergence) expression of the crack face motion, for use in Equation (1).

In the present work, the basis was specified as a mesh of constant elements, with 10 elements per transverse center frequency wavelength. An ensemble of crack profiles is generated by filtering sequences of pseudo-random numbers with a Hanning window. By definition of the original random sequence, the mean of the profile autocorrelation over the ensemble approaches the autocorrelation of the window function. The *correlation length* of the profile is therefore designated as the half-amplitude half-width of the filter window autocorrelation, denoted γ . Realizations of crack profiles having unit maximum peak-to-valley roughness height are shown in Figure 78 for $\gamma=0.13$ and $\gamma=0.25$. It is seen that shorter correlation length results in sharper crack features, whereas the crack transitions into a “wavy” profile at long correlation lengths. Ensembles with up to 1000 entries were compiled for a range of correlation length, γ , and profile height, h . Pulse-echo frequency spectra were computed for each ensemble entry, as a function of angle of incidence, wave mode type, and crack length, L . Time domain responses were evaluated through Fourier transformation for each ensemble entry, over a range of frequency bandwidths. The mean and variance of the peak time signal amplitudes were then compiled by summing over the ensemble.

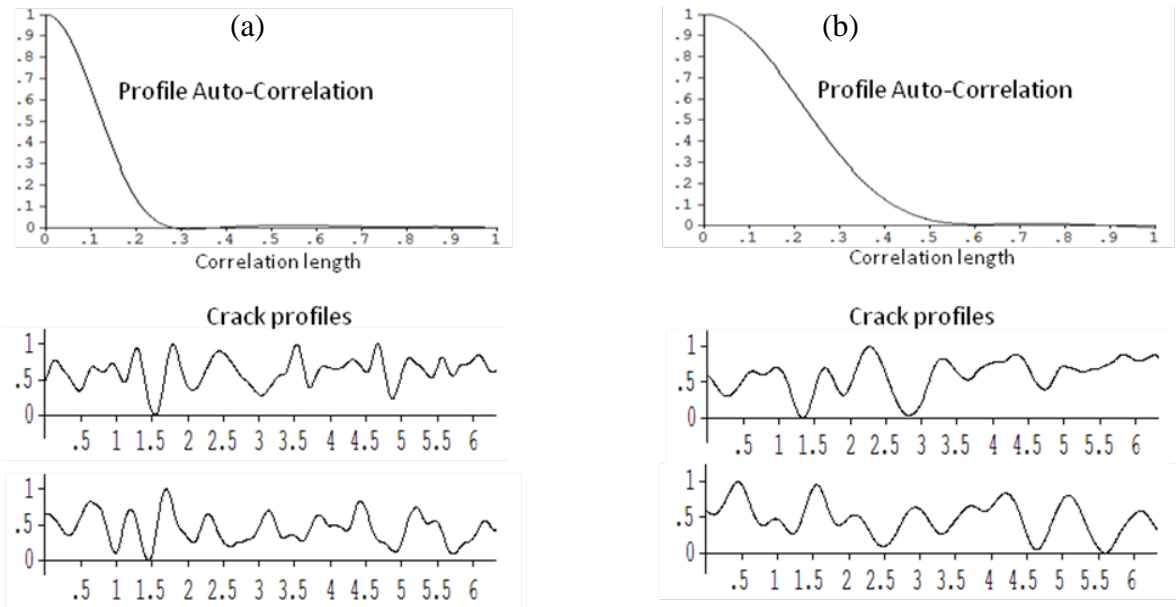


Figure 78. Statistical Descriptors Of Roughness Are Maximum Peak-To-Valley Height And Correlation Length. Profile Autocorrelation Function And Two Representative Profile Realizations For: A) $\gamma=0.13$, B) $\gamma=0.25$

3.8.3 Numerical Results

Numerical results are presented showing the dependence of pulse-echo signal amplitude on crack profile roughness height and correlation length, for a crack contained in aluminum ($c_L=6320$ m/s, $c_T=3080$ m/s) under plane wave incidence. Results are first shown for the case of perpendicular incidence on a crack with length $L=6.32 \lambda_L$ (longitudinal wave length at center frequency), corresponding to a 4 mm crack at 10 MHz. In all that follows here, all lengths are specified in units of λ_L . The mean and standard deviation (square root of variance) of signal amplitude are plotted, for both exact (BEM) and approximate (Kirchhoff) calculations. These results, and all that follow, are normalized by the response at perpendicular incidence on a smooth crack of corresponding length. Figure 79 plots the mean and standard deviation of peak signal amplitude for 100% bandwidth L-wave incidence as a function of roughness height, for roughness correlation lengths of $\gamma=0.13$ and $\gamma=0.25$. The statistics were compiled using 100 entry ensembles. For the longer correlation length of Figure 79a, the Kirchhoff and BEM results are nearly indistinguishable in both mean and standard deviation, until they start to diverge above profile height $h=0.9$. A modestly greater disagreement is seen for the shorter correlation length of Figure 79b, corresponding a greater crack roughness. The corresponding result for T-wave incidence is shown in Figure 80. Compared to L-wave incidence in Figure 79, it is seen that the mean amplitude decreases more rapidly with increasing roughness. In Figure 79a, the mean amplitude is half the smooth crack amplitude at a profile roughness of $h=0.35$, whereas in Figure 80a the mean amplitude is half the smooth crack amplitude at a profile roughness of $h=0.16$. It is noted, however, that the transverse wavelength is approximately half the longitudinal wavelength, hence it is seen that in both cases the half-amplitude mean value occurs at a height

of approximately 0.35 incident wavelength. It is seen that the exact BEM and approximate Kirchhoff predictions agree closely for profile roughness height up to $h=0.25$, beyond which the predictions diverge. As with L-wave incidence, results for the shorter roughness correlation length in Figure 80b diverge somewhat more quickly.

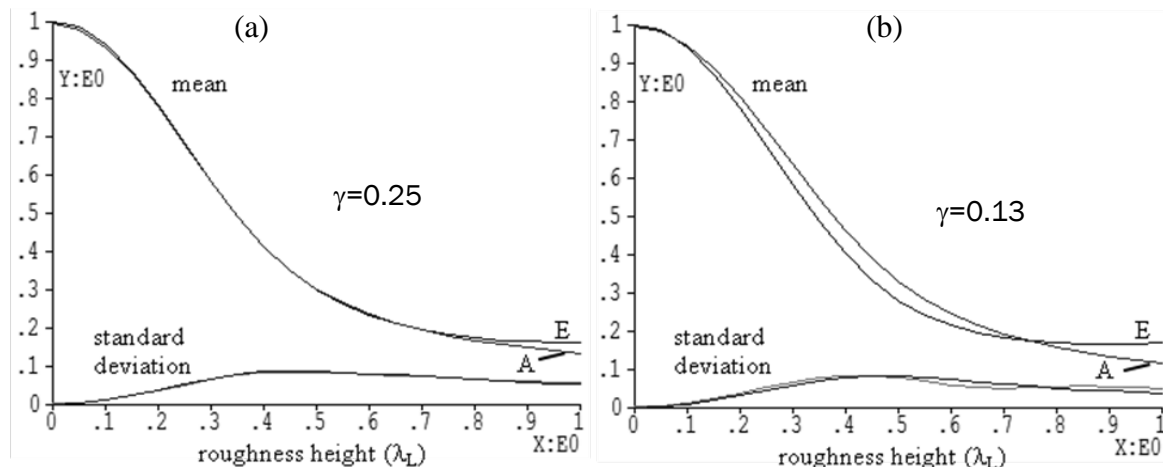


Figure 79. Mean And Standard Deviation Of Pulse-Echo Signal Amplitude: Comparison Of 100% Bandwidth Broadband Exact (E) BEM And Approximate (A) Kirchhoff Predictions For Perpendicular L-Wave Incidence. Crack Length $L=6.32$, Roughness Correlation Length A) $\gamma=0.25$, B) $\gamma=0.13$

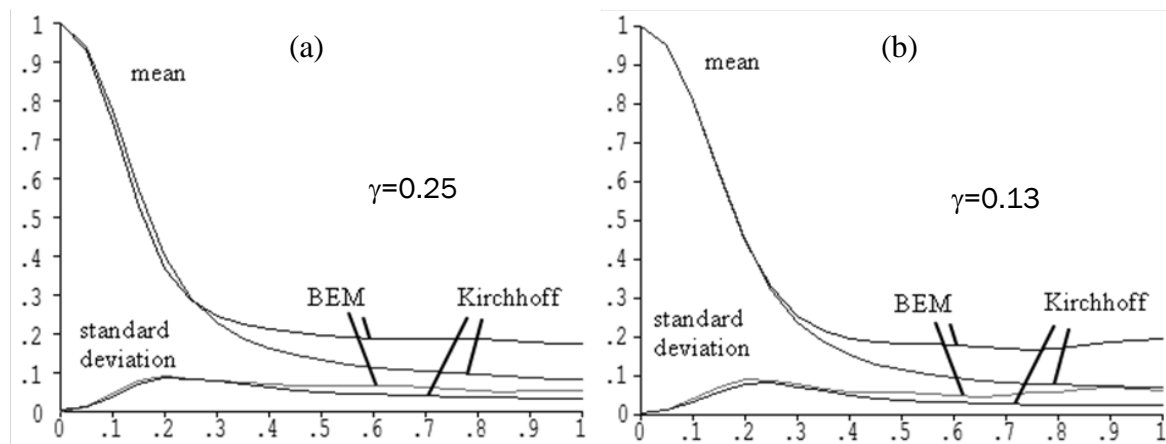


Figure 80. Mean And Standard Deviation Of Pulse-Echo Signal Amplitude: Comparison Of 100% Bandwidth Broadband Exact (E) BEM And Approximate (A) Kirchhoff Predictions For Perpendicular T-Wave Incidence. Crack Length $L=6.32$, Roughness Correlation Length A) $\gamma=0.25$, B) $\gamma=0.13$

Since it is generally easier to compute single frequency responses, it is of interest to compare broadband and single frequency predictions to assess the viability of a single frequency approximation to a broadband response. Figure 81 compares 100% bandwidth broadband and single frequency (at the broadband center frequency) predictions for perpendicular L-wave

incidence, crack length $L=6.32$, and roughness correlation length $\gamma=0.25$. It is seen in this configuration that the single frequency result provides a reasonable approximation to the broadband result. In contrast, Figure 82 compares 100% bandwidth broadband and single frequency L-wave incidence predictions as a function of incidence angle, for a crack of length $L=6.32$ having both a smooth and rough profile with $h=0.35$ and $\gamma=0.25$. The single frequency result for the smooth crack displays pronounced minima over the 90 degree angular range, associated with interference between crack tip diffracted signals. In contrast, the broadband response displays a monotonically decreasing angular dependence. It is significant to notice that the BEM prediction approaches -30 dB at 90 degrees, whereas the Kirchhoff prediction decreases to zero amplitude at 90 degrees.

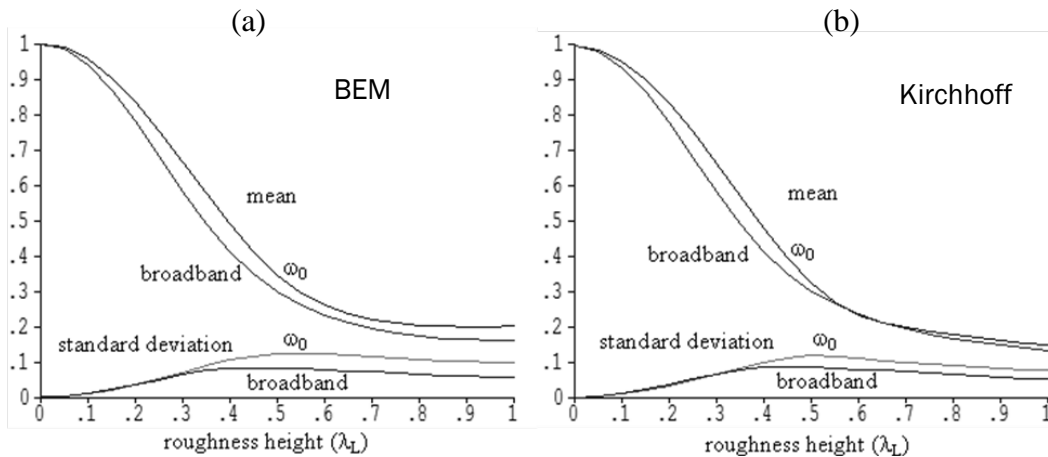


Figure 81. Mean And Standard Deviation Of Pulse-Echo Signal Amplitude: Comparison Of Single Frequency (ω_0) And 100% Bandwidth (Broadband) Predictions For Perpendicular L-Wave Incidence. Crack Length $L=6.32$, Correlation Length $\gamma=0.25$, For A) BEM Computation And B) Kirchhoff Computation

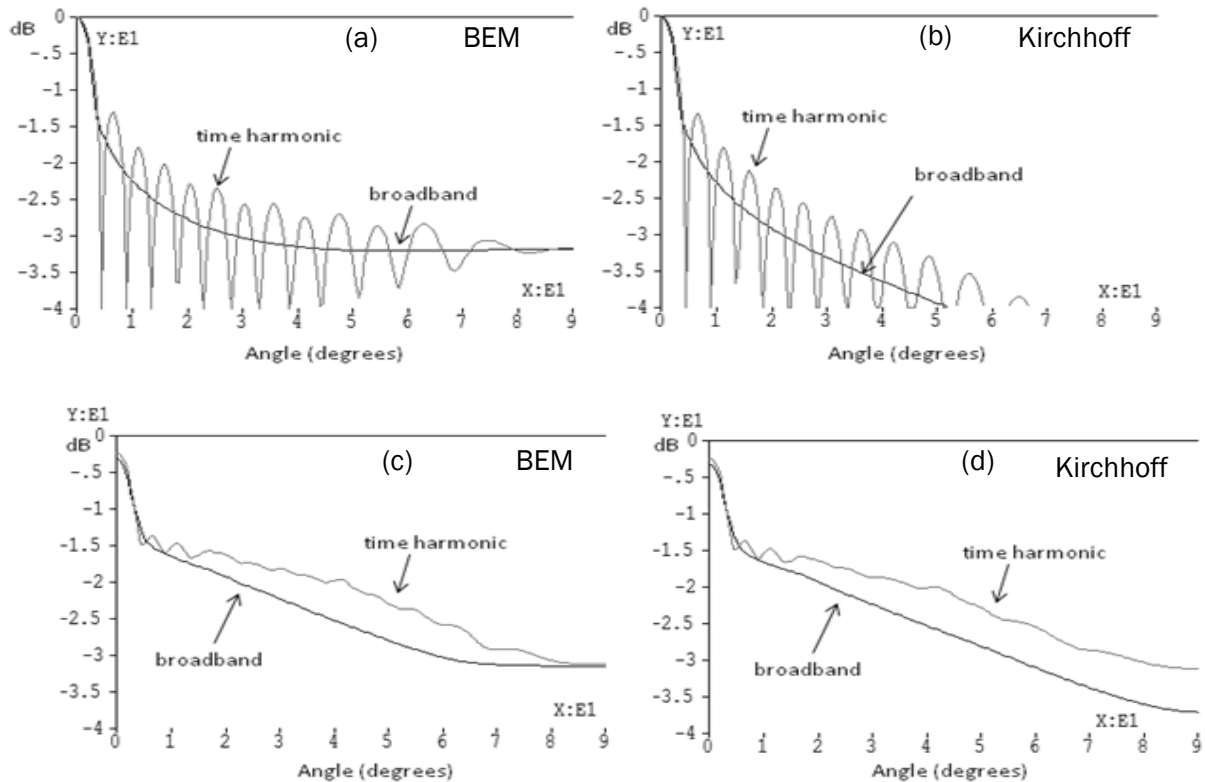


Figure 82. Comparison Of Single Frequency (Time Harmonic) And Broadband Mean Amplitude Predictions For Crack Length $L=6.32$. A) Smooth Crack BEM, B) Smooth Crack Kirchhoff, C) Rough Crack BEM D) Rough Crack Kirchhoff. Roughness Correlation Length $\gamma=0.25$, Roughness Height $H=0.25$

The structure seen in Figures 82a, b is readily explained by examining associated time domain responses, plotted in Figure 83 for 24 degree incidence. The BEM calculation of Figure 83a reveals numerous component signals, the interference of which gives rise to the single frequency structure seen in Figure 82a. Two dominant signals are noted, arising from diffraction at the near and far crack tips. Other smaller signals are noted, corresponding to diffraction into two Rayleigh surface waves types. Significantly, it is noted that the Kirchhoff prediction of Figure 83b displays only edge diffracted signals, with amplitudes having compromised accuracy. Note that the far tip diffracted signal is about 1dB less than the near tip signal in the BEM computation, whereas the Kirchhoff theory predicts tip signals of comparable amplitude. This observation explains why the spectral peaks in Figure 82a, b exceed the broadband predictions by 5db and 6db for the BEM and Kirchhoff results, respectively. Attention is turned to the effect of roughness in Figure 82c, d, which compare 100% bandwidth and single frequency L-wave pulse-echo angular responses from a rough crack having correlation length $\gamma=0.25$, roughness height = 0.25, and crack length $L=6.32$, for both BEM and Kirchhoff computations. The structure arising from component signal interference is seen to be much less pronounced in the single frequency result than that noted in Figure 82a, b. It is still seen, however, that the time harmonic result exceeds the broadband prediction by up to 6dB. As with the flat crack, this is

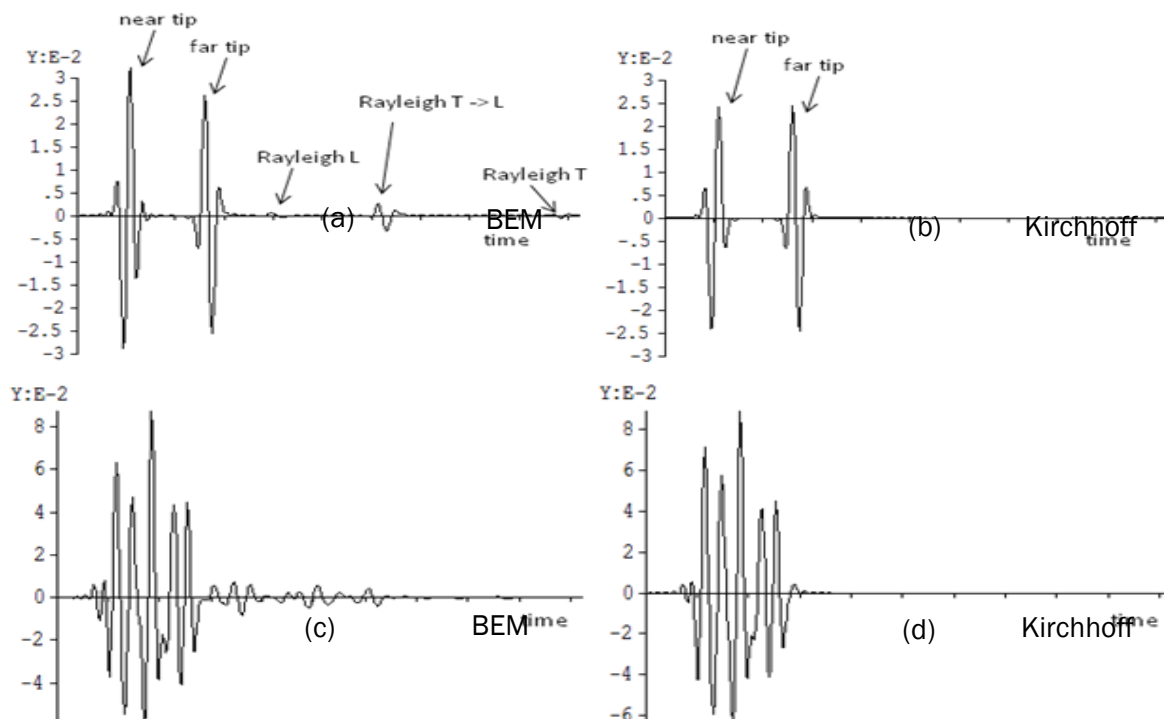


Figure 83. Time Domain Signals Contributing To Figure 82. 100% Bandwidth Broadband L-Wave Pulse-Echo Signals At 24 Degree Incidence: A) Flat Crack BEM Prediction B) Flat Crack Kirchhoff Prediction C) Rough Crack BEM Prediction D) Rough Crack Kirchhoff Prediction. $L=6.32$, $\gamma=0.25$, $H=0.25$

attributed to constructive interference between multiple signal components. BEM and Kirchhoff time domain signals are plotted in Figure 83c, d for a selected ensemble member at 24 degree incidence in the compilation of the statistics of Figure 82c, d. Comparing Figure 83c, d to Figure 83a, b, it is evident that numerous randomly arriving signal components are received between the arrival of the near and far tip diffracted signals, and that these signals exceed the tip diffracted signals by ~ 8 dB. It is to be expected that the mean spectra of these randomly arriving signals would not display coherent spectral minima.

Mean signal amplitudes for broadband L-wave incidence are plotted as a function of incidence angle in Figure 84 for $h=0.25$, $h=0.5$, and $\gamma=0.25$, $\gamma=0.13$. Kirchhoff and BEM predictions are compared. It is seen that increasing roughness reduces the angular directivity of pulse-echo scattering. It was previously observed in Figure 82a, b that the Kirchhoff approximation under-predicts the signal at off-perpendicular incidence for the smooth crack, with under-prediction most pronounced near grazing. Figure 84 shows how the validity of the Kirchhoff approximation improves at off-perpendicular incidence with increasing roughness, until a point is reached at which the Kirchhoff result begins over-predicting the mean signal. This transition with increasing profile height is seen to occur more rapidly for the shorter roughness correlation length. Corresponding results for T-wave incidence are presented in Figure 85. Figure 85a compares BEM and Kirchhoff 100% bandwidth pulse-echo T-wave peak amplitude responses as

a function of angle, for a flat crack of length $L=6.32$. A greater angular directivity than that for L-wave incidence in Figure 82 is seen, arising from the shorter wavelength. Similar under-

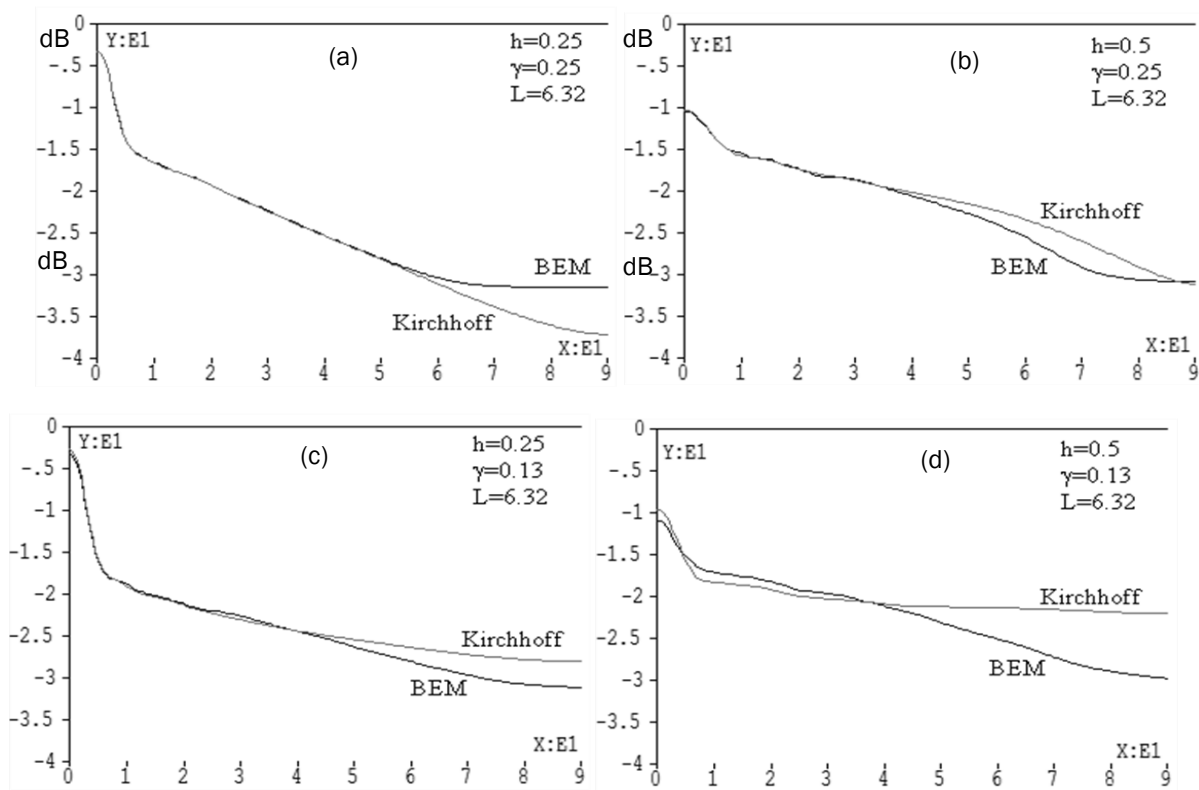


Figure 84. Comparison Of BEM And Kirchhoff Broadband Pulse-Echo L-Wave Mean Amplitude Predictions: $L=6.32$. A) $\gamma=0.25$, $H=0.25$, B) $\gamma=0.25$, $H=0.5$, C) $\gamma=0.13$, $H=0.25$ D) $\gamma=0.13$, $H=0.5$

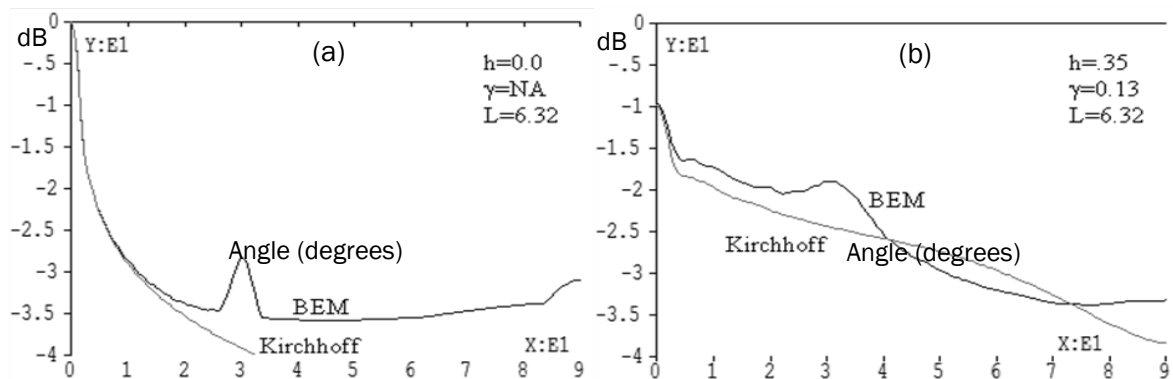


Figure 85. Comparison Of BEM And Kirchhoff Broadband Pulse-Echo T-Wave Mean Amplitude Predictions: $L=6.32$. A) $H=0.0$, B) $\gamma=0.13$, $H=0.35$

prediction of the Kirchhoff result at off-perpendicular incidence is also observed. A notable phenomenon is the peak in the BEM response prediction at 30 degree incidence, arising from the far crack edge reflection of the leaking surface wave which is generated near the L-wave critical angle. This reflection results in a pronounced amplitude enhancement of the far-edge tip diffracted signal, corresponding to the second dominant signal in Figure 83a. The Kirchhoff approximation by design does not include this phenomenon. The introduction of roughness having profile height $h=0.35$ and correlation length $\gamma=.13$ results in Figure 85b. A lessening of angular directivity is noted, as is an improvement in agreement between the BEM and Kirchhoff predictions. Note that the enhancement of the far-tip diffracted signal is still observed, although to a lesser extent than the flat crack.

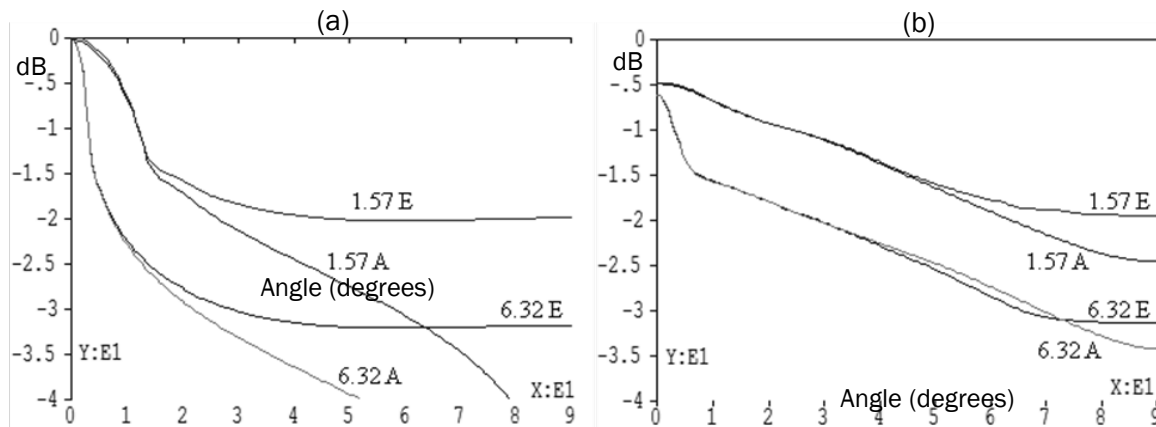


Figure 86. Comparison Of Broadband L-Wave BEM (E) And Kirchhoff (A) Mean Amplitude Predictions As A Function Of Angle For Crack Lengths $L=6.32$ And $L=1.57$. A) $H=0.0$, B) $\gamma=0.25$, $H=0.35$

Differences in angular scattering arising from varying crack length are examined in Figure 86. Kirchhoff and BEM L-wave incidence pulse-echo responses are plotted for two crack lengths, $L=6.32$, and $L=1.57$, and for two roughness heights, $h=0.0$ and $h=0.35$ with $\gamma=0.25$. As expected, a lesser degree of angular directivity in scattering is seen for the shorter crack. As observed in preceding results, the introduction of roughness further decreases the angular directivity, and brings the Kirchhoff and BEM predictions into closer agreement.

Conclusions and Recommendations

Results of this study show that moderate degrees of plate curvature and taper have a minimal effect on the transmission efficiency of plate waves. Examination of dispersion characteristics in circular cylindrical shells revealed that the plate curvature has a negligible effect for curvatures appreciably larger than the plate thickness. It was observed that displacement depth profiles vary curvature, indicating that mode coupling will occur when transitions in radius are encountered. However, an examination of transmission at abrupt curvature transitions revealed a negligible degree mode conversion for 3/16 inch plate radii as small as 2 inches. Finally, an examination of guided mode transmission in tapered plates displaying gradual transitions in plate thickness

revealed only a modest degree of mode conversion. Smooth transitions were examined for which the length over which the transition occurs was as small as twice the plate thickness. Energy loss through mode conversion was observed to be less than 10 percent for transitions in thickness of 60 percent and 150 percent. A 400 percent change in plate thickness resulted in an energy loss of 25 percent. These behaviors were consistently observed when examining plate structures containing both curvature and taper. A structure containing a two inch radius double curvature with two 100 percent transitions in thickness displayed transmission characteristics showing little mode conversion loss for both A0 and S0 wave incidence.

The range of plate curvatures and taper examined in this study represent the range over which, if such features were to present issues requiring consideration in inspection deployment, such issue would have been apparent. The observation that the curvature and taper examined in this study has little effect on guided wave transmission efficiency indicates that neglecting these effects for features represented by this study may in practice be justified.

3.9 Fundamental Studies Of Guided Wave Propagation For Structural Health Monitoring (Roberts)

Investigation Team: Ron Roberts

Motivation

Ultrasonic measurements for nondestructive evaluation (NDE) and structural health monitoring (SHM) of airframe structures often involve the transport of ultrasonic signals as guided wave modes in plate structures. Efforts in development of guided wave measurements for NDE and SHM applications are by-and-large carried out using uniformly thick planar plate test structures, in which guided wave propagation occurs in the form of truly independent modes of motion, i.e., motion that propagates through the plate without energy loss or conversion into other possible modes of propagation. Actual airframe structures consist of non-planar plate geometries displaying non-uniform thickness. It is prudent therefore to ask what influence these non-ideal geometric attributes have on the transmission of guided wave signals. The objective of this project is to quantify using computational modeling what influence curvature and thickness taper has on guided wave signal propagation. Tasks in this project are organized in increasing complexity. Initial activity examined the propagation characteristics of circular cylindrical shells, the simplest of non-planar shell geometries. Work next examined guided wave transmission between joined circular shell sections, which forms the basis of an effective approach to model propagation in generally curved uniformly thick plates. Lastly, work studied the introduction of taper in plate thickness. Interest in this study is in plate curvature having curvature radii much larger than the thickness of the plate. Similarly, interest is in gradual tapers of plate thickness, occurring over lengths substantially greater than the thickness of the plate. Generally speaking, it was observed in this study that variation in plate curvature and thickness of this type has minimal influence on the transmission of guided wave energy.

Results – Theory and Experiment

3.9.1 Model Formulation

The guided wave propagation problem is formulated assuming a linearly elastic, homogeneous, isotropic solid medium, for which wave propagation and scattering is governed by corresponding elastodynamic field equations. The guided waves of interest in this study arise from multiple reflections between traction free boundaries of a plate like structure. In the case of a flat uniformly thick plate, a rigorous mathematical analysis is straightforward, revealing the existence of independent modes of propagation which traverse the structure freely, without loss of energy or conversion into alternate modes of propagation [101]. Modes of motion in the planar plate are characterized by either symmetry or asymmetry about the plate mid-plane. Propagating modes are correspondingly denoted A0, S0, A1, S1, etc., where A and S denote asymmetric and symmetric motions, respectively, and the numerical designation indicates order of emergence from evanescent to propagating with increasing temporal frequency. Similarly, the case of a circular cylindrical shell of uniform thickness can be modeled by a straightforward analysis [102]. As with the flat plate, guided wave propagation is revealed to consist of freely propagating modes of motion, which correspond precisely to those in the flat plate as the cylinder radius becomes large. Initial work examined these established problem solutions to

examine the dependence of guided mode propagation characteristics (motion profiles, velocity dispersion) as a function of plate curvature. Details of the analysis employed in the flat plate and circular shell will not be elaborated upon here, as they are widely available in common texts on guided waves.

To examine more general plate geometries, methods of analysis based on a boundary integral formulation were applied. In this method of analysis, solutions to governing field equations are sought through application of the divergence theorem to the body under study, expressing a reciprocal relation between two possible field solutions. Taking one these solutions to be the response of a canonical body of like material properties (e.g., an unbounded medium) to an applied point load, referred to as the Green function response, a boundary integral equation for the second wave field is obtained, which is by construction is the solution to the problem geometry of interest [103]. In the problem at hand, the boundary integral equation is expressed as

$$\int_B (u_i(x) \tau_{ijk}^G(x|x') - u_{i;k}^G(x|x') \tau_{ij}(x)) n_j(x) dx + \frac{1}{2} u_k(x') = 0 \quad , x' \in B \quad (1)$$

where $u_i(x)$ and $\tau_{ij}(x)$ are displacements and stresses at the boundary, B , of the body of interest, with tensor components $i=1,2,3$, and with outward normal vector n_j . $u_i^G(x|x')$ and $\tau_{ij}^G(x|x')$ are displacements and tractions of the associated canonical Green function problem, arising in response to a point load positioned at x' . It is assumed in writing Equation (1) that the boundary, B , of the plate structure has a continuously varying normal vector at x' , and that the integral is interpreted in the principal value sense at x' . Time harmonic motion is assumed in deriving Equation (1), and the dependence of all field quantities on frequency, ω , is implicitly assumed. Wave motions are restricted in this study to two Cartesian dimensions, implying that all plate geometries and wave fields display no dependence upon the x_3 direction.

The integral equation formulation expressed in Equation (1) is solved numerically using the boundary element method (BEM). In this approach, the field quantities to be solved for are represented by weighted sums of appropriate functions (e.g., piecewise polynomials) prescribed over the boundary of the body (boundary elements). Use of these field representations in Equation (1) results in a matrix equation for the weighting coefficients (boundary element matrix), where the matrix coefficients are evaluated through numerical integration. A well-conditioned matrix is obtained by evaluating Equation (1) at points x' judiciously positioned over the boundary surface. The accuracy of the BEM computation is monitored by examining the balance between incident and transmitted/reflected energy. The fineness with which boundary surfaces are divided into boundary elements is established by summing total energy carried by all transmitted and reflected propagating modes. Element refinement is prescribed to assure that the sum of reflected and transmitted energies equals the energy carried by the incident wave to within one percent.

The problem considered at the next level of complexity beyond the circular cylindrical shell is the transmission of a guided wave at the junction between two cylindrical shells having different radii. To address this problem, the Green function employed in Equation (1) is the response to a point load acting in a circular cylindrical shell. To facilitate the examination of guided wave

transmission, the Green function is derived in non-periodic form following the methods of Felsen [104]. Using this formulation, a Green function is derived which satisfies traction free boundary conditions over an angular section of shell under consideration, and transitions naturally to the corresponding Green function for an infinite plate when the shell radius becomes large. The satisfaction of traction free boundary conditions by the Green function on the shell surfaces serves to reduce the support of the integral equation to the surfaces joining the shell sections. An example of application is depicted in Figure 91, which considers transmission between three shell sections: two flat semi-infinite plates (infinite radius), and a 90 degree section of circular shell of corresponding thickness. An incident guided wave, $u_i^{inc}(x)$, propagates towards the curved section in the left semi-infinite plate, and transmitted and reflected guided mode amplitudes are sought in the bottom and left plate sections, respectively. Three coupled integral equations are obtained by applying Equation (1) to each shell section in Figure 91. The radiation condition at infinity is applied to reflected and transmitted fields in the semi-infinite plates. Additionally, Equation (1) is applied to the incident field in the semi-infinite plate sections which complements the left plate section in Figure 91, along with the radiation condition at infinity. The Green function for an infinite flat plate is used in the boundary integral equations for the semi-infinite plates. The Green function for the circular cylindrical shell is used in the boundary integral equation for the circular shell section. The inherent satisfaction of the traction free boundary conditions on the shell surfaces leads to a system of three equations, involving integrations over the edges, E_1 and E_2 , of the shell sections at which the sections are joined.

$$\begin{aligned} \int_{E_1} (u_i(x) \tau_{ijk}^{GP}(x|x') - u_{i:k}^{GP}(x|x') \tau_{ij}(x)) n_j^A(x) dx + \frac{1}{2} u_k(x') &= u_k^{inc}(x') \quad , x' \in E_1 \\ \int_{E_1+E_2} (u_i(x) \tau_{ijk}^{GC}(x|x') - u_{i:k}^{GC}(x|x') \tau_{ij}(x)) n_j^B(x) dx + \frac{1}{2} u_k(x') &= 0 \quad , x' \in E_1 + E_2 \\ \int_{E_2} (u_i(x) \tau_{ijk}^{GP}(x|x') - u_{i:k}^{GP}(x|x') \tau_{ij}(x)) n_j^C(x) dx + \frac{1}{2} u_k(x') &= 0 \quad , x' \in E_2 \end{aligned} \quad (2)$$

where $\tau_{ij}^{GP}(x|x')$ is the Green function stress response to a point load acting in a planar infinite plate, $\tau_{ij}^{GC}(x|x')$ is the Green function stress response to a point load acting in a circular cylindrical shell, and n_j^A , n_j^B , and n_j^C are the outward normal vectors for the three constituent bodies. Application of the boundary element method leads to a matrix equation for the evaluation of the displacements $u_i(x)$ and tractions $\tau_{ij}(x) n_j$ on the plate edges E_1 and E_2 . Following computation of the wave fields on the plate edges, transmitted and reflected field amplitudes are obtained by application of Equation (1) to the bottom and left semi-infinite plates, respectively, with the point source position x' placed at a large distance from the plate edge. In this configuration, the Green function response $u_i^{GP}(x|x')$, $\tau_{ij}^{GP}(x|x')$ can be evaluated asymptotically for large $|x-x'|$, and is found to be dominated by a sum of terms $u_i^{GPm}(x|x')$, $\tau_{ij}^{GPm}(x|x')$, representing the individual propagating guided modes. The amplitude of a specific transmitted or reflected mode, m , is obtained by integrating the corresponding term of the Green function far-field expression over the plate edge, where $u_k^m(x')$ is the displacement associated

$$u_k^m(x') = \int_{E_n} (u_i(x) \tau_{ijk}^{GPm}(x|x') - u_{i:k}^{GPm}(x|x') \tau_{ij}(x)) n_j(x) dx \quad , x' \rightarrow \infty \quad (3)$$

with mode type, $m=A0, S0$, etc. Reflected modes are obtained by integrating over edge E_1 with x' positioned at large distance in the left semi-infinite plate section, whereas transmitted modes

involve integration over edge E_2 with x' positioned at large distance in the bottom semi-infinite plate section.

Guided mode propagation in generally curved plates of uniform thickness can be modeled by segmenting the shell into a concatenation of circular shell sections, and applying the methods described by eqs. (2, 3). A generally curved shell can be represented to any desired degree of accuracy by refining the discrete representation through reduction of the extent of the constituent circular shell sections. Indeed, this type of representation is commonly employed to model structures in CAD software. A representation employing N sections will result in a system of N coupled integral equations for the determination of displacements on the joining plate edges, as demonstrated in Equation (2) for $N=3$. Transmission and reflection coefficients for the generally curved structure are determined using Equation (3) in the same fashion as described for Figure 91.

Guided mode propagation in plates displaying tapered thickness is modeled by applying Equation (1) using the Green function response for an unbounded space. This formulation is applicable to any geometry without restriction, and is the basis of previous work examining guided plate wave transmission at anomalous features such as joints, corners, and attachments [105, 106, 107].

Application to a generally curved plate section with tapered thickness proceeds as described in the preceding discussion of generally curved plates of uniform thickness. The structure is segmented into multiple sections, and Equation (1) is applied to each section. It is desirable to configure the structure so that transmitted and reflected energy propagates to infinity without return, enabling imposition of the radiation condition in the problem formulation. This is most straightforwardly accomplished by terminating the structure in planar semi-infinite plates, as depicted in Figures 91, 94, and 97. For two dimensional structures as studied here, this can be done without loss of generality for any structure of interest. The computational cost of using the Green function for an unbounded medium in Equation (1) arises in the determination of the wave motions on the traction free surfaces of the structure. In the case of the uniformly thick generally curved structure, use of the Green function response of a circular shell section reduced the support of integration to only the joining plate edges, due to the satisfaction of the traction free boundary condition on the shell surfaces by the Green function. This condition significantly reduces the size of the resulting BEM matrix. Since the Green function for the unbounded medium does not satisfy the traction free boundary condition, the displacements must be explicitly determined everywhere on the surface of the shell section, resulting in a substantially larger BEM matrix.

Application of Equation (1) to the tapered plate structure depicted in Figure 94 will be considered as an illustration. The structure consists of three sections: a tapered transition in thickness connecting two semi-infinite plates of different thicknesses. Application of Equation (1) to the semi-infinite plate sections proceeds as previously discussed, where the Green function response for an infinite planar plate is employed, along with imposition of radiation conditions at infinity. Application of Equation (1) to the tapered section employs the Green function response for an infinite medium. As before, an incident plate mode is assumed in the left semi-infinite plate. Incorporation of the incident mode as input data into the system of integral equations is

accomplished by applying Equation (1) to the complement of the semi-infinite plate from which the incident mode emerges. Results are then combined to form a system of integral equations expressed as

$$\begin{aligned}
& \int_{E_1} (u_i(x) \tau_{ijk}^{GP}(x|x') - u_{i:k}^{GP}(x|x') \tau_{ij}(x)) n_j^A(x) dx + \frac{1}{2} u_k(x') = u_k^{inc}(x') \quad , x' \in E_1 \\
& \int_{E_1+E_2} (u_i(x) \tau_{ijk}^{GU}(x|x') - u_{i:k}^{GU}(x|x') \tau_{ij}(x)) n_j^B(x) dx \\
& + \int_F u_i(x) \tau_{ijk}^{GU}(x|x') n_j^B(x) dx + \frac{1}{2} u_k(x') = 0 \quad , x' \in E_1 + E_2 + F \\
& \int_{E_2} (u_i(x) \tau_{ijk}^{GP}(x|x') - u_{i:k}^{GP}(x|x') \tau_{ij}(x)) n_j^C(x) dx + \frac{1}{2} u_k(x') = 0 \quad , x' \in E_2
\end{aligned} \tag{4}$$

where $\tau_{ij}^{GP}(x|x')$ is the Green function stress response to a point load acting in a planar infinite plate, $\tau_{ij}^{GU}(x|x')$ is the Green function stress response to a point load acting in an unbounded medium, n_j^A , n_j^B , and n_j^C are the outward normal vectors for the three constituent bodies, and F denotes the traction free surface of the joining body. Application of the boundary element method leads to a matrix equation for the evaluation of the displacements, $u_i(x)$, and tractions $\tau_{ij}(x) n_j$ on the plate edges, E_1 and E_2 , and displacements $u_i(x)$ on F . Following computation of the wave fields on the plate edges, transmitted and reflected field amplitudes are obtained in the same fashion as previously described, using the far-field expression for the planar plate Green function response in Equation (3). The system of equations in Equation (4) is used to examine guided wave transmission in the most general configurations of curved, tapered plates.

3.9.2 Computational Study

The initial work of this study examined the properties of guided mode propagation in a cylindrical shell of constant curvature, representing the most fundamental canonical problem of the study. An exact analytical solution for guided mode propagation in a cylindrical shell is obtainable owing to the separability of the governing elastodynamic equations in cylindrical coordinates, enabling the expression of the solution in cylindrical wave functions. The analytical formulation and solution of this problem has been published by Liu and Qu [102]. This analytical solution was encoded and propagation behaviors were examined in the range of parameters of interest to the applications motivating this study. Results are presented demonstrating the fundamental propagation characteristics of guided modes in a cylindrical shell. Results first examine the effect of curvature on guided mode dispersion characteristics, relating frequency dependent wave speed to frequency. Dispersion curves are presented which plot the spatial frequency ($2\pi/\lambda$, where λ is wavelength measured along the inner shell wall) of a time harmonic wave field as a function of frequency. Figure 87a plots the dispersion relation for a 3/16 inch thick flat aluminum plate in the frequency range of 20 KHz to 400 KHz. For this calculation and all subsequent calculations presented in this report, the relevant ultrasonic properties of aluminum are the longitudinal and shear wave speeds, taken to be $c_L=6094$ m/s and $c_T=3263$ m/s, respectively. Three modes are seen to propagate in this frequency range, identified as A0 (zero order anti-symmetric motion), S0 (zero order symmetric motion), and A1 (first order anti-symmetric motion). For non-dispersive propagation (wave speed independent of frequency), the

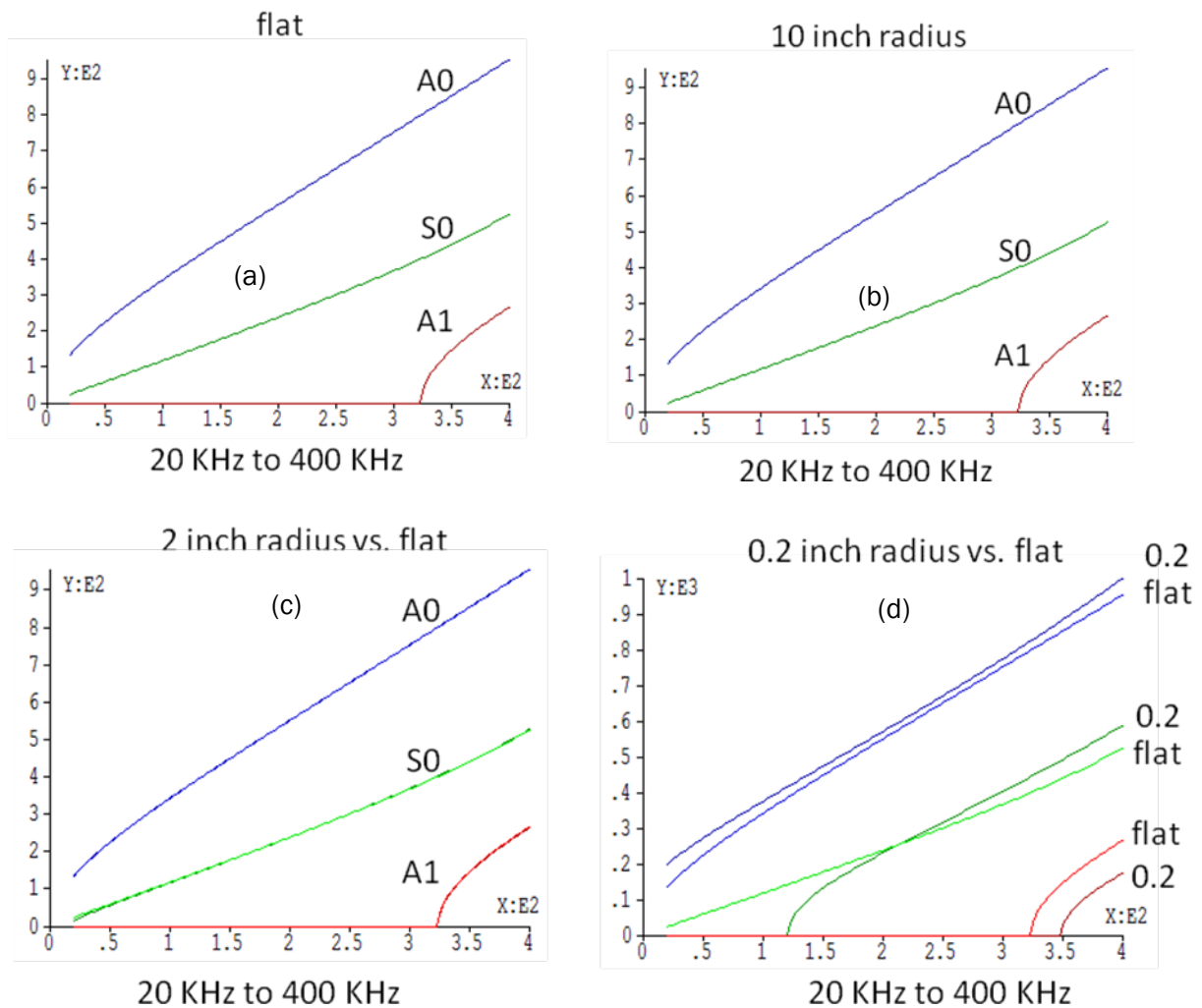


Figure 87. Dispersion Relation For Guided Modes In 3/16 Inch Thick Cylindrical Shell: A) Flat Plate, B) 10 Inch Inner Wall Radius, C) 2 Inch Inner Wall Radius, D) 0.2 Inner Wall Radius. Vertical Axis Is Circumferential Wave Number At The Inner Radius

dispersion relation would be a straight line through the origin, with a slope equal to the reciprocal of the wave speed. Curvature in the dispersion relation indicates a frequency dependence of wave speed, and hence a temporal dispersion of the transported signal with distance.

The dispersion relation for circumferential propagation in a 3/16 inch thick cylindrical shell having a 10 inch inner wall radius is plotted in Figure 87b. The mode structure is seen to be similar to that of the flat plate shown in Figure 87a. Figure 87c overlays the dispersion curves for a 3/16 inch thick cylindrical shell having a 2 inch inner wall radius with those for a flat plate. Very little difference is observed, with only a slight difference seen at 20 KHz in the S0 mode. A similar overlay of dispersion curves for a 3/16 inch thick cylindrical shell having a 0.2 inch

inner wall radius is shown in Figure 87d. In this case, an appreciable difference in dispersion properties is noted. It is noted that the 0.2 inch inner radius is on the order of the 3/16 inch shell thickness. From the results of Figure 87, it is concluded that shell wall curvature has little influence on the temporal signal transport for radii of curvature substantially greater than the shell thickness.

Attention is now directed to the displacement profiles through the wall thickness for the cylindrical shell guided modes. Figure 88 depicts the motions discussed in the following plots. Plots are made in Figure 89 of the tangential and normal wall motions associated with the A0 mode as a function of depth through the shell wall, computed at 100 KHz. Figure 89a, b, c plots the motion for a flat plate, 10 inch inner wall radius, and 2 inch inner wall radius, respectively. The left edge of the plot indicates motion at the inner wall, the right edge of the plot indicates motion at the outer wall. It is seen in the case of the flat plate that both the normal and tangential motions are opposite one another about the centerline of the plate, hence the anti-symmetric designation. In Figure 89b, c, it is seen that the motions are not purely anti-symmetric about the centerline of the shell, with motions on the inner wall being greater than those at the outer wall. Similar plots of the motion profile are shown in Figure 90 for the S0 mode. In this case, it is seen that motion is not purely symmetric in the case of the curved shell. Normal motions are

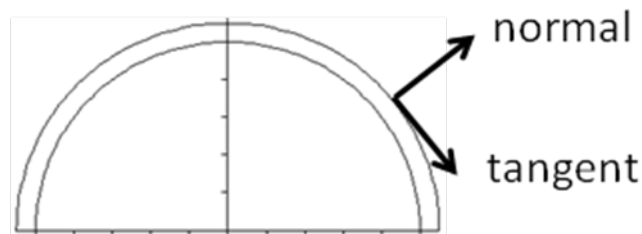


Figure 88. Definition Of Motion Vector Components In Cylindrical Shell

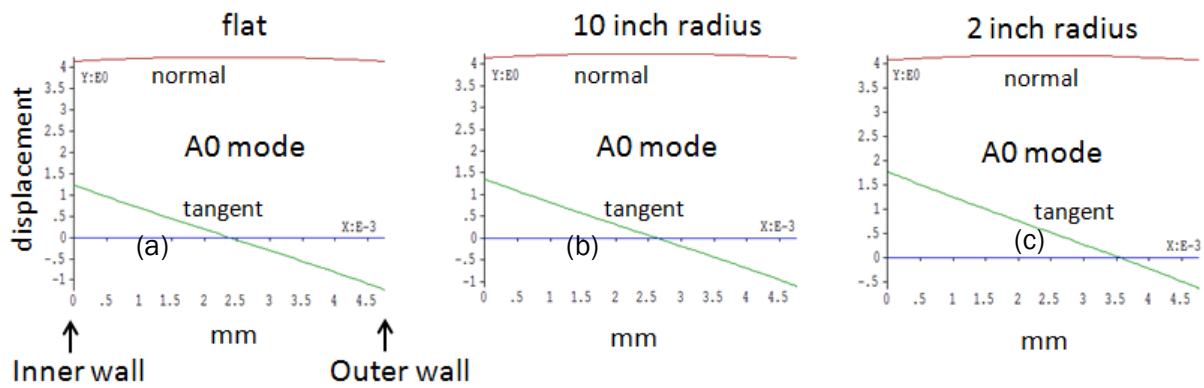


Figure 89. Motion Profiles Through Shell Wall For A0 Mode At 100 KHz: A) Flat Plate, B) 10 Inch Inner Radius, C) 2 Inch Inner Radius

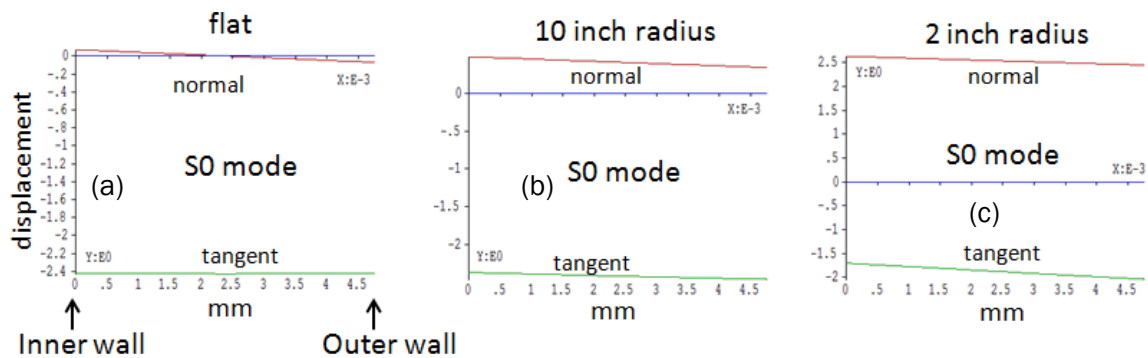


Figure 90. Motion Profiles Through Shell Wall For S0 Mode At 100 KHz: A) Flat Plate, B) 10 Inch Inner Radius, C) 2 Inch Inner Radius

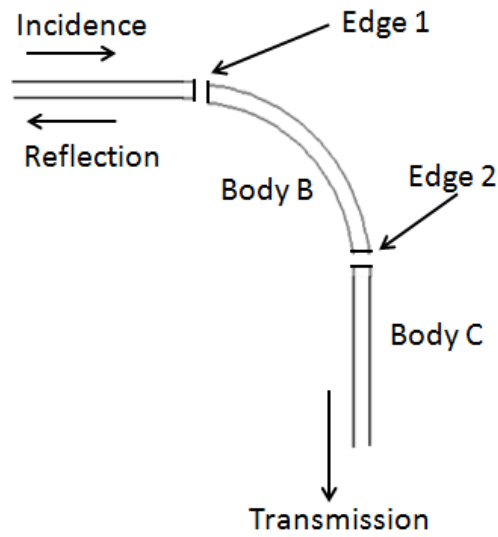


Figure 91. Guided Mode Transmission At 2 Inch Radius 90 Degree Bend In 3/16 Inch Thick Plate

Seen to be slightly larger at the inner shell wall, whereas tangential motions are seen to be slightly larger at the outer shell wall.

The observed difference in motion profiles for different curvatures has an implication for propagation in shells displaying non-uniform curvature. A mode freely propagating in a shell section of a given curvature will not transmit unaffected into the corresponding mode of a shell section with a different curvature when encountering a transition in curvature. A degree of mode conversion will accompany the transition as the mode profile adapts to the new local curvature. The question of interest in this study is the significance of this mode conversion in the structural geometries under consideration. Efforts were directed at quantifying the mode coupling phenomena associated with spatially varying curvature, using the integral formulation summarized by Equation (2).

To examine this question, the configuration of Figure 91 was studied. The structure consists of three shell segments: two semi-infinite plates, plus a circular cylindrical section with a specified radius. Transmission and reflection coefficients are calculated using the model formulation described in the previous section. Numerical results are presented here which applies the formulation to a 2 inch radius 90 degree bend in an otherwise flat 3/16 inch thick aluminum plate. The 2 inch radius represents a lower bound on curvature in the structures of interest to this study. Boundary element method solutions to Equation (2) are computed by representing edge displacement and tractions by piecewise constant functions, with 15 elements prescribed over the joining edges. Computed reflection and transmission coefficients for the problem geometry of Figure 91 are presented in Figures 92 and 93, which quantifies the energy carried by each mode.

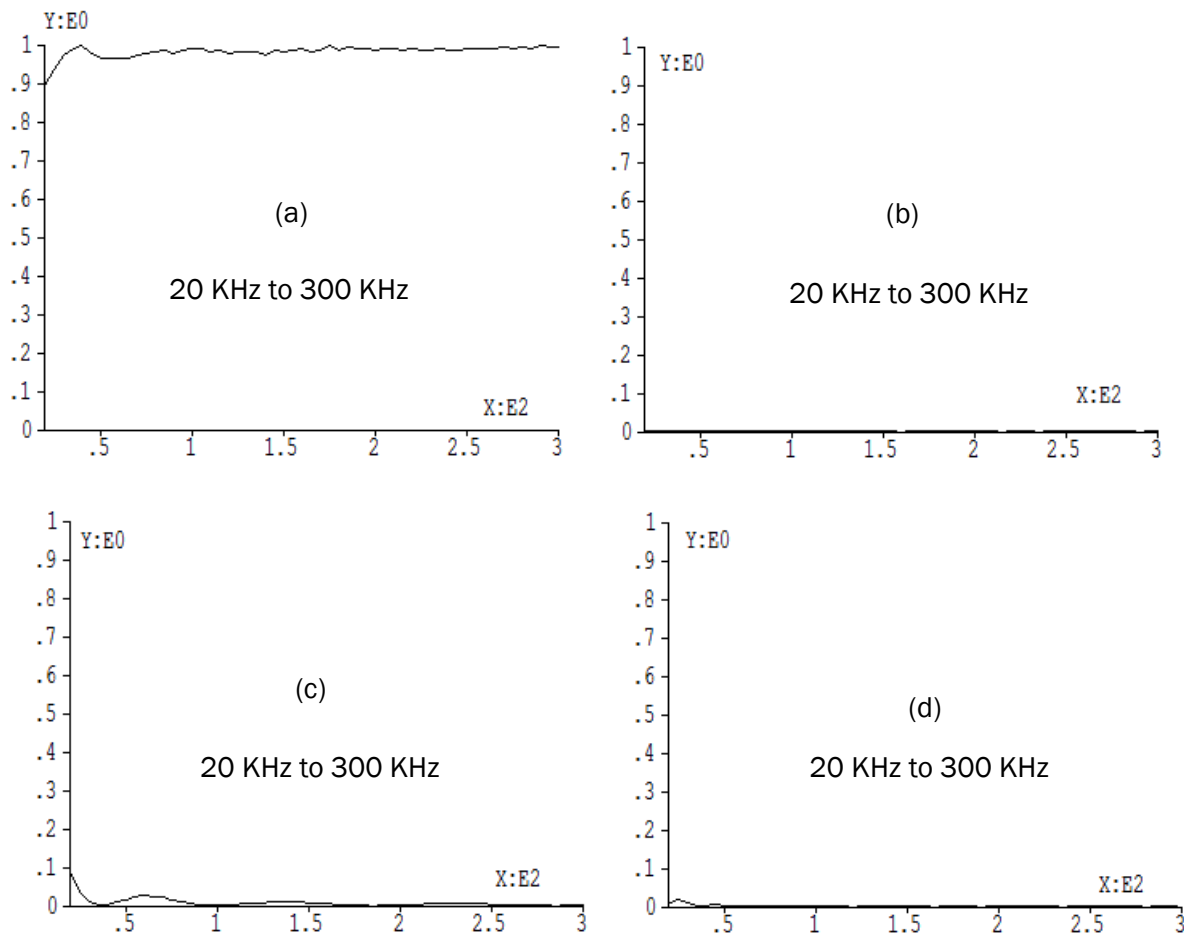


Figure 92. Energy Transmission And Reflection Coefficients For A0 Mode Incidence On The Geometry Of Figure (1): A) A0 To A0 Transmission, B) A0 To A0 Reflection, C) A0 To S0 Transmission, D) A0 To S0 Reflection

A unit incident energy is prescribed. Parameters in the numerical model are adjusted (e.g., spatial increments) such that the reflected and transmitted mode energies sum to the incident energy to within less than one percent. Figure 92 presents results for A0 wave incidence, computed in the frequency range of 20 KHz to 300 KHz. It is seen that the A0 guided wave transmits around the 90 degree bend with little attenuation. A small reduction in transmitted amplitude is seen at the lowest frequencies. Correspondingly, a small degree of A0 to S0 mode conversion is seen on transmission. No appreciable A0 mode reflection is observed.

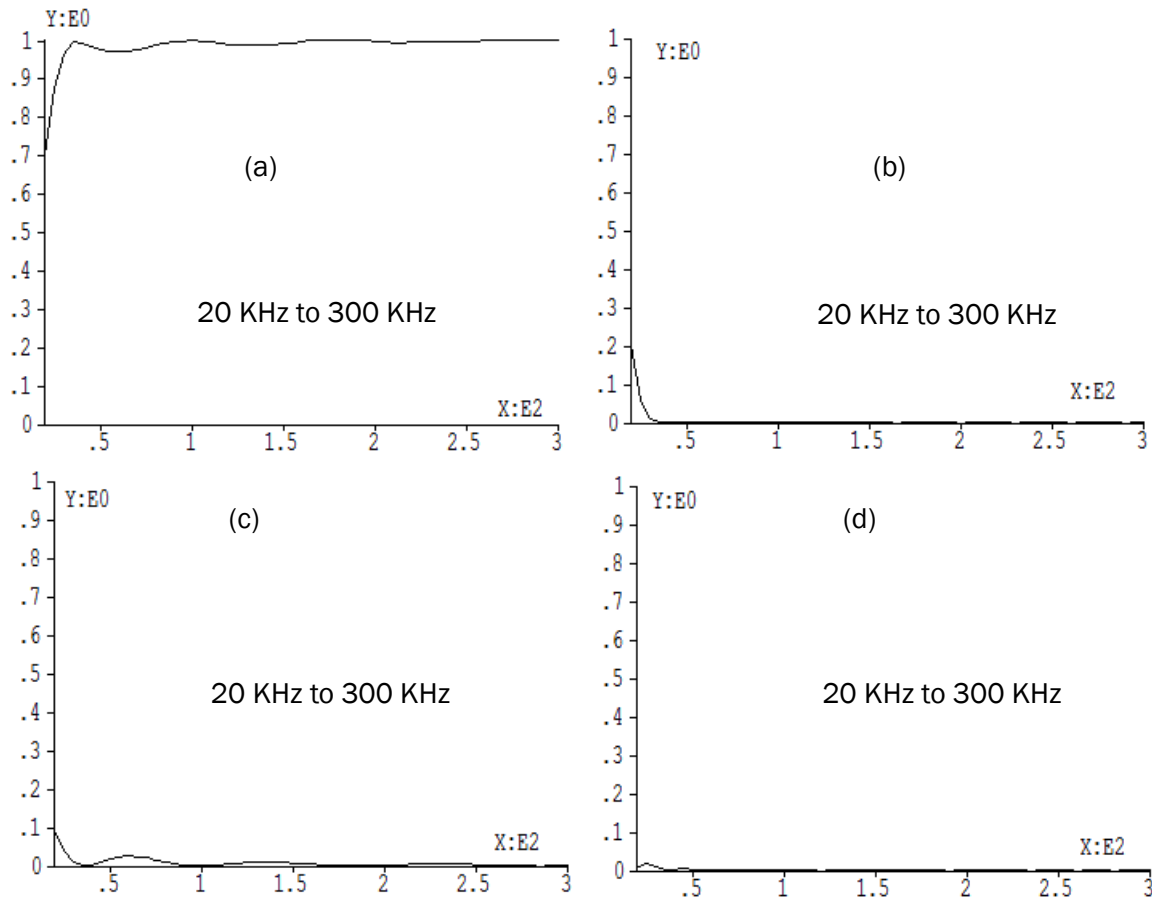


Figure 93. Energy Transmission And Reflection Coefficients For S0 Mode Incidence On The Geometry Of Figure 87: A) S0 To S0 Transmission, B) S0 To S0 Reflection, C) S0 To A0 Transmission, D) S0 To A0 Reflection

Figure 93 presents corresponding results for S0 wave incidence, computed in the frequency range of 20 KHz to 300 KHz. As with A0 incidence, it is seen that the S0 guided wave transmits around the 90 degree bend with little attenuation. It is observed, however, that noticeably more S0 reflection occurs at the lowest frequencies. It is interesting to note that the S0 to A0 mode conversion on both transmission and reflection appear the same as the A0 to S0 mode conversions of Figure 92, indicating that these conversions are reciprocal. Overall, it is noted that energy lost due to mode conversion upon encountering the transition in radius is by-and-large negligible for the 2 inch radius. This result indicates that although mode conversion does occur at mild transitions in curvature, it does not have a serious deleterious effect on transmission efficiency.

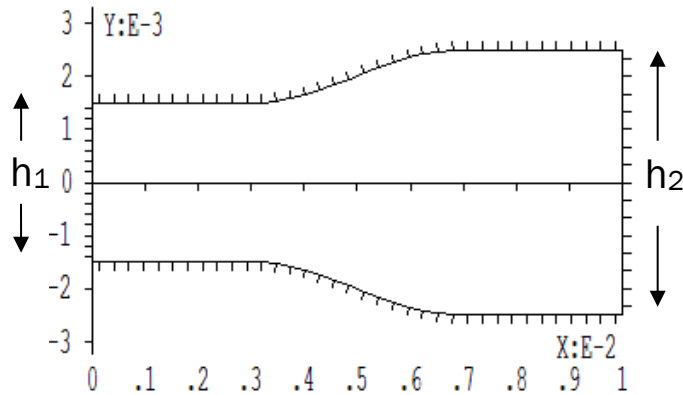


Figure 94. Tapered Plate Section: Transitions From 3 Mm To 5 Mm Over A 100 Mm Section

The most general geometry encountered in the transmission of guided plate wave signals is that of a generally curved plate of tapered thickness. Guided wave transmission in this case is modeled using the formulation expressed by Equation (4), in which motions are explicitly computed over all bounding surfaces of the curved tapered section. Cases are examined here considering first a straight tapered section, followed by consideration of a generally curved tapered section. The straight tapered section, depicted in Figure 94, consists of two semi-infinite flat plates connected by a 1 cm long transition region having sinusoidal top and bottom surface profiles such that surface normals are continuously varying. The shell section displays a taper in thickness from h_1 on the left edge to h_2 on the right edge. In evaluating the BEM matrix coefficients, surface mesh points are prescribed to assure a minimum of 20 points per wavelength for the slowest propagating mode (the A0 mode in the h_1 plate section). A typical surface mesh is indicated in the drawing of Figure 94. The BEM matrix is inverted, and transmission and reflection coefficients are computed using the approach described in the previous section. Transmission and reflection responses are plotted in Figure 95 for A0 mode incidence in the left-hand semi-infinite plate section, which displays energy transmission coefficients for a unit energy incident mode. Transmission results are compared using left edge thicknesses of $h_1 = 1\text{mm}$, 2mm , and 3mm , and a right edge thickness of $h_2 = 5\text{mm}$. Results are plotted from 100 KHz to 300 KHz. It is seen that transmission from the 3mm thick section to the 5 mm thick section has a negligible effect on transmitted energy. This result indicates that a substantial transition in A0 phase velocity occurs within the taper with a negligible loss of transmitted energy. For example, at 200 KHz, a transition in A0 phase velocity from 2039 m/s to 2383 m/s occurs over the length of the taper. A more pronounced effect on energy transmission is seen in the 2mm to 5mm transition, where a ~8 percent energy reflection and transmission reduction is seen in the lower frequency band. The most pronounced effect on energy

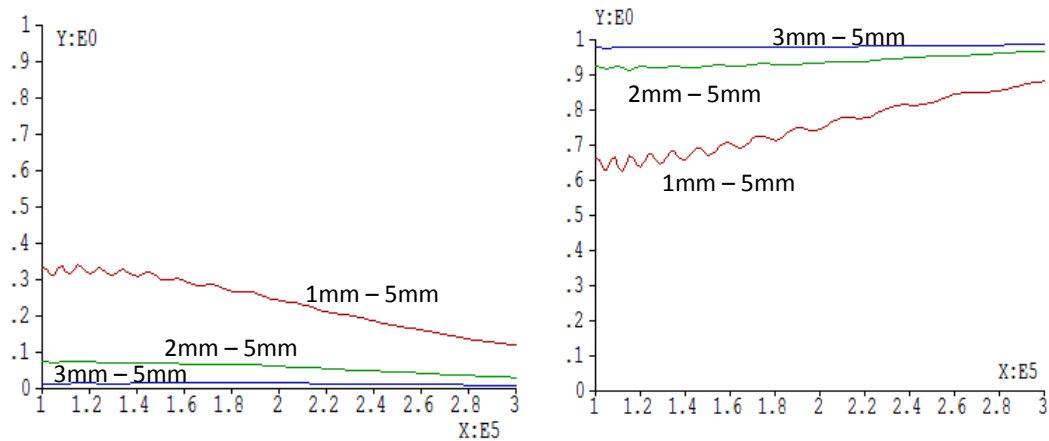


Figure 95. Energy Transmission And Reflection Coefficients For 100 KHz To 300 KHz A0 Mode Incidence On The Geometry Of Figure (87): A) A0 To A0 Reflection, B) A0 To A0 Transmission

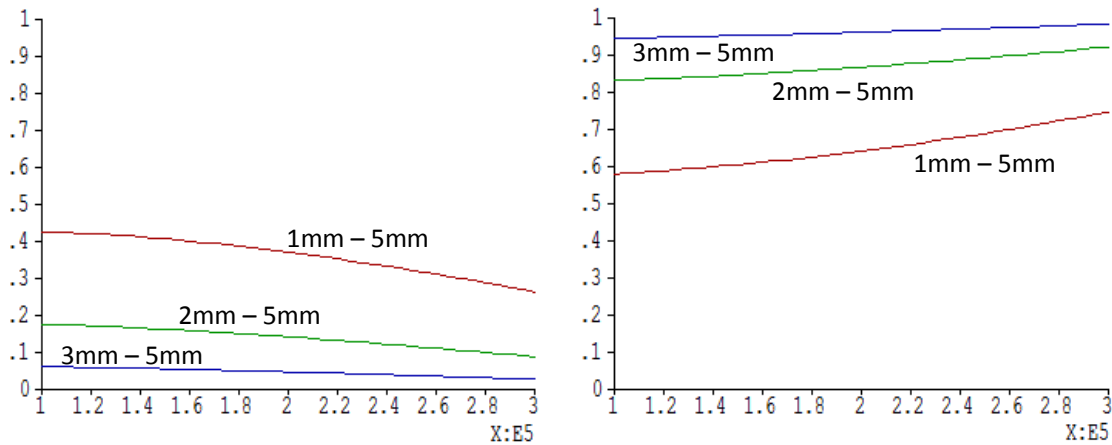


Figure 96. Energy Transmission And Reflection Coefficients For 100 KHz To 300 KHz S0 Mode Incidence On The Geometry Of Figure (87): A) S0 To S0 Reflection, B) S0 To S0 Transmission

transmission is seen in the 1mm to 5mm transition, where a ~33 percent energy reflection and transmission reduction is seen around 120 KHz. A0 to S0 mode conversion was negligible in all cases, and was therefore not plotted. Transmission and reflection responses are plotted in Figure 96 for S0 mode incidence in the left-hand semi-infinite plate section. Similar to the case of A0 incidence, it is seen that transmission from the 3mm thick section to the 5 mm thick section occurs with minimal effect on transmitted energy, although it is noted that the effect is somewhat more pronounced than that seen in Figure 95 for A0 incidence. As with A0 incidence, transmission efficiency is seen to decrease as the difference in plate thicknesses increases. As before, S0 to A0 mode conversion was negligible in all cases, and was therefore not plotted.

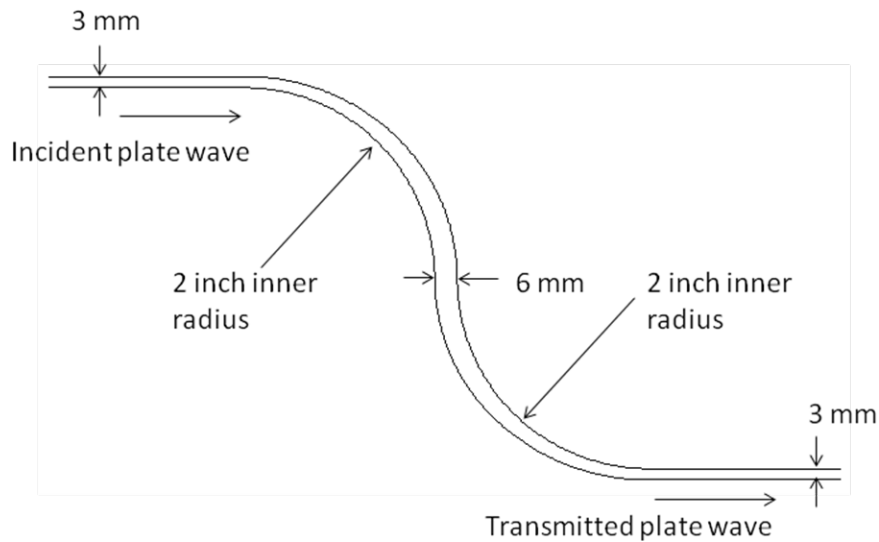


Figure 97. Generally Curved And Tapered Plate Geometry

The case of a generally curved and tapered plate geometry is depicted in Figure 97. This configuration combines the attributes of both Figure 91 and Figure 94. A doubly-curved plate section having a 2 inch inner radius connects two 3 mm semi-infinite plate sections. The thickness of the curved connecting plate section transitions from 3 mm at the interfaces with the semi-infinite plates to 6 mm at the interface between the two curved sections. An incident plate wave of either A0 or S0 motion is incident on the configuration from the left semi-infinite plate. Transmission and reflection coefficients are sought. The problem formulation of Equation (4) is applied, and the computation is reduced to a BEM matrix equation by dividing the traction-free surfaces of the doubly-curved connecting section into 584 elements over which surface displacements are represented by piecewise constant functions. As in the previous examples, the plate edges are divided into 15 elements over which displacements and tractions are represented by piecewise constant functions, resulting in a 1288x1288 BEM matrix for inversion. Inversion of the matrix yields displacements and tractions on the plate edges joining the semi-infinite plates to the doubly-curved tapered section. Energy reflection and transmission coefficients are computed by applying Equation (3) to the left and right semi-infinite plate sections, respectively. Results are plotted in Figure 98 for A0 incidence between 100 KHz and 300 KHz. Figure 98a presents A0 to A0 transmission, whereas Figure 98b plots A0 to S0 mode conversion. It is seen that A0 energy is transmitted by-and-large unaffected by the curved and tapered plate geometry. A small degree of A0 to S0 mode conversion is observed to occur in frequency bands around 135 KHz and 230 KHz. No appreciable reflection into either A0 or S0 modes were observed, and therefore was not plotted. Figure 99 plots results for S0 mode incidence. Transmission characteristics quite similar to A0 incidence are observed. Notably, energy is by-and-large transmitted into a like S0 mode, with only a small degree of A0 mode coupling in frequency bands around 135 KHz and 230 KHz. Again, no appreciable reflected energy was observed.

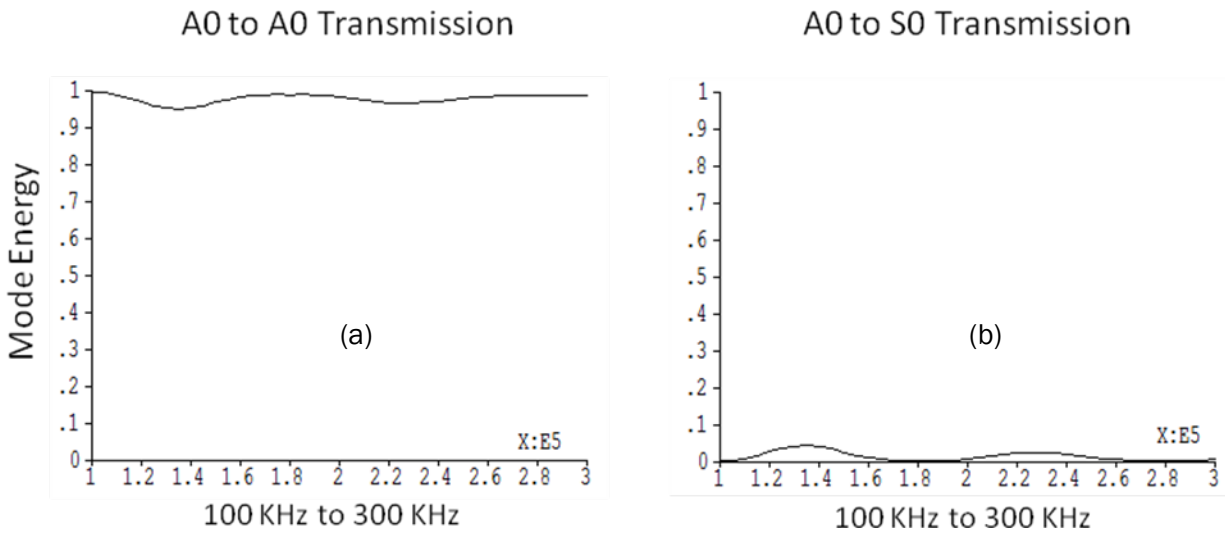


Figure 98. Energy Transmission And Reflection Coefficients For 100 KHz To 300 KHz A0 Mode Incidence On The Geometry Of Figure 97: A) A0 To A0 Transmission, B) A0 To S0 Transmission

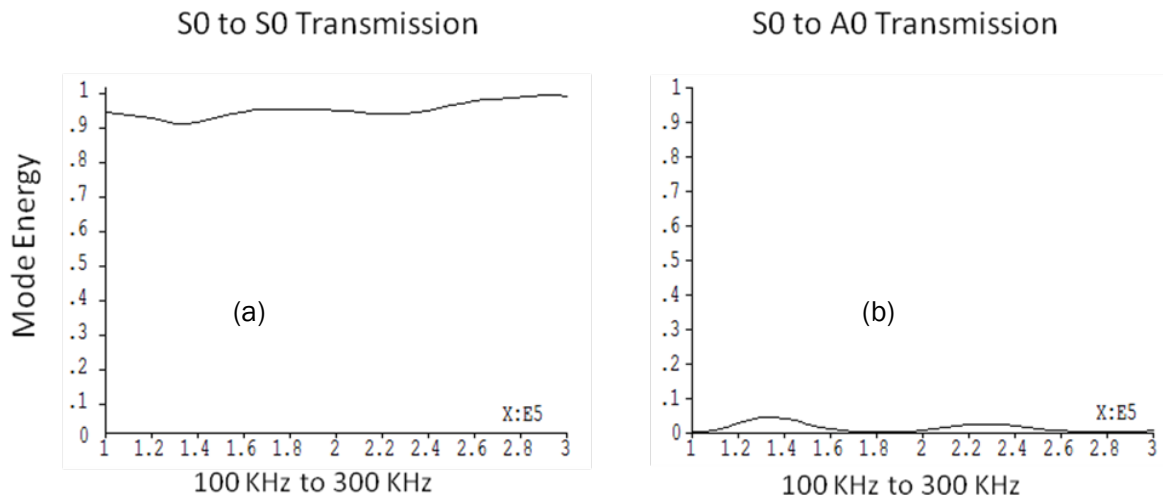


Figure 99. Energy Transmission And Reflection Coefficients For 100 KHz To 300 KHz S0 Mode Incidence On The Geometry Of Figure 97: A) S0 To S0 Transmission, B) S0 To A0 Transmission

Conclusions

Results of this study show that moderate degrees of plate curvature and taper have a minimal effect on the transmission efficiency of plate waves. Examination of dispersion characteristics in circular cylindrical shells revealed that the plate curvature has a negligible effect for curvatures appreciably larger than the plate thickness. It was observed that displacement depth profiles vary with curvature, indicating that mode coupling will occur when transitions in radius are encountered. However, an examination of transmission at abrupt curvature transitions revealed a negligible degree mode conversion for 3/16 inch plate radii as small as 2 inches. Finally, an examination of guided mode transmission in tapered plates displaying gradual transitions in plate thickness revealed only a modest degree of mode conversion. Smooth transitions were examined for which the length over which the transition occurs was as small as twice the plate thickness. Energy loss through mode conversion was observed to be less than 10 percent for transitions in thickness of 60 percent and 150 percent. A 400 percent change in plate thickness resulted in an energy loss of 25 percent. These behaviors were consistently observed when examining plate structures containing both curvature and taper. A structure containing a two inch radius double curvature with two 100 percent transitions in thickness displayed transmission characteristics showing little mode conversion loss for both A0 and S0 wave incidence.

3.10 Fundamentals Of Detecting Tight Cracks Using Vibrothermography Inspection (Holland)

Investigation Team: S. Holland, R. B. Thompson, L. Brasche, and D. Eisenmann

Graduate students: J. Renshaw, C. Uhl, J. Vaddi, W. Zhang, and R. Reusser

Multiple undergraduate students

Motivation

Vibrothermography is an NDE technique that finds cracks based on thermal imaging of the heat generated by vibration-induced frictional rubbing of crack surfaces. Vibrothermography, also known as “Sonic IR” and “thermosonics”, is an emerging NDE method that has been proposed as a possible alternative or supplement to fluorescent penetrant inspection (FPI). Possible candidate applications for the Air Force include wheels, airfoils, and engine disks.

Vibrothermography has the advantages of being a relatively fast, automatable process, with only minimal specimen preparation required. Unlike most other NDE techniques it has the potential to find tight (closed) cracks, because it relies on rubbing contact rather than void detection.

Vibrothermography remains immature, although less so now than when this project began. There have been persistent questions about repeatability and there is a lack of basic scientific understanding of the crack heating process and the parameters which affect it. This project was created to begin to address those problems, and thereby enable broader use of and reliance on this technique.

Results – Theory and Experiments

The fundamental technical challenge of vibrothermography is that it is a multi-stage process where uncontrolled variability in the first stage (vibration) makes it difficult to quantitatively analyze the later stages. The approach in this project was to develop an experimental capability where we could manage and control the vibration, and then to exploit that capability to make quantitative measurements that would enhance knowledge of the process.

3.10.1 Development Of The Excitation System, Measurement System, And Software

We developed a broadband measurement system for vibrothermography [108]. This includes broadband excitation using a piezoelectric stack actuator and high power amplifier, quantitative measurement thermal and vibrational measurement capability, and flexible software that integrates the system.

The system gives us the ability to do broadband and frequency agile measurements where we have control over what resonances are excited. Since resonances have well defined mode shapes, it becomes possible to measure the vibration, a key ingredient in quantitative studies of crack heating.

The data acquisition software (“Dataguzzler”) was published on-line to the community as open source [109]. The excitation system technology was commercialized as part of a separate ONR-

funded STTR with Thermal Wave Imaging. A key result of the ONR STTR research was that much of the complexity and non-repeatability of traditional vibrothermography measurements comes from system resonances of the specimen, transducer, and/or mounts. Proper elastic coupling and mounting breaks these system resonances and makes the vibrothermography process much more repeatable.

3.10.2 Measurement And Modeling Of Vibration

Complexity of the vibration process has been the most significant confounding factor for quantitative study of vibrothermography. Real clamps and transducers do not behave according to idealized models at KHz frequencies. A full linear model would require knowledge of vector mechanical impedances of each mounting point evaluated over the entire frequency range. Such a measurement is wholly impractical and yet still rather idealized (linearity assumption) compared with reality.

We started by realizing that the vibrothermography process is driven by resonance. The minimum vibrational stress levels (tens of megapascals) required for crack heating are impractically high for traveling wave excitation, so crack heating requires some sort of resonance phenomenon. We can take advantage of resonance because with the right boundary conditions, resonances are quite predictable and repeatable. For simple bar geometries, low order bending resonances are predicted by elementary flexural wave theory. More generally resonance frequencies and mode shapes can be predicted using finite-element tools.

If the resonant mode shape is known, whether from theory or calculation, and the motion is known at a single point – such as from a laser vibrometer measurement – then the motion, including stresses and strains can be calculated everywhere within the specimen, including at the crack. Thus the key input of the crack heating process – the local stress or strain – is now measurable and can be related to observed crack heating [110-112].

3.10.3 Evaluation Of The Effect Of Crack Closure

Given that vibrothermographic heating is generated by rubbing of contacting asperities between crack faces, it is not at all surprising that heating would be dependent on the closure forces between those crack faces [113, 114]. Indeed, crack heating is strongly dependent on closure state. We discovered that in a large crack the zones of heating move as the closure state is varied by applying an external load. Our conclusion is that crack heating occurs only when there is light contact between crack faces. If there is too much contact force, the asperities become locked together by static friction and do not generate heat. In the other extreme if the contact force drops to zero and the asperities break contact, then no heat is generated either. In between, with light contact, there is enough force to ensure contact, and the asperities will rub against each other as the specimen vibrates, generating heat and locating the crack.

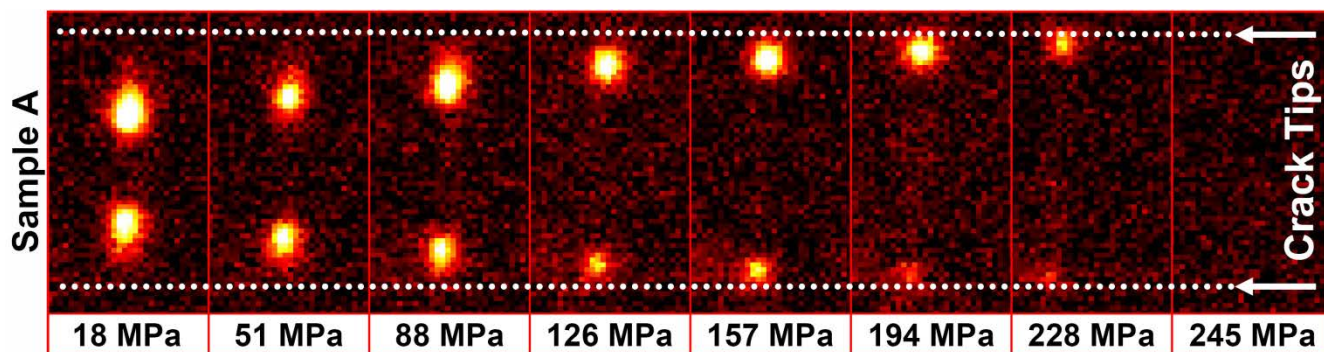


Figure 100. A Sequence Of Vibrothermography Images Of A Crack Taken Under Different External Loading. As The External Load Increases, The Loci Of Heating Move Toward The Tips And Eventually Vanish Once The Crack Is Entirely Open. The Amount Of Crack Heating Is Dependent On The Closure State

Figure 100 shows vibrothermographic images of the heating of a crack as a static bending load is applied to open it. The crack length is constant but the locus of the heating shifts towards the crack tips as the load increases. The heating only occurs at those points where the crack faces are in light contact.

Unfortunately, crack closure is not a quantity that is readily measurable for practical specimens, and there is no accepted way to predict it from the intrinsic parameters of the fatigue. So our knowledge of crack closure, aside from the physical insight, is not yet particularly useful from a prediction standpoint.

3.10.4 Probability Of Detection

We collaborated with a parallel QIT project on probability of detection (POD) for vibrothermography led by Dr. W. Q. Meeker. We provided his group with data, both processed and unprocessed from this project [115, 116]. We also provided data from a parallel POD study funded by the FAA where we demonstrated physical equivalence between the vibrothermography measurement system at ISU and those at GE Aviation and Pratt & Whitney.

3.10.5 Effects Of Excitation Amplitude And How Vibrothermographic Excitation Affects Crack Faces

One of our first quantitative experiments on crack behavior was to look at the effect of excitation amplitude on crack heating. We found linear/quadratic behavior predicted by a simple frictional model, but we quickly discovered that the amount of crack heating would often change over multiple tests, especially for large cracks that generated a lot of heat. We also observed that sometimes the eddy current response of the crack after vibrothermographic testing was different from that prior to the testing. This suggests that the vibrothermographic rubbing was changing the crack surfaces.

To evaluate how vibrothermographic excitation affects crack surfaces, we prepared several

fatigue crack samples. We left some samples as untested pristine control samples and subjected the rest to vibrothermographic testing. We tested the samples from low to very high amplitudes. After testing, we broke open the samples and measured the surface roughness using different optical methods like surface profilometry, SEM and Raman spectroscopy. We compared these results with that of untested/pristine cracks.

We observed that cracks subjected to vibrothermographic excitation underwent substantial change in surface roughness [117]. We observed fretting, adhesive wear, plowing, oxidation and even clear evidence of melting (in a lower melting-point material). Electron microscope images showing oxidation, melting, and fretting are included in Figure 101.

3.10.6 Determination Of The Effect Of Loading Mode (Opening/Closing, Shear, Etc.) On Crack Heating

It is a long standing question how the vibrational loading mode (opening/closing mode I versus shear mode II) effects the vibrothermographic heating. It has long been hypothesized that since heating is driven by friction and friction is largely a shear effect, that heating should be dominated by mode II shear.

According to our experiments this is not the case. In test after test, we load specimens vibrationally in mode I and still observe crack heating. So the question became not “does mode I vibrational loading cause heating?” because it most clearly does, but “does mode II vibrational loading also cause heating?”

After extensive experimentation (it was quite difficult to find a suitable geometry and resonance that included mode II loading but not mode I), we determined that mode II loading also causes heating and at roughly the same vibrational stress levels as for mode I. We also did similar experiments funded by NSF to determine the frequency dependence of crack heating. We verified the simple mechanistic theory that at equal stress levels the frequency dependence is approximately linear.

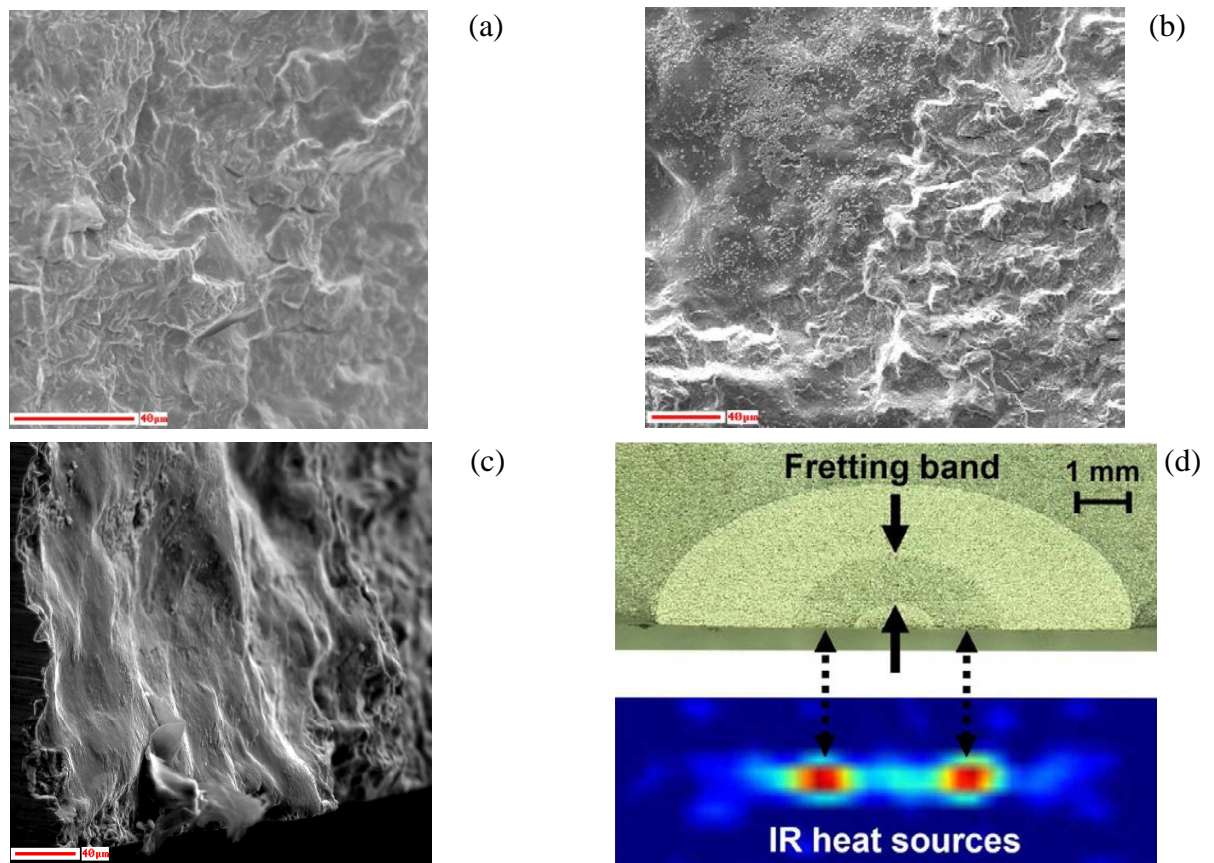


Figure 101. (A) Scanning Electron Microscope (SEM) Image Of A Pristine (Unvibrated) Crack In Ti 6-4 Alloy. (B) SEM Image Of A Ti 6-4 Fracture Surface After Vibrothermographic Testing, Showing Numerous Oxide Particles (Small Bright Dots And Patches Concentrated Towards The Upper-Left Region Of The Image). (C) SEM Image Of Fracture Surface Melting On The Ti 6-4 Sample, Evidenced By The Smooth, Featureless Surface. (D, Top) Microscope Image Of The Cross-Section Of A Vibrated Crack Showing A Fretting Band On The Fracture Surface. (D, Bottom) Processed Image Of Surface Infrared Heating Of The Crack, Showing That Vibrothermographic Heating Correlates With The Fretting Band

3.10.7 Development Of Prototype Synthetic Defects For Vibrothermography

Many NDE test specimens are not suited to vibrothermography because they contain manufactured flaws such as EDM notches or flat bottom holes that do not contain rubbing surfaces. A big question has been how to create suitable synthetic defects for vibrothermography. Our idea was to use a viscous fluid that could be embedded in a hole or notch that would absorb vibrational energy similar to a crack. We experimented with various materials and procedures for embedding the material in the hole or notch. We had the most success with honey, applied using a vacuum technique so that air pressure would force it into the hole. The honey-filled holes heat with vibration and appear similar to cracks in the vibrothermographic image sequence. The limitation of this technique is that honey properties vary and can degrade (crystallize) over time [118, 119]. Given the current need for repeatable, long-lasting reference defects, it would be well

worth following up this work with a more exhaustive search for a more ideal material.

3.10.8 Development Of A Thermal Image Sequence Reconstruction And Noise-Rejection Algorithm

A vibrothermography experiment generates a sequence of infrared images that represent the temperature increase of the crack. One of the long-standing questions is how to best process this sequence to extract the most useful information while rejecting noise and interference. We developed an algorithm that compresses the information from the entire sequence of 150 frames into approximately 2 1/2 coefficients per pixel [120]. These coefficients are sufficient to reconstruct the sequence with a high degree of accuracy. In fact, the reconstructed sequence has lower noise than the original because the coefficients are not sufficient to reconstruct the noise.

The algorithm is based on the observation that the time-temperature curves for each pixel near a crack have a characteristic shape. They show a process of heating while the excitation is turned on followed by cooling after it is turned off. This characteristic shape can be calculated from theory and is a function of distance to the heat source and the dimensionality of the heat flow. By constraining the heating and cooling process to follow the theoretical shape, most of the noise and interference can be eliminated. In addition, the useful information is compressed from 150 frames down to just two frames that represent source distance and intensity. These two frames can be represented graphically in a single false color image, such as the one in Figure 102.

Real crack indications show a characteristic bulls-eye pattern of short distance (red or yellow) and large intensity surrounded by larger distance (green) at lower intensity. In Figure 102 there is a strong bulls-eye indication in the lower left of the blade as well as several weaker indications farther up. The characteristic pattern is suitable for automated recognition and analysis.

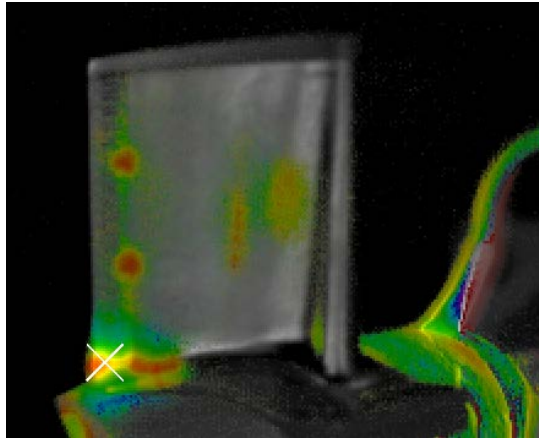


Figure 102. Processed False-Color Representation Of A Vibrothermographic Image Sequence. Hue Is Mapped To A Normalized Source Distance And Brightness To Intensity. The Raw Thermal Image Shows Through As A Grayscale Background. The Characteristic Bulls-Eye Pattern Of Vibrothermographic Indications, With Red In The Center Surrounded By Yellow And Then Green, Can Be Seen At Several Locations, Including The Position Marked With An 'X' And Two Other Indications On The Trailing Edge

3.10.9 Fabrication Of A Test Apparatus For Future Measurement Of The Effect Of Fatigue Parameters On Crack Heating

The most substantial remaining question about the physics of crack heating is how different crack morphologies and surface characteristics affect heating. These are determined by the fatigue process that gave rise to the crack. In fracture mechanics, Delta-K and R-ratio are the parameters that govern fatigue crack growth. Since cracks developed under different fatigue conditions may have different morphologies and may respond differently to vibrothermographic testing, it is necessary to study the underlying effect of the fatigue parameters on crack heating.

To measure the effect of fatigue parameters on crack heating, we plan to perform a design of experiments study with delta-k and R-ratio as the key control parameters. The idea is to manufacture fatigue cracks with varying delta-k and R-ratio, test them vibrothermographically at different closure stresses and correlate the crack heating with the control parameters.

To do these measurements, we built a bending fixture that can generate different static closure stresses on the specimen as we test it vibrothermographically. The static bending stresses are measured using a load cell mounted on the fixture and the dynamic stresses are measured according to the method explained above. We have not yet made substantial use of this fixture but hope to do so in the future.

3.10.10 Development Of “Vibrothermographically Active” Coatings That May Be Useful In The Future For Vibration Monitoring And/Or Coverage Analysis

The amount of crack heating in vibrothermography depends on the local dynamic stress or strain near the crack. To accurately predict crack detectability, we need to know the stress or strain field. We can apply a “vibrothermographically active” coating that heats due to viscoelasticity onto the specimen surface. In a vibrothermography test, the coating will heat in proportion to the surface strain field, and this field can be imaged with the infrared camera.

We discovered several 3M acrylic foam vibration dampening adhesives that gave good performance in terms of sensitivity. We tested Ti 6-4 rectangular bars in resonance and verified against laser vibrometer measurements that the coatings indeed dissipate heat according to the dynamic strain on the surface. Figure 103 shows mode shape illustrations on several turbine blades.

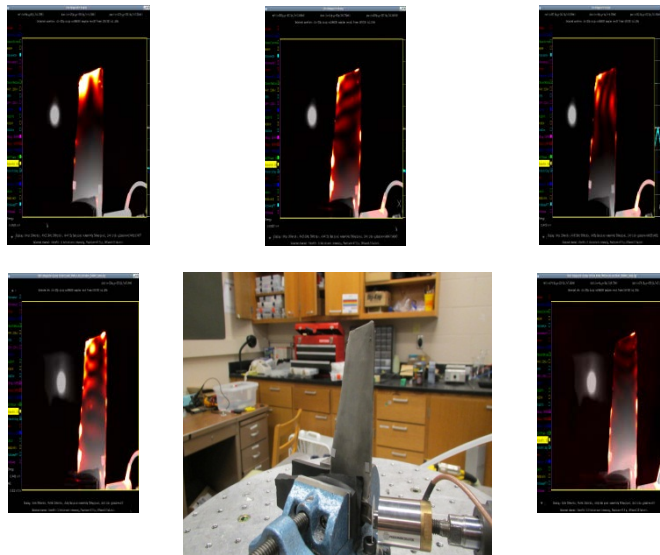


Figure 103. Mode Patterns Represented As Heating Of A Vibration Dampening Coating Applied To The Surface Of A Turbine Blade. This Coating Is Thin Enough That It Does Not Substantively Affect The Resonance Characteristics, But Absorptive Enough To Generate Detectable Heat Under Vibration. The Amount Of Heating Of The Coating Can Be Quantitatively Related To The Local Vibration Field In The Specimen

Conclusions

- Vibrothermography remains an emerging technique, but it is rapidly maturing.
- Our work in this project has provided a major increment in understanding
- We have pioneered better processes to characterize the vibration-induced heating behavior of a crack.

- We have applied these processes to measure the dependence of crack heating on parameters such as crack closure, crack length, excitation amplitude, vibrational stress, loading mode, and frequency.
- Some parameters remain largely unexplored, for example the effects of fatigue parameters and possible ingress of contaminants.
- We have collaborated on POD studies and developed a thermal image sequence processing algorithm that improves sensitivity and condenses the useful information.
- We have developed prototype synthetic defects and coatings that heat with vibration. These will be useful for process monitoring and coverage analysis.
- Taken together, the contributions from this project will help to transition vibrothermography from a qualitative NDE technique to a well-characterized crack-detection process built on quantitative knowledge.
- Work still remains to explore the dependence of crack heating on the remaining parameters and integrate knowledge of the process into a unified model.

Recommendations

- Vibrothermography is a promising technique but more work is needed to understand all the aspects of the underlying physical process.
- Vibrothermography has developed a reputation for large variability and poor reproducibility. Knowledge of underlying physics will be critical to optimizing processes to reduce that variability.
- The spatial variation in crack detectability caused by vibrational resonances means that vibrational modeling or measurement will be needed to adequately assess POD.
- Our empirically-driven statistical models of crack detectability are reaching the maturity where it will soon be possible to meaningfully integrate them into a unified predictive model for vibrothermography. Such a model, successfully validated against experiment, would provide a relatively straightforward means to predict POD for a vibrothermographic test.

3.11 Electromagnetic Characterization Of Composite Materials Using Microwave And Capacitive Methods (N. Bowler)

Investigation Team: Nicola Bowler
Students: Tianming Chen and Yang Li

Motivation

The motivation for this research is the nondestructive detection and characterization of anomalies, such as ingressed water, excessive resin and imperfect repairs, in low-conductivity sandwich structures. Motivated by the fact that microwave NDE techniques are often qualitative and complex to apply, we designed and developed a simple patch resonator sensor whose changes in resonant frequency indicate local permittivity changes. A theoretical model was developed, from which real permittivity of any particular layer of a three-layered structure can be inferred accurately. Motivated by the potential of achieving sub-wavelength resolution microwave imaging, non-metallic metamaterial structures were analyzed theoretically. Motivated by the observed sensitivity of qualitative capacitive NDE sensors to the presence of moisture in structures, quantitative capacitive sensing systems were developed, capable of detecting moisture, resolving anomalies with lower dielectric contrast and measuring complex permittivity.

Results – Theory and Experiments

3.11.1 Microwave NDE

3.11.1.1 Resonant Patch Sensor

A closed-form model for the resonant frequency of a rectangular patch sensor covered with multilayered dielectric structures (see Figure 104) has been derived by means of conformal mapping, the concept of equivalent capacitance, and an improved cavity model. The full theoretical development is presented in [121]. As a result, the resonant frequency of the structure shown in Figure 104 can be expressed as

$$f_r = \frac{c}{2(L_{\text{eff}} + 2\Delta L)\sqrt{\epsilon_{r,\text{eff}}}} \quad (1)$$

where c is the speed of light in vacuum, L_{eff} is the effective length of the patch, ΔL is the effective open-line length extension, and $\epsilon_{r,\text{eff}}$ represents the effective permittivity that combines the influence of the various layers. Equations relating the parameters shown in Figure 104 to those in (1) are listed in [121].

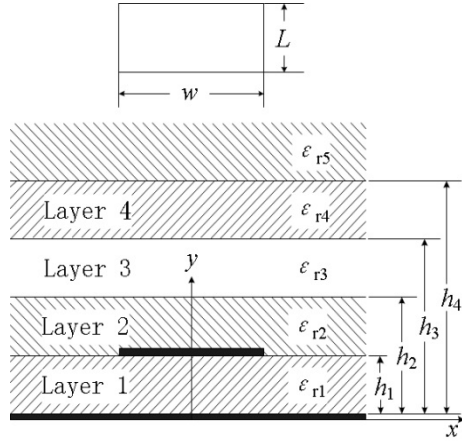


Figure 104. Top View And Cross-Sectional View Of A Rectangular Patch Sensor Covered With A Three-Layer Dielectric Structure. Layer 1 Is The Sensor Substrate, Backed By A Conducting Ground Plane

Based on the analysis presented in [122] and the operating frequency range of the measurement equipment (Anritsu 37347C Vector Network Analyzer, 40 MHz to 20 GHz), patch length $L = 10$ mm was chosen to guarantee $f_r \approx 10$ GHz. For a near-field NDE sensor, its spatial resolution is inversely proportional to the probe dimension, which is $L \times w$ in this case. Since it has been suggested that patch width w should lie in the range $[L, 2L]$ for radiation efficiency, and considering the conclusion of that changing w has little effect on f_r , w was chosen equal to L in order to achieve a good spatial resolution. For the substrate selection, firstly, h_1 should be less than 0.11λ in order to guarantee that the sensor can resonate. Further, larger h_1 and smaller ϵ_{r1} can provide a better sensitivity while the latter is also capable of yielding a better performance in penetration depth as concluded in. Thirdly, since the resonant frequency is defined as the frequency at which the return loss is the minimum, the value of h_1 should guarantee that the return loss at resonance is less than -10 dB in order to achieve an unambiguous observation of resonance. The value $h_1 = 1.1$ mm, corresponding to $\epsilon_{r1} = 1.046$ (Rohacell foam), was selected since it's the largest value in the interval $[0.5, 3.3]$ mm for which the return loss at resonance is always less than -10 dB while ϵ_{r3} of a radome structure, as shown in Figure 104, takes a range of permittivity values up to that of water.

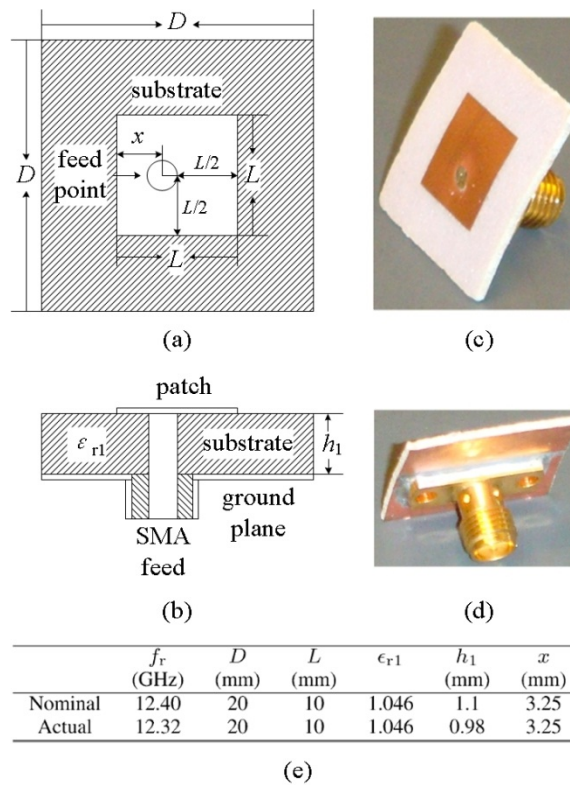


Figure 105. Schematic (A) Plan View And (B) Cross-Sectional View Of A Square Patch Sensor. (C) Front View And (D) Back View Of The Fabricated Sensor Whose Parameter Values Are Given In (E)

The geometry and chosen parameters of the square patch sensor are illustrated in Figs. 105 (a)-(b) and listed in Figure 105 (e). A prototype patch sensor with actual parameters also listed in Figure 105 (e) was fabricated for testing, as shown in Figs. 105 (c)-(d).

The sensitivity of the patch sensor to changes in the core permittivity of a three-layer structure was tested by comparing f_r while the sensor was covered with a three-layer dielectric structure having different core permittivity ϵ_{r3} and thickness $h_3 - h_2$, Figure 104.

Measured and corresponding theoretical results are shown in Figure 106, illustrating that measured f_r decreases as ϵ_{r3} increases. The difference between measured and theoretical results is due to the fact that (1) is an approximation. From Figure 106, it can be concluded that the sensitivity of

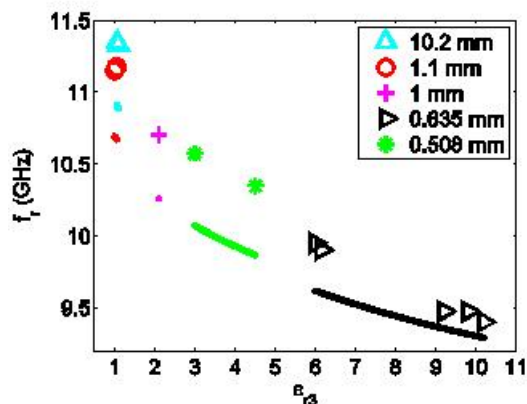


Figure 106. Measured And Theoretical Predicted Resonant Frequencies Of A Patch Sensor Versus Relative Permittivity ϵ_{r3} Of The Test Layer With Different Thickness $h_3 - h_2$, Figure 104. Symbols: Measured; Lines: Theoretical. $h_2 - h_1 = h_4 - h_3 = 0.508$ mm, $\epsilon_{r2} = \epsilon_{r4} = 3.27$, $\epsilon_{r5} = 1$

this patch sensor is better than $\Delta\epsilon_{r3} = 0.046$, which is the relative permittivity difference between air ($\epsilon_{r3} = 1$) and Rohacell 31HF ($\epsilon_{r3} = 1.046$) with the same geometric dimension.

Spatial resolution of an imaging or optical system is usually regarded as its ability to separate two closely-spaced identical point sources. In this case of near-field imaging, Rayleigh's criterion is used: two point sources are resolved if the valley-to-peak ratio is 0.80 or less. Two $10 \times 10 \times 6.35$ mm³ Teflon blocks sandwiched between two dielectric sheets were used to evaluate the resolving power of the patch sensor. For this sensor it was found that the two Teflon blocks are resolved when their separation is $d = 5.08$ mm, but not for $d = 4$ mm. It is concluded that the spatial resolution of this patch sensor is around 5 mm under this test configuration.

To test the patch sensor's performance in detecting water ingression, a 2-D scan was conducted over a honeycomb core with fiberglass skins, Figure 107, similar to that used in a typical radome. Approximately 0.25 cc of water was injected into a single honeycomb cell. In the image result, Figure 107 (d), the area of water ingression (blue) can be clearly observed. Regarding sensitivity, the f_r contrast between the non-defective region (red) and the area containing water (blue), is approximately 1.2 GHz, which is very clearly distinguishable. As for the spatial resolution, the total image area of the water-injected region $4 \text{ mm}^2 \times 6 = 24 \text{ mm}^2$, is very close to the actual surface area, 22 mm^2 , of a single honeycomb hexagon. It can be concluded that this sensor shows good NDE performance in detection of water present in this sandwich structure.

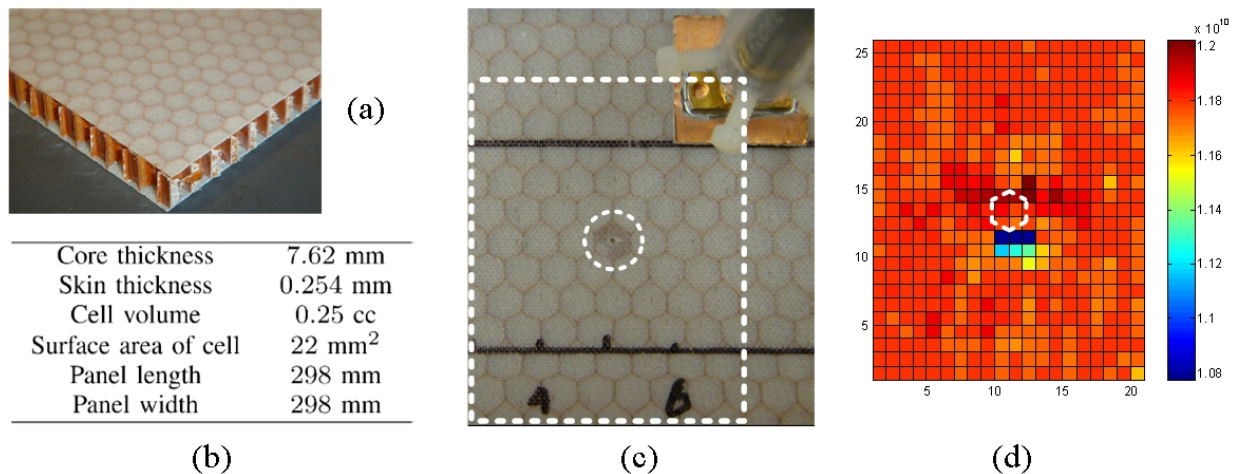


Figure 107. (A) Fiberglass–Honeycomb–Fiberglass Panel G8057 (The Composites Store Inc.) (B) Panel Properties. (C) Test-Piece Top Surface With Water Injected Into One Honeycomb Cell (Within The Circle). The Imaged Region Is Indicated By The Dashed Rectangle, Using The Sensor Geometric Center As The Origin. (D) Sensor Resonant Frequency Measured Over The Scan Region: Length \times Width = 52 \times 42 mm². The Actual Position Of The Water-Filled Honeycomb Cell Is Indicated By The White Dashed Line

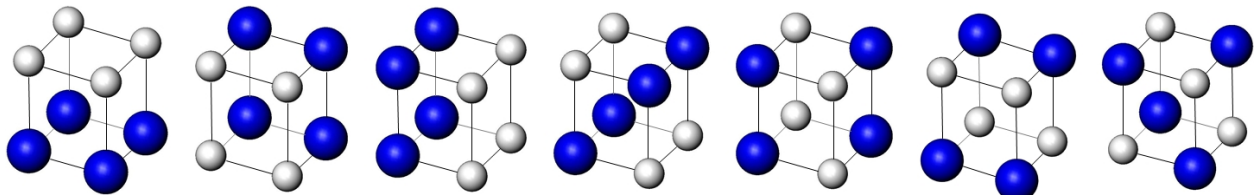


Figure 108. Seven Different Arrangements Of Two Types Of Spheres Within The Tetragonal Unit Cell

3.11.1.2 Towards Sub-Wavelength Resolution Imaging

A dielectric metamaterial with negative index of refraction that is capable of sub-wavelength resolution imaging can be designed only by employing theoretical techniques. Here, two sets of magnetodielectric spheres are arbitrarily arranged on each lattice point of the unit tetragon. Seven different potential arrangements of spheres on the vertices of the unit cell are investigated, Figure 108, to determine which one gives the widest bandwidth. Each sphere is modeled by a pair of crossed electric and magnetic dipoles, which are oriented in the x - and y -directions, respectively. It is assumed that the array is excited by a wave traveling in the z - direction, with real propagation constant β , and that all the spheres are excited identically. In the presence of the excitation, the electric and magnetic fields that are incident on the sphere at position

$(x, y, z) = (0, 0, 0)$ are obtained by summing the contributions from all the

Table 4. Three Investigated Combinations Of Sphere Types

| Combination | Electrical parameters | Radius |
|-------------|---|----------------|
| I | $\epsilon_{r1} = \epsilon_{r2}, \mu_{r1} = \mu_{r2} = 1$ | $a_1 \neq a_2$ |
| II | $\epsilon_{r1} \neq \epsilon_{r2}, \mu_{r1} = \mu_{r2} = 1$ | $a_1 = a_2$ |
| III | $\epsilon_{r1} = \mu_{r2}, \mu_{r1} = \epsilon_{r2} = 1$ | $a_1 = a_2$ |

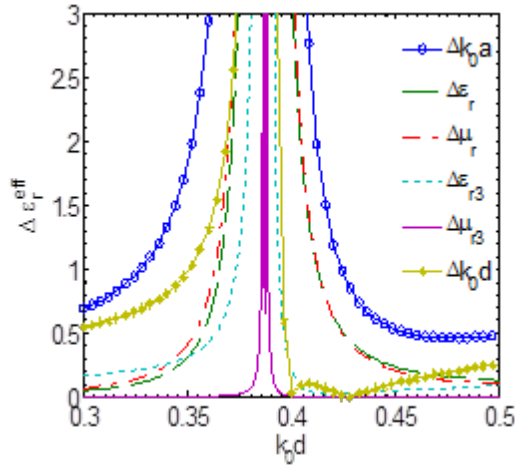


Figure 109. Effect On Metamaterial Effective Permittivity Of Varying The Constituent Parameters Shown In The Legend For An Array Of Identical Spheres With Sphere Parameters $\epsilon_r = \mu_r = 23.9$ And Radius $\frac{a}{d} = 0.45$

other spheres of the array. This traveling wave is characterized by the $k - \beta$ (dispersion) equation ((9) in [123]), which is obtained by a spherical-wave source scattering-matrix method under the assumption that spheres are sufficiently electrically-small that only the dipole scattered fields are excited. The $k - \beta$ equation relates the propagation constant, β , of the traveling wave, to the free-space wavenumber, k . For a given kd and an array of lossless scatters, the $k - \beta$ equation can be solved for real βd by a search procedure [123]. For a 3-D array whose sphere elements are sufficiently close to each other, $kd, \beta d < 0.5$, the array can be treated macroscopically as a homogeneous medium with effective permittivity ϵ_r^{eff} and permeability μ_r^{eff} , which can be obtained based on the solution to the $k - \beta$ equation. The performance of 3D periodic arrays with different arrangements of spheres on the vertices of the unit cell, Figure 108, were analyzed for three combinations of sphere types, Table 4. The maximum bandwidths of the double negative (DNG) region provided by different spheres arrangements for spheres combinations I and III are, respectively, 0.21% for arrangement (d) and 7.4% for arrangement (b). The maximum achievable bandwidth for combination II is less than 0.1%. With regard to the goal of fabricating a non-metallic metamaterial with negative index of refraction, it is important

to study the effect of parameter variations on the achievable DNG properties of the metamaterial [124]. If sufficiently tight fabrication tolerances are not achievable, then DNG behavior is extinguished. Variational analysis was performed on a cubic arrays of spheres with combinations I and III given in Table 4. Varying each parameter in turn by 5% while the others are held constant shows that variation in the sphere radius gives the largest change in effective permittivity of the metamaterial, Figure 109. Effective permeability behaves similarly. The largest variation permitted in all parameters, still preserving the existence of a DNG band, is an important consideration in fabricating DNG metamaterials. Very tight tolerances ($<0.02\%$) are required in fabricating purely dielectric metamaterials whereas slightly looser tolerances ($<0.8\%$) are needed for magneto-dielectric sphere arrays. While purely dielectric materials with high dielectric constant are readily available in the GHz frequency range, the tight fabrication tolerances required to achieve DNG behavior are prohibitive. On the other hand, high permeability materials are not readily available above 1 GHz suggesting that another approach to sub-wavelength imaging is needed for >1 GHz applications.

3.11.2 Capacitive NDE

3.11.2.1 Co-Planar Disk-And-Ring Capacitive Sensor For Defect Detection And Quantitative Dielectrometry

A concentric coplanar capacitive sensor was analyzed for the quantitative characterization of material properties for multi-layered dielectrics [125], Figure 110. The sensor output signal, transcapacitance C_T , is related to the thickness and dielectric constant of each layer of the material under test. Electrostatic Green functions due to point charges over different dielectric structures were derived utilizing the Hankel transform given the cylindrical symmetry of the proposed sensor. Numerical calculations based on the Green functions were implemented. The sensor electrodes were divided into a number of circular filaments, and the sensor surface charge distribution calculated using the method of moments (MoM). From the sensor surface charge, C_T was calculated. Numerical calculations were conducted for the purpose of optimizing the sensor and showed that normalized C_T as a function of sensor configuration is determined solely by its

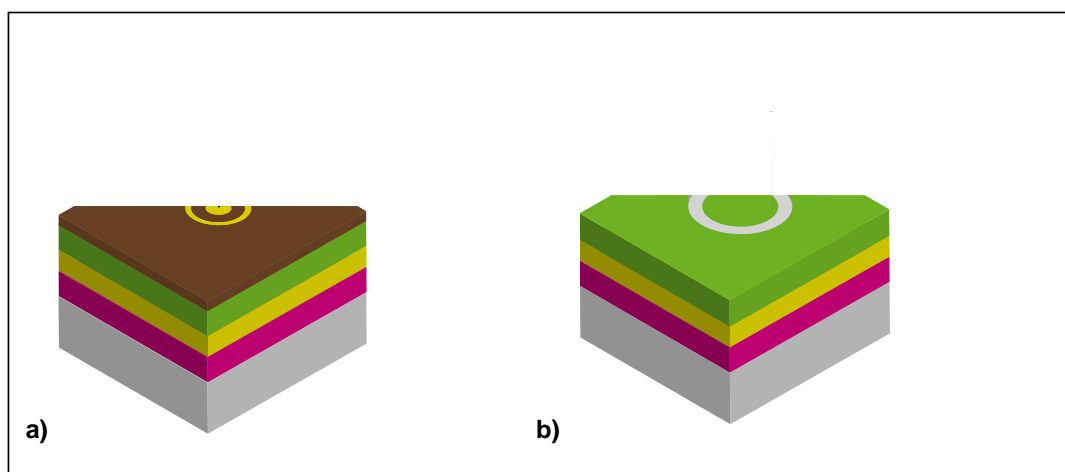


Figure 110. Illustrations Of Concentric Capacitive Electrodes On Top Of A Multi-Layer Dielectric: (A) Sensor Configuration And Test-Piece Structure Used In The Numerical Modeling; (B) Assembled Hand-Held Probe Based On The Modeling In (A)

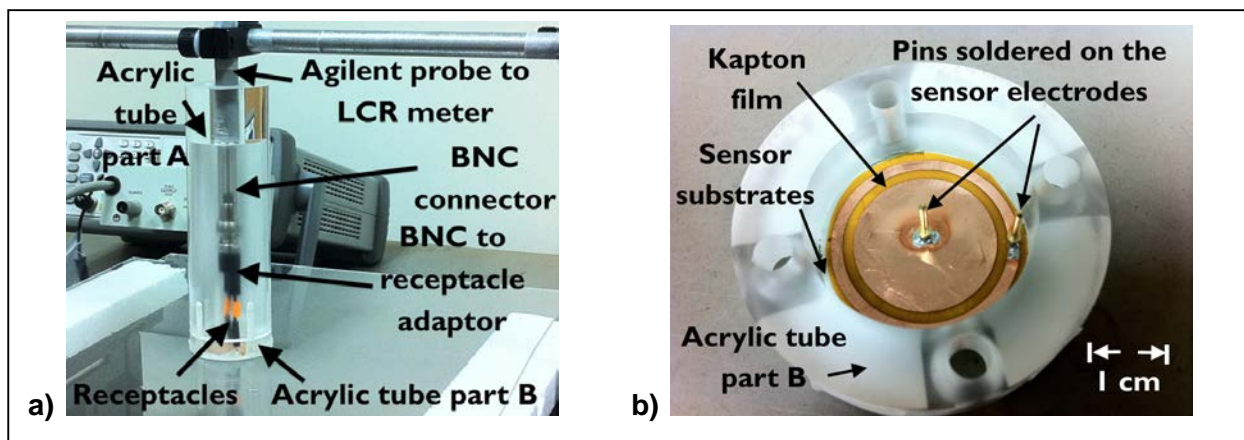


Figure 111. Photograph Of The Assembled Probe: (A) Experiment Setup Used In Probe Lift-Off Measurements; (B) Concentric Capacitive Sensor Fabricated By Photolithography

own relative dimensions, regardless of the overall dimensions of the sensor. In addition, calculations indicated how the sensor can be optimized for sensitivity to changes in core permittivity of a three-layer test-piece such as an aircraft radome. Benchmark experiment results were collected for one, two-, and three-layer test-pieces and very good agreement with calculated C_T was observed. The sensor was successfully applied to detection of ingressed water in a sandwich structure.

Building upon the benchmark activities described above, a prototype rotationally-invariant capacitive probe with concentric coplanar electrodes was designed, Figure 111. Two versions of the probe, with different target sensing penetration depths, were constructed in such a way that removal of parasitic capacitances can be achieved. Capacitance measurements for the probes in surface contact with laminar structures showed agreement with theoretical predictions to within 10%. Important factors governing the penetration depth of concentric capacitive sensors were investigated numerically, followed by experimental investigation on stepped samples, whose results were found to be in accordance with numerical predictions. The effect of probe lift-off on inferred permittivity of dielectric slabs was also investigated. As lift-off increases, uncertainty in inferred permittivity increases dramatically. On the other hand, the capacitive probes show good sensitivity to low-contrast inhomogeneities embedded in laminar structures; 1 cc of a low contrast liquid injected into the core of a glassfiber-honeycomb-glassfiber sandwich structure was detected successfully.

3.11.2.2 Co-Planar Interdigital Capacitive Sensors For Defect Detection And Quantitative Dielectrometry

To increase signal-to-noise (SNR) ratio, two circular coplanar interdigital sensors with i) a spiral interdigital configuration and ii) a concentric interdigital configuration for the nondestructive evaluation of multilayered dielectric structures were developed [b], Figure 112. A numerical model accounting for sensor geometry, test-piece geometry and real permittivity, and metal electrode thickness was developed to calculate the capacitance of the sensors when in contact

with a planar test-piece comprising up to four layers. The validity of the numerical model was demonstrated by good agreement (to within 5%) between numerical predictions and benchmark experiment results. Compared with the two-electrode coplanar capacitive sensor discussed above, the interdigital configurations were found to have higher signal strength and SNR, better accuracy in materials characterization, and higher sensitivity in detecting surface flaws when prior knowledge of approximate flaw size is available. On the other hand, the disk-and-ring sensor shows a deeper penetration depth for same electrode separation, less susceptibility to lift-off variations and better sensitivity in detecting internal flaws in sandwich structures.

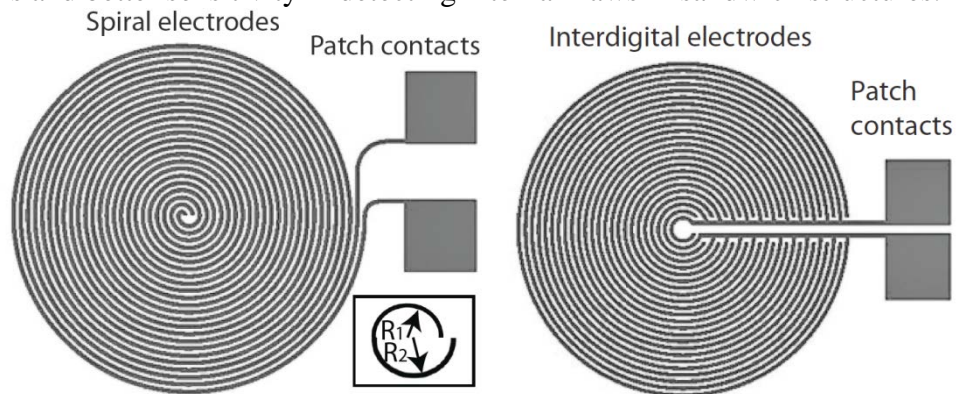


Figure 112. Schematic Diagram Of Spiral And Concentric Interdigital Coplanar Capacitive Sensors

For example, the capacitance measured as a spiral sensor is scanned over a glassfiber-honeycomb-glassfiber sandwich panel containing various volumes of injected water is shown in Figure 113. Comparing with the same scan by a disk-and-ring sensor, configuration shown in Figure 110 and result shown in Figure 113, the percentage change in capacitance is higher for the disk-and-ring sensor whereas the measured C is higher in the case of the interdigital sensor.

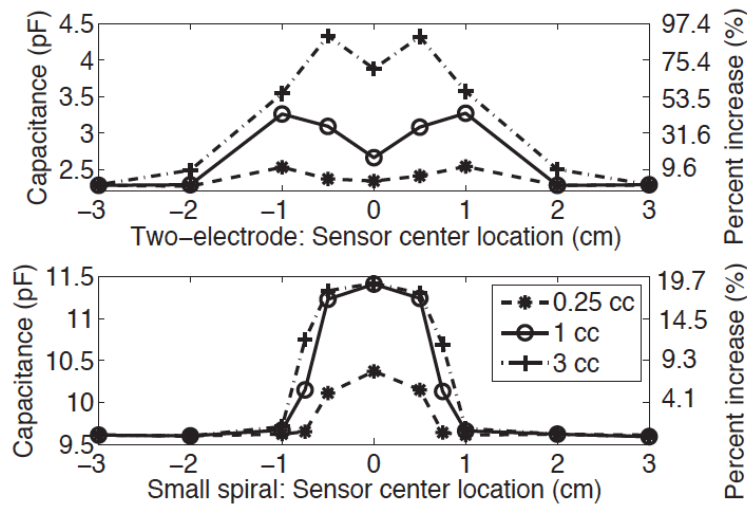


Figure 113. Capacitance Measured As The Small Spiral And The Disk-And-Ring Sensors Scan Over Glassfiber-Honeycomb-Glassfiber Sandwich Panels Containing Various Volumes Of Injected Water. Percentage Increase In C Is Relative To The Capacitance Measured On A Region Remote From The Injected Water

Conclusions

1. A resonant patch microwave sensor for inspecting individual layers of a three-layer dielectric structure was designed, fabricated and tested. Using theoretical techniques, the sensor was designed for good sensitivity, penetration depth and spatial resolution. Experimental results obtained with a prototype sensor showed that it achieved sensitivity $\Delta\epsilon = 0.046$, spatial resolution 5 mm, and penetration depth 4.35 mm in inspecting the core of a fiberglass-honeycomb-fiberglass radome structure. It was also shown that this sensor is able to detect 0.25 cc water in one honeycomb cell easily.
2. The backward wave and DNG bandwidths of 3D periodic arrays with different arrangements of spheres have been analyzed for various combinations of sphere types, Table 4 Results show that arrangements (d), (c), and (b), Figure 108, can provide, respectively, the widest DNG bandwidths 0.21 %, 0.069 %, and 7.4 % for spheres combinations i), ii), and iii), Table 4 respectively. Compared with these reported in other literature with arrangement (g); 0.17 %, 0.075 %, and 2.9 %, analysis of those available arrangements of the spheres shows similar narrow DNG bandwidths for spheres combinations i) and ii), and wider DNG bandwidths for spheres combination iii).
3. Electrostatic Green functions for a point charge on top of multi-layered dielectric structures have been derived using the Hankel transform given the cylindrical symmetry of the concentric sensor. Output signal of a disk-and-ring coplanar capacitive sensor, transcapacitance $|C_T|$, has been calculated through the method of moments and corresponding benchmark experiments have been carried out. Very good agreement

(within 4%) between theory and experiment on one-, two-, and three-layer dielectric test-pieces in free space has been observed. This suggests that the sensor is suitable for quantitative dielectrometry in order to determine permittivity of individual layers in multi-layered structures.

4. Two handheld capacitive probes with different target penetration depths were built and tested. Following a calibration procedure that accounts for stray capacitances and the presence of the probe casing, which is not accounted for explicitly in the accompanying model, agreement to within 10% between measured and calculated capacitances was demonstrated for experiments on laminar structures. The penetration depth of concentric capacitive sensors was defined and studied both numerically and experimentally. In order to acquire inversely determined material permittivities close to the actual values, small liftoff values are desirable because such measurement setups give rise to the best signal strength. If the probe is to be used for quantitative permittivity measurement, then calibration on a known test sample may be preferable to calibration in air. The outstanding capability of the handheld sensors in detecting relatively small contrast zones in one- layered and multi-layered structures was demonstrated experimentally.
5. Spiral interdigital sensors and concentric interdigital sensors have been developed, to improve the output capacitance and signal-to-noise ratio when compared with the disk-and-ring coplanar concentric capacitor mentioned above. A numerical model was developed to describe the behavior of the interdigital sensors. Experimental verifications showed that the numerical predictions and measurement results agreed to within 5%. Through numerical and experimental comparisons, the two-electrode configuration was found to possess advantages such as deeper penetration depth, better immunity to lift-off variations and higher sensitivity in detecting internal inhomogeneities in sandwich structures. The interdigital configurations were found to be able to achieve higher output signal strength, better signal-to-noise ratio, better accuracy in materials characterization and higher sensitivity in detecting surface defects when prior knowledge of approximate flaw size is available.

Recommendations

1. Develop electronics to replace costly vector network analyzer component of the resonant patch sensor measurement system and develop theory to infer more than a single parameter (real permittivity) from the measurement.
2. Design and develop metamaterials as a 'superlens' in a microwave NDE system for achieving sub-wavelength spatial resolution imaging in biological and industrial applications.
3. Develop quantitative dielectrometry (capacitive NDE) for monitoring degradation in polymers, polymer-matrix composites, ceramics and ceramic-matrix composites.

3.12 Advanced Terahertz Capabilities For Aerospace Material Inspections (Chiou)

Investigation Team: C. Thomas Chiou and R. Bruce Thompson

Motivation

This project was focused on (1) developing novel modeling and data processing techniques for terahertz radiation (THz) and Fourier-transform infrared (FTIR) inspections of advanced materials used in U.S. Air Force aeronautical and aerospace vehicles, (2) supporting AFRL projects already in place to evaluate ceramic mirrors, imaging aerospace coating integrity, inspecting composite patch integrity and potential defects beneath the patches, and inspecting thermal protection materials, and (3) providing assistance in optimizing the performance of AFRL's THz and FTIR systems.

Results – Theory and Experiments

During the course of this project, significant progress has been made in modeling and material characterization involving both THz and FTIR. In the following, highlights are given to a few representative topics.

3.12.1 THz Beam Modeling Using Point Source Synthesis

Current in the THz field, the most capable technology suitable for NDE flaw detection is time-domain spectroscopy (TDS). The transmitter of a TDS system bears the same functionality of the transducer for a ultrasonic pulsed system. Figure 114 illustrates the inner working of one typical THz transmitter, where the impinging ultra-fast laser pulse train excites a biased photoconductive antenna (dipole) which in turn emits the THz radiation. Through the adjacent lens, this THz generation mechanism produces a rather complicated radiation pattern in the field, and requires a thorough study. Below describes the development of point source synthesis model to meet such a need.

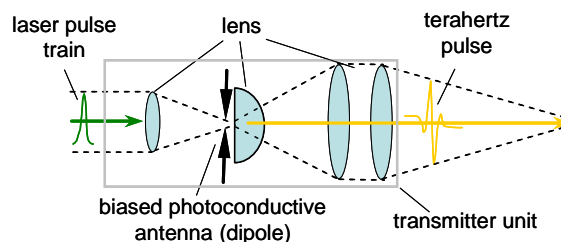


Figure 114. Inner Working Of A Typical THz Transmitter Using Photoconductive Antenna

The point source synthesis model is based on the concept of Huygens principle. Kirchhoff further laid down the mathematical foundation to develop the Fresnel-Kirchhoff diffraction theory, which has been utilized in early THz radiation studies [126, 127]. In our development of THz simulation, we have implemented point source synthesis models using Fresnel-Kirchhoff formulation (hereafter abbreviated as F-K model) and the second Rayleigh-Sommerfeld formulation (R-S model). The effort was focused on the validation these two models with a fast Gauss-Hermite beam model (G-H model) that was modified from an existing ultrasonic counterpart. For simplicity, this preliminary validation process was limited to planar circular probe interfaces, although both R-S and F-K models are capable of handling complicate interface geometry.

The basic geometry for the diffraction theory of an aperture (probe interface) is illustrated in Figure 115. For a field point, P, at distance, R, away from a point, T, on the aperture surface, S, (denoted by vector, \underline{R} , pointing from P to T), its electric field strength, E, in the F-K model can be expressed as

$$E_{F-K}^{\text{point}}(P) = \frac{A}{4\pi} \int_S \frac{e^{-ik \cdot \underline{R}}}{R} \frac{e^{-ik \cdot \underline{r}}}{r} \left[\cos(\underline{n}, \underline{R}) \left(ik + \frac{1}{R} \right) - \cos(\underline{n}, \underline{r}) \left(ik + \frac{1}{r} \right) \right] ds \quad (1)$$

where A is the amplitude of the incoming point (spherical wave) source, Q, at distance, r, (denoted by vector \underline{r} from Q to T) before the aperture surface. $\cos(\underline{n}, \underline{r})$ and $\cos(\underline{n}, \underline{R})$ are the directional cosines between outward unit normal, \underline{n} , at point T and vector \underline{r} , and between \underline{n} and vector \underline{R} , respectively. \underline{k} is the wave number vector with magnitude k. The circular aperture considered here is specified by its diameter, D. The surface integration is carried out over the entire circular aperture area. If the incoming source is of plane-wave type instead, then Equation (1) reduces to

$$E_{F-K}^{\text{plane}}(P) = \frac{A'}{4\pi} \int_S \frac{e^{-ik \cdot \underline{R}}}{R} \left[\cos(\underline{n}, \underline{R}) \left(ik + \frac{1}{R} \right) - \cos(\underline{n}, \underline{r}) ik \right] ds \quad (2)$$

where \underline{r} now denotes the direction of the incident plane-wave and A' also absorbs the phase of the incident plane-wave source.

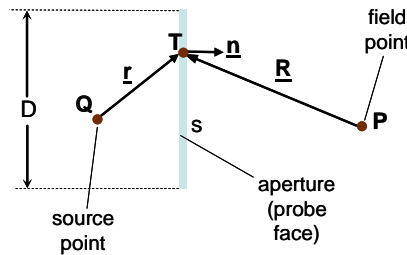


Figure 115. Schematics Of Ray Paths In The Diffraction Formulation

Although the Fresnel-Kirchhoff theory has been widely used in the literature, its boundary conditions bear certain internal inconsistencies. Rayleigh-Sommerfeld formulation resolves this

problem by employing alternative Green functions, which led to two formulations. The R-S model considered here takes the second formulation:

$$E_{R-S}^{\text{point}}(\mathbf{P}) = \frac{-A}{4\pi} \int_S \frac{e^{-ik \cdot \mathbf{R}}}{R} \frac{e^{-ik \cdot \mathbf{r}}}{r} \cos(\underline{\mathbf{n}}, \underline{\mathbf{r}}) \left(ik + \frac{1}{r} \right) d\mathbf{s} \quad (3)$$

and the plane-wave source version is:

$$E_{R-S}^{\text{plane}}(\mathbf{P}) = \frac{-ikA'}{4\pi} \int_S \frac{e^{-ik \cdot \mathbf{R}}}{R} \cos(\underline{\mathbf{n}}, \underline{\mathbf{r}}) d\mathbf{s} \quad (4)$$

In this work, we are able to improve on the near-field accuracy by keeping all secondary terms in these equations.

To cross check the accuracy and applicability of these models, we have computed several 1-THz beam fields situated in vacuum. In all cases, the field covers a rectangular area of 99.75 mm horizontally by 20 mm vertically at 0.25mm resolution. The source excites the field through a 10mm-diameter aperture (probe face) located 3.1 mm away from the middle of the field's left edge. Each beam field was normalized by its own maximum peak amplitude. Figure 116 shows the benchmark beam field using G-H beam model for a circular planar probe. This is equivalent to plane-wave source excitation in both F-K and R-S models. Figure 117 plots one such beam field using F-K model via Equation (2). We see that both models predict very similar beam patterns with comparable amplitude in the far-field main beam, while F-K model is able to reveal much more definite details in the near-field main beam and in the side lobes. These detailed results of F-K model, however, are obtained with the trade-off in computation time, which is order-of-magnitude more than that of G-H model.

The field computed by using R-S model (Equation (4)) is almost identical to that of Figure 117 except for some minor differences in the near-field main beam. This shows the close relationship between these two models. In fact, it has been pointed out that the F-K solution is actually the arithmetic average of the two R-S solutions [128]. Lastly, we demonstrate the feasibility by using point source as plane-wave excitation. If the plane-wave excitation in previous cases is replaced by a point source (0.1 mm behind the aperture via Equation (1)), it is not surprising to see that the beam structure changes into a uniformly all-directional spreading pattern (Figure 118). The highly directional straight beam pattern, as seen in Figure 117, can be "recovered" by increasing the distance between the point source and the aperture to, say, 1000mm. This practically turns the point source into a plane-wave excitation coming from infinity. Overall, we have observed very good agreement between the three models.

Based on these point-source synthesis models, we went on to model THz inspection of space shuttle's spray-on foam insulation structure under NASA grant #NAG102098 and successfully made comparisons with experimental data of drilled holes embedded in a foam sample. Theoretical modeling efforts were motivated by the NASA funded grant and leveraged to the benefit of this program. The readers are referred to [129] for more details.

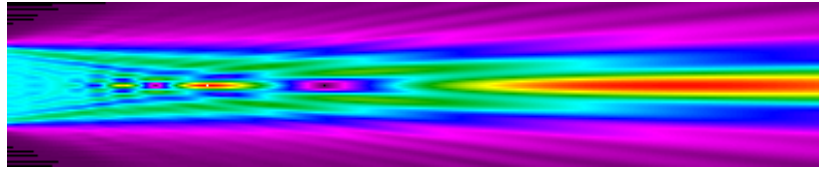


Figure 116. Benchmark Beam Field Using G-H Beam Model For A Circular Planar Probe

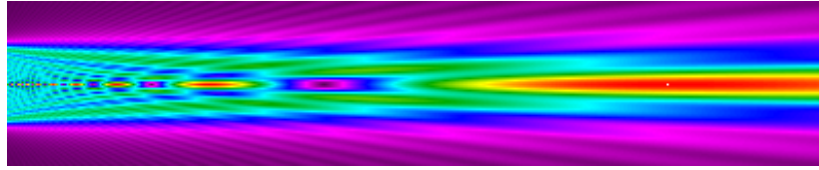


Figure 117. Same Beam Field As Figure 3 By Using F-K Model Via Equation (2)



Figure 118. Spherically Spreading Beam Field Of Point Source By Using F-K Model Via Equation (1)

THz Characterization Of Polyimide Disk

The work described below was to calibrate a new AFRL time-domain spectroscopy (TDS) system and to model the THz thru-transmission measurement from a polyimide disk of 850 micron thickness. The polyimide resin is thought to be the critical component with regard to heat-induced damage and matrix cracking in a glass-fiber composite material, and therefore its characteristic response to THz radiation as an NDE methodology was investigated. The preliminary beam calibration using simple Gaussian beam model is shown in Figure 119. For the specified focal length of 50mm, effective diameters of 26 and 30mm for the two orthogonal axes were determined to best fit the slightly elliptical beam profile. Using these parameters, a focal spot of 4 mm seems to agree with the experiment as well. In characterizing the electromagnetic properties of the polyimide disk, it is reasonable to assume the relative permeability, μ_r , of polyimide is unity as is the case for most non-magnetic materials. Given this, the relative permittivity, ϵ_r , can then be calculated through

$$\epsilon_r = \left(1 + \frac{c\Delta t}{L} \right)^2 \quad (5)$$

where c is speed of light and L is the thickness of the polyimide disk. Δt is the delay of time-of-flight between the peaks of thru-air and thru-disk waveforms. Using the Δt measurement, we

estimated ϵ_r to be 3.43, which is very close to the value of 3.24 in a related work [130]. In terms of index of refraction, this amounts to 1.85 vs. 1.8. For the glass fiber composite sample, the index of refraction was estimated to be 2.05 ± 0.01 and the absorption coefficient was estimated to be between $17.5 \pm 0.8 \text{ cm}^{-1}$ (0.5 THz) and $38 \pm 1.6 \text{ cm}^{-1}$ (1 THz), which are in reasonable agreement with other published results [131].

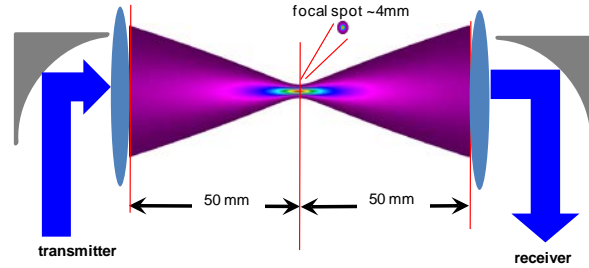


Figure 119. Simulated Beam Profile Of The AFRL THz TDS System

For the task of signal modeling, the core framework is based on a reciprocity-based measurement model, which has been widely used in many fields including THz and UT. In this approach, reference data are taken in order to obtain the system response. For example, to simulate the THz signal propagating through the polyimide disk, a separate thru-air measurement under the same experimental settings was collected as the reference. In the frequency domain (denoted as f), the thru-disk polyimide signal $\Gamma_{PI}(f)$ can be expressed as a modular product:

$$\Gamma_{PI}(f) = \Gamma_{air}(f) \exp[-\alpha(f)L]T(f) \quad (6)$$

where $\Gamma_{air}(f)$ is the thru-air reference signal obtained from a separate measurement. Term $\exp[-\alpha(f)L]$ accounts for the attenuation/absorption of the media, in which $\alpha(f)$ is the attenuation factor and L is again the disk thickness. $T(f)$ denotes the transmission coefficient.

To apply Equation (6) for material characterization, all terms involved must be known. As a starter, $T(f)$ can be approximated by plane-wave half-space transmission coefficients at the front and back surfaces of the polyimide disk:

$$T(f) \approx T_{half-space} = T_{air \rightarrow PI} T_{PI \rightarrow air} = \frac{2\eta_{PI}}{\eta_{air} + \eta_{PI}} \frac{2\eta_{air}}{\eta_{air} + \eta_{PI}} \quad (7)$$

where h is the intrinsic impedance. Then attenuation factor $\alpha(f)$ can be computed by

$$\alpha(f) = -\frac{1}{L} \ln \left(\frac{1}{T(f)} \frac{\Gamma_{PI}(f)}{\Gamma_{air}(f)} \right) \quad (8)$$

given the ratio between $\Gamma_{PI}(f)$ and $\Gamma_{air}(f)$ is available throughout the frequency range. A common practice to obtain numerically stable values for this ratio is to apply Wiener filter deconvolution, which in the frequency domain is often expressed as

$$\frac{\Gamma_{PI}}{\Gamma_{air}} \approx \frac{\Gamma_{PI}\Gamma_{air}^*}{|\Gamma_{air}|^2 + \left(\frac{S}{N}\right)^{-1}} \quad (9)$$

in which, * denotes the complex conjugate. S/N represents an estimate of the signal-to-noise ratio in the data, and can be treated as a damping factor in the deconvolution process. Figure 120 plots the deconvolved ratio vs. frequency subjected to two different damping factors. With the ratio determined, the absorption coefficient, equal to two times of attenuation factor $\alpha(f)$, can be readily computed by Equation (8). As shown in Figure 121, the absorption coefficient curve agrees reasonably well with the data of reference 3, from 3 cm^{-1} (at 0.5 THz), 7.5 cm^{-1} (0.8 THz) to 10.5 cm^{-1} (1.0 THz).

With all terms determined on the right hand side of Equation (8), we can compute the thru-transmission component of polyimide disk over the frequency range of interest. The time-domain signal can then be “recovered” via a Fourier transform. Figure 122 shows the comparison of the polyimide signal between the experiment and model. Very good agreement is clearly seen. Further details of this work can be found in [132].

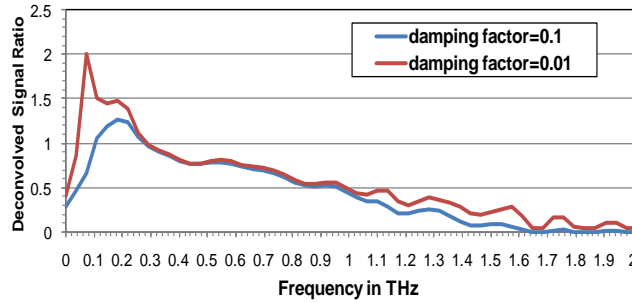


Figure 120. Signal Ratio By Wiener Filter Deconvolution

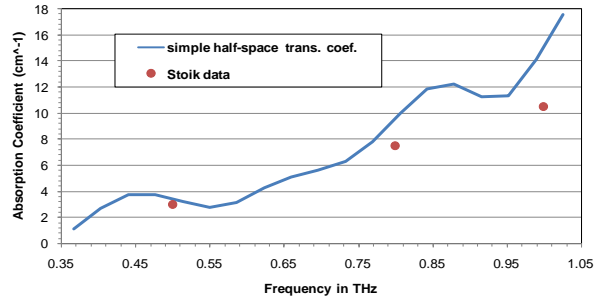


Figure 121. Absorption Coefficient Estimates In Good Agreement With [130]

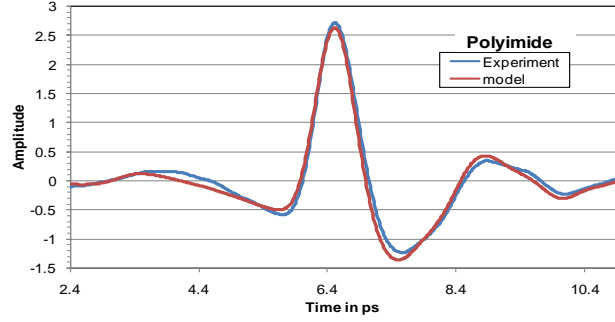


Figure 122. Good Agreement In Polyimide Signals Between Experiment And Model

3.12.2 FTIR Material Inversion

In this project, we have conducted a simulation study for the Air Force's ongoing work of material characterization using Fourier transform infrared (FTIR) spectroscopy. The main effort was to simulate FTIR reflection from an air-dielectric interface at oblique incidence (Figure 123) and to determine the dielectric's electromagnetic properties such as the refractive index by using the reflection data taken at various incident angles. With sufficient thickness, the dielectric can be considered as a half-space medium. A simple uniform plane-wave model was then developed for such configuration involving the Fresnel equations. For an unpolarized IR source, the irradiance (intensity) of the reflected wave consists of both parallel polarization (TM mode) and perpendicular polarization (TE mode) components as functions of both the refractive index, n_d , and the incident angle, θ (Figure 123):

$$I_r(n_d, \theta) \propto A_{TE} R_{TE}^2(n_d, \theta) + A_{TM} R_{TM}^2(n_d, \theta) \quad (10)$$

in which the Fresnel reflection coefficients R_{TM} and R_{TE} are of the form (with the air refractive index taken as unity implicitly) [133]

$$R_{TM} = \frac{\left[n_d^2 - \sin^2 \theta \right]^{\frac{1}{2}} - n_d^2 \cos \theta}{\left[n_d^2 - \sin^2 \theta \right]^{\frac{1}{2}} + n_d^2 \cos \theta}; R_{TE} = \frac{\cos \theta - \left[n_d^2 - \sin^2 \theta \right]^{\frac{1}{2}}}{\cos \theta + \left[n_d^2 - \sin^2 \theta \right]^{\frac{1}{2}}} \quad (11)$$

We assume a “well mixed” unpolarized source so that $A_{TE}=A_{TM}$ in Equation (10).

In order to remove the dependence of A_{TE} and A_{TM} in Equation (10), we normalize all reflected irradiance $I_r(n_d, \theta)$ by that at 5° incident angle. This 5° angle is chosen to match with the configuration in the experiment where 5° is the closest possible to normal incidence. To determine the electromagnetic properties of a dielectric like the lossless refractive index, n_r , and the extinction coefficient n_i here, a nonlinear least squares fitting procedure is proposed. A least squares sum $S(n_r, n_i)$ can be formed between N sets of theoretical $I_r(\theta_j, n_r, n_i)$ (Equation (10)) and the corresponding experimental data $I_r'(\theta_j, n_r, n_i)$ measured at the N incident angle θ_j :

$$S(n_r, n_i) = \sum_{j=1}^N \left[I_r(\theta_j, n_r, n_i) - I_r'(\theta_j, n_r, n_i) \right]^2 \quad (12)$$

The best fitted solutions for n_r and n_i can then be found by iteratively minimizing $S(n_r, n_i)$ with an initial guess.

In this study, we simulated the experimental data $I_r'(\theta_j, n_r, n_i)$ by adding different levels of “noise” to the theoretical $I_r(\theta_j, n_r, n_i)$. The “noise” was obtained from a uniform distribution using a numerical random number generator. A total of eight data sets from 15° to 85° in increments of 10° were used in the least squares sum (Equation (12)). We again considered the case of lossy glass with $n_r=1.5$ and $n_i=0.3$. For the minimization software, we utilized a Fortran90 update of the original MINPACK-1 [134], which implemented a modified version of the popular Levenberg–Marquardt method.

Extensive numerical experiments at several controlled noise amplitude ranges were conducted. At each noise amplitude range, a total of 100 runs were made. For each run, renewed noise values were added to the theoretical $I_r(\theta_j, n_r, n_i)$ and the minimization procedure was executed five times, each time with a different initial guess. Figures 124 and 125 depict the deviation of the best-fit solutions from the true values of n_r and n_i vs. the several root-mean-square (RMS) noise levels. We are pleased to see that the simulation results are quite stable, showing small deviations at linear increase with noise level. At RMS noise level nearly 0.5 which is 50% of the irradiance amplitude of lower angle data sets, the average of the worst deviations from the true extinction coefficient n_i at 0.3 is only 30%. The performance of MINPACK-1 minimization routine is also exceptional: for 90% of the 100 runs at each noise level, all 5 initial guesses converged to the same best-fit solutions, and for the remaining 10% runs, at least 4 initial guesses converged. Further details can be found in [135].

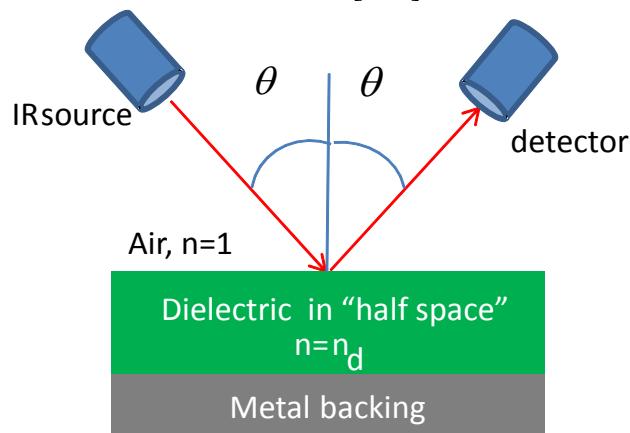


Figure 123. The FTIR Sample And Measurement Settings

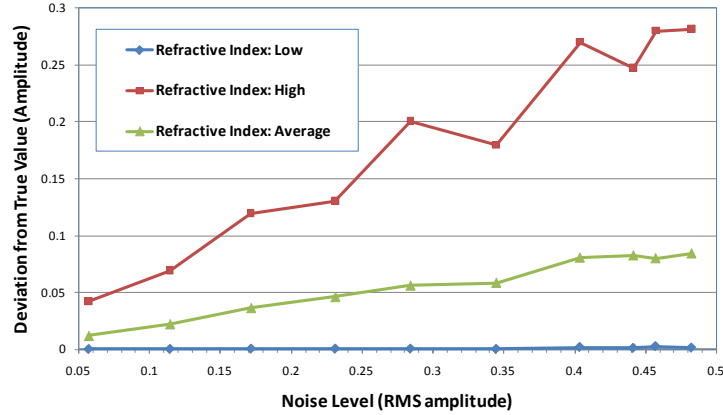


Figure 124. The High-Average-Low Deviations (From The True Value) Of The Best-Fit Refractive Index Vs. Different Noise Levels

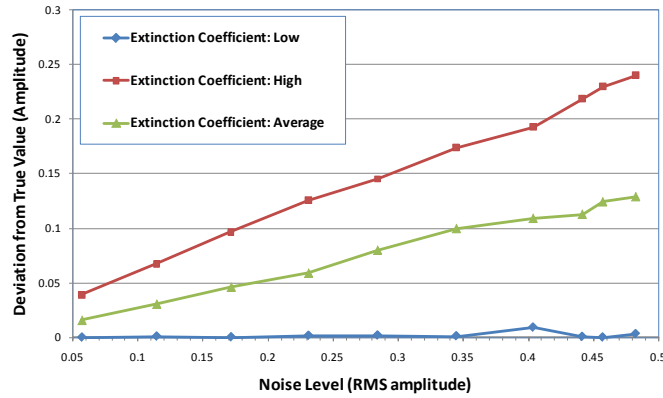


Figure 125. The High-Average-Low Deviations (From The True Value) Of The Best-Fit Extinction Coefficient Vs. Different Noise Levels

3.12.3 Multi-Layered Fresnel Model

In FTIR, it is often observed that the half-space Fresnel model provides sufficient accuracy even for complicated layered media. The applicability of this model in practical situations, however, is not well understood. Here we set out to determine its ranges of applicability, and particularly, the conditions and regions where the layer model overlaps with the half-space model.

The layer Fresnel model used in this study applies to isotropic multilayer dielectric lossless or lossy structure at oblique incidence. Denote the multilayer structure as layers 1 to k separated by 0 to $k+1$ interfaces in $k+2$ media, with 0 and $k+1$ being the incident or exiting interface, respectively (Figure 126). The Snell's law applies to all interfaces:

$$n_0 \sin \theta_0 = \dots = n_i \sin \theta_i = \dots = n_{k+1} \sin \theta_{k+1} \quad (13)$$

where n_i is the complex refractive index for media i and θ_i is the incident angle at interface i . Define the propagating phase p_i as

$$p_i = \frac{2\pi}{\lambda} d_i n_i \sqrt{1 - \frac{n_0^2 \sin^2 \theta_0}{n_i^2}} \quad (14)$$

in which d_i is the thickness of layer i and λ is the wavelength. Also define the local reflection coefficient α at interface, i , as

$$\begin{aligned} \alpha_i &= \frac{n_{i-1} \cos \theta_i - n_i \cos \theta_{i-1}}{n_{i-1} \cos \theta_i + n_i \cos \theta_{i-1}} \text{ (TM polarization)} \\ &= \frac{n_{i-1} \cos \theta_{i-1} - n_i \cos \theta_i}{n_{i-1} \cos \theta_{i-1} + n_i \cos \theta_i} \text{ (TE polarization)}. \end{aligned} \quad (15)$$

Then the reflection coefficient, R_i , at incident interface, i , satisfies the following recursion, starting at $R_{k+1} = \alpha_{k+1}$:

$$R_i = \frac{\alpha_i + R_{i+1} e^{2ip_i}}{1 + \alpha_i R_{i+1} e^{2ip_i}}, i = k, k-1, \dots, 1. \quad (16)$$

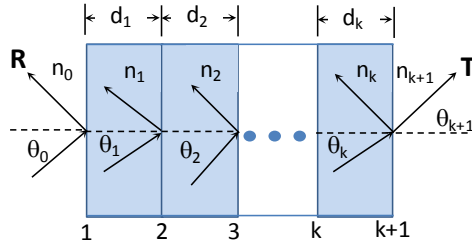
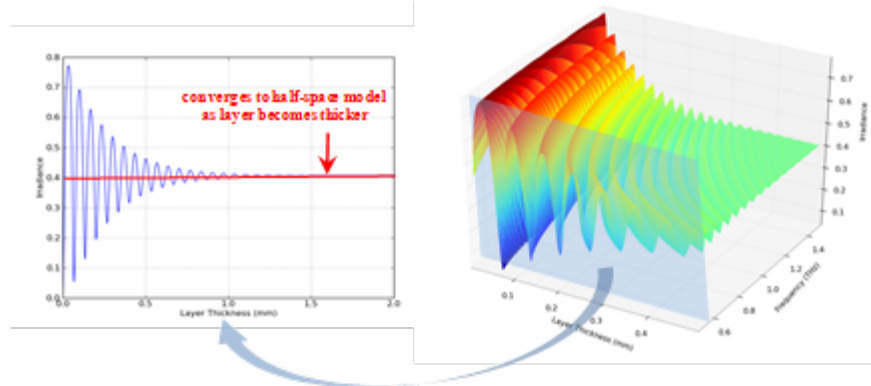


Figure 126. The Multilayer Dielectric Structure Considered In The Layer Fresnel Model

The above expressions can be used to calculate the reflecting irradiance from, for example, a single isotropic dielectric layer in air under unpolarized illumination at variable incident angle as a function of layer thickness and frequency. Left of Figure 127 shows one such plot at incident angle 25 degrees and complex refractive index (4.5, 0.2). Right of Figure 127 is a cross-sectional profile at frequency 0.5THz. It is clearly seen that the oscillation of irradiance gradually decreases and converges to the magnitude of half-space model at 0.41, as the layer

thickness increases above 1mm. This indicates that in practice the simpler half-space model can be used instead at such layer thickness, given the scan frequency and material properties.



sak12345

Figure 127. (Right) Reflecting Irradiance As A Function Of Frequency And Layer Thickness For Incident Angle 25 Deg. And Complex Refractive Index (4.5, 0.2); (Left) A Cross-Sectional Profile At 0.5 THz

We followed with an extensive model calculation to explore the range of “matched thickness” in which the half-space model value agrees with that of the layer model within certain tolerance. Figure 128 plots the “matched thickness” as a function of the complex refractive index with real part (real refractive index n) in the range of 0.1 to 5 and imaginary part (extinction coefficient k) from 0.1 to 1.5 and incident angle at 25 degrees and frequency at 0.5 THz. For all calculations, the “matched thickness” is called when irradiances of both models are converged within 1%. It is seen that the “matched thickness” is relatively uniform with respect to real refractive index n . Relating to the extinction coefficient k , the “matched thickness” increases gradually at higher value k and much faster to above 2mm when $k < 0.2$. Similar pattern to Figure 128 repeats as frequency increases from THz range into far IR region with continuing decrease in “matched thickness”. The “matched thickness” drops below 0.1mm at 15THz, even in the region of low extinction coefficient.

We also examined the pattern of irradiance as the function of the complex refractive index (n, k). Left of Figure 129 plots the irradiance pattern vs. (n, k) at incident angle 25 degrees, frequency at 8THz and layer thickness at 0.1mm. The irradiance increases relatively linearly with real refractive index, n , ranging from 1 to 4, subjected to most values of extinction coefficient, k . In the low k region, the increase of irradiance is perturbed with small oscillation. The magnitude of this oscillation increases as the layer thickness decreases (right of Figure 129 vs. left of Figure 130). The cycles of the oscillation also increases with frequency (Figure 130). With respect to the dependence on the incident angle, the increase of irradiance seems to be slower and to a lower magnitude, when the incident angle increases to 65 degrees. It should be pointed out that the ranges studied in these surface plots are purely for scientific merits; those rare cases, for which the magnitude of the complex refractive index below 1, would not apply to the majority of real-world materials.

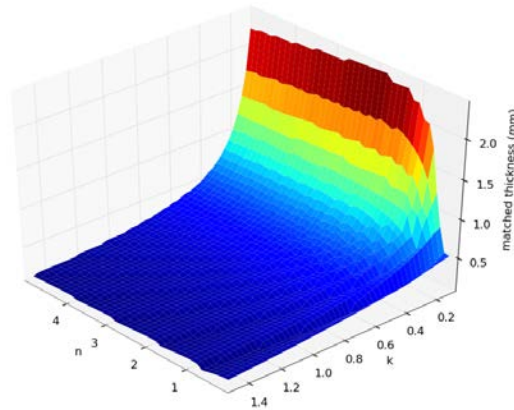


Figure 128. “Matched Thickness” Under Unpolarized Illumination As A Function Of The Complex Refractive Index (N, K). The Incident Angle Is 25 Degrees And Frequency Is At 0.5 THz

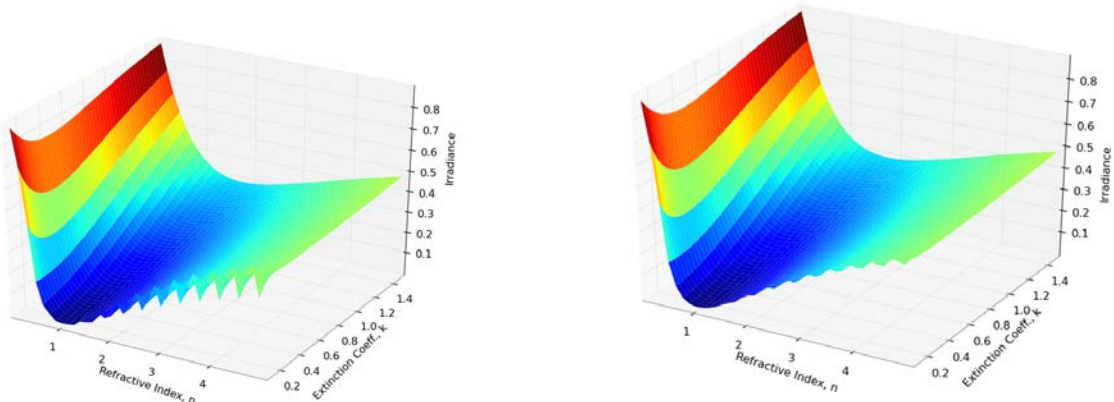


Figure 129. Irradiance Under Unpolarized Illumination As A Function Of The Complex Refractive Index (N, K) For Layer Thickness At 0.1mm (Left) And 0.05mm (Right). The Incident Angle Is 25 Degrees And Frequency At 8 THz

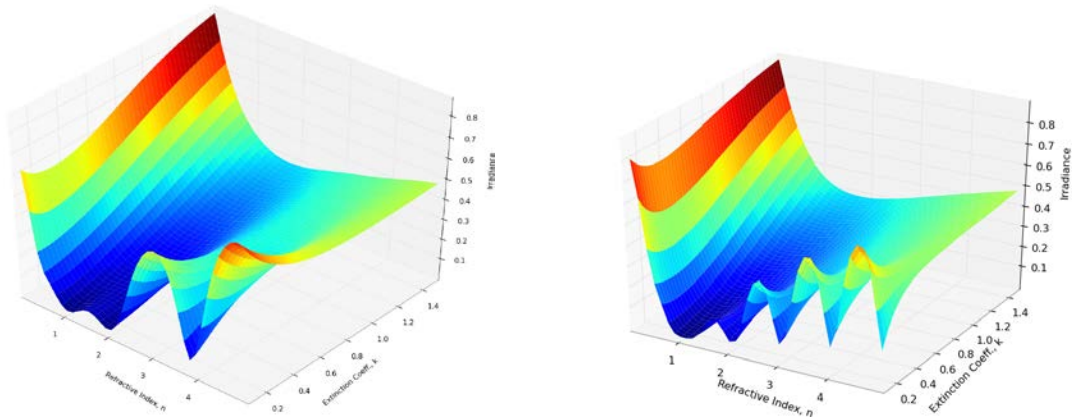


Figure 130. Irradiance Under Unpolarized Illumination As A Function Of The Complex Refractive Index (N, K). For Frequency At 8 THz (Left) And 15 THz (Right). The Layer Thickness Is At 0.01mm And Incident Angle At 25 Degrees

Conclusions

As described above, this project studied a wide range of research topics in modeling and material characterization involving THz and FTIR. Many of the results directly supported AFRL's in-house research, and most contributed to general NDE applications with experimental validation. This project also provided a good education platform for training future engineers and scientists in these areas.

Recommendations

- Continue exploring the application of THz/FTIR for advanced aerospace materials, e.g., Thermal Barrier Coatings (TBCs) and Ceramic Matrix Composites (CMCs).
- Maximize the use of the unique spectral "fingerprints" of THz/FTIR for material characterization and identification.
- Study the feasibility of complimentary technique or technology/data fusion in combining THz and FTIR.
- Determine the optimal usage (and necessary rectification) of THz/FTIR in harsh military environment.

3.13 Novel NDE Concepts For Inspection Of Inaccessible And Complicated Structures (Barnard)

Investigation Team: Dan Barnard and David Hsu (Retired)

Students: Brice Herbers, Lucy Ferneau, Dan Forsman and Zi Rui Pua

Motivation

In the application of NDI modalities to engineering components and structures, the inspector is required to bring a sensor into either near proximity or direct contact with the part to be inspected, so as to allow the probing energy source to interact with the part. In most cases, this is easily accomplished as the area to be inspected is in plain view and accessible. However, other inspections require the removal of access panels or fairings, and in a smaller group of these inaccessible locations, the movements or path required to move the inspection probes around parts to place the probe at the inspection area is physically impossible for the inspector, necessitating removal of additional components/structures to provide access. For this latter group, it would therefore be useful to develop inspection tools that facilitate inspection of these locations that would minimize or eliminate the removal of impeding components. In addition, it would also be of value to have a means of ensuring complete coverage of the inspection area, particularly in locations where it is difficult to visually monitor the track of the probe during an inspection.

Although not inaccessible, other locations requiring NDI are situated in a way that is physically taxing for the operator. Inspectors are often required to hold mirrors and flashlights to make visible the inspection area, contort their arms and bodies to fit into confined spaces, or work with arms at extended reach or overhead to place the probes. All of these requirements, just to place the inspection probe at the desired inspection locale, take concentration away from the interpretation of the NDI signals and significantly increases operator fatigue. The design of robust inspection aids for reducing operator fatigue and gaining accessibility should not simply be an updated version of a "probe-on-a-stick" solution. Many probe designs, such as long, right-angle eddy current pencil probes or the so-called "Sonopens", are just that, and although they do aid in difficult to access locations, they still suffer from (and in some cases exacerbate) problems such as probe tilt variations, inconsistent coupling of the probe to the inspection surface, and increased operator fatigue because of added mass. A robust solution should minimize the incidence of probe tilt (or at least keep the tilt angle low and constant), be rigid enough to ensure proper placement and coupling of the probe to the inspection surface, and allow the mounting of different probe types, sizes and shapes. Also, methods of mounting or securing the fixtures/inspection aids onto the structure or airframe in ways that minimize the weight held and moved by the operator should be exploited to minimize fatigue.

Results – Design and Testing

3.13.1. Problem Definition

Examples of a difficult inspection not suitable for automated inspection are highly stressed components that are prone to fatigue cracking and presenting a significant safety issue. An example of these complex aircraft structures is shown in Figure 131. Inspection is time consuming and fatiguing, with the inspector being required to continuously translate and rotate the placement and orientation of the eddy current probe to maintain the probe axis normal to the part surface at all locations while monitoring the eddy current instrument display. This is particularly difficult in the inspection of the lower fitting, done in an overhead position.



Figure 131. Sample Photograph Of Complex Aircraft Structure [5]

To minimize fatigue, ensure complete coverage and minimize false calls/maintain high probability of detection (by minimizing probe tilt and liftoff), two scanners were conceived. The first, a pantograph style four-bar link mechanism was developed to allow scanning of the nominally flat regions. The second scanner was designed specifically for the arc shaped regions of the fitting, which presents a cylindrically shaped surface to be inspected. Both scanners were designed to produce C-scan type images of the scan area by using the eddy current alarm signal as inputs to change the scan pixel color and encoders to provide probe location information.

3.13.2 Pantograph Scanner

The pantograph scanner, Figure 132, used the software and encoding components of the Generic Scanner, or GenScan [136], with modifications that added scaling and orientation of the image. A pantograph mechanism is commonly used as a “duplicator” or “tracer”, where a stylus at position

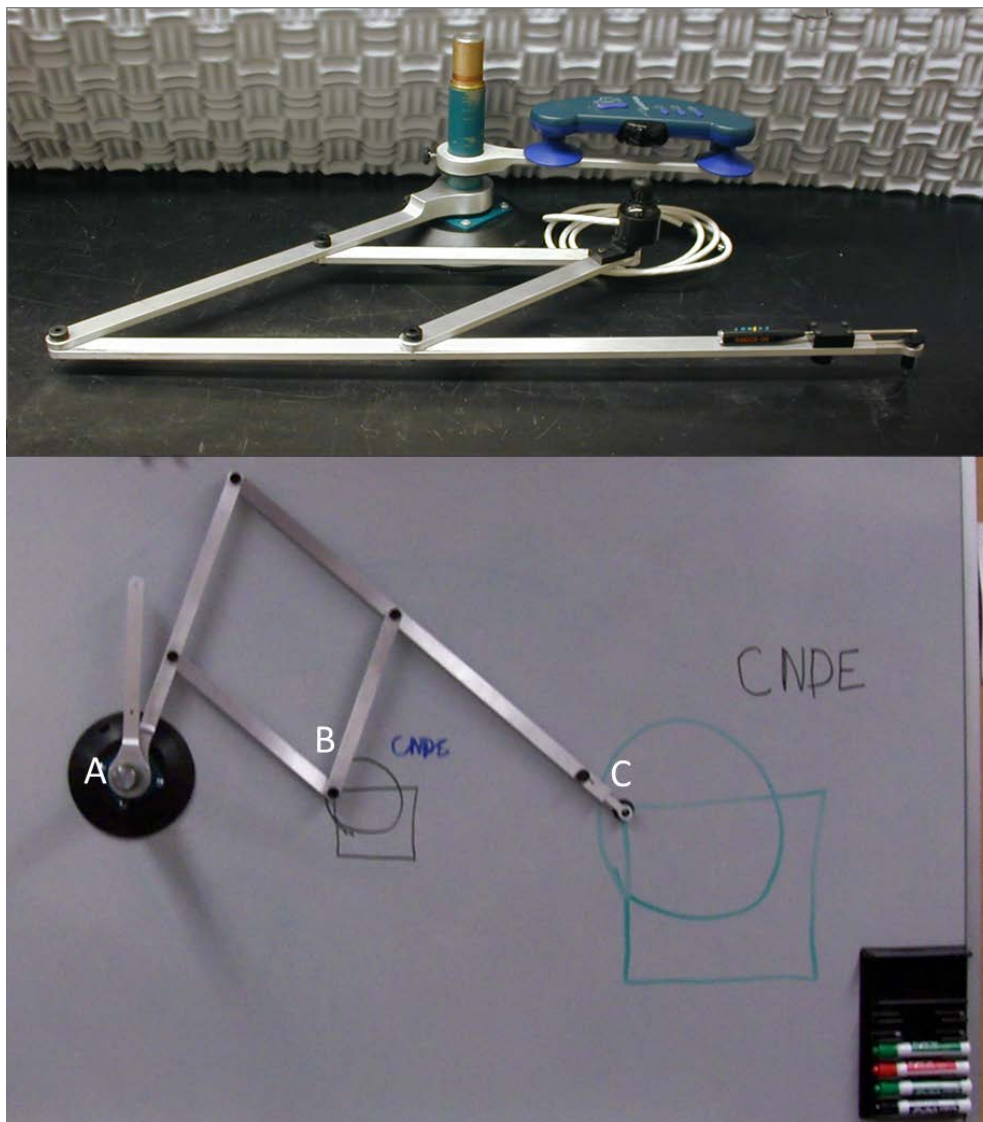


Figure 132. Assembled Pantograph Scanner With Encoding Components And EC Probe , Top, And Tracing/Scaling Capability And Linkage Reference Points Noted

C is guided over a path that is traced (and scaled) by a tracer (either a tool or marker) at position B. The scaling factor is determined by the ratio AC/AB . For this scanner, the eddy current probe is located at position C, with the position tracking head (by Mimio [137]) located at position B. The links of the pantograph and the eddy current probe mount were designed to eliminate as much backlash, flex and probe tilt as possible and be rigid enough to keep the probe in contact with the inspection surface even when scanning upside-down during inspection of the lower wing/fuselage aircraft structures.

A mockup of a complex part, Figure 133, was designed and fabricated from a thick aluminum plate, with EDM notches to simulate cracks placed on both flat and arc-shaped sections, with locations marked as red dots on the panel and numbered in the magnified images. Testing of the pantograph scanner coupled to the GenScan software on the mockup panel produced the results

shown in the following figures. Figure 134 represents the first tests of the completed system, with a photo of the mockup panel and the resulting scaled scan. Note that the scan used two pixel sizes (1/4" and 1/8") and identifies the first four EDM notches scanned, but also includes liftoff signals when edges were encountered (x's) or then translating up and over the button head rivets (y). Figure 135 is the results of using the 1/8" pixel for the entire scan, completed without looking at the pc screen to gauge coverage of the area. This scan took approximately 4 minutes, and coverage is reasonably good, greater than 93%. This test employed the eddy current instrument analog output for pixel gray-scale values and the instruments alarm output for liftoff detection to stop data collection so as not to write invalid pixel data to the image. However, the delay in the alarm latch electronics of the eddy current instrument is quite high, so numerous edge effect signals (black pixels), which are similar to crack signals, are seen around the edge of the scan area.



Figure 133. Aircraft Mockup With EDM Notches Marked As Red Dots And Numbered In Magnified Photos

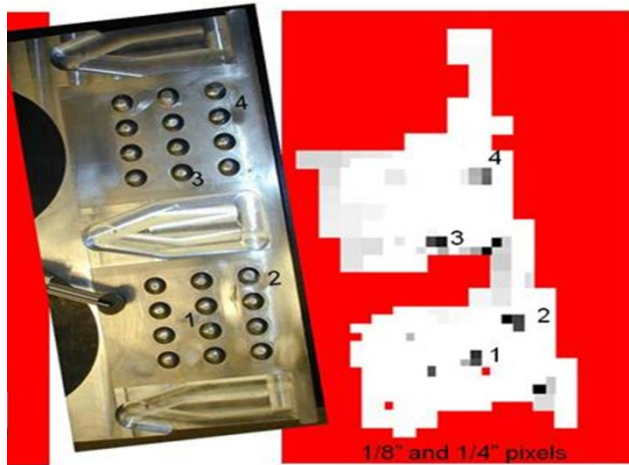


Figure 134. First Test Of The Pantograph Scanner On The Mockup Aircraft Structure Panel, Showing EDM Notch Locations As Well As Liftoff And Edge Signatures

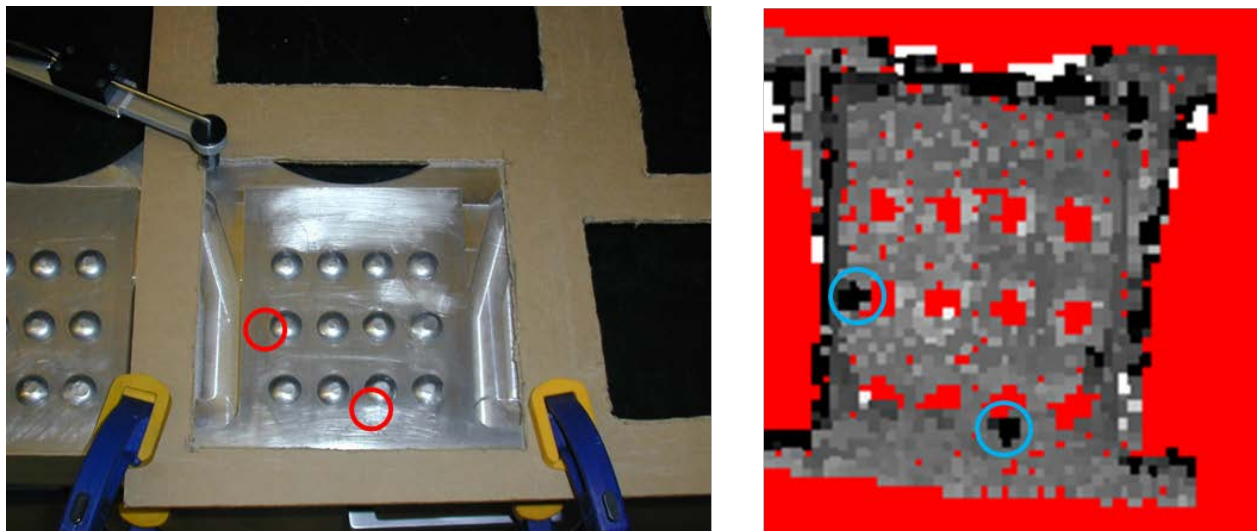


Figure 135. Test Of Pantograph Scanner To Determine Coverage (Operator Did Not View PC Screen To Gauge Areas Not Covered, Shown As Red Pixels). EDM Notches Are Shown Circled In Each Image

The Figure 136 photo was taken during inverted testing of the pantograph scanner. This test was simply to evaluate the stiffness of the pantograph links, to determine if the clearance in the link pivots is excessive enough to allow the linkages to flex under their own weight and that of the cabling to cause the probe to lift off the surface. It was found that the linkage only allowed liftoff of the probe at the farthest extension of the links. Therefore, the high rigidity of the linkages should support the weight of the scanner links, probes and cabling and therefore minimize the fatigue experienced by the operator, who only has to guide the probe over the scan surface.



Figure 136. Inverted Tests Of Pantograph Scanner To Evaluate Rigidity Of Linkages And Ability To Support Probes And Cabling So To Eliminate Liftoff Of The Probes And Minimize Operator Fatigue

Because the smallest pixel size employed in the scans was 1/8", this is the minimum size crack increment that could be identified with the scanner. The 1/8" pixels were used because of the minimum resolution of the Mimio encoder, ± 0.020 inches. With a scale factor of nominally 0.4, this makes the minimum resolution at the probe approximately ± 0.050 inches, which spans approximately 1/8". It is expected that the scan resolution does not need to be smaller than the effective probe aperture. However, if additional resolution is necessary, the small inner links could be made longer, which would increase the scale factor and increase the effective spatial resolution at the probe.

3.13.3 Arc Scanner

For the arc section of the aircraft structure scanner, a different approach was chosen that aimed at eliminating the need for a laptop pc in making manual scans. For this inspection area, a simple pivoting fixture was designed that incorporates a simple magnetic rotary encoder. A Z-axis translation tube that mounts the eddy current probe was affixed to the pivot, allowing the operator to index the probe up or down, along the axis of the arc. Z-axis increments are 1/24 inch and features a spring loaded detent to allow the operator to easily move the probe to each successive scan line. The angular resolution of the rotary encoder of 0.35° and coupled with arc radius of 4 inches, spatial resolution along the arc is on the order of 0.012 inches, making the overall resolution of this scanner smaller than the probe diameter. The scanner is held to the

wing/fuselage surface by a manually pumped suction cup rated at 70 lbs. pull-off (the same as that for the pantograph scanner). A CAD image of the arc scanner is shown in Figure 137.

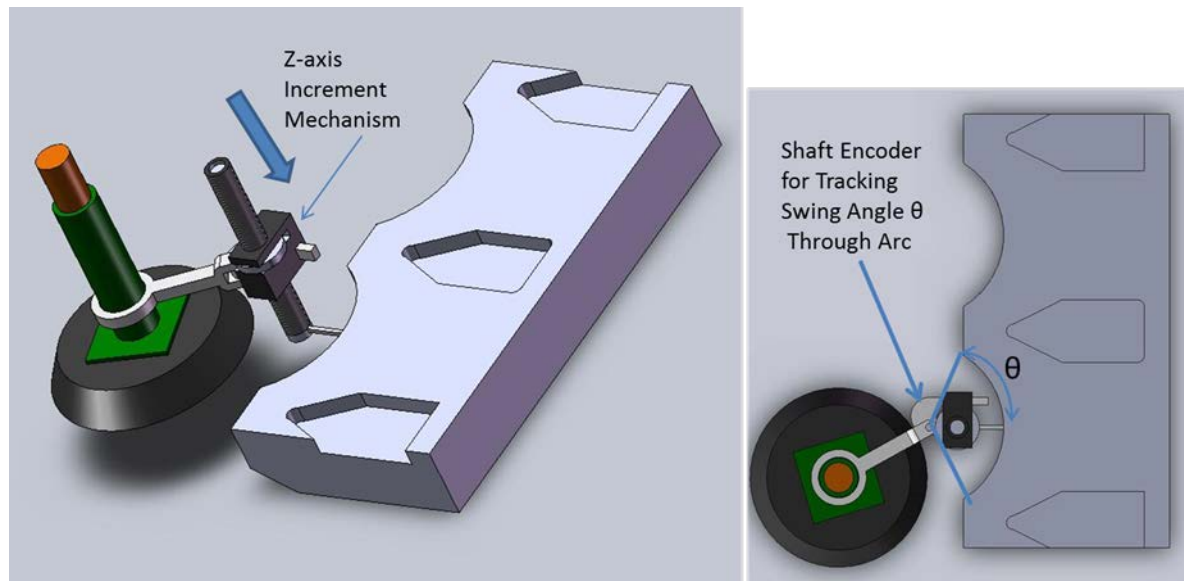


Figure 137. CAD Model Of Arc Scanner And Simulated Aircraft Fitting Mockup Panel

The approach used to allow the elimination of the laptop pc but still facilitate C-scan production and image archiving involved the use of a commercially available miniature LCD screen and microprocessor. The LCD, by 4DLabs [138], is used in cell phones and is inexpensive, and features a touch screen, onboard SD memory card for image and operating software storage, is capable of serial inputs and digital IO. For this work, a menu system was created and ran on the onboard microprocessor that reads serial inputs from the rotary encoder and converts these to position on the screen. The alarm output of the eddy current instrument is used for the NDE signal that changes pixel colors: green for no alarm (no flaw) and red for an alarm condition (flaw detected). In this way, a simple GO/NO GO image is created as the probe is rotated about the scanner pivot (scan direction) and translated in the Z-direction (step direction). Because no encoder is connected to the Z-axis, each time the operator increments the Z-axis position, a simple tap on the LCD touchscreen instructs the software to increment one scan line in the image. Additional icons allow the operator to jump forward or backward any number of scan lines if desired. The operator sets the scan arc length at the start of a scan by moving the probe along the arc to the derived starting position and selecting the arc scan start position icon (labeled “head” on the LCD), pivoting the probe along the arc to the end position and selecting the arc scan end position icon (labeled “tail”). Then simply selecting the “scan” icon starts a scan. When finished, the operator can save the scan or erase the scan and start again. Images can also be transferred to a pc over a USB connection or deleted via icons on the LCD touchscreen.

Additional images of the mechanical and electronic hardware are shown in Figure 138. Figure 139 shows a test scan of the scanner, with a close-up of the LCD screen showing EDM notches 7, 8 and 9 (Figure 133) as red/orange regions. Other red/orange pixels at the top and bottom of

the image are from edge effects/liftoff at the ends of the arc scan, where the probe has been rotated enough to interact with the edge of the arc section of the sample. The upper left image in Figure 139 shows the suction cup mounted below the top surface of the mockup panel.

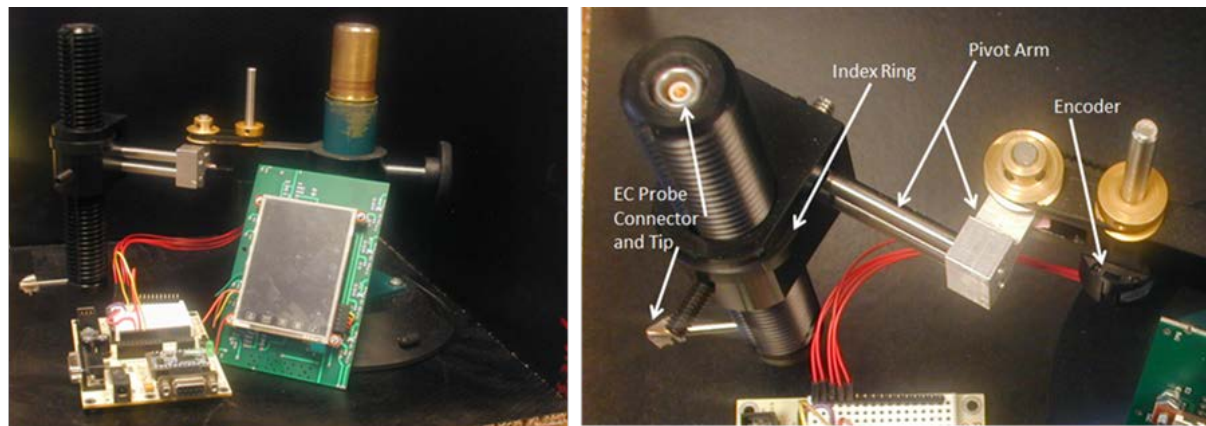


Figure 138. Electronic Hardware For The Arc Scanner Are Shown, Left, A Close-Up Of The Scanner, Right



Figure 139. Testing Of The Arc Scanner, With Zoom Of LCD Screen Showing EDM Notch Indications And Edge/Liftoff Effects At Top And Bottom Of Image Corresponding To The Edges Of The Arc Section On The Mockup Panel

This will not be the case in actual operation on the fuselage or wing, but was convenient for these simple lab tests. The arm mounting the scanner to the suction cup has adequate travel, along with the Z-axis translation tube, to cover the depth of the arc section when mounted flush with the aircraft panel surface. A test scan image saved at the end of the scan and downloaded to a pc is shown, with the scan menu system shots, in Figure 140. This test was also of the mockup

panel, and shows all the EDM notches as well as the tapered bottom of the mockup panel, which shows up as red/orange triangular regions at the bottom corners of the scan image. EDM Notch 8 is a very shallow notch, and the signal along its length was significantly lower than the other notches and likely why its length was not shown accurately in the scan image.

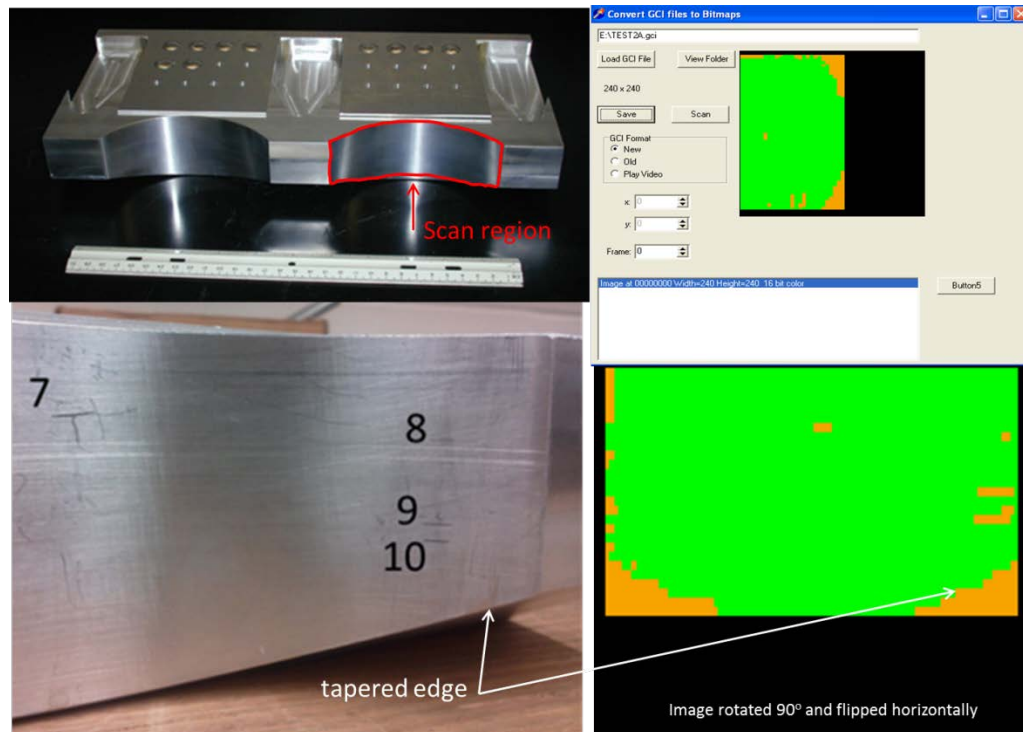


Figure 140. Scan Results From Arc Section Of Mockup Panel Of Aircraft Structure, Showing Indications From EDM Notches And Edge Effect Signals From Bottom Of Mockup Panel Tapered Edge

During scanning, every so often a red pixel indicating a flaw would be written to the screen when the eddy current flying dot would move outside the alarm box. As can be seen in the photo of the eddy current instrument in Figure 139, the alarm box is quite small. When a suspect alarm indication is seen, the operator can simply rescan the area by sweeping through the arc several times. If the alarm is genuine, a real flaw exists, the pixels will remain red. If the red pixels were the result of noise, they will be overwritten by green (no flaw) pixels when rescanned. In this way, the operator can recheck any suspect indications before moving to the next scan line.

Conclusions

The pantograph and arc scanners are novel approaches to manual inspection aides where the inspections are physically difficult or taxing to perform and where it essential to achieve 100% inspection of the target areas. Both scanners held the eddy current probes rigid enough to significantly minimize any probe tilt and liftoff, and the weight of the scanners and cabling is supported by the scanner mounts, so minimized the weight supported by and fatigue of the operator. With both scanners, the operator is essentially relieved of the duties of carefully maintaining probe orientation and contact with the inspection surface and can therefore concentrate on coverage and monitoring the NDE signal.

The pantograph was fabricated with straight linkages, but could be made with bent links to facilitate moving probes around objects but still allowing tracking. The arc scanner made the inspection of the arc section significantly easier to accomplish, a result of the probe keeping the probe normal to the arc surface throughout the side-to-side sweep and z-axis translations during a scan.

The novel use of the miniature LCD/microprocessor to eliminate the need for a laptop PC to capture and save c-scans could certainly be applied to many other NDI modalities. Bond testing and UT inspections, using larger aperture probes, could be coupled with the miniature LCD to facilitate simple scan image production without encoders of any kind with the use of the “assumed encoding” scheme used by the Computer Aided Tap Tester [139]. However, with the small diameter eddy current probes, position encoders are necessary.

Presentations

- “Inspecting Complex Geometries in Aero Structures: Methods for Tracking Eddy Current Probes to Ensure Complete Coverage”, D. Barnard, A. Patz, D. Hsu, 39th Annual Review of Progress in Quantitative Nondestructive Evaluation, San Diego, CA, July 2010.

Recommendations

1. Apply miniature LCD/microprocessor to other manual inspections with appropriate position encoding schemes.
2. AF inspection personnel should suggest additional applications/inspections that might benefit from inspection aide development, then review and prioritize.

3.14 Contributions to NDE Education

Investigation Team: N. Bowler, J. Gray, R. Bruce Thompson, and L. Brasche

Motivation

NDE has become an independent area of research and specialization; this has been an outgrowth of the last 30 years, where quantitative methods and approaches to NDE have been developed. Indeed, NDE is now much like materials science was in the early 1970s (a rather loose collection of metallurgists, analytical chemists, ceramists and solid state physicists). The emerging maturity of NDE is also signaled by industry's growing interest in utilizing NDE engineers to complement the more traditional technician's role. With this expansion comes the need for additional education resources for traditional on campus students and the practicing engineer looking for effective continuing education options.

Understanding the physics of NDE measurements and the role that NDE and probability of detection plays in life management of aviation systems and components was an essential function of the research performed under contract no. # FA8650-04-C-5528. The value of a research program is further enhanced when the results of the efforts are transitioned out of the laboratory and into practical use. While this concept sounds simple, the effort involved in making a successful transition can be quite complex. A variety of mechanisms can be utilized in that process, ranging from the preparation of new procedures and standards, to prototype development and beta site testing, to education and training programs. A more highly trained workforce is crucial to the implementation of advanced NDE techniques. Distance education is the key to providing this training in today's highly mobile workforce and was the focus of this task.

Results – Theory and Experiments:

The Center for NDE has a number of unique resources available for the development of NDE educational materials. Many institutions have at most a few individuals with strong NDE expertise and hence would have difficulty in developing a comprehensive NDE education curriculum. However, CNDE has had a critical mass of expert NDE personnel, supported by an active web site (www.ndt-ed.org), simulation tools suitable for developing tutorial lessons on the major NDE methods, and a strong academic connection to the College of Engineering of Iowa State University. The total activity of developing a leading role in all aspects of NDE education requires significant resources and long term dedication of effort. New NDE textbooks, distance education courses at both the undergraduate and graduate levels, and short courses for general audiences and specialists are needed. NDE data also needs to be collected and assembled in web formats. In this task, one aspect of this broad strategy was addressed, the development of distance education materials. With support from AFRL, CNDE leveraged this unique opportunity to build a first of a kind NDE Graduate Certificate program.

The Graduate Certificate is focused on a graduate level extension of a BS engineer or scientist. The purpose of this certificate is to provide the equivalent of MS level training in an NDE related topic without a thesis. The certificate could, with appropriate extensions, form the basis of a

formal MS degree in NDE. The offering of the certificate does not require this step and, while not as prestigious as a formal degree, will address the growing trend towards the additional training that engineers often prefer for career development in large corporations and government. Among the requirements for issuance of a Graduate Certificate by the College of Engineering at ISU is successful completion of at least thirteen graduate credit hours. An existing graduate survey course, *MSE 550/EM 550 Fundamentals of Nondestructive Evaluation*, is a required core course. *EM 518 Waves in Elastic Solids with Application to NDE*, covers principles of ultrasonics and application to inspection methods. Pre-existence of these two courses provided a starting point for the Graduate Certificate but additional NDE-specific offerings were needed. Support from this program was used to develop core graduate courses in electromagnetics and radiography, *Mat E/EE 588 Eddy Current NDE* and *ME 529X. Penetrating Radiation Methods in NDE*, respectively.

The new 3-credit graduate course “Eddy Current Nondestructive Evaluation” was developed and first offered first in Fall 2007 at Iowa State University. The course was made available in distance-learning format with the traditional classroom providing the center of the learning experience. Lectures were delivered live on campus and via web-based streaming video format for off-campus students. The additional educational materials provided were:

- Textbook entitled, “Electromagnetic Nondestructive Evaluation”
- Clips of pre-recorded video in order to illustrate concepts and applications
- A ‘home’ experiment kit to provide the student with hands-on experience of simple experiments. For the virtual experiment kit, Labview software was developed to play the role of laboratory instruments such as a lock-in amplifier. This will provided a highly portable system that is mostly personal computer-based, allowing students to imitate practical investigations and carry out assignments even when located off-campus.

To date, the graduate eddy current course has been taught 3 times with ~25 students taking the course at ISU and ~15 students enrolling using the distance education option. The course will be taught again in Fall 2014.

A second task focused on development of an x-ray techniques and methods course which covered the basic x-ray based techniques including radiography, computed tomography, scattering effects, diffraction and the applications of these techniques. The emphasis was to develop a science basis for the treatment of x-ray methods with an emphasis on application of these methods to industrial inspections or characterization needs. Recent work has focused on computed tomography and its applications. This has included CT experimental configurations, reconstruction methods, experimental issues such as artifacts; resolution limits, and scan optimization. Sections covering the generation of x-rays and the basic physics of how x-rays interact with matter including detectors were developed.

The general approach was to develop the physics basis for x-ray methods in NDE including projection radiography and computed tomography methods. The generation of x-ray radiation, it’s interaction with matter, x-ray detector properties were the focus of the course development. Scattering components control the image quality. Issues such as geometric unsharpness, undercut, Scattering effects, intensifying screens, and part geometry all contribute to image quality. Radiation safety, shielding and the biological effects of radiation were included along

with a number of example inspection techniques including relevant ASTM standards requirements.

Materials were developed to support the communication of conceptual ideas to the students that included data from experimental systems, animations and “simlets”. The simlets mentioned are small computer programs based on first principles physics principles that are focused at providing a means to illustrate a specific idea related to x-ray NDE methods. These simlets can include, for example, radiation shielding calculations, x-ray scattering effects, and the effects of using look up tables to view digital data. The outcome of this course is to provide detailed knowledge for engineering level NDE personnel in x-ray methods commonly used in NDE. The x-ray course has not yet been offered.

Conclusions

Universities worldwide are responding to the need to support the advances and innovation in nondestructive evaluation (NDE) by expanding their related research activities and training more graduate students in this field. In order to address the diverse routes that people enter the field of NDE, ISU has developed a distance learning program leading to a Graduate Certificate in NDE and has aspirations of offering a Masters of Science (MSc) degree in NDE. Many engineers in NDE have training in other engineering disciplines or need to take continuing education training to keep abreast of some rapidly evolving areas in NDE. The size and strength of activity in NDE at Iowa State University places the Center for Nondestructive Evaluation (CNDE) in the unique position of being able to support a degree program leading to an MSc in NDE.

The existing Graduate Certificate in NDE qualification is suitable for aspiring senior engineers, equipping them to contribute to the development of new inspection procedures and NDE techniques. These advances can be encouraged through an understanding of the fundamental principles underpinning practical NDE, as well as knowledge of the practical implementation of these principles. Support from AFRL provided the course development for two graduate level courses, *Eddy Current Nondestructive Evaluation* and *Penetrating Radiation Methods in NDE*. *The course Eddy Current NDE has been offered 3 times since development in 2007: in Fall 2007, 2008, and 2011, attracting around 15 students on each occasion with approximately half of those in 2008 and 2011 being enrolled in the online course section.*

Recommendations

- Graduate certificate presently (at April 2013) has around 6 enrollees. Advertising campaign is underway towards the national and international markets.
- MS/MEng in NDE is actively being developed. Further course development funds are being sought from industry and other agencies.
- Possible PhD program in Materials Characterization (or similar) is being considered and may be potentially funded with support from an NSF IGERT program for which a proposal is being considered.

4. Concluding Remarks

This multi-year effort has made significant contributions towards advancing quantitative inspection technologies:

Electromagnetic Characterization of Near Surface Treatment, Roughness, Damage, and Material Deviation (Nakagawa, Lo)

This task has provided developments in the area of high-frequency eddy current probes and instrumentation suitable for characterizing near-surface material conditions. A swept high frequency eddy current system (SHFEC) capable of making measurements up to 60 MHz was developed, and during the program activities have continually improved it to give better signal-to-noise and to improve ease of use (Sec. 3.1.1). The project has advanced the swept frequency EC measurement technique, and established a near-surface conductivity deviation profile inversion methodology. Measurement techniques that use the vertical component (V-component) signals, which permits direct comparison between experimental and modeling signals, was developed thus enabling model-based inversion of conductivity profiles (Sec. 3.1.2). This method addresses challenges due to liftoff and parasitic noise, as well as some instrumentation dependency. A model-based inversion technique to convert SHFEC signals into conductivity profiles for material characterization (Sec. 3.1.3) was developed. Progress was made toward understanding the effects of near-surface material condition deviations on EC signals, particularly those induced by shot peening. The understanding gained in this project is beneficial to other related NDE problems including characterization of coating, roughness and anomalous machining damages. A fundamental study of the origins of conductivity variations in shot peened Inconel 718, was performed with the focus of this project on the relative importance of the stress and microstructure effects (Sec. 3.1.4), in conjunction with the examination of the cold work effects conducted in a companion project. The project examined the possible influence of crystallographic texture on the piezoresistivity (Sec. 3.1.4.D). In our early studies of an Inconel 718 sample that was shot peened at high Almen intensity of 17A, we observed shot-induced changes in crystallographic texture with depth. This work generalized the piezoresistivity relationship to account for the texture effect, and showed a possibility of fitting the AFEC data to the texture-influenced piezoresistivity theory.

High Energy X-Ray Diffraction Measurements Of Stress Profiles In Bulk Materials (Jensen, J. Gray)

X-ray diffraction is a well-established method for measuring surface residual stress. We have demonstrated that the technique can be extended to nondestructively measure strain profiles in samples by using a high-energy x-ray source. We fabricated a system from standard off-the-shelf equipment, albeit, configured in a unique way. Using this first generation prototype we have measured strain profiles in aluminum, titanium and nickel alloys ranging to depths of several millimeters in aluminum, to 300-400 microns in titanium and up 200 microns in nickel. The probing volume thickness for the depth scan ranges from 75 microns to 150 microns. At present this method is the only demonstrated nondestructive measurement that works for titanium and nickel alloys. These measurements were compared to standard θ - 2θ angular scans, with excellent agreement.

While these laboratory measurements remain slow, typically taking several hours, we have identified a number of straightforward modifications to the instrument that can reduce the measurement time by 10-50x and increase the penetration depth by a factor of two. These include a more compact method of beam collimation, and a laser distance gauge to give a better definition of the sample surface. It should also be possible to develop an algorithm for determining the strain profile that is based on theoretical models. This approach will require fewer data points to determine the strain profile, thus speeding up measurement. Finally, the measurement speed can also be improved by using a more intense source. A custom design will optimize the flux for HEXRD measurements.

Simulation Of Eddy Current Inspection Of Aircraft (J. Bowler)

We have developed a comprehensive modeling scheme for borehole inspection, including a capability for crack characterization using inverse methods which estimate crack profiles using non-linear iterative inversion. The forward model and the inversion in the codes produced deal with both moderate frequencies, where the skin depth is of the order of the crack size, and with the thin-skin regime, where the skin depth is small compared with the crack depth. We have also evaluated a representation of surface distortion and surface roughness in bolt, bore, and fastener holes with a view to accounting for such effects in procedures for damage characterization.

The main accomplishment of this project is the development of a means of calculating crack signals in cylindrical systems based on a scalar decomposition formulation. The code to implement the theoretical model is fast, accurate and at least internationally competitive with others reported in the current literature.

Model-Assisted Probability Of Detection (MAPOD) (Brasche, Meeker)

Given the importance of probability of detection to the aviation community, federal agencies who are most interested in safe commercial and military flight operations, i.e., the US Air Force, FAA and NASA, have worked collaboratively to develop and promote the use of Model-assisted POD methodologies. To ensure broader impact and perspectives, colleagues from energy, nuclear power generation, infrastructure and transportation were also invited to participate in MAPOD activities. The MAPOD Working Group was established in 2004 and support from this contract enabled a series of meetings which are fully documented in a companion website, www.cnde.iastate.edu/MAPOD. Through a series of a dozen formal meetings and numerous other interactions and collaborations, several demonstrations were reported by members of the working group, providing a foundation upon which future MAPOD studies can build. As of November 2012, activities of the MAPOD working group transitioned to the Reliability Committee of ASNT. CNDE continues to host and provide updates to the MAPOD website.

Eddy Current Model Validation Toward Model-Assisted POD Methodology (Nakagawa)

The study of the notch width effects on EC signals presented validation of an eddy current NDE model based on the boundary element method, implemented for test specimens of generalized half space geometry with a probe of any construction and dimensions. Specifically, the study:

- Established a calibration approach that enables the comparison between theoretical predictions and experimental data.
- Showed that, after being mapped to the vector voltage plane, model-predicted notch signal traces agree with experimental signals in the same voltage plane.
- Obtained the validation results for commercial absolute and differential probes.
- The overall magnitude comparisons, as well as the matching trends of the notch width effects, are shown within approximately 10% errors or less.
- Showed ~35% reduction of the EC signal for a tightly closed (mathematically idealized) crack of no leakage current, compared to the 0.005" wide notch of the otherwise identical dimensions.

The study of EC crack signals under dynamic and static loading presented the crack morphology effects on EC responses:

- Under dynamic tension, Al crack samples showed that the EC signal amplitude increases with the load amplitude, while the effect is stronger for longer cracks.
- Under compression, Al crack signal amplitude remains relatively unchanged, presumably due to the insulation effect of the oxidation layer on the crack face.
- EC scans on Al fatigue cracks under static loads confirmed the load-signal relations observed under dynamic loading.
- EC scans on Ti 6-4 fatigue cracks under static loads revealed significantly stronger stress effects on crack signal than what the Al samples exhibited, notably under compression. It was argued that the difference comes from the propensity difference toward oxide layer formation.

The overall study of the notch vs. fatigue crack signal relationship comparison study confirmed that the signals from low-cycle fatigue cracks were smaller in magnitude than the signals from similar sized EDM notches. However, there is a difference in reduction factors between cracks in Al and the other materials examined.

- For Al, the signals from the fatigue crack specimens correlate very well to the predicted zero-width notch signals, indicating that there is measurable (but calculable) discontinuity volume effects but minimal current leakage effects due to insulating surface oxide layer formation.
- For the titanium and nickel-base super alloys, it was found that mechanical loading could produce a significant change in the eddy current signal from the cracks. Crack signals tend to be further reduced from zero-width notch signals, where the reduction factor is strongly dependent on the crack's stress state, indicating current leakage effects being present. Because of the randomness of contacting asperities, the reduction factor is hence random in nature, with significant variability.

The study of edge crack detection and its modeling is an industrially relevant and thus complex problem. Nevertheless, progress has been made in the study, and at this stage of the development, the conclusions are that we:

- Demonstrated advanced experimental and theoretical capabilities on EC edge crack detection and simulation. The experimental method has achieved large suppression of edge effects. The computation has demonstrated the ability to simulate industrial inspection problem.
- Demonstrated correlation between computed and measured signals by the use of the notch-signal-based calibration.
- Gave prospect toward MAPOD approach, i.e., it may be possible to convert POD from notches on flat surface to cracks on edge, except that one must pay attention to skewed (downward) crack signal distributions.

As a part of this project, draft documents were generated to describe recommended protocols for next steps of EC NDE model validation.

Probability Of Detection Advances (Meeker)

Modern quantitative nondestructive evaluation, given the data that is generated, is inherently a statistical operation. While existing methods for estimating POD (e.g., those described in MIL-HDBK 1823) can answer many of the needed questions, as new technologies are developed, it may be necessary to develop new approaches. Use of inappropriate statistical methods can increase the probability of making bad decisions related to inspection outcomes. There is no magic in statistics, but the application of appropriate statistical methods will ensure that available information is used as efficiently as possible. Methods of statistical design of experiments and careful use of Bayesian methods can be usefully employed to obtain efficiency needed for economical experimentation, even in complicated situations.

Phased Array Measurement Model And POD Calculation (T. Gray and F. Margetan)

Analytical models for phased array transducers were implemented for linear probes fabricated from rectangular elements. The probe and beam model employs the multi-Gaussian approximation, which is a paraxial model. The Thompson-Gray measurement model is employed to integrate the MG model into a tool for predicting a measured ultrasonic response using PA probes. This approach is computationally efficient and has the flexibility to handle complex geometrical components.

Due to the paraxial approximation used in the MG model, there are errors in its predictions of the UT fields generated by linear PA transducers comprising rectangular elements. A semi-analytical improvement to the MG model was developed by modifying the directivity of PA probe elements to point in the steering angle and by applying an amplitude correction factor. That correction factor has been tabulated for a range of steering angles as a function of the dimensionless element width, d/l , where l is the ultrasonic wavelength in the propagating medium. This model, dubbed the Linear Phased MultiGaussian model, significantly reduces the paraxial errors while maintaining computational efficiency and flexibility of the model.

A new, streamlined approach to PA probe characterization was developed for obtaining the system efficiency factors for element pairs in a PA probe. The method uses the pulse-echo response measured from each element, applies corrections based upon differences in amplitude and time delay among the elements, and computes all of the inter-element system efficiency factors from the pulse-echo responses.

A model was developed and demonstrated for predicting grain noise for a pulse-echo PA measurement using linear arrays. The model is an extension of models for grain noise in pulse-echo and pitch-catch UT measurements from single element transducers. Ray-tracing approaches for anisotropic media were developed and demonstrated for homogeneous and, in a limited fashion, for nonhomogeneous media. The homogeneous case has been integrated in to UTSim and initial experimental tests performed in partnership with an OEM.

Effect Of Defect Morphology On Ultrasonic NDE Signals (Roberts and Lo)

Results of this study show that moderate degrees of plate curvature and taper have a minimal effect on the transmission efficiency of plate waves. Examination of dispersion characteristics in circular cylindrical shells revealed that the plate curvature has a negligible effect for curvatures appreciably larger than the plate thickness. It was observed that displacement depth profiles vary curvature, indicating that mode coupling will occur when transitions in radius are encountered. However, an examination of transmission at abrupt curvature transitions revealed a negligible degree mode conversion for 3/16 inch plate radii as small as 2 inches. Finally, an examination of guided mode transmission in tapered plates displaying gradual transitions in plate thickness revealed only a modest degree of mode conversion. Smooth transitions were examined for which the length over which the transition occurs was as small as twice the plate thickness. Energy loss through mode conversion was observed to be less than 10 percent for transitions in thickness of 60 percent and 150 percent. A 400 percent change in plate thickness resulted in an energy loss of 25 percent. These behaviors were consistently observed when examining plate structures containing both curvature and taper. A structure containing a two inch radius double curvature with two 100 percent transitions in thickness displayed transmission characteristics showing little mode conversion loss for both A0 and S0 wave incidence.

The range of plate curvatures and taper examined in this study represent the range over which, if such features were to present issues requiring consideration in inspection deployment, such issue would have been apparent. The observation that the curvature and taper examined in this study has little effect on guided wave transmission efficiency indicates that neglecting these effects for features represented by this study may in practice be justified.

Fundamental Studies Of Guided Wave Propagation For Structural Health Monitoring (Roberts)

Results of this study show that moderate degrees of plate curvature and taper have a minimal effect on the transmission efficiency of plate waves. Examination of dispersion characteristics in circular cylindrical shells revealed that the plate curvature has a negligible effect for curvatures appreciably larger than the plate thickness. It was observed that displacement depth profiles vary with curvature, indicating that mode coupling will occur when transitions in radius are encountered. However, an examination of transmission at abrupt curvature transitions revealed a negligible degree mode conversion for 3/16 inch plate radii as small as 2 inches. Finally, an examination of guided mode transmission in tapered plates displaying gradual transitions in plate thickness revealed only a modest degree of mode conversion. Smooth transitions were examined for which the length over which the transition occurs was as small as twice the plate thickness. Energy loss through mode conversion was observed to be less than 10 percent for transitions in thickness of 60 percent and 150 percent. A 400 percent change in plate thickness resulted in an energy loss of 25 percent. These behaviors were consistently observed when examining plate structures containing both curvature and taper. A structure containing a two inch radius double curvature with two 100 percent transitions in thickness displayed transmission characteristics showing little mode conversion loss for both A0 and S0 wave incidence.

Fundamentals Of Detecting Tight Cracks Using Vibrothermography Inspection (Holland)

Vibrothermography remains an emerging technique, but it is rapidly maturing. The present work has provided major advances in the understanding of this inspection approach. We have pioneered better processes to characterize the vibration-induced heating behavior of a crack. We have applied these processes to measure the dependence of crack heating on parameters such as crack closure, crack length, excitation amplitude, vibrational stress, loading mode, and frequency. It is found that some parameters remain largely unexplored, for example the effects of fatigue parameters and possible ingress of contaminants. The task collaborated with those engaged in POD studies and developed a thermal image sequence processing algorithm that improves sensitivity and condenses the useful information. We have developed prototype synthetic defects and coatings that heat with vibration and these will be useful for process monitoring and coverage analysis.

Taken together, the contributions from this project will help to transition vibrothermography from a qualitative NDE technique to a well-characterized crack-detection process built on quantitative knowledge. Work still remains to explore the dependence of crack heating on the remaining parameters and integrate knowledge of the process into a unified model.

Electromagnetic Characterization Of Composite Materials Using Microwave And Capacitive Methods (N. Bowler)

A resonant patch microwave sensor for inspecting individual layers of a three-layer dielectric structure was designed, fabricated and tested. Using theoretical techniques, the sensor was designed for good sensitivity, penetration depth and spatial resolution. Experimental results obtained with a prototype sensor showed that it achieved sensitivity $\Delta\epsilon = 0.046$, spatial resolution 5 mm, and penetration depth 4.35 mm in inspecting the core of a fiberglass-honeycomb-fiberglass radome structure. It was also shown that this sensor is able to detect 0.25 cc water in one honeycomb cell easily.

The backward wave and DNG bandwidths of 3D periodic arrays with different arrangements of spheres have been analyzed for various combinations of sphere types, Table 4 Results show that arrangements (d), (c), and (b), Figure 108, can provide, respectively, the widest DNG bandwidths 0.21 %, 0.069 %, and 7.4 % for spheres combinations i), ii), and iii), Table 4 respectively. Compared with these reported in other literature with arrangement (g); 0.17 %, 0.075 %, and 2.9 %, analysis of those available arrangements of the spheres shows similar narrow DNG bandwidths for spheres combinations i) and ii), and wider DNG bandwidths for spheres combination iii).

Electrostatic Green functions for a point charge on top of multi-layered dielectric structures have been derived using the Hankel transform given the cylindrical symmetry of the concentric sensor. Output signal of a disk-and-ring coplanar capacitive sensor, transcapacitance $|C_T|$, has been calculated through the method of moments and corresponding benchmark experiments have been carried out. Very good agreement (within 4%) between theory and experiment on one-, two-, and three-layer dielectric test-pieces in free space has been observed. This suggests that the sensor is suitable for quantitative dielectrometry in order to determine permittivity of individual layers in multi-layered structures.

Two handheld capacitive probes with different target penetration depths were built and tested. Following a calibration procedure that accounts for stray capacitances and the presence of the probe casing, which is not accounted for explicitly in the accompanying model, agreement to within 10% between measured and calculated capacitances was demonstrated for experiments on laminar structures. The penetration depth of concentric capacitive sensors was defined and studied both numerically and experimentally. In order to acquire inversely determined material permittivities close to the actual values, small liftoff values are desirable because such measurement setups give rise to the best signal strength. If the probe is to be used for quantitative permittivity measurement, then calibration on a known test sample may be preferable to calibration in air. The outstanding capability of the handheld sensors in detecting relatively small contrast zones in one- layered and multi-layered structures was demonstrated experimentally.

Spiral interdigital sensors and concentric interdigital sensors have been developed, to improve the output capacitance and signal-to-noise ratio when compared with the disk-and-ring coplanar concentric capacitor mentioned above. A numerical model was developed to describe the behavior of the interdigital sensors. Experimental verifications showed that the numerical

predictions and measurement results agreed to within 5%. Through numerical and experimental comparisons, the two-electrode configuration was found to possess advantages such as deeper penetration depth, better immunity to lift-off variations and higher sensitivity in detecting internal inhomogeneities in sandwich structures. The interdigital configurations were found to be able to achieve higher output signal strength, better signal-to-noise ratio, better accuracy in materials characterization and higher sensitivity in detecting surface defects when prior knowledge of approximate flaw size is available.

Advanced Terahertz Capabilities For Aerospace Material Inspections (Chiou)

This project studied a wide range of research topics in modeling and material characterization involving THz and FTIR. Many of the results directly supported AFRL's in-house research, and most contributed to general NDE applications with experimental validation. This project also provided a good education platform for training future engineers and scientists in these areas.

Novel NDE Concepts For Inspection Of Inaccessible And Complicated Structures (Barnard)

The pantograph and arc scanners are novel approaches to manual inspection aides where the inspections are physically difficult or taxing to perform and where it essential to achieve 100% inspection of the target areas. Both scanners held the eddy current probes rigid enough to significantly minimize any probe tilt and liftoff, and the weight of the scanners and cabling is supported by the scanner mounts, so minimized the weight supported by and fatigue of the operator. With both scanners, the operator is essentially relieved of the duties of carefully maintaining probe orientation and contact with the inspection surface and can therefore concentrate on coverage and monitoring the NDE signal.

The pantograph was fabricated with straight linkages, but could be made with bent links to facilitate moving probes around objects but still allowing tracking. The arc scanner made the inspection of the arc section significantly easier to accomplish, a result of the probe keeping the probe normal to the arc surface throughout the side-to-side sweep and z-axis translations during a scan.

The novel use of the miniature LCD/microprocessor to eliminate the need for a laptop PC to capture and save c-scans could certainly be applied to many other NDI modalities. Bond testing and UT inspections, using larger aperture probes, could be coupled with the miniature LCD to facilitate simple scan image production without encoders of any kind with the use of the "assumed encoding" scheme used by the Computer Aided Tap Tester [4]. However, with the small diameter eddy current probes, position encoders are necessary.

Contributions to NDE Education (N. Bowler, J. Gray, R. Bruce Thompson, and L. Brasche)

Universities worldwide are responding to the need to support the advances and innovation in nondestructive evaluation (NDE) by expanding their related research activities and training more graduate students in this field. In order to address the diverse routes that people enter the field of NDE, ISU has developed a distance learning program leading to a Graduate Certificate in NDE and has aspirations of offering a Masters of Science (MSc) degree in NDE. Many engineers in NDE have training in other engineering disciplines or need to take continuing education training to keep abreast of some rapidly evolving areas in NDE. The size and strength of activity in NDE at Iowa State University places the Center for Nondestructive Evaluation (CNDE) in the unique position of being able to support a degree program leading to an MSc in NDE.

The existing Graduate Certificate in NDE qualification is suitable for aspiring senior engineers, equipping them to contribute to the development of new inspection procedures and NDE techniques. These advances can be encouraged through an understanding of the fundamental principles underpinning practical NDE, as well as knowledge of the practical implementation of these principles. Support from AFRL provided the course development for two graduate level courses, *Eddy Current Nondestructive Evaluation* and *Penetrating Radiation Methods in NDE*. *The course Eddy Current NDE has been offered 3 times since development in 2007: in Fall 2007, 2008, and 2011, attracting around 15 students on each occasion with approximately half of those in 2008 and 2011 being enrolled in the online course section.*

4.1 Future Directions

Nondestructive evaluation continues to play a critical role in ensuring flight safety. Recent years has seen considerable progress in both the basic science, with increased interest in assessment of material state, and the technologies used to deploy NDT for Air Force systems.

The directions for future work are considered in the context of the AFRL vision which is to provide materials and damage characterization regardless of scale, with needs from microstructure to macrostructure. In looking for needed future directions, the activities reported in this document, which have focused on six topics, and provide guidance with regard to further work.

- Residual Stress Assessment and Instrumentation Development
- Simulation-Based Inspection Design, Evaluation and Optimization
- Probability of Detection Studies and Demonstration
- Materials Characterization and Damage (Crack, Corrosion) Detection
- Vehicle Health Monitoring and Prognosis
- Education, Technology Transition, and Infrastructure Support

Three areas for action are identified:

1. Inspection Reliability

To achieve the AFRL vision NDE is required that is both reliable and quantitative. Two areas are identified for action.

a. NDE reliability

Probability of detection (POD) is now viewed as increasingly mature. In developing its utilization the next step is the integration of simulation tools, such as inspection maps and stress analysis with a POD assessment. This development could be transformational and bring together, and build on prior work at CNDE, the MAPOD group and South West Research Institutes (SWRI) stress analysis tools, such as DARWIN.

b. Spatial awareness

Increased data fusion and integration in the context of a digital twin could transform NDE for complex systems. Such activities form a key step towards use of automated and robotic NDE. NDE systems need to be able to recognize a location on a specimen and store NDT/NDE data in a spatial context. There is a need to add a geometric register to scans, and provide tools to combine data from various modalities (based on different physics – i.e., ultrasound, electromagnetic, radiography and also photographic data from MPI and FPI). To be able to facilitate and combine data from inspections there is a need to integrate measurement modalities that provide shape and geometry (i.e., photogrammetry, laser range finders and contact sensing), approaches usually treated separately from NDT. The geometric data are needed to form the basis for the digital twin that can then be used for fusion of NDT data that moves beyond manual and rectilinear scans. The next step is to provide tools that can integrate robotic inspection and data from multiple modalities. This activity could be initiated using selected parts/systems which could form the basis for an initial proof-of-concept demonstration. Such tasks would

build on and combine with capabilities needed to address and extract useable/actionable material state insights effectively from Gigabyte (or even Terabyte) data sets.

2. Material State Assessment

There remain needs for a new generation of NDE tools, including novel approaches that can measure properties, including residual stress. The nondestructive measurement of mechanical properties has been called one of the “holy grails” of NDT [141]. A review of the assessment of microstructures and mechanical behavior of metallic materials through non-destructive characterization was provided by Baldev Raj et al. [142]. Since this time the nuclear and aerospace communities have focused considerable effort in this area, and some progress has been made [143]. However, it is increasingly clear that it will require new approaches with utilization of more than one sensing modality and data fusion to achieve the desired outcomes.

(a) X-ray residual stress

Nondestructive measurement of residual stress at various points on a sample at different times through life cycle can provide valuable information for life-cycle modeling. Prior work has shown a capability to measure stress depth profile in engine materials. Residual stresses in materials cause small changes in lattice spacing. When high intensity, narrow-energy characteristic lines are selected for probing material structure including measurement of residual stress state can be assessed. The current status is that laboratory feasibility has been demonstrated and measurements have been performed and applied to several material types (aluminum, titanium, nickel, and SiC ceramic samples). Using high-energy x-rays and appropriate collimation, depth of penetration can be extended to up to 1 mm in Al and 500 microns in ceramics. These approaches appear to have the potential to be developed and applied to provide surface measurement of stress with depth profile at selected points. Prototype system used to demonstrate strain depth-profile measurements could potentially be used on any crystalline material. Different lattice planes can be selected to obtain greatest sensitivity.

(b) Multi-physics stress and property measurement

The literature on the use of both electromagnetic and ultrasonic methods for material state awareness is extensive. It is clear that no single measurement modality can provide all the needed data. It would appear that an approach that combines integrated ultrasonic and electromagnetic sensors, could be utilized, with novel data fusion to extract additional materials properties. This could potentially include stress, fracture toughness and quality indicators. Such an approach could be tested and validated against radiographic methods for residual stress and structure assessment (discussed above).

In addition to property determination there remain needs for enhanced material characterization studies and tools. Ultrasonic backscatter has been shown to provide signatures that correlate with part quality and performance. With new material development there are needs for further characterization studies. Such activities can provide “signatures” that can build a bridge between manufacturing process control and process non-conformity detection, as indicated by material property deviation from nominal. These approaches provide for enhanced quality assurance and would enable deployment of fast nondestructive methods to enable per-component/machining QA assessments in parts such as turbine disks. This same concept can be utilized for in-service applications, to provide early detection of degradation, in a pre-crack state, together with

characterization of underlying material noise characterization, needed for S/N and POD assessments

3. New NDE Measurements

There are areas where there are opportunities to develop and deploy new and improved measurement capabilities. Three technologies identified as having specific potential are: THz, phased array and thermography.

(a) THz measurements

Terahertz radiation (THz) is the basis for an electromagnetic technique which was relatively recently introduced in to NDE applications. The radiation is in the spectrum between microwave and mid-infrared. It possesses superior resolution in both longitudinal (depth/time) and lateral (spatial extent) dimensions for inspecting layered dielectric materials, including thin film/coatings. Operationally, pulsed THz is very similar to a non-contact “high-definition” pulsed ultrasound. CNDE has extensive experience with characterization of thin film, coatings measurement, detection of delamination under coatings, spectroscopic analysis, and inspection for damage to composites. Commercial THz inspection systems are available for field implementation, but these typically require some modifications. Additional engineering development work is needed to be applied to existing systems, so as to maximize inspection throughput and optimize detection capability. These systems would be suitable for field deployment and applicable to impact damage, thermal damage, hidden delaminations, and other phenomena that change dielectric properties. Additional modeling and data processing is needed to provide inspection simulation and hence enable enhanced inspections to be performed. With reasonable investments in terms of cost and time, THz inspection systems can be tailored for field implementation.

(b) Quantitative Imaging using phased arrays

Phased array ultrasonic inspection is seeing increased utilization in a diverse range of applications. Beam steering and then data post processing, is enabling inspections to move beyond scans with transducers operating with fixed wedge angles. To optimize and diversify use there is a need to develop new imaging algorithms, similar to physical optics far field inverse scattering (POFFIS), based on inversion of the Thompson-Gray measurement model. CNDE studies have already demonstrated equivalent flaw sizing of cracks to provide more information than time-of-flight-diffraction (TOFD), which was reported in a RPQNDE 2012 paper [144]. The next development that is needed would be a software test bed to simulate and evaluate flaw images, and such capabilities would have potential for inclusion in inspection simulation codes.

(c) Vibrothermography

A modular approach, involving physical modeling and knowledge of fracture mechanics is proposed that would reduce the need for physical experimentation and allow for reasonable extrapolation from data. Work should use a low-dimensional set of physics-based variables in place a larger set of variables (e.g., using crack closure gradient and roughness invariant to describe crack characteristics). The study should employ statistical design of experiments (DoE) that can be used to focus experimental effort where it is needed to fill knowledge gaps. In such an activity model verification (involving, for example confirmatory experiments to test model predictions) will play a key role. [NOTE: a UTC/AFRL project has been initiated in this area and a kickoff meeting was held January 17, 2013].

5. References

1. Incorporating Residual Stresses in Life Prediction of Turbine Engine Disks. John, R., et al. Manchester, UK: s.n., 2001. NATO RTO (AVT) Symposium on Monitoring and Management of Gas Turbine Fleets for Extended Life and Reduced Costs.
2. Residual Stress: Measurement by Diffraction and Interpretation. Noyan, I. C. and Cohen, J. B. s.l.: Springer-Verlag, 1987.
3. Thompson, R. B., Lu, W. Y. and Clark, Jr., A. V. Handbook of Measurement of Residual Stresses. [ed.] J. Lu. Upper Saddle River: Fairmont Press, 1996. pp. 149-178.
4. Schoenig, F. C., et al. 22, 1995, Materials Evaluation, Vol. 53.
5. Blaszkiewicz, M., Albertin, L. and Junker, W. 179, 1996, Materials Science Forum, Vols. 210-213.
6. Chang, H., Schoenig, F. C. and Soules, J. A. 1257, 1999, Materials Evaluation, Vol. 57.
7. Washabaugh, A., et al. 2003, Non-Destructive Testing, Vol. 765.
8. Blodgett, M. P. and Nagy, P. B. [ed.] D. O. Thompson and D. E. Chimenti. Melville: American Institute of Physics, 2004. Review of Progress in Quantitative Nondestructive Evaluation. Vol. 23B, pp. 1216-1223.
9. Blodgett, M. P. and Nagy, P. B. [ed.] R. Bruce Thompson. 107, 2004, Journal of Nondestructive Evaluation, Vol. 23.
10. Dynamic Piezoresistivity Calibration for Eddy Current Nondestructive Residual Stress Measurements. Yu, F. and Nagy, P. B. [ed.] R. Bruce Thompson. 4, 2005, Journal of Nondestructive Evaluation, Vol. 24, pp. 143-151.
11. Yu, F., Blodgett, M. P. and Nagy, P. B. 17, 2006, Journal of Nondestructive Evaluation, Vol. 25.
12. Yu, F. and Nagy, P. B. 8340, 2004, Journal of Applied Physics, Vol. 95.
13. Yu, F. and Nagy, P. B. 1257, 2004, Journal of Applied Physics, Vol. 96.
14. High Frequency Eddy Current Inspection System and Its Application Residual Stress Characterization. Nakagawa, N., Lee, C. and Shen, Y. [ed.] D. O. Thompson and D. E. Chimenti. Melville, NY: American Institute of Physics, 2006. Review of Progress in Quantitative Nondestructive Evaluation. Vol. 25, pp. 1418-1424.
15. Unconventionally High and Low Frequency Eddy Current Methods for Material Surface Characterization. Nakagawa, N. and Lo, C. C. H. [ed.] D. O. Thompson and D. E. Chimenti. Melville, NY: American Institute of Physics, 2010. Review of Progress in Quantitative Nondestructive Evaluation. pp. 1471-1478.
16. Nondestructive Residual Stress Characterization Methodologies: An Overview of Developments of High Frequency Eddy Current and High Energy XRD Methods. Nakagawa, N., et al. Berlin: s.n., 2010. Proceeding of the 8th NDE Conference.
17. Conductivity Profile Determination by Eddy Current for Shot Peened Superalloy Surfaces Toward Residual Stress Assessment. Shen, Y. P., et al. 014907-1, 2007, Journal of Applied Physics, Vol. 101.
18. Advances in Swept High Frequency Eddy Current Residual Stress Characterization. Shen, Y., et al. [ed.] D. O. Thompson and D. E. Chimenti. Melville, NY: American Institute of Physics, 2008. Review of Progress in Quantitative Nondestructive Evaluation. Vol. 27, pp. 1222-1227.
19. Cheng, C. C., Dodd, C. V. and Deeds, W. E. 109, 1971, International Journal of Nondestructive Testing, Vol. 3.

20. Validation of a Residual Stress Measurement Method by Swept High-Frequency Eddy Currents. Lee, C., et al. [ed.] D. O. Thompson and D. E. Chimenti. Melville, NY: American Institute of Physics, 2007. Review of Progress in Quantitative Nondestructive Evaluation. Vol. 26B, pp. 1213-1219.
21. Effects of Microstructure on Eddy Current Residual Stress Characterization of Shot Peened Inconel 718. Chandrasekar, R., et al. 2, 2012, JOM, Vol. 64, pp. 257-264.
22. Self-Calibrated Swept Frequency Eddy Current Measurements for Surface Characterization. Lo, C. C. H., et al. [ed.] Y.-K. Shin. s.l.: OIP Press, 2009, Studies in Applied Electromagnetics and Mechanics 32, Electromagnetic NDE (XII), pp. 99-106.
23. Abu-Nabah, B. A., et al. 209, 2009, NDT&E, Vol. 24.
24. Abu-Nabah, B. A., et al. 143, 2010, Journal of NDE, Vol. 29.
25. Hillmann, S., et al. [ed.] D. O. Thompson and D. E. Chimenti. 2009. Review of Progress in Quantitative Nondestructive Evaluation. Vol. 28B, p. 1349.
26. Influences of Secondary Phase Precipitate Density and Residual Stress on Conductivity Profiles of Shot Peened Nickel-Base Superalloy. Chandrasekar, R., et al. [ed.] D. O. Thompson and D. E. Chimenti. s.l.: American Institute of Physics, 2012. Review of Progress in Quantitative Nondestructive Evaluation.
27. Residual Stress Profile Assessment by Eddy Current for Shot Peened Nickel Superalloy. Shen, Y., et al. 1, 2010, Journal of Nondestructive Evaluation, Vol. 29, pp. 1-13.
28. X-Ray Diffraction Residual Stress Techniques. Prevey, P. S. 380, s.l.: American Society for Metals, 1986, Metals Handbook, Vol. 10.
29. Kandil, F. A., et al. A Review of Residual Stress Measurement Methods. Middlesex, UK: NPL Materials Centre, 2001. Technical Report.
30. Applications of the Incremental Bore-Drilling Method for Measurement of Residual Stress Distribution. Lu, J. and Flavenot, J. F. 11, November 1989, Experimental Techniques, Vol. 13, pp. 18-24.
31. The Measurement of Residual Stresses Using Neutron Diffraction. Krawitz, A. D. and Holden, T. M. 11, 1990, MRS Bulletin, Vol. 15, pp. 57-64.
32. Croft, M. 578, 2002, Journal of Applied Physics, Vol. 92.
33. Nondestructive Residual Stress Characterization Methodologies: An Overview of Developments of High Frequency Eddy Current and High Energy XRD Methods. Nakagawa, N., et al. Berlin: s.n., 2010. Proceedings of the 8th International Conference on NDE in Relation to Structural Integrity for Nuclear and Pressurized Components.
34. Al-Shorman, Muhammad Y. Residual Stress Measurement Using High Energy X-Ray Diffraction. Ph.D. Thesis-Iowa State University. Ames, IA: s.n., 2008.
35. Cullity, B. D. and Stock, S. R. Elements of X-Ray Diffraction. 3rd. s.l.: Prentice Hall, 2001.
36. Eddy-Current Probe Impedance Due to a Volumetric Flaw. Bowler, J. R., et al. 5, August 1 1991, Journal of Applied Physics, Vol. 70, pp. 1107-1114.
37. Evaluation of Eddy Current Probe Signals due to Cracks in Fastener Holes. Bowler, J. R., et al. 3, March 2012, IEEE Trans. Mag, Vol. 48, pp. 1159-1170.
38. Impedance of a Horizontal Coil in a Borehole: A Model for Eddy-Current Borehole Probes. Burke, S. K. and Theodoulidis, T. P. 2004, J. Phys. D: Appl. Physics, Vol. 37, pp. 485-494.
39. Dyad-Based Model of the Electric Field in a Conductive Cylinder at Eddy-Current Frequencies. Micolau, G., et al. 2, 2004, Vol. 40, pp. 400-409.

40. Waves and Fields in Inhomogeneous Media. Chew, W. C. New York: s.n., 1995, IEEE Press.
41. Thin-Skin Eddy-Current Interaction with Semi-Elliptical and Epi-Cyclic Cracks. Bowler, J. R. and Harfield, N. 1, 2000, IEEE Trans. Mag, Vol. 36, pp. 281-291.
42. Thin-Skin Eddy-Current Inversion for the Determination of Crack Shapes. Bowler, J. R. 2002, Inverse Problems, Vol. 18, pp. 1-15.
43. Xie, Hui. Thin Crack Signals in Cylindrical Structures Using Eddy-Current NDE Theory. Ph.D. Thesis-Iowa State University. 2012.
44. Eddy Current Probe Signals Due to a Crack at a Right-Angled Corner. Bowler, J. R., Theodoulidis, T. and Polakis, N. 2012, IEEE Trans. Mag.-IEEE Xplore.
45. Xie, H., Ji, Y. and Bowler, J. R. Eddy Current Pancake Coil Measurements on a Longitudinal Through Notch in an Inconel Tube. World Federation of NDE Centers Benchmark Problem-QNDE/CNDE. [Online] 2012.
46. General Guidelines for the Aircraft Structural Integrity Program. MIL-HDBK 1530-C. 1996.
47. Nondestructive Evaluation System Reliability Assessment. MIL-HDBK-1823. November 2009.
48. Engine Structural Integrity Program (ENSIP). MIL-HDBK 1783B. February 2002.
49. Damage Tolerance for High Energy Turbine Engine Rotors. 2001.
50. Turbine Rotor Materials Design. 2000.
51. NDE Requirements for Fracture-Critical Metallic Components. 2008.
52. Planning Meeting for the Formation of a Consortium on Computational NDE for Modeling POD-Final Report. 2003.
53. A Unified Approach to the Model-Assisted Determination of Probability of Detection. Thompson, R. B. 6, 2008, Materials Evaluation, Vol. 66, pp. 667-673.
54. Simulation Models: Critical Tools in NDT Engineering. Thompson, R. B. 3, 2005, Materials Evaluation, Vol. 63, pp. 300-308.
55. Using Physical Models of the Testing Process in the Determination of Probability of Detection. Thompson, R. B. 2001, Vol. 59, pp. 861-865.
56. Physical Model Assisted Probability of Detection in Nondestructive Evaluation. Li, M., Meeker, W. Q. and Thompson, R. B. [ed.] D. O. Thompson and D. Chimenti. Vol. 30B, pp. 1541-1548.
57. Early Work on the Use of Models in the Determination of POD/Inspection Reliability in the US and UK. Thompson, R. B. [ed.] D. O. Thompson and D. Chimenti. Review of Progress in Quantitative Nondestructive Evaluation. Vol. 30B, pp. 1581-1588.
58. A Unified Approach in the Model-Assisted Determination of Probability of Detection. Thompson, R. B. [ed.] D. O. Thompson and D. Chimenti. 2008. Review of Progress in Quantitative Nondestructive Evaluation. Vol. 27B, pp. 1685-1692.
59. Use of Physics-Based Models to Guide the Extrapolation of Aircraft Engine Ultrasonic POD Data to Small Flaw Sizes. Thompson, R. B., Gray, T. A. and Meeker, W. Q. [ed.] D. O. Thompson and D. Chimenti. Melville, NY: American Institute of Physics, 2006. Review of Progress in Quantitative Nondestructive Evaluation. Vol. 25B.
60. Uses of Physics-Based Models in the Determination of POD: Current Status. Thompson, R. B. [ed.] D. O. Thompson and D. Chimenti. Melville, NY: American Institute of Physics, 2005. Review of Progress in Quantitative Nondestructive Evaluation. Vol. 24B, pp. 1917-1924.

61. Issues in the Determination of Default POD for Hard-Alpha Inclusions in Titanium Rotating Components for Aircraft Engines. Thompson, R. B., et al. [ed.] D. O. Thompson and D. Chimenti. Melville, NY: American Institute of Physics, 2004. Review of Progress in Quantitative Nondestructive Evaluation. Vol. 23B, pp. 1587-1594.
62. Recent Advances in Model-Assisted Probability of Detection. Thompson, R. B., et al. Berlin: DGZIP Proceedings, 2009. 4th European-American Workshop on Reliability of NDE. Vol. BB116 We1.A.1.
63. Model Assisted Probability of Detection Validation for Immersion Ultrasonic Application. Smith, K., et al. [ed.] D. O. Thompson and D. Chimenti. Melville, NY: American Institute of Physics, 2007. Review of Progress in Quantitative Nondestructive Evaluation. Vol. 26B, pp. 1816-1822.
64. Model-Assisted Probability of Detection (MAPOD) Evaluation for Eddy Current Inspection of Fastener Sites. Aldrin, J. C., et al. [ed.] D. O. Thompson and D. Chimenti. Melville, NY: American Institute of Physics, 2009. Review of Progress in Quantitative Nondestructive Evaluation. Vol. 28.
65. Reliability Demonstration for an Eddy Current NDE Technique Using a Computational Electromagnetic Model-Assisted Approach. Aldrin, J. C., et al. Verona, Italy: s.n., 2007. The 23rd Annual Review of Progress in Applied Computational Electromagnetics.
66. Investigation of a Model-Assisted Approach to Probability of Detection Evaluation. Knopp, J. S., et al. [ed.] D. O. Thompson and D. Chimenti. Melville, NY: American Institute of Physics, 2007. Review of Progress in Quantitative Nondestructive Evaluation. Vol. 26, pp. 1775-1782.
67. Model-Assisted Approach to Probability of Detection Evaluation for Structural Applications. Aldrin, J. C., et al. Houston, TX: s.n., 2006. ASNT Fall Conference 2006 Proceedings. pp. 248-252.
68. Numerical Modeling as a Cost-Reduction Tool for Probability of Detection of Bolt Hole Eddy Current Testing. Mandache, C., et al. 2011, Nondestructive Testing and Evaluation.
69. Transfer Function Model Assisted Probability of Detection for Lap Joint Multi-Site Damage Detection. Bode, M., Newcomer, J. and Fitchett, S. 2011. Review of Progress in Quantitative Nondestructive Evaluation. Vol. 30.
70. Transfer Function Approach Based on Simulation Results for the Determination of POD Curves. Jensen, F. and Lakovieva, E. 2011. Review of Progress in Quantitative Nondestructive Evaluation. Vol. 30.
71. Application of Model-Assisted POD Using a Transfer Function Approach. Harding, A., Hugo, G. R. and Bowles, S. J. 2009. Review of Progress in Quantitative Nondestructive Evaluation.
72. Physical Model Assisted Probability of Detection in Nondestructive Evaluation for Detecting of Flaws in Titanium Forgings. Li, M., Meeker, W. Q. and Thompson, R. B. 2013, Technometrics.
73. Study of the Effects of EDM Notch Width on Eddy Current Signal Response. Nakagawa, N., et al. [ed.] D. O. Thompson and D. Chimenti. Melville, NY: American Institute of Physics, 2009. Review of Progress in Quantitative Nondestructive Evaluation. Vol. 28, pp. 287-294.
74. Effects of Dynamic and Static Loading on Eddy Current NDE of Fatigue Cracks. Lo, C. C.H. and Nakagawa, N. [ed.] D. O. Thompson and D. Chimenti. Melville, NY: American

- Institute of Physics, 2009. Review of Progress in Quantitative Nondestructive Evaluation. Vol. 28, pp. 355-362.
75. Notches Versus Cracks: Effects on Eddy Current NDE Signals from Defect Volume and from Crack Morphology Altered by Mechanical Loading. Larson, B. F., Lo, C. C.H. and Nakagawa, N. [ed.] M. Blodgett, B. Wincheski, and N. Bowler J. Knopp. s.l.: IOS Press, 2010, Electromagnetic Nondestructive Evaluation (XIII). Studies in Applied Electromagnetics and Mechanics, Vol. 33, pp. 155-162.
 76. Investigation of the Effects of Notch Width on Eddy Current Response and Comparison of Signals from Notches and Cracks. Larson, B. F., Lo, C. C.H. and Nakagawa, N. [ed.] D. O. Thompson and D. Chimenti. Melville, NY: American Institute of Physics, 2010. Review of Progress in Quantitative Nondestructive Evaluation. Vol. 29, pp. 1973-1979.
 77. An Element-Free Boundary Integral Equation Method for Modeling Eddy-Current Nondestructive Evaluation Problems. Chen, Z. and Nakagawa, N. [ed.] D. O. Thompson and D. Chimenti. Melville, NY: American Institute of Physics, 2007. Review of Progress in Quantitative Nondestructive Evaluation. Vol. 26, pp. 287-293.
 78. A Fast Multipole Boundary Integral Equation Method for Two-Dimensional Diffusion Problems. Yang, M., et al. [ed.] D. O. Thompson and D. Chimenti. Melville, NY: American Institute of Physics, 2007. Review of Progress in Quantitative Nondestructive Evaluation. Vol. 26, pp. 294-301.
 79. Gao, C. and Meeker, W. Q., An Algorithm for Screening Sonic IR Movies, [ed]. D. O. Thompson and D. Chimenti, Melville, NY: American Institute of Physics, 2007. Review of Progress in Quantitative Nondestructive Evaluation, Vol. 26, pp. 555-562.
 80. Gao, C., Mayton, D. and Meeker, W. Q., Determination of Sonic IR Experimental Conditions and Estimation of POD for Cracks in Fan Blades, [ed]. D. O. Thompson and D. Chimenti, Melville, NY: American Institute of Physics, 2008. Review of Progress in Quantitative Nondestructive Evaluation, Vol. 27, pp. 1708-1715.
 81. Gao, C. and Meeker, W. Q. (2012), A Statistical Method for Crack Detection Using Vibrothermography Inspection Data, Quality Technology and Quantitative Management 9, pp. 59-77.
 82. Gao, C., Meeker, W. Q., and Mayton, D. (2012), Detecting Cracks in Aircraft Engine Fan Blades Using Vibrothermography Nondestructive Evaluation, to appear in Reliability Engineering & System Safety.
 83. Hovey, P., Meeker, W. Q., and Li, M., Joint Estimation of the Flaw Size Distribution and POD Function, [ed]. D. O. Thompson and D. Chimenti, Melville, NY: American Institute of Physics, 2009. Review of Progress in Quantitative Nondestructive Evaluation, Vol. 28, pp. 1832-1839.
 84. Koh, Y. M. and Meeker, W. Q., (2012), Quantile POD for Nondestructive Evaluation with Hit-Miss Data (in preparation).
 85. Koh, Y. M. and Meeker, W. Q., (2012), Signal-Response NDE Inspection Test Planning with POD Estimation Precision as a Performance Metric, [ed]. D. O. Thompson and D. Chimenti, Melville, NY: American Institute of Physics, 2012. Review of Progress in Quantitative Nondestructive Evaluation, Vol. 32, in preparation.
 86. Koh, Y. M. and Meeker, W. Q., 2012, Hit-Miss Data NDE Inspection Test Planning with POD Estimation Precision as a Performance Metric, in preparation.
 87. Li, M., Meeker, W. Q., and Hovey, P., Using a Bayesian Model to Jointly Estimate the Flaw Size Distribution and the POD Function, [ed]. D. O. Thompson and D. Chimenti,

- Melville, NY: American Institute of Physics, 2010. Review of Progress in Quantitative Nondestructive Evaluation, Vol. 29, pp. 687-694.
88. Li, M., Meeker, W. Q., and Hovey, P., 2012, Using a Bayesian Model to Jointly Estimate the Flaw Size Distribution and the POD Function, *Research in Nondestructive Evaluation*, 23, pp. 104-123.
 89. Thompson, R. B. and Gray, T. A., "A Model Relating Ultrasonic Scattering Measurements Through Liquid-Solid Interfaces to Unbounded Medium Scattering Amplitudes", *Journal of the Acoustical Society of America* 74 (1983), pp. 1279-1290
 90. Wen, J. J. and Breazeale, M. A., "A Diffraction Beam Field Expressed as the Superposition of Gaussian Beams", *Journal of the Acoustical Society of America* 83 (1988), pp. 1752-1756.
 91. Wen, J. J. and Breazeale, M. A., "Computer Optimization of the Gaussian Beam Description of an Ultrasonic Field", in Lee, D., Cakmak, A., Vichenevetsky, R., (eds.), *Computational Acoustics: Scattering, Gaussian Beams, and Aeroacoustics*, Vol. 2, Elsevier Science Publishers, Amsterdam, The Netherlands, 1990, pp. 181-196.
 92. Garton, M., Gray, T., Thompson, R. B., and Gray, I., "UTSim: Overview and Application", in *Review of Progress in Quantitative Nondestructive Evaluation*, Vol. 29, pp. 2141-2148, 2010.
 93. Smith, K., Thompson, R. B., Meeker, W., Gray, T., and Brasche, L., "Model-Assisted Probability of Detection Validation for Immersion Ultrasonic Application", in *Review of Progress in Quantitative Nondestructive Evaluation*, Vol. 26, pp. 1816-1822, 2007.
 94. Margetan, F. J., Gray, T. A., and Thompson, R. B., "Measurement and Modeling of Ultrasonic Pitch/Catch Grain Noise", in *Review of Progress in Quantitative Nondestructive Evaluation*, Vol. 27B, pp. 1132-1139 (the steel specimen whose properties are described in this reference is the same one used in this PA modeling study).
 95. Conry, M., "Notes on Wave Propagation in Anisotropic Elastic Solids", available online at the URL: http://www.acronymchile.com/anisotropic_with_lamb_waves.pdf.
 96. Achenbach, J., *Wave Propagation in Elastic Solids*, Elsevier, 1982.
 97. Auld, B., "General Electromechanical Reciprocity Relations Applied to the Calculation of Elastic Wave Scattering Coefficients", *Wave Motion* Volume 1, 1979.
 98. Achenbach, J., Gautesen, A., and McMaken, H., *Ray Methods for Rays in Elastic Solids*, Pitman, Boston, 1982.
 99. Achenbach, J., *Reciprocity in Elastodynamics*, Cambridge, UK, 2003.
 100. Roberts, R., "The Effect of Crack Morphology on Ultrasonic Response", in *Review of Progress in Quantitative Nondestructive Evaluation*, Vol. 31, D. O. Thompson and D. E. Chimenti, eds., AIP, NY, 2012.
 101. Achenbach, J., *Wave Propagation in Elastic Solids*, Elsevier, 1982.
 102. Liu, G. and Qu, J., "Guided Circumferential Waves in a Circular Annulus", *Trans. ASME*, Vol. 65, pp. 424-430, 1998.
 103. Achenbach, J., *Reciprocity in Elastodynamics*, Cambridge, UK, 2003.
 104. Felsen, L. and Marcuvitz, N., *Radiation and Scattering of Waves*, IEEE Press, 1994.
 105. Roberts, R., "Plate Wave Transmission/Reflection at Geometric Obstructions: Model Study", in *Review of Progress in Quantitative Nondestructive Evaluation*, Vol. 29, D. O. Thompson and D. E. Chimenti, eds., AIP, NY, 2010.

106. Roberts, R., "Plate Wave Transmission/Reflection at Arbitrarily Shaped Obstructions", in Review of Progress in Quantitative Nondestructive Evaluation, Vol. 31, D. O. Thompson and D. E. Chimenti, eds., AIP, NY, 2012.
107. Roberts, R., "Benchmark Guided Wave Transmission at an Adhered Stringer", in Review of Progress in Quantitative Nondestructive Evaluation, Vol. 31, D. O. Thompson and D. E. Chimenti, eds., AIP, NY, 2012.
108. Holland, S. D., "First Measurements From a New Broadband Vibrothermography Measurement System", in Review of Progress in Quantitative Nondestructive Evaluation, Vol. 26, D. O. Thompson and D. E. Chimenti, eds., AIP, NY, 2007, pp. 478-483.
109. Holland, S. D., Dataguzzler <http://thermal.cnde.iastate.edu/dataguzzler/>
110. Renshaw, J. and Holland, S. D., "Full-Field Vibration Measurement For Vibrothermography," Review of Quantitative Nondestructive Evaluation **27**, 498-503 (2008). <http://dx.doi.org/10.1063/1.2902702>.
111. Holland, S. D., Uhl, C., and Renshaw, J., "Toward A Viable Strategy For Estimating Vibrothermographic Probability Of Detection" Review of Quantitative Nondestructive Evaluation **27** 491-497 (2008). <http://dx.doi.org/10.1063/1.2902701>.
112. Holland, S. D., Renshaw, J., and Roberts, R., "Measurement Of Dynamic Full-Field Internal Stresses Through Surface Laser Doppler Vibrometry", Applied Physics Letters **91**, 134101 (2007) <http://dx.doi.org/10.1063/1.2790379>.
113. Renshaw, J., Holland, S. D., and Thompson, R. B., "Measurement Of Crack Opening Stresses And Crack Closure Stress Profiles From Heat Generation In Vibrating Cracks", Applied Physics Letters **93**, 081914 (2008) <http://dx.doi.org/10.1063/1.2976310>.
114. Renshaw, J., Holland, S. D., Thompson, R. B., and Uhl, C., "The Effect Of Crack Closure On Heat Heneration In Vibrothermography" Review of Quantitative Nondestructive Evaluation **28** 473-480 (2009).
115. Li, M., Holland, S. D., and Meeker, W. Q., "Automatic Crack Detection Algorithm for Vibrothermography Sequence-of-Images Data" Review of Quantitative Nondestructive Evaluation **29** 1919--1926 (2010).
116. Li, M., Holland, S. D., and Meeker, W. Q., "Statistical Methods For Automatic Crack Detection Based On Vibrothermography Sequence-Of-Images Data", Applied Stochastic Models in Business and Industry **26** (5) 481-495 (2010).
117. Renshaw, J., Holland, S. D., Thompson, R. B., and Anderegg, J., "Vibration-Induced Tribological Damage To Fracture Surfaces Via Vibrothermography", International Journal of Fatigue **33** (7) (2011), pp. 849-857.
118. Renshaw, J., Holland, S. D., and Barnard, D. J., "Viscous Material-Filled Synthetic Defects For Vibrothermography", NDT& E International **42** (8), 753-756 (2009).
119. Renshaw, J., Holland, S. D., Thompson, R. B., and Eisenmann, D. J., "Synthetic Defects for Vibrothermography" Review of Quantitative Nondestructive Evaluation **92** 498-504 (2010).
120. Holland, S. D., "Thermographic Signal Reconstruction For Vibrothermography" Infrared Physics and Technology, **54** (6): 503-511.
121. Li, Y. and Bowler, N., "Resonant Frequency Of A Rectangular Patch Sensor Covered With Multilayered Dielectric Structures", *IEEE Trans. Antennas Propagat.*, Vol. 58, No. 6, pp. 1883-1889, June 2010.

122. Li, Y., Bowler, N., and Johnson, D., "A Resonant Microwave Patch Sensor For Detection Of Layer Thickness Or Permittivity Variations In Multilayered Dielectric Structures", *IEEE Sensors J.*, Vol. 11, No. 1, pp. 5-15, January 2011.
123. Li, Y. and Bowler, N., "Analysis Of Double-Negative (DNG) Bandwidths For Metamaterials Composed Of Three-Dimensional Periodic Arrays Of Two Different Magnetodielectric Spheres Arbitrarily Arranged On A Simple Tetragonal Lattice", *IEEE Antennas Wireless Propag. Lett.*, Vol. 10, 2011.
124. Li, Y. and Bowler, N., "Effects Of Non-Metallic Parameter Variations On Negative Effective Constitutive Parameters Of Metalmaterials", *J. Appl. Phys.*, Volume 113, 063501, 2013.
125. Chen, T. and Bowler, N., "Analysis Of A Concentric Coplanar Capacitive Sensor For Nondestructive Evaluation In Multi-Layered Dielectric Structures", *IEEE Trans. Dielectr. Electr. Insul.*, 17, pp. 1307-1318, 2010.
126. Jepsen, P. U. and Keiding, S. R., "Radiation Pattern From Lens-Coupled Terahertz Antennas", *Opt. Lett.*, Vol. 20, No. 8, pp. 807-809, 1995.
127. Rudd, J. V., Johnson, J. L., and Mittleman, D. M., "Cross-Polarized Angular Emission Patterns From Lens-Coupled Terahertz Antennas", *J. Opt. Soc. Am. B*, Vol. 18, No. 10, pp. 1524-1533, 2001.
128. Goodman, J. W., *Introduction To Fourier Optics*, 3rd edition, Roberts & Co., 2004.
129. Chiou, C.-P., Thompson, R. B., and Blackshire, J. L., "Modeling Of Terahertz Ray Signals For NDE Applications", in *Review of Progress in Quantitative Nondestructive Evaluation*, Vol. 27A, pp. 414-420, 2008.
130. Stoik, C. D., Bohn, M. J., and Blackshire, J. L., "Nondestructive Evaluation Of Aircraft Composites Using Transmissive Terahertz Time Domain Spectroscopy", *Opt. Express* 16, 17039-17051, 2008.
131. Rutz, F., Koch, R., Khare, S., Moneke, M., Richter, H., and Ewert, U., *Int'l J. Infra. Mm. Waves* 27, 547-556, 2006.
132. Chiou, C.-P., Blackshire, J. L., and Thompson, R. B., "Terahertz Ray System Calibration And Material Characterizations", in *Review of Progress in Quantitative Nondestructive Evaluation*, Vol. 28A, pp. 410-417.
133. Orfanidis, S. J., *Electromagnetic Waves and Antennas*, 2008, Rutgers University.
134. More, J. J. et al., *User Guide for MINPACK-1*, ANL-80-74, Argonne National Lab, 1980.
135. Chiou, C.-P., Hsu, D. K., Barnard, D. J., Im, K.-H., and Thompson, R. B., "Signal Modeling In The Far-Infrared Region For Nondestructive Evaluation Applications", in *Review of Progress in Quantitative Nondestructive Evaluation*, Vol. 30A, pp. 581-588, 2011.
136. Barnard, D. J., Peters, J. J., and Hsu, D. K., "Towards A Generic Manual Scanner For Nondestructive Inspection", in *Review of Progress in Quantitative Nondestructive Evaluation*, AIP Conf. Proc. 760, pp. 1669-1676.
137. Mimio, 1 Charles Park, 3rd Floor, Cambridge, MA 02142, www.mimio.com
138. 4D Systems Pty. Ltd., Unit 3, 51 York Road, Penrith, 2750, NSW, Australia, www.4dsystems.com.au
139. Peters, J. J., Barnard, D. J., Hudelson, N. A., Simpson, T. S., and Hsu, D. K., "A Prototype Tap Test Imaging System: Initial Field Test Results", in *Review of Progress in Quantitative Nondestructive Evaluation*, AIP Conf. Proc. 509, pp. 2053-2060.

140. <http://prometheus.med.utah.edu/~bwjones/2008/06/c-130-hercules/comment-page-1/>
141. Thompson, R. B., "Ultrasonic Measurement of Mechanical Properties", 1996 IEEE Ultrasonics Symposium, pp. 735-744.
142. Raj, B., Moorthy, V., Jayakumar, T., and Rao, K. Bhanu Sankara, "Assessment of Microstructures and Mechanical Behaviour of Metallic Materials Through Non-Destructive Characterisation", International Materials Reviews, 2003, 48(5): 273-325.
143. Bond, L. J., Doctor, S. R., and Taylor, T. T., "Proactive Management of Materials Degradation-A Review of Principles and Programs, August, 2008, PNNL-17779 and Bond, L. J., Doctor, S. R., Griffin, J. W., Hull, A. B., and Malik, S. N., "Damage Assessment Technologies for Prognostics and Proactive Management of Materials Degradation (PMMD), Nucl. Tech., 2011, 173:46-55.
144. Engle, B. J., Schmerr, Jr., L. W., and Sedov, Alexander, "Equivalent Flaw Time-of-Flight Diffraction Sizing with Ultrasonic Phased Arrays", in *Review of Progress in Quantitative Nondestructive Evaluation*, Vol. 32, pp. 895-901.

Appendix A - Project Presentations and Publications

Presentations

1. N. Nakagawa, C. Lee, and Y. Shen, "High frequency eddy current inspection system and its application residual stress characterization", presented at the 32st Annual Conference of the Review of Progress in Quantitative Nondestructive Evaluation (RPQNDE), Bowdoin College, Brunswick, Maine, Colorado, July 31-August 5, 2005.
2. C. Lee, Y. Shen, C. C. H. Lo and N. Nakagawa, "Characterization of Residual Stress in Nickel-based Superalloys Using High-frequency Eddy Currents", presented at the 17th Annual AeroMat Conference and Exposition, Washington State Convention & Trade Center, Seattle, Washington, May 15-18, 2006.
3. C. C. H. Lo, Y. Shen, S. J. Lee, A. M. Frishman, and N. Nakagawa, "Advances in swept high frequency eddy current residual stress characterization". Presented at the 18th Annual AeroMat (Advanced Aerospace Materials and Processes) Conference & Exposition held in Baltimore, Maryland, June 25-28, 2007.
4. Y. Shen, A. M. Frishman, S. J. Lee, C. C. H. Lo and N. Nakagawa, "Advances in Swept High Frequency Eddy Current Residual Stress Characterization", presented at the 33rd Annual Conference of the Review of Progress in Quantitative Nondestructive Evaluation (RPQNDE) held in Golden, Colorado, July 22 to 27, 2007.
5. C. C. H. Lo, A. M. Frishman, Y. Shen, and N. Nakagawa, "Self-calibrated Swept Frequency Eddy Current Measurements for Residual Stress Characterization", presented at the 13th Conference in Electromagnetic NDE held in Seoul, Korea from June 10-12, 2008.
6. C. C. H. Lo, A. M. Frishman, Y. Shen, and N. Nakagawa, "Self-calibrated Swept Frequency Eddy Current Measurements for Characterization of near surface material conditions", presented at the 35rd Annual Conference of the Review of Progress in Quantitative Nondestructive Evaluation (RPQNDE) held in Chicago, Illinois, July 20 to July 25, 2008.
7. N. Nakagawa, A. M. Frishman, Y. Shen and C. C. H. Lo, "Shot-peening intensities vs. eddy current signals as seen in iterative treatment-measurement experiment", presented at the 35rd Annual Conference of the Review of Progress in Quantitative Nondestructive Evaluation (RPQNDE) held in Chicago, Illinois, July 20 to July 25, 2008.
8. A. M. Frishman, C. C. H. Lo, Y. Shen and N. Nakagawa, "A Scaling Law for Nondestructive Evaluation of Shot Peening Induced Surface Material Property Deviations", presented at the 35rd Annual Conference of the Review of Progress in Quantitative Nondestructive Evaluation (RPQNDE) held in Chicago, Illinois, July 20 to July 25, 2008.
9. A. M. Frishman, C. C. H. Lo, Y. Shen, and N. Nakagawa, "A Scaling Law in Shot Peening Induced Surface Material Property Deviations", presented at the 10th International Conference on Shot Peening held in Tokyo, Japan, September 15-18, 2008.
10. N. Nakagawa, and C. C. H. Lo, "Unconventionally high and low frequency eddy current methods for material surface characterizations", presented at the 36rd Annual Conference of the *Review of Progress in Quantitative Nondestructive Evaluation*, University of Rhode Island, July 26-31, 2009.
11. N. Nakagawa, J. N. Gray, T. Jensen, C. C. H. Lo, "Nondestructive Residual Stress Characterization Methodologies: An Overview of Developments of High Frequency Eddy Current and High Energy XRD Methods", presented at the 8th International Conference on

- NDE in Relation to Structural Integrity for Nuclear and Pressurized Components, September 29 to October 1, 2010, Berlin, Germany.
12. N. Nakagawa, C. C. H. Lo, and A. M. Frishman, "Conductivity profile determination via model-based inversion of swept frequency eddy current data, and its use for near-surface material characterization", presented at the TMS Annual Meeting 2011, San Diego, California, Feb 27-March 3, 2011.
 13. N. Nakagawa, R. Chandrasekar, A. M. Frishman and C. C. H. Lo, "Swept Frequency Eddy Current Measurements and Near-Surface Conductivity Profiling towards Residual Stress Characterization", presented at the AA&S 2011, San Diego, California, April 18-21, 2011.
 14. C. C. H. Lo, N. Nakagawa, R. Chandrasekar, A. M. Frishman and B. F. Larson, "Effects of Microstructure on Nondestructive Near Surface Conductivity Characterization and Residual Stress Profiling in Nickel-base Superalloy by Swept Frequency Eddy Current", presented at The 38th Annual Review of Progress in QNDE, University of Vermont, Burlington, Vermont, July 17-22, 2011.
 15. N. Nakagawa and C. C. H. Lo, "Eddy current methods for surface material characterization with multiple high and low frequencies", presented at The ISNT NDE 2011, Chennai Technical Center, Chennai, India, December 6-11, 2011.
 16. R. Chandrasekar, T. Lesthaeghe, A. M. Frishman, B. F. Larson, C. C. H. Lo and N. Nakagawa, "Characterization of Near Surface Conductivity Profiles of Shot Peened and Laser Peened Inconel 718", presented at the AeroMat (Advanced Aerospace Materials and Processes) Conference & Exposition held in Charlotte Convention Center, Charlotte, North Carolina, June 18-21, 2012.
 17. R. Chandrasekar, A. M. Frishman, C. C. H. Lo and N. Nakagawa, "Influences of Secondary Phase Precipitate Density and Residual Stress on Conductivity Profiles of Shot Peened Nickel-base Superalloy", presented at the 39th Annual Review of Progress in QNDE, Hyatt Regency Denver Tech Center, Denver, Colorado, July 15-20, 2012.

Publications

1. N. Nakagawa, C. Lee, and Y. Shen, "High frequency eddy current inspection system and its application residual stress characterization", the Proceeding of *Review of Progress in Quantitative Nondestructive Evaluation* (RPQNDE), vol. 25, pp. 1418-1424, 2006.
2. Y. P. Shen, A. M. Frishman, C. Lee, C. C. H. Lo and N. Nakagawa, "Conductivity Profile Determination by Eddy Current for Shot Peened Superalloy Surfaces toward Residual Stress Assessment", *Journal of Applied Physics*, 101, 014907-1, 2007.
3. Y. Shen, C. C. H. Lo, A. M. Frishman, C. Lee and N. Nakagawa, "Conductivity Profile Determination by Eddy Current for Shot Peened Superalloy Surfaces toward Residual Stress Assessment", the Proceeding of *Review of Progress in Quantitative Nondestructive Evaluation* (RPQNDE), 26B, 1229-1236, 2007.
4. C. Lee, Y. Shen, C. C. H. Lo and N. Nakagawa, "Validation of a Residual Stress Measurement method by Swept High-frequency Eddy Currents", the Proceeding of *Review of Progress in Quantitative Nondestructive Evaluation* (RPQNDE), 26B, 1213-1219, 2007.
5. Y. Shen, A. M. Frishman, S. J. Lee, C. C. H. Lo and N. Nakagawa, "Advances in Swept High Frequency Eddy Current Residual Stress Characterization", the Proceeding of *Review*

- of Progress in Quantitative Nondestructive Evaluation* (RPQNDE) 2008, Vol. 27, pp. 1222-1227, 2008.
6. C. C. H. Lo, A. M. Frishman, Y. Shen and N. Nakagawa, "Self-consistent swept frequency eddy current measurements for characterization of near surface material conditions", AIP Conference Proceedings (2009), 1096, *Review of Progress in Quantitative Nondestructive Evaluation*, Volume 28B, 1363-1370.
 7. N. Nakagawa, A. M. Frishman, Y. Shen and C. C. H. Lo, "Shot-peening intensities vs. eddy current signals as seen in iterative treatment-measurement experiment", AIP Conference Proceedings (2009), 1096, *Review of Progress in Quantitative Nondestructive Evaluation*, Volume 28B, 1356-1362.
 8. A. M. Frishman, C. C. H. Lo, Y. Shen and N. Nakagawa, "A scaling law for nondestructive evaluation of shot peening induced surface material property deviations", AIP Conference Proceedings (2009), 1096, *Review of Progress in Quantitative Nondestructive Evaluation*, Volume 28B, 1341-1348.
 9. C. C. H. Lo, A. M. Frishman, Y. Shen, and N. Nakagawa, "Self-calibrated Swept Frequency Eddy Current Measurements for Surface Characterization", *Studies in Applied Electromagnetics and Mechanics* 32, *Electromagnetic Nondestructive Evaluation (XII)*, Y.-K. Shin et al (Eds.), OIP Press, 2009, pp. 99-106.
 10. Y. Shen, C. C. H. Lo, N. Nakagawa, and A. M. Frishman, "Residual Stress Profile Assessment by Eddy Current for Shot Peened Nickel Superalloy", *Journal of Nondestructive Evaluation*, Volume 29, Number 1, Pages 1-13, 2010.
 11. N. Nakagawa and C. C. H. Lo, "Unconventionally high and low frequency Eddy current methods for material surface characterizations", AIP Conference Proceedings (2010), 1211 *Review of Progress in Quantitative Nondestructive Evaluation*, Volume 29B, 1471-1478.
 12. N. Nakagawa, J. Gray, T. Jensen, and C. C. H. Lo, "Nondestructive Residual Stress Characterization Methodologies: An Overview of Developments of High Frequency Eddy Current and High Energy XRD Methods", Proceeding of the 8th NDE Conference, Berlin, Germany, September 29 to Oct 1, 2010.
 13. R. Chandrasekar, A. M. Frishman, B. F. Larson, C. C. H. Lo and N. Nakagawa, "Effects of Microstructure on Eddy Current Residual Stress Characterization of Shot Peened Inconel 718", JOM: Volume 64, Issue 2 (2012), Page 257-264.
 14. R. Chandrasekar, C. C. H. Lo, A. M. Frishman, B. F. Larson, and N. Nakagawa, "Quantification of Precipitates and their Effects on the Response of Nickel-Base Superalloy to Shot Peening", Proceeding of the *Review of Progress in Quantitative Nondestructive Evaluation*, vol. 31. AIP Conference Proceedings, Volume 1430, pp. 1437-1444 (2012).

Appendix B – Additional Technical Results

3.1.A Validation of SHFEC Measurement Methodology

A four-stage study on simulated layer specimens was performed in order to validate the SHFEC measurement and model-based inversion procedures. Artificially made specimens consist of alloy foils placed on metal substrate as illustrated schematically in Figure A1, where the foils have known thicknesses with slightly different conductivities from the substrate, in order to simulate modified surface layers of shot-peened components. The foil materials and thicknesses are listed in Table A-1. The purposes of the validation procedure were to (1) calibrate and evaluate the accuracy of the SHFEC measurement system, and (2) validate the EC inversion procedure, i.e., solving conductivity profile perpendicular to a stratified alloy plate. For validation of the forward model (stage 1), the conductivity profile was considered known; and the measured and computed V-components as a function of frequency were compared. For stages 2 through 4, which were aimed at validating the inverse model, the NiCr and IN718 foil conductivities were determined by inversion from SHFEC signals and compared with direct measurements using the direct current potential drop (DCPD) method.

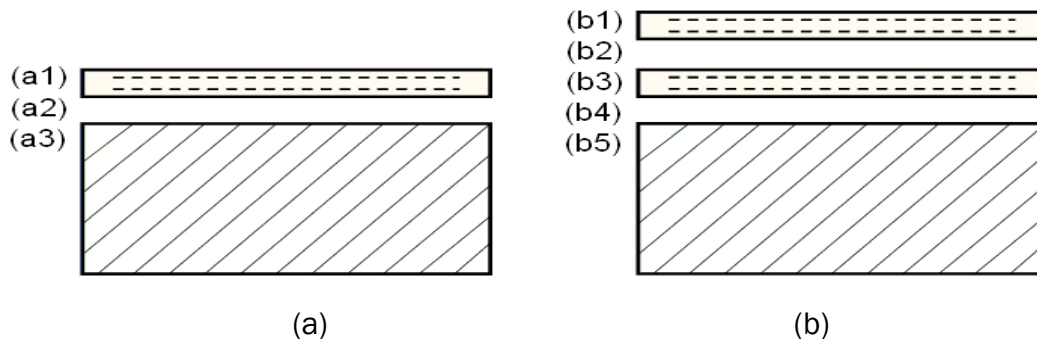


Figure A1. (a) Illustrations Of Simulated Layer Specimen Configurations (Not To Scale): (a) The Single-Layer Configuration Consists Of A Top Layer (a1), An Air Gap (a2) And The Substrate (a3). (b) The Double-Layer Configuration Consists Of Two Metal Layers [(b1), (b3)], And Two Air Gaps [(b2), (b4)] And The Substrate [(b5)]

Table A-1. Configurations Of Simulated Layer Specimens Used In The Validation Study Of The Conductivity Profile Inversion Procedure

| Configurations of simulated layer specimen | | | |
|--|------------------------|------------------------|-------------|
| Stage | Top-most layer | 2nd layer | Substrate |
| 1 | 25 μ m Cu foil | None | Al Block |
| 2 | 103 μ m IN718 foil | None | IN718 Block |
| 3 | 133 μ m NiCr foil | None | IN718 Block |
| 4a | 133 μ m NiCr foil | 103 μ m IN718 foil | IN718 Block |
| 4b | 103 μ m IN718 foil | 133 μ m NiCr foil | IN718 Block |

As shown in Figure A1, the EC model takes into account the air gap between two adjacent surfaces which is inevitably present in the simulated layer specimens due to the imperfect matching of the two surfaces. In applying the inversion algorithm, the foil conductivity and the air gap thickness were treated as fitting parameters when minimizing the difference between V_{EX} and V_{TH} over the entire frequency range. The inclusion of the air gaps affects only low-frequency predictions and its fitted values are typically of the order of 10 μ m for stages 1-4 (Table A-2).

Table A-2. Inversion Results Of Stages 2, 3 And 4 Study With The Following Fixed Input Parameters: Bulk Conductivity Of IN718 Block $\Sigma_{in718} = 1.38\%$ IACS, And Measured Thicknesses Of The IN718 And Nicr Foils Are 103 Mm And 133 Mm, Respectively. Also Shown Are The Conductivities Of The IN718 And Nicr Foils Measured Using The DCPD Method

| Specimen | | Stage-2 | Stage-3 | Stage-4a | Stage-4b | DCPD |
|-----------------------------|--------------------------------|---------|---------|----------|----------|-------|
| Inversion output parameters | σ of IN718 foil (%IACS) | 1.348 | — | 1.352 | 1.352 | 1.342 |
| | σ of NiCr foil (%IACS) | — | 1.629 | 1.595 | 1.626 | 1.562 |
| | Air gap 1 (μ m) | 15.0 | 12.9 | 10.0 | 13.2 | — |
| | Air gap 2 (μ m) | — | — | 17.0 | 13.5 | — |
| Relative fitting error (%) | | 3.7 | 9.2 | 11.5 | 11.5 | — |

Results of the four stages of the validation study are shown in Figure A2. In general, the computed and measured V components (with variance of ~10%) show agreement in all four stages, validating the forward model. The experimental H component is prone to lift-off noise and could be significantly different from the theoretical value (e.g., Figure A2 (a)). The H-

component is therefore unusable in validation. The results of all the four test stages are summarized in Table A-2, including the inverted foil conductivities where applicable. The inverted conductivities of the NiCr and IN718 foils agree with those measured by the DCPD method. The present results show that (1) our inverse procedure functions properly for our SHFEC measurement setup and the frequency range. (2) Our forward and inversion modeling procedures work adequately at 12% at worst in terms of fitted relative norm over the entire frequency range of 1-50 MHz.

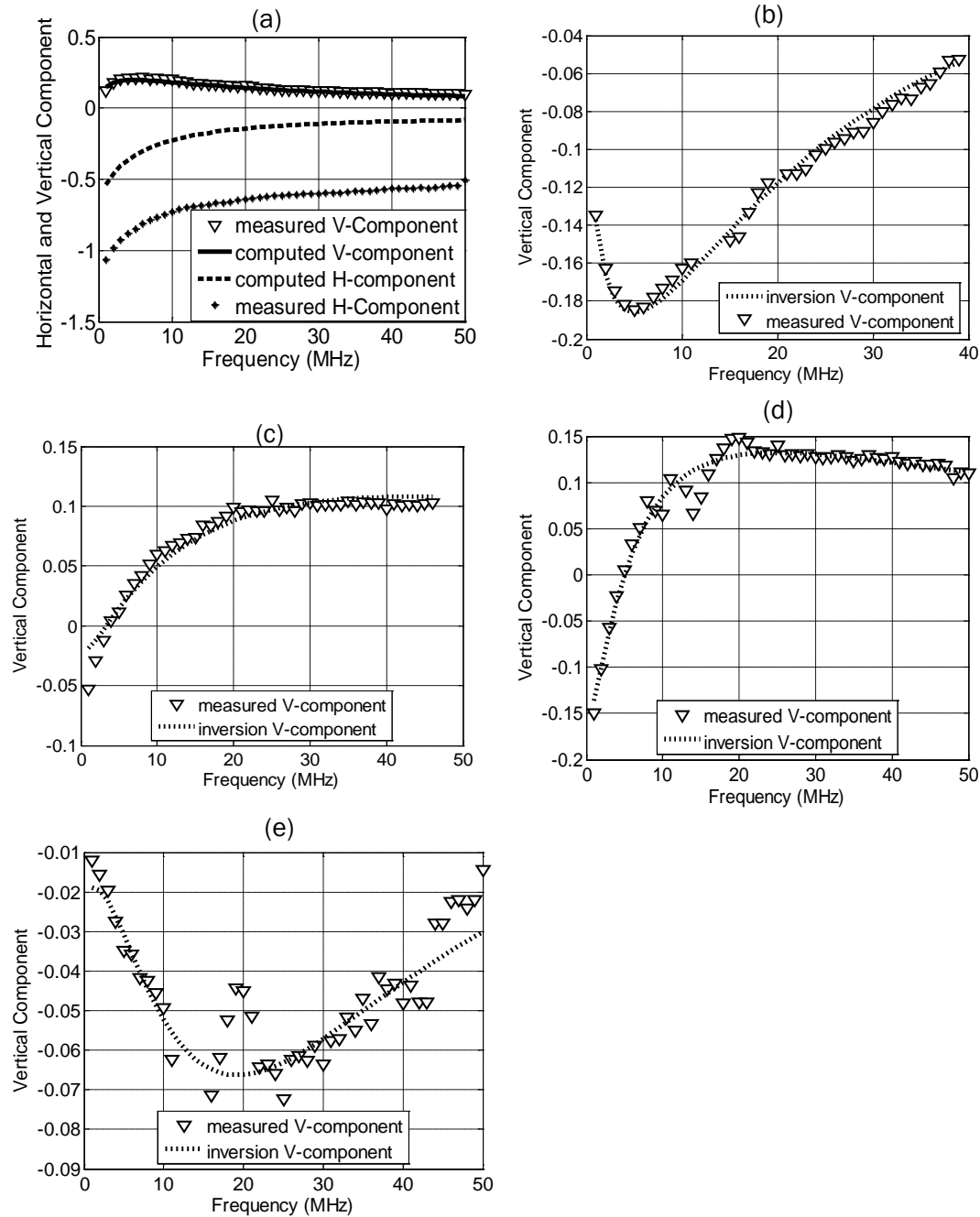


Figure A2. (a) The Calculated And Experimental H And V Components Versus Frequency For Stage 1. Note The Agreement In The V-Components And The Disagreement In The H Components. (b) Through (e) The Calculated And Experimental V Components Vs. Frequency For Stages 2, 3, 4a, And 4b, Respectively

3.1.B Conductivity Profile Functions For Model-Based Inversion

Starting with the perturbation formula [Equation (5)]

$$H + jV_{TH} = -\frac{1}{l} \int_0^\infty \frac{\Delta\sigma(z)}{\sigma_0} \exp(-pz) dz, \quad p \equiv 2jk = 2j(1-j)/\delta = 2(1+j)/\delta \quad (1)$$

we find, after re-scaling, that

$$(4l/\delta)V = \frac{4}{\delta} \int_0^\infty \frac{\Delta\sigma(z)}{\sigma_0} e^{-2z/\delta} \sin \frac{2z}{\delta} dz = 2 \int_0^\infty \frac{1}{\sigma_0} \Delta\sigma\left(\frac{\delta}{2}u\right) e^{-u} \sin u du.$$

Thus, in general, V takes the form

$$\boxed{\sqrt{f} \cdot V \propto F(\sqrt{f})} \quad (2)$$

More than twenty conceivable profile functions have been studied regarding their potential use to fit the experimental results. Some of the profile functions and the corresponding expressions of F are shown in Table B-1.

Table B-1. Basic profile functions and the corresponding expression of $F(\xi)$, where $\xi=2d/\delta$.

| | | $\frac{\Delta\sigma(z)}{\sigma_0}$ | $(4l/\delta)V$ | $F(\xi)$ |
|---|------------------------------------|--|--|---|
| 1 | Uniform offset | 1 | $F\left(\frac{2d}{\delta}\right)$ | 1 |
| 2 | Step Function | $\theta(d-z)$ | $F\left(\frac{2d}{\delta}\right)$ | $1 - \sqrt{2}e^{-\xi} \sin\left(\xi + \frac{\pi}{4}\right)$ |
| 3 | Exponential decay | $e^{-z/d}$ | $F\left(\frac{2d}{\delta}\right)$ | $2\xi^2 \left[(1+\xi)^2 + \xi^2 \right]^{-1}$ |
| 4 | Linear with a cut off | $\left(1 - \frac{z}{d}\right)\theta(d-z)$ | $F\left(\frac{2d}{\delta}\right)$ | $\frac{1}{\xi} \left(\xi - 1 + e^{-\xi} \cos \xi \right)$ |
| 5 | 1/z with an exponential decay | $\frac{d}{z} e^{-z/d}$ | $F\left(\frac{2d}{\delta}\right)$ | $2\xi \arctan \frac{\xi}{\xi+1}$ |
| 6 | 1/z ... with low z cut off | $\left(1 - e^{-\lambda z}\right) \frac{d}{z} e^{-z/d}$ | $F\left(\frac{2d}{\delta}\right) - (1+\lambda d)F\left(\frac{2d}{\delta(1+\lambda d)}\right)$ | $2\xi \arctan \frac{\xi}{\xi+1}$ |
| 7 | Rational function, peak with decay | $\frac{\zeta z}{\zeta^2 + z^2} e^{-z/d}$ | $F\left(\frac{2d}{\delta}, \frac{\zeta}{d}\right)$ | (*) |
| 8 | Rational function, no peak | $\frac{\zeta^2}{\zeta^2 + z^2} e^{-z/d}$ | $F\left(\frac{2d}{\delta}, \frac{\zeta}{d}\right)$ | (**) |
| 9 | Rational, offset peak | $\frac{(\alpha z + \beta \zeta)\zeta}{\zeta^2 + z^2} e^{-z/d}$ | $\alpha F^{(7)}\left(\frac{2d}{\delta}, \frac{\zeta}{d}\right) + \beta F^{(8)}\left(\frac{2d}{\delta}, \frac{\zeta}{d}\right)$ | |

* For Type 7:

Scale to d = depth of the exponent

$$\frac{\zeta z}{\zeta^2 + z^2} e^{-z/d} = \frac{\varepsilon(z/d)}{\varepsilon^2 + (z/d)^2} e^{-z/d}$$

$$F(\xi, \varepsilon) = (-\varepsilon)\xi \operatorname{Im} [e^{j\theta} E_1(j\theta) + e^{-j\theta} E_1(-j\theta)]$$

$$\theta \equiv \varepsilon [1 + (1 + j)\xi]$$

**** For type 8:**

$$\frac{\zeta^2}{\zeta^2 + z^2} e^{-z/d} = \frac{\varepsilon^2}{\varepsilon^2 + (z/d)^2} e^{-z/d}$$

$$F(\xi, \varepsilon) = (-\varepsilon\xi) \operatorname{Im} j [e^{j\theta} E_1(j\theta) - e^{-j\theta} E_1(-j\theta)]$$

$$\theta \equiv \varepsilon [1 + (1 + j)\xi]$$

Here $E_1(z) = \int_z^\infty t^{-1} \exp(-t) dt$ is the exponential integral function.

3.1.C Dependence of Bulk Conductivity and Hardness on Microstructure of the Heat-Treated Inconel 718 Samples

The bulk conductivity and hardness of the heat-treated Inconel 718 samples are shown in Figure C1 (refer to Table 1 for the details of heat treatment). The bulk conductivity of the samples tends to increase with hardness, except for Sample III which is less conducting but is harder than the solutionized Samples I and II. The general trend of increasing bulk conductivity with hardness observed in the other samples is attributed to the formation of secondary phase precipitates that contribute to the sample hardness, and at the same time withdraws solute elements from the matrix. This reduces electron scattering by solute atoms in the solid solution and therefore results in higher conductivities of the aged samples (IV, V, VI and VII) than in the solutionized ones (I and II).

High resolution transmission electron microscopy (TEM) study revealed that Sample III has a high density of very fine secondary phase precipitates (Figure C2) that contribute to its hardness. The exceptionally low conductivity of Sample III is attributable to this fact, namely, the small precipitates could act as scatterers for conduction electrons and reduce the conductivity compared to the solutionized samples (I and II), when the inter-particle spacing is comparable to, or smaller than, the electron mean free path.

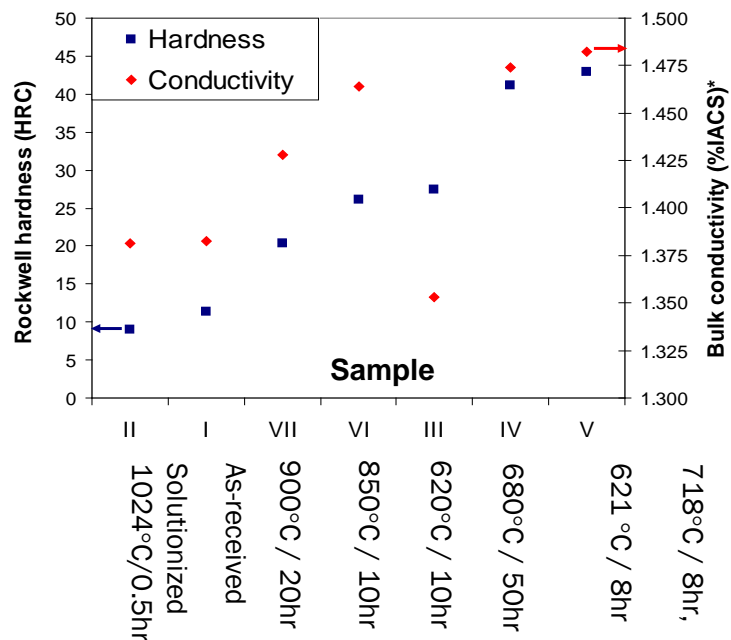


Figure C1. Rockwell C-Scale Hardness (HRC) And Bulk Conductivity Of The Heat-Treated Inconel 718 Samples In The Ascending Order Of Hardness From Left To Right

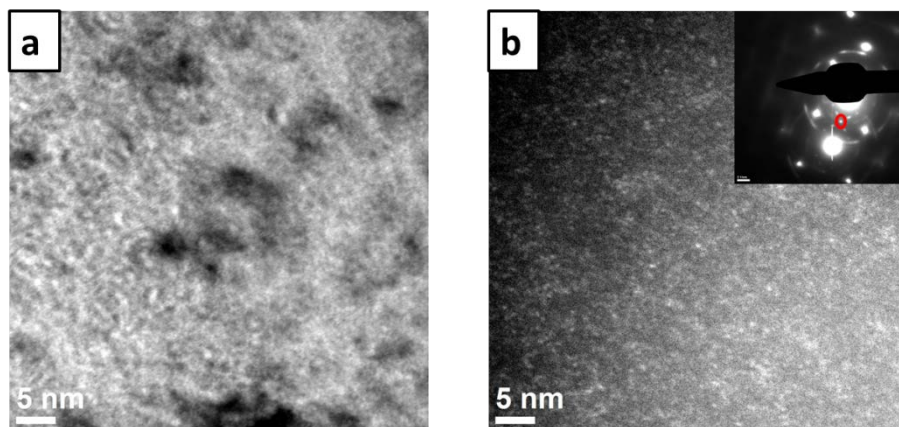


Figure C2. (a) Bright Field Image, And (b) Dark Field Image Of Sample III Formed By Using The Superlattice Spot Circled In Red In The Inset Showing The Presence Of Secondary Phase Precipitates ~ 2-3 nm In Size

Appendix C – MAPOD Prospectus

Microsoft Word - POD WORKING GROUP-Prospectus.doc - POD WO... [http://www.cnde.iastate.edu/mapod/POD WORKING GROUP-Prospectus.pdf](http://www.cnde.iastate.edu/mapod/POD%20WORKING%20GROUP-Prospectus.pdf)

MODEL-ASSISTED POD WORKING GROUP

Prospectus

July 11, 2004

Objective:

- To promote the increased understanding, development and implementation of model-assisted POD methodologies.

Background:

There is an increasing recognition that the use of physics-based models has the potential to assist in the determination of POD by reducing the time and cost of conducting POD studies, quite likely increasing the accuracy and portability of the results in the process. However, the definition of procedures and protocols to best realize these advantages is in its early days; initial demonstrations have been made but the results have not been widely discussed. The Model-Assisted POD Working Group will consist of a broad community with interests in POD determination. It will serve as a forum to discuss and provide input on a wide variety of issues related to this emerging approach.

Approach:

The working group will meet periodically and conduct the following activities:

- Discuss strategies for model-assisted POD determination
- Discuss requirements for models to be used in POD studies
- Identify gaps that need to be addressed between state of the art models and real world problems
- Provide input regarding examples of specific problems that would demonstrate the utility of model-assisted POD activities
- Communicate the results of model-assisted POD demonstrations

The working group would not be expected to do the detailed work in these areas but rather serve as a sounding board and provide general input. Examples of topics that might be considered in each of these activities are the following:

Discuss strategies for model-assisted POD determination

- Empirical approaches, refined to include insight from physics-based models
- Model-assisted methodologies based on flaw response
- Model-assisted methodologies based on image data

Discuss requirements for models to be used in POD studies

- Accuracy expected of models
- Extent of validation required

- Strategies/requirements for determining input parameters

Provide input regarding examples of specific problems that would demonstrate the utility of model-assisted POD activities

- How models can be used to establish the acceptability of replacement inspection techniques, e.g., transition from single frequency eddy current methods to transient eddy current methods
- Use of models to assist in the transfer the results of assessments under one set of conditions to a related set of conditions
- Full POD determinations as required to meet lifing requirements

Share the results of model-assisted POD demonstrations

- Details will be depend on the demonstrations that are undertaken in other, focused projects or data that can be made available from working group members.

Metric:

The Model-Assisted POD Working Group will be considered a success if, during its duration, activities under a variety of programs lead to

- Draft protocols for model-assisted POD
- Draft requirements for model qualification for use in POD determination
- Model-assisted POD demonstrations

Duration:

The Model-Assisted POD Working Group will be initially constituted for a period of 18 months.

Output:

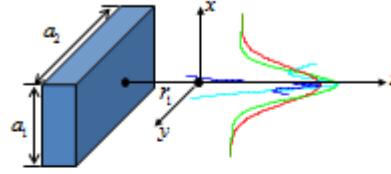
A final report will be prepared summarizing the findings of the Model-assisted POD Working Group, including suggested

- Strategies for model-assisted POD determination
- Requirements for models to be used in POD determinations
- Examples of specific opportunities for future demonstrations
- Future directions

APPENDIX D

MG beam model for rectangular probes

The pressure generated by a rectangular transducer can be simulated by superposition of 15 Gaussians:



$$\frac{p(x, y, z=0)}{\rho_1 c_1 v_0} = \exp(ik_z r_1)$$

$$\sum_{n=1}^{15} \sum_{m=1}^{15} A_n A_m \sqrt{\frac{1}{1+c_{z1} r_1 [\mathbf{M}_{mn}(0)]_{1,1}}} \sqrt{\frac{1}{1+c_{z1} r_1 [\mathbf{M}_{mn}(0)]_{2,2}}} \exp\left[\frac{i\omega}{2} \mathbf{X}^T \mathbf{M}_{mn}(r_1) \mathbf{X}\right]$$

$$[\mathbf{M}_{mn}(r_1)]_{1,1} = \frac{[\mathbf{M}_{mn}(0)]_{1,1}}{1+c_{z1} r_1 [\mathbf{M}_{mn}(0)]_{1,1}}, [\mathbf{M}_{mn}(r_1)]_{2,2} = \frac{[\mathbf{M}_{mn}(0)]_{2,2}}{1+c_{z1} r_1 [\mathbf{M}_{mn}(0)]_{2,2}}$$

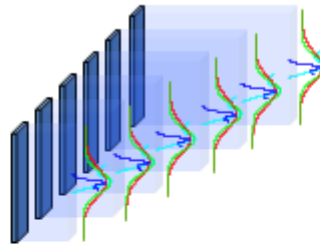
$$[\mathbf{M}_{mn}(0)]_{1,1} = \frac{iB_n}{c_{z1} D_{n1}}, [\mathbf{M}_{mn}(0)]_{2,2} = \frac{iB_m}{c_{z1} D_{m2}}, [\mathbf{M}_{mn}(0)]_{1,2} = [\mathbf{M}_{mn}(0)]_{2,1} = 0 \quad \mathbf{X} = [x, y]$$

$$D_{n1} = k_{z1} a_1^2 / 2 \quad D_{m2} = k_{z1} a_2^2 / 2$$

A_n and B_n are coefficient tabulated in Wen and Breazeale's papers:

Figure D.1. Multigaussian Model For A Single Rectangular Element

MG beam model for linear phased arrays



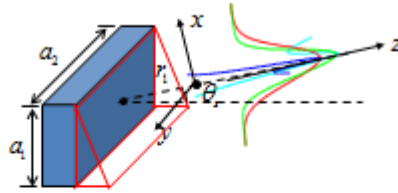
Wave field generated by a linear phased array is superposition of wave fields from all active elements modulated by a time delay t_n

$$p = \sum_{n=1}^N p_n \exp[i\omega t_n]$$

t_n is time delay applied to obtain beam steering and focusing

Figure D.2. Phased Array Model For A Linear Array Of Rectangular Elements

Linear-phased MG beam model



With these linear phased Gaussian beams, the normalized pressure generated by a single rectangular element is given by:

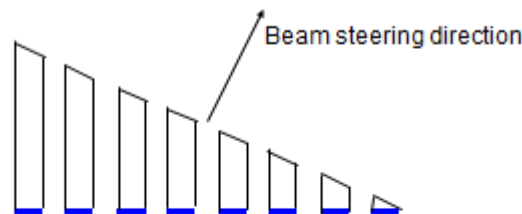
$$\frac{p(x, y, z = 0) \cos \theta_z}{\rho_0 c_0 v_0} = \exp(ik_z r_1) \sum_{n=1}^{15} \sum_{m=1}^{15} A_n A_m \sqrt{\frac{1}{1 + c_{z1} r_1 [\mathbf{M}_{mn}(0)]_{1,1}}} \sqrt{\frac{1}{1 + c_{z1} r_1 [\mathbf{M}_{mn}(0)]_{2,2}}} \exp\left[\frac{i\omega}{2} \mathbf{X}^T \mathbf{M}_{mn}(r_1) \mathbf{X}\right]$$

with D_{n1} to be modified as $D_{n1} = \frac{k_z a_1^2 \cos^2 \theta_z}{2}$

3

Figure D.3. Linear Directivity Correction For A Single Rectangular Element

Linear-phased MG beam model for linear phased arrays



Wave field generated by a linear phased array with piecewise linear phasing on each element is superposition of wave fields from all active elements modulated by a delay time t_n

$$p = \sum_{n=1}^N p_n \exp[i\omega t_n]$$

t_n is time delay applied to obtain beam steering and focusing

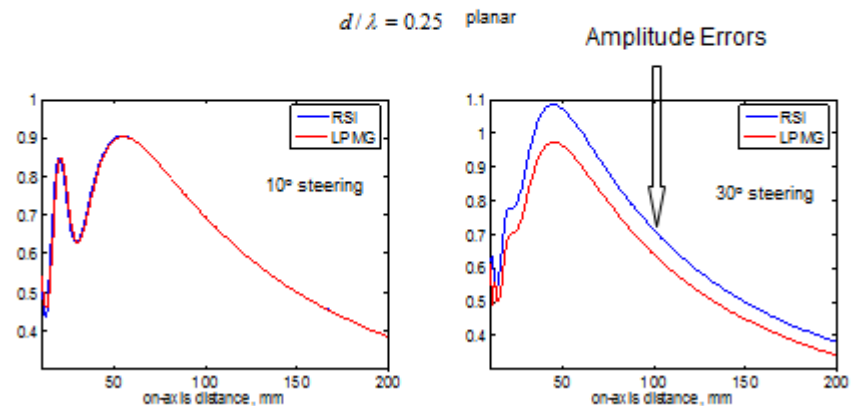
4

Figure D.4. Linear Phased Multigaussian Model Concept

Linear-phased MG beam model

Wave fields predicted by the linear-phased MG beam model are compared with a more exact solution given by Rayleigh-Sommerfeld integrals.

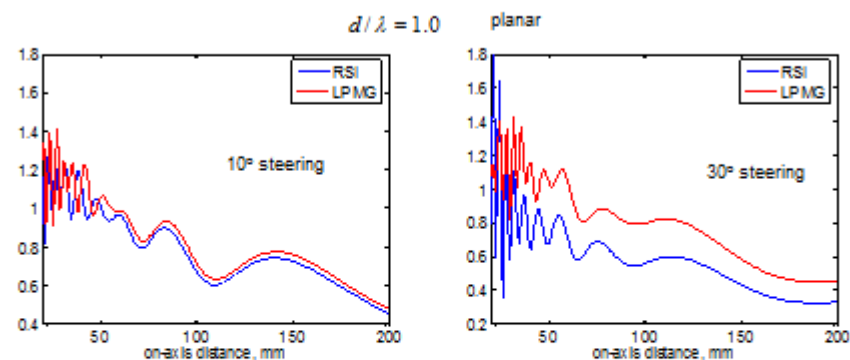
A 32 element 5MHz linear array radiating into steel is simulated.



5

Figure D.5. Amplitude Errors In Linear Phased MG Model

Linear-phased MG beam model



These amplitude differences come from

Paraxial errors
Directivity function errors

An amplitude correction factor can be generated by comparing the linear-phased MG beam model with a more exact beam model for a steered array.

6

Figure D.6. Amplitude Errors In Linear Phased MG Model

A look-up table

| d/λ θ | 0.25 | 0.33 | 0.42 | 0.5 | 0.58 | 0.67 | 0.75 | 0.83 | 1.0 | 1.08 | 1.25 | 1.5 | 1.67 | 1.83 | 2.0 |
|-------------------------|--------|--------|--------|--------|--------|--------|--------|--------|--------|--------|--------|--------|--------|--------|--------|
| 5 | 0.9933 | 0.9924 | 0.9912 | 0.9901 | 0.9889 | 0.9912 | 0.9891 | 0.9869 | 0.9824 | 0.9800 | 0.9724 | 0.9662 | 0.9596 | 0.9525 | 0.9477 |
| 10 | 1.0028 | 0.9998 | 0.9963 | 0.9923 | 0.9877 | 0.9861 | 0.9796 | 0.9724 | 0.9568 | 0.9482 | 0.9292 | 0.8967 | 0.8723 | 0.8459 | 0.8180 |
| 15 | 1.0187 | 1.0124 | 1.0050 | 0.9963 | 0.9863 | 0.9782 | 0.9645 | 0.9494 | 0.9160 | 0.8975 | 0.8585 | 0.7889 | 0.7388 | 0.6856 | 0.6321 |
| 20 | 1.0418 | 1.0312 | 1.0183 | 1.0030 | 0.9852 | 0.9688 | 0.9451 | 0.9193 | 0.8623 | 0.8310 | 0.7664 | 0.6531 | 0.5746 | 0.4938 | 0.4121 |
| 25 | 1.0734 | 1.0572 | 1.0372 | 1.0132 | 0.9856 | 0.9543 | 0.9233 | 0.8843 | 0.7990 | 0.7529 | 0.6661 | 0.5016 | 0.3971 | 0.2943 | 0.1960 |
| 30 | 1.1155 | 1.0920 | 1.0630 | 1.0285 | 0.9889 | 0.9444 | 0.8955 | 0.8476 | 0.7301 | 0.6679 | 0.5435 | 0.3446 | 0.2233 | 0.1097 | |
| 35 | 1.1700 | 1.1378 | 1.0980 | 1.0507 | 0.9969 | 0.9370 | 0.8717 | 0.8146 | 0.6606 | 0.5926 | 0.4392 | 0.1991 | 0.0682 | 0.0589 | |
| 40 | 1.2409 | 1.1981 | 1.1452 | 1.0828 | 1.0123 | 0.9345 | 0.8505 | 0.7617 | 0.5961 | 0.5008 | 0.3242 | 0.0680 | 0.0854 | 0.1852 | |
| 45 | 1.3328 | 1.2773 | 1.2090 | 1.1286 | 1.0384 | 0.9399 | 0.8347 | 0.7250 | 0.4999 | 0.4279 | 0.1793 | 0.0807 | 0.2010 | 0.2752 | |
| 50 | 1.4538 | 1.3835 | 1.2961 | 1.1941 | 1.0804 | 0.9574 | 0.8278 | 0.6943 | 0.4273 | 0.2995 | 0.0680 | 0.1931 | 0.2930 | 0.3327 | |



correction factors are small (12 % or less)



beam steering not possible without 6 dB or greater amplitude losses

7

Figure D.7. Amplitude Correction Factors For Linear Phased MG Model

Simulation examples (with amplitude corrections)

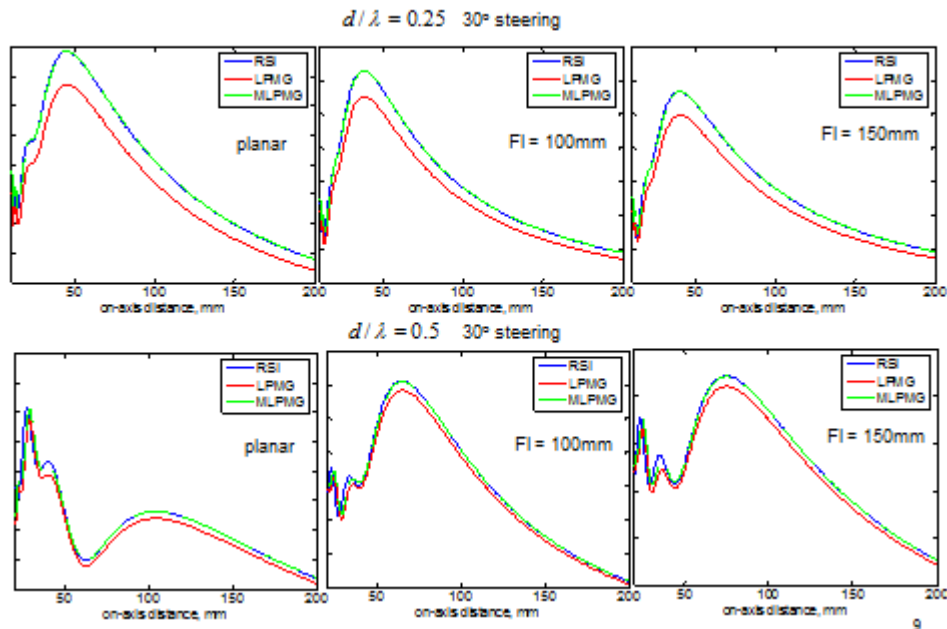


Figure D.8. Examples Of Amplitude-Corrected LPMG Model Calculations

Simulation examples (with amplitude corrections)

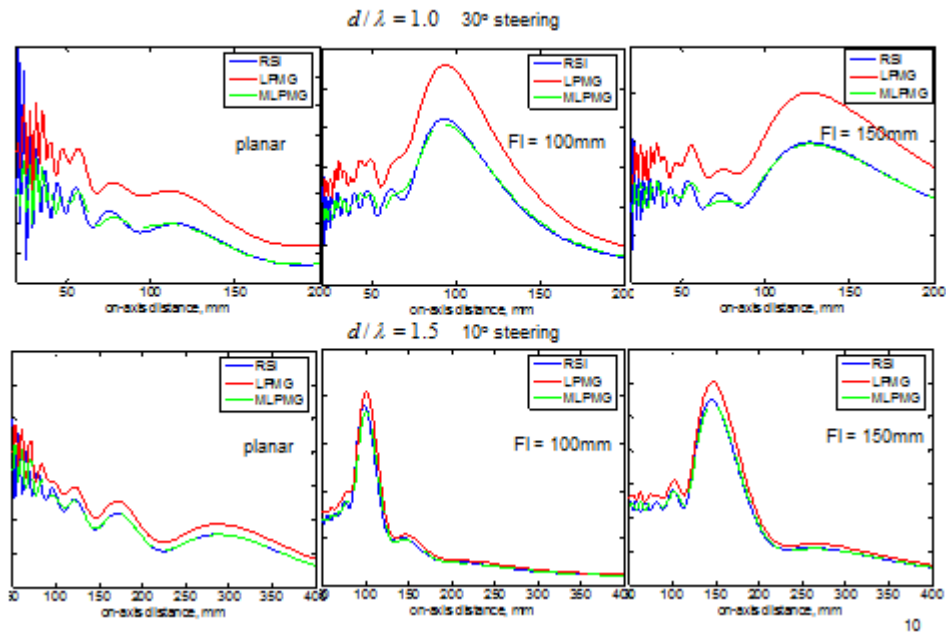


Figure D.9. Examples Of Amplitude-Corrected LPMG Model Calculations

Simulation examples (for cases not in the table)

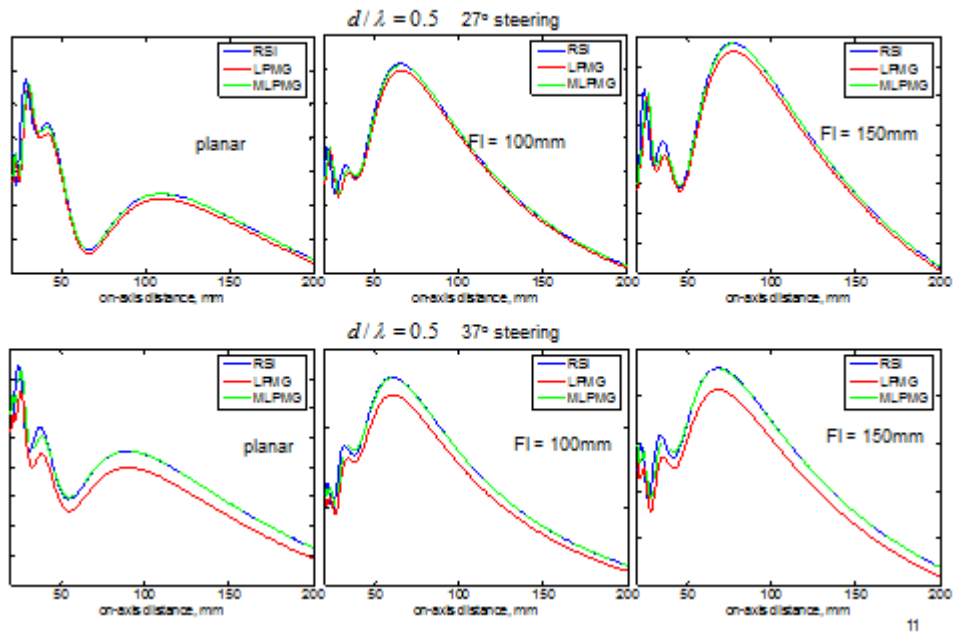
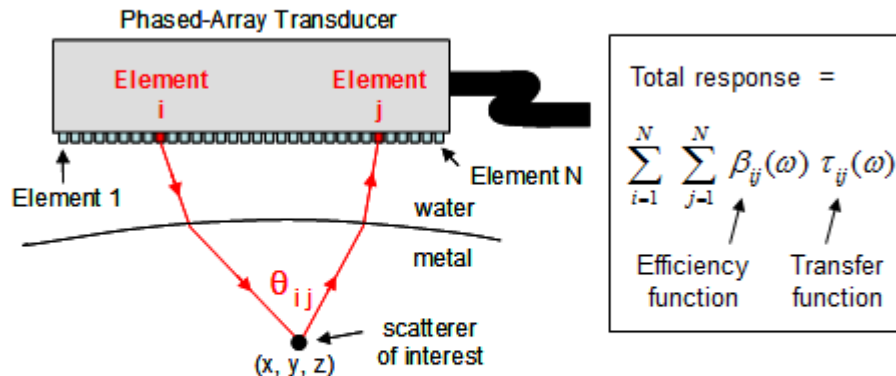


Figure D.10. Examples Of Amplitude-Corrected LPMG Model Calculations

- For phased-array transducers, many combinations of transmitting (i) and receiving (j) elements contribute to the total response.



- To model the response, the system frequency-dependent system efficiency functions must be known. These govern the efficiency of the element pair for converting electrical energy \longleftrightarrow sound.
- There are many independent (i, j) pairs, hence many independent efficiency functions to be determined.

1

Figure D.11. PA Measurement Model Concept

- Assume that array elements behave pretty much the same, except for certain "residual differences".
- Element-to-element differences are accounted for by two "residual" parameters:
 - 1) A strength factor (A) which describes the relative "hotness" of an element compared to its peers; and
 - 2) A time delay (Δt) which describes the extent to which an element fires later or earlier than its peers when all elements are instructed to fire in unison.
- These residuals are used to relate the system efficiency function for any pair of elements to that of an average efficiency which can be readily measured.

$$\beta_{ij}(\omega) = \beta_{average}(\omega) \sqrt{A_i A_j} \exp[-i\omega(\Delta t_i + \Delta t_j)/2]$$

$\uparrow \uparrow$
 Residual strength
parameters

$\uparrow \uparrow$
 Residual time
delays

2

Figure D.12. System Efficiency Factor Determination For PA Model

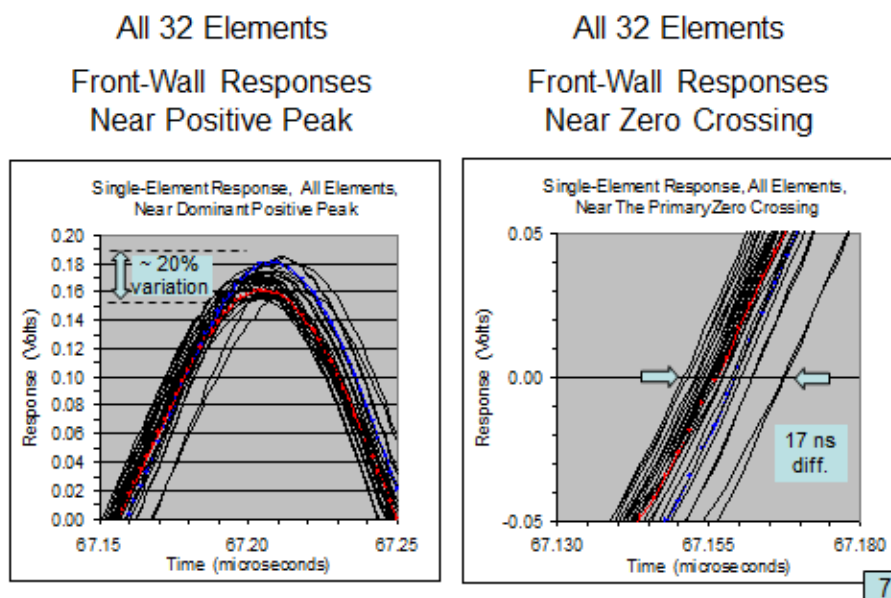
How This Works In Practice

- To determine the residuals, the N array elements are fired one-at-a-time in pulse/echo mode toward a "matching surface". The N responses are compared to each other to determine the residuals.
- This is meant to be done only occasionally (say to check for transducer changes over time).
- On any day that the transducer is used for inspections, a single "reference signal" is acquired (typically with the transducer elements operating in concert as a phased array).
- This reference signal can be used to deduce the average efficiency function for use in model simulations of the inspections.

3

Figure D.13. PA Probe Characterization Concept And Use

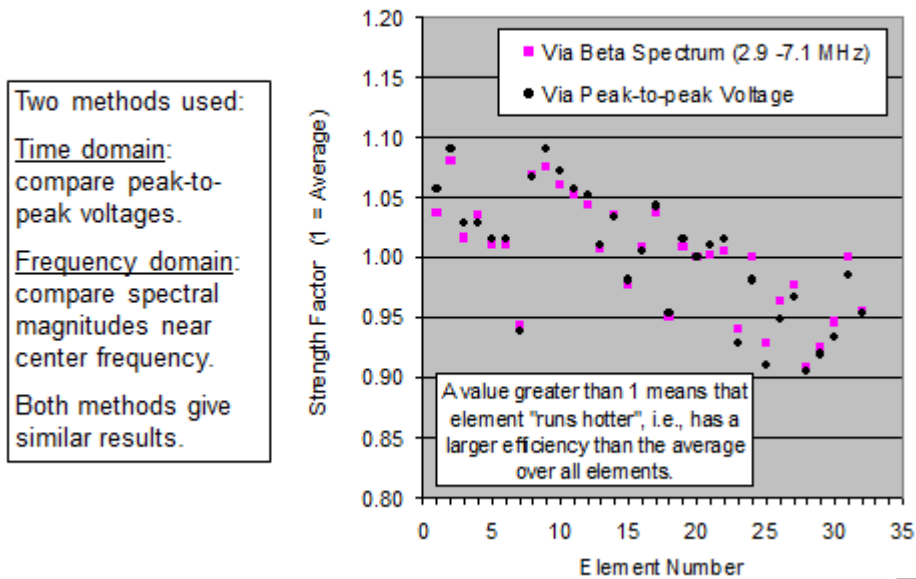
Differences Between Elements Are Readily Seen



7

Figure D.14. Measured Amplitude And Time Delay Deviations For A 5 MHz, 32 Element PA Transducer

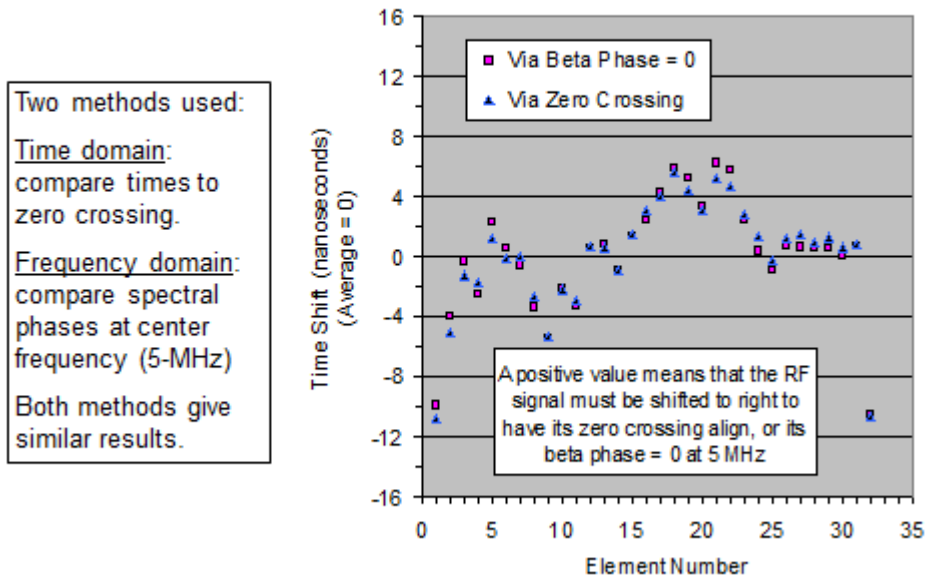
Measured Residual Strength Factors



8

Figure D.15. Amplitude Residuals For 5 MHz, 32 Element PA Probe

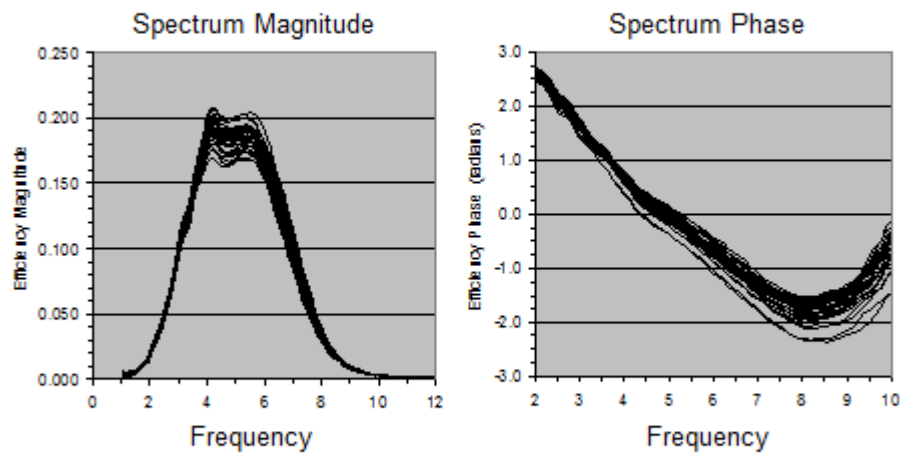
Measured Residual Time Delays



9

Figure D.16. Time Delay Residuals For 5 MHz, 32 Element PA Probe

Measured Single-Element P/E System Efficiency Factors [$\beta_{ii}(\omega)$]

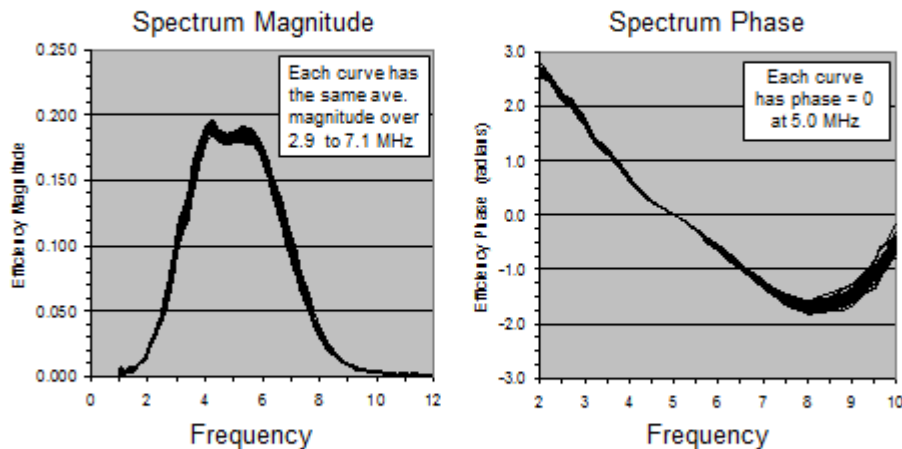


- Each plot has 32 curves, one for each element. The differences between single-element operating characteristics are indicated by the vertical spread of the curves.

10

Figure D.17. Single Element System Efficiency Factors, Uncorrected

Rescaled and Time-Shifted Single-Element Efficiency Factors

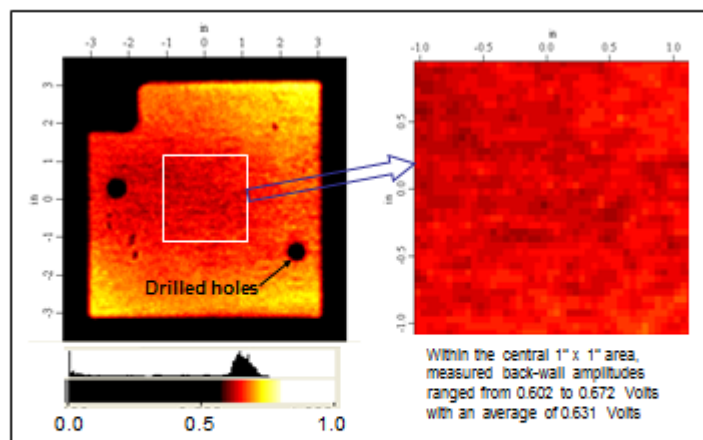


- Each plot has 32 curves, one for each element. If our approximation were exact, all 32 curves would be identical. Most (but not all) of the element-to-element variation is accounted for by our approach.

11

Figure D.18. Single Element System Efficiency Factors, Corrected

The Stainless Steel Test Specimen

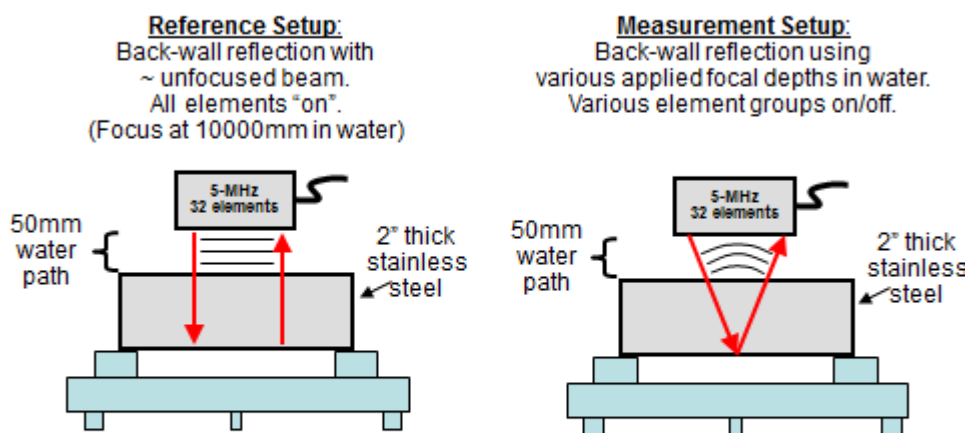


- Above is a back-wall amplitude C-scan of the specimen obtained using a conventional 5-MHz fixed-focus transducer.
- Some variation is seen due to the forging microstructure (roughly 90 micron average grain diameter). Attenuation-vs-frequency was measured and used as one model input (~ 2.3 dB/inch at 5 MHz).

12

Figure D.19. UT C-Scan Image Of Steel Test Block

Experiment Setups

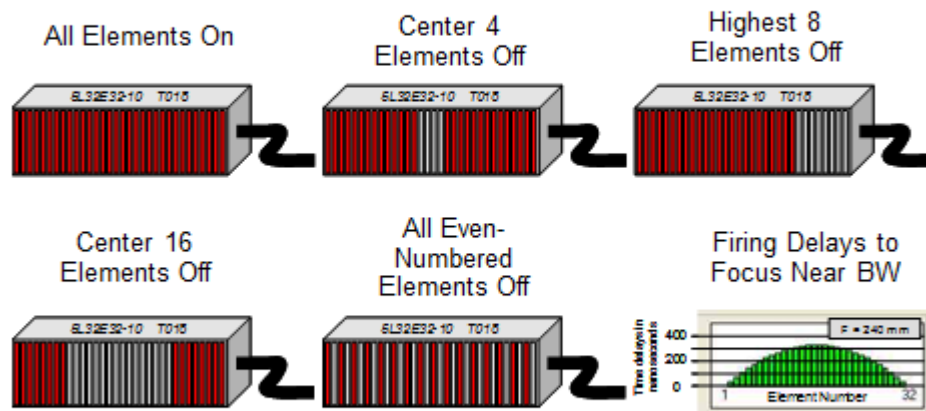


- For each experimental trial there is a "reference setup" (used to determine the average system efficiency factor) and a "measurement setup" (used to acquire data for comparison to computer simulations).
- Examples are shown above.

13

Figure D.20. Measurement Configurations For PA Probe Characterization Tests

Firing Pattern Study: Various Choices For The Elements Which Are Active For Transmission And Reception

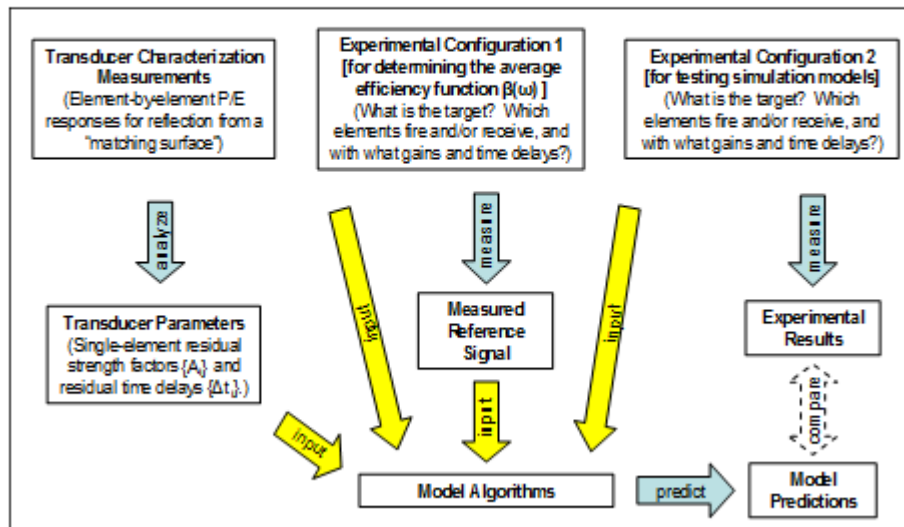


- To test simulation capabilities, some measurements were made with various groups of elements turned off.

14

Figure D.21. Various PA Focal Laws Used In Probe Characterization Tests

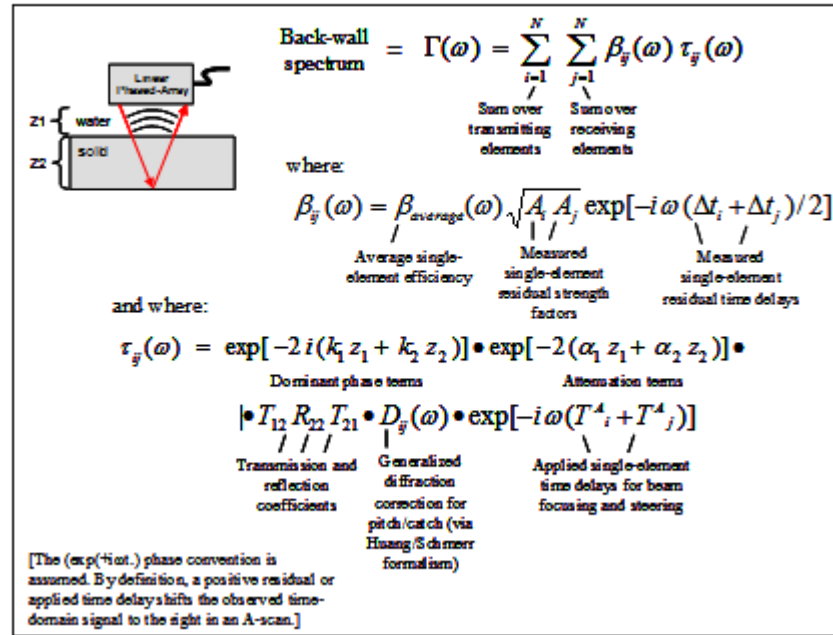
Flow Chart For Using Measured Residuals As Inputs To Test Simulation Models for Phased-Array Inspections



15

Figure D.22. Approach Used To Test PA Probe Characterization Method

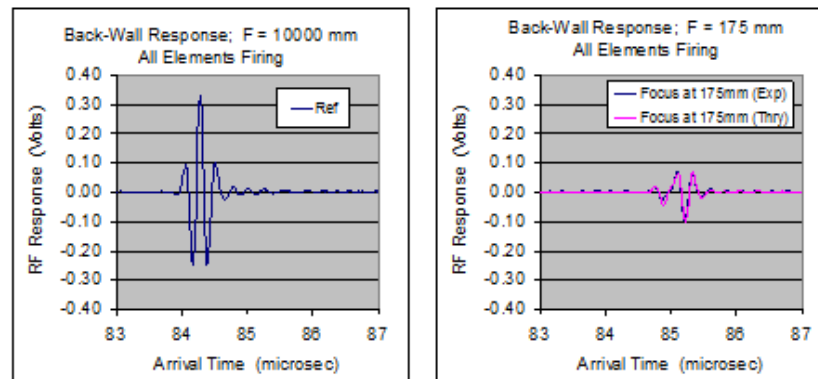
Inspection Simulation Formalism



16

Figure D.23. PA Measurement Model Description For Backwall Reflection

Examples of Measured and Predicted Back-Wall Waveforms



Measured Reference Signal
(All elements firing, unfocused beam)

Measured & Predicted BW
(All elements firing, beam
focused in front of back wall)

17

Figure D.24. Reference Signal And Comparison Of Model And Experiment For One Focal Law

Examples of Measured and Predicted Back-Wall Waveforms

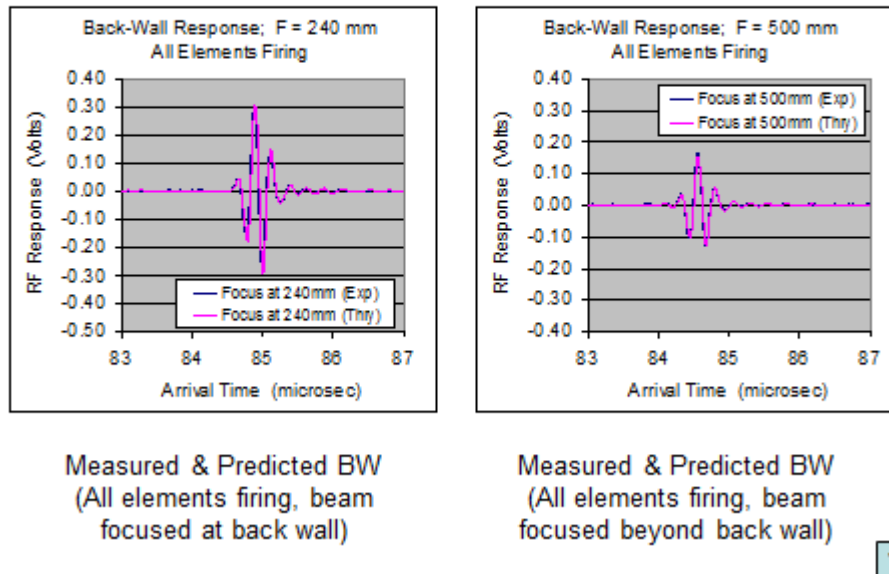


Figure D.25. Comparisons Of Model To Experiment For Two Focal Laws

Examples of Measured and Predicted Back-Wall Waveforms

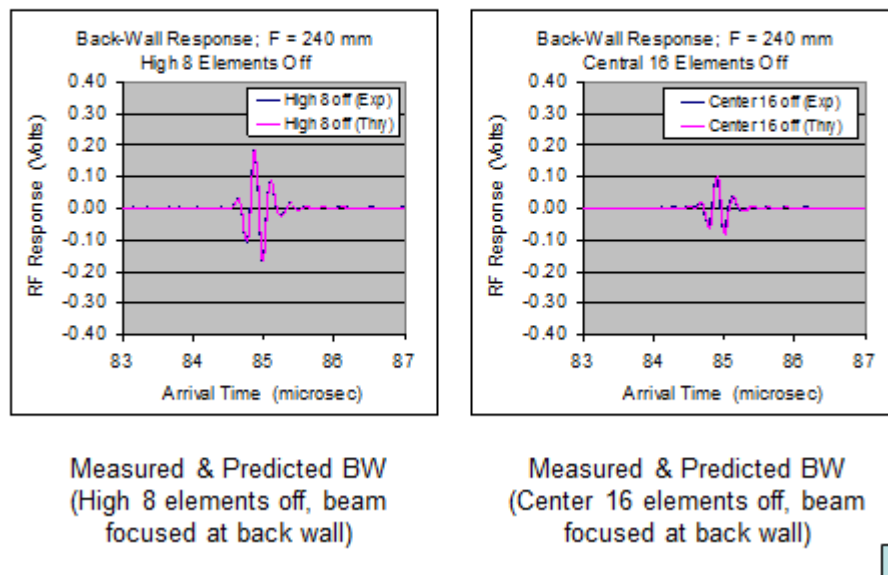


Figure D.26. Comparisons Of Model To Experiment For Two Focal Laws

Comparing Measured and Predicted BW Spectra

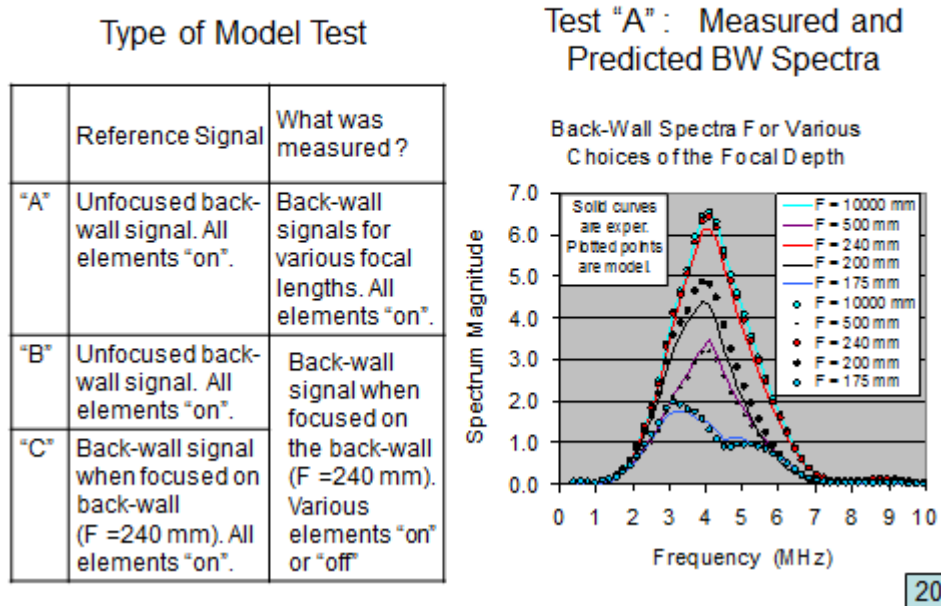


Figure D.27. Model Versus Experiment Comparisons Of Spectra For Various Focal Laws

Comparing Measured and Predicted BW Spectra

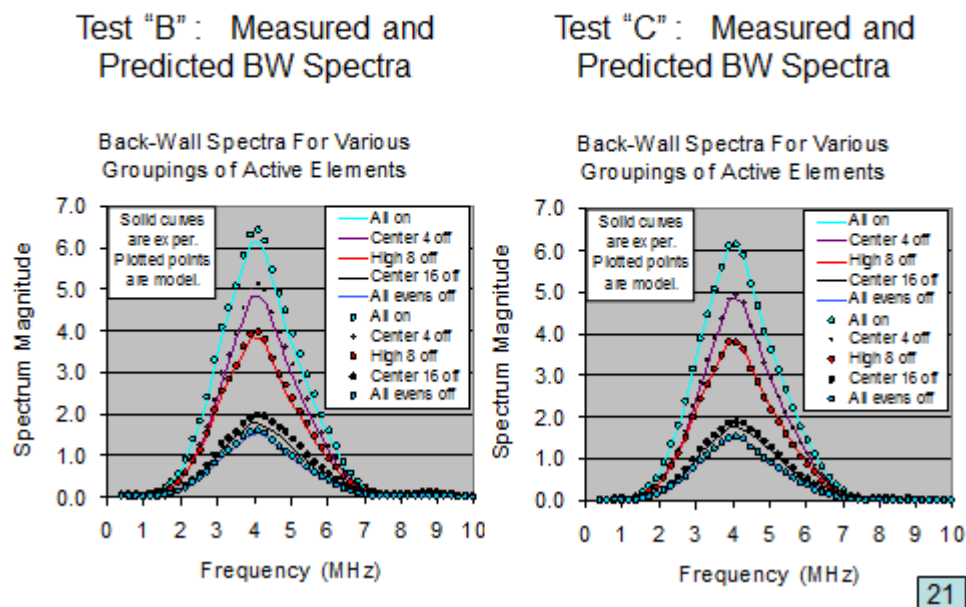


Figure D.28. Model Versus Experiment Comparisons Of Spectra For Various Focal Laws

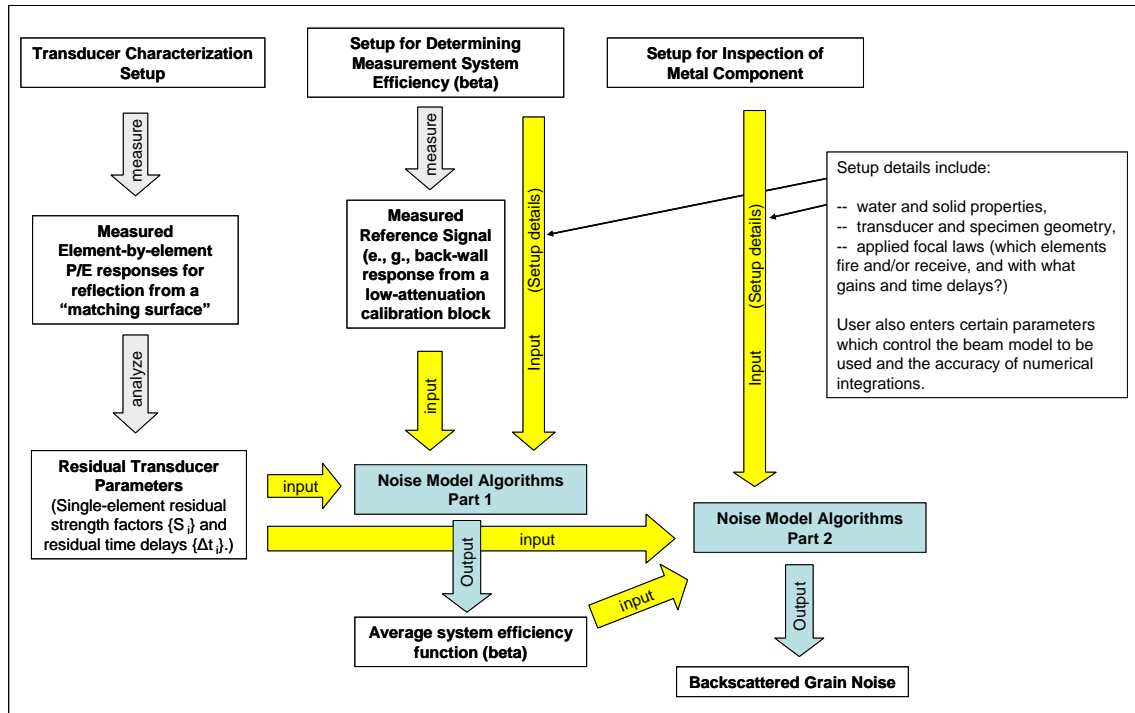


Figure D.29. Flowchart For PA Noise Model Calculations

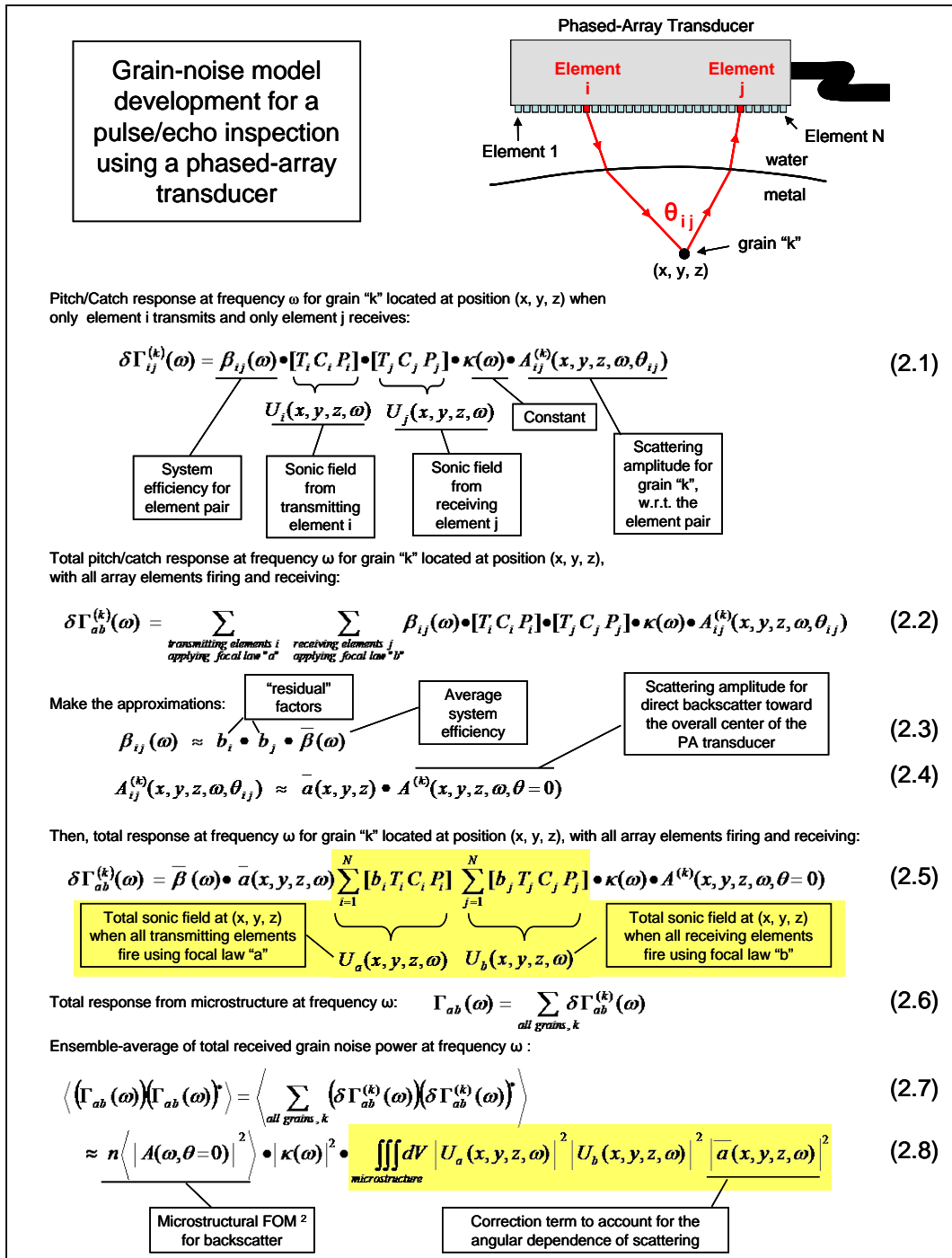


Figure D.30 PA Model For Computing RMS Grain Noise